Summer 8-15-2022

Understanding Control of Metabolite Dynamics and Heterogeneity

Christopher John Hartline
Washington University in St. Louis

WASHINGTON UNIVERSITY IN ST. LOUIS

McKelvey School of Engineering
Department of Energy, Environmental & Chemical Engineering

Dissertation Examination Committee:
Fuzhong Zhang, Chair
Petra Levin
Diego Oyarzún
Yinjie Tang
Joshua Yuan

Understanding Control of Metabolite Dynamics and Heterogeneity

by
Christopher John Hartline

A dissertation presented to
the McKelvey School of Engineering
of Washington University
in partial fulfillment of the
requirements for the degree of
Doctor of Philosophy

August 2022

St. Louis, Missouri

Table of Contents

List of Figures

List of Tables

Acknowledgements

I am grateful for the many friends, family and colleagues who have supported me during my studies at Washington University. First, I would like to thank my Ph.D. advisor and committee chair Dr. Fuzhong Zhang for his mentorship and support over the many years. I would also like to thank my committee members, Dr. Petra Levin, Dr. Tae Seok Moon, Dr. Diego Oyarzún, Dr. Yinjie Tang, and Dr. Joshua Yuan who helped contribute their unique perspectives to my graduate studies. I will always remember the many discussions with my mentors which helped me grow both as a researcher and as a person. I also want to thank my collaborators, Dr. Ahmad Mannan and Dr. Diego Oyarzún. I enjoyed working with them and learned a lot as a result of our collaborations.

I want to thank my wonderful lab mates who were a source of fun and friendship throughout my time at Washington University. In particular, I want to thank Drs. Alexander Schmitz, Di Liu, Chris Bowen, Wen Jiang, and Cameron Sargent along with Yichao Han, and Ruixue Zhang for their great discussions, and good times both in and out of the laboratory. I would like to give special thanks to Dr. Jeffrey Czajka and Dr. Austin Rottinghaus who started the Ph.D. program with me and shared in my trials and joys.

I would also like to acknowledge research funding from the Human Frontier Science Program (grant no. RGY-0076-2015), the United States National Science Foundation (MCB1453147) the United States Department of Energy (DOE DESC 0018324), and the National Institute of General Medical Sciences of the National Institutes of Health (Award Number R35GM133797).

Finally, I would like to thank my parents for always encouraging me to do my best. Most importantly, I would like to thank my wife Jillian for her unending patience, encouragement, and support. Without her, this Ph.D. would not have been possible, and I am truly grateful to have her in my life.

Christopher J. Hartline

Washington University in St. Louis

August 2022

Dedicated to my family.

ABSTRACT OF THE DISSERTATION

Understanding Control of Metabolite Dynamics and Heterogeneity

by

Christopher John Hartline

Doctor of Philosophy in Energy, Environmental & Chemical Engineering

Washington University in St. Louis, 2022

Professor Fuzhong Zhang, Chair

Microbes live in complex and continually changing environments. Rapid shifts in nutrient availability are a common challenge for microbes, and cause changes in intracellular metabolite levels. Microbial response to dynamic environments requires coordination of multiple levels of cellular machinery including gene expression and metabolite concentrations. This coordination is achieved through metabolic control systems, which sense metabolite concentrations and direct cellular activity in response. Several reoccurring control architectures are found throughout diverse metabolic systems, which suggests underlying evolutionary advantages for using these control systems to coordinate metabolism. One common, yet understudied, control architecture is the positive feedback metabolite uptake loop, which features a metabolite responsive-transcription factor (MRTF) that activates genes necessary to uptake its cognate metabolite. Understanding the design principles behind these complex metabolic control systems is a fundamental issue across many biological sub-disciplines since metabolism is a central feature of cellular behavior.

The goal of this dissertation is to elucidate how the architecture and parameters of a MRTF-based control system shape metabolite dynamics and heterogenous metabolic response to changing nutrient environments. This dissertation focuses on the *Escherichia coli* fatty acid degradation

system, which employs the positive feedback uptake loop architecture. The function and performance of these control systems to three common metabolic tasks was evaluated. First, after a nutrient depletion, microbes must rapidly turn off metabolic pathways to conserve resources. Second, microbes must maintain sensing ability in the face of metabolic conditions which impact cellular growth rate. Finally, upon abrupt shifts between nutrients, microbes must shift metabolic resources to uptake the new nutrient or otherwise cease growth. This shifting process can be heterogenous, with a sub-population which maintains a non-growing state that confers tolerance to antimicrobial compounds. Taken together, this work provides deeper understanding of the design principles for the control of metabolite dynamics and heterogeneity for applications in metabolic engineering and synthetic biology.

Chapter 1: Introduction

This chapter contains text and figures published as:

Hartline, C.J.*, Schmitz, A.C.*, Han, Y.*, and Zhang, F. (2021). Dynamic control in metabolic engineering: Theories, tools, and applications. *Metab. Eng.* 63, 126–140. doi:10.1016/j.ymben.2020.08.015.

and

Schmitz, A. C.*, Hartline, C. J.*, and Zhang, F. (2017). Engineering microbial metabolite dynamics and heterogeneity. *Biotechnol. J.* 12, 1700422. doi:10.1002/biot.201700422.

Reprinted with permission.

*Authors contributed equally to work.

Microbes are highly adaptive living creatures capable of self-replication and complex chemistry. These properties make microbes a potentially useful tool in solving complex environmental challenges. For example, engineering microbes for chemical production is a growing field which has enabled the renewable synthesis of a wide range of target products including fuels (Jiang et al., 2017, 2018; Bai et al., 2019), polymer precursors (Bowen et al., 2016; Zheng et al., 2020), medicines and nutraceuticals (Yuan and Alper, 2019; Rahmat and Kang, 2020), flavors and fragrances (Chen et al., 2020), and even metallic nanoparticles (Reed and Alper, 2018). Despite these promising starts, commercial production of these compounds in industrial scales has been lagging, largely due to the inability of the engineered strains to maintain stable performance at large scales while meeting stringent titer, rate, and yield (TRY) requirements

(Wehrs et al., 2019). Similar to how control systems in chemical processes can improve performance and safety metrics (Ng and Stephanopoulos, 1996), incorporating genetic control systems to sense and control microbial metabolite concentrations is beginning to be explored as a method to improve microbial production of chemicals.

At the same time, microbes can adapt to and replicate in the human body and cause disease. Bacterial infection due antimicrobial resistant bacteria are thought to contribute to at least 700,000 deaths annually as of 2016, and some estimates that number will grow to 10 million annually by 2050 without action to limit the spread of antimicrobial resistance in bacteria (O'Neill, 2016; Theriault et al., 2021). Ongoing research into antimicrobial resistance mechanism have shown the importance of metabolism in providing protection against antimicrobial compounds (Amato et al., 2014; Stokes et al., 2019). Microbes have evolved natural metabolite-sensing control systems which allow them to sense changes in their environment and tune metabolism in response. These control systems can drive metabolism to enhance growth in fluctuating environments (Nguyen et al., 2021), reduce growth to protect against toxic compounds (Peng et al., 2015), and can even activate disease-causing phenotypes under varying metabolic conditions (Abu Kwaik and Bumann, 2013). Additionally, these control systems are implemented through stochastic molecular mechanisms which allow a population of cells to display a range of responses to their environment. These diversified responses of microbes to their environment can make treatment of disease more challenging.

Because metabolism is central to many aspects of microbial life, understanding how cells control their metabolite concentrations over time (called 'metabolite dynamics') and the variation of metabolite concentration in a population of cells (called 'metabolite heterogeneity') is critical

to many fields of microbiology including the development of advanced microbial chemical synthesis platforms and the treatment of disease caused by microbes.

1.1 Metabolite Dynamics in Natural and Engineered Microbes

1.1.1 Overview of Metabolite Dynamics

Microbial function relies on thousands of molecular components constituting a complex network of gene-protein-metabolite interactions. These systems display a wide range of temporal responses which are difficult to understand based on knowing the presence of molecular interactions alone (Tyson and Novak, 2020). Because of these complexities, biologists from a broad range of disciplines have begun to adopt language and ideas from the mathematical analysis of dynamical systems and control theory to aid in analyzing and designing network interactions in biological systems (He et al., 2016; Vecchio et al., 2016). At the heart of these analyses is the conversion of a map of network interactions into a set of ordinary differential equations of the form:

$$\frac{\mathrm{d}\,\mathbf{x}}{\mathrm{dt}} = \mathrm{f}(\mathbf{x}) + \mathrm{d}(\mathrm{t})$$

Here, $\boldsymbol{x}$ is a vector representing the metabolic state of the cell, which is the concentration of all molecular species being analyzed. The time derivative of $\boldsymbol{x}$ represents the rate of change of those molecular species. Thus, the temporal change in each species depends both on the current metabolic state, and on the specific molecular interactions which map the current state into a rate of change for the concentration of each molecular species. Additionally, an external disturbance d can be introduced which impacts the temporal evolution of the systems. This framework has been widely successful in describing the how gene networks respond to stimuli (Smolen, 2000; Tegnér

et al., 2003; Dayarian et al., 2009) and have been used in the development of novel gene-protein interactions for controlling microbial behavior (Kelly et al., 2018; Aoki et al., 2019).

Metabolite dynamics focuses on how metabolite concentrations inside the microbial cell change over time. Metabolite dynamics occur when there is an imbalance in the rate of production and consumption of a metabolite which causes a net change in the metabolite concentration over time, i.e. $d\mathbf{x}/dt \neq 0$. Several factors can lead to this imbalance, particularly the presence of a new disturbance such as a change in the external concentration of one or more metabolites. If the metabolic network is asymptotically stable, the system will eventually reach a steady-state condition where there is no net change in metabolite concentrations. Analysis of the metabolite dynamics can reveal several key properties of the system which affect its biological function. As examples, the rate of convergence to a steady state (Liu and Zhang, 2018), the existence of multiple steady states (Venturelli et al., 2012), oscillations in metabolite concentrations (Fung et al., 2005), and the presence of delays and overshoots (Novák and Tyson, 2008) are all important properties of metabolite dynamics. These properties can impact cell growth, productivity, and response and therefore are key metrics of analyzing performance. Additionally, the use of optimality principles can be included in the analysis to uncover trade-offs and design principles in controlling metabolite dynamics in both natural and engineered control systems (Chubukov et al., 2012; Oyarzún and Stan, 2013). These many lines of analysis can provide deeper insight into the biological role of evolved gene-protein-metabolite interactions, as well as the design of new interactions to enhance metabolite productivity in fermentations.

1.1.2 Metabolite Dynamics Affect Fitness of Natural Microbes

Metabolite dynamics serve as a driver of cellular response to the environment (Gerosa and Sauer, 2011), rather than simply being an output of cellular functions. These driving mechanisms

occur at all levels of cellular function including transcription, translation, and post-translation. At the transcriptional level, metabolites can directly drive cell adaptations through metabolite-responsive transcription factors (MRTFs) to continuously control gene expression profiles. Nearly half of all transcription factors in *E. coli* are regulated directly through binding to metabolites (Madan Babu, 2003; Krishna et al., 2007). Changes in metabolite availability often dive changes in expression of metabolite-specific pathways, to allocate more resources to that metabolite's catabolism or anabolism. Well known examples include *lacI* and *araC*, which strongly upregulate lactose and arabinose catabolic pathways, respectively, when these sugars are available intracellularly. Other MRTFs more globally coordinate many metabolic processes and genes, such as Lrp, which upregulates up to 10% of *E. coli* genes, including amino acid biosynthesis and catabolism and pili synthesis in response to leucine (Tani et al., 2002).

In addition to binding MRTFs, metabolite binding to RNA aptamers is gaining recognition as an important way in which metabolites drive cell response through regulation of protein translation, which can drive changes in metabolite concentrations in some cases (Barrick et al., 2004; Mandal et al., 2004; Serganov et al., 2008). For example, a wide-spread guanidine responsive *ykkC* riboswitch is found in urea carboxylases, arginases, nitrate/sulfate/bicarbonate transporters, and in small multidrug resistance efflux pumps (Nelson et al., 2017). This riboswitch senses the concentration of guanidine, and increases export if concentrations are too high to prevent cytotoxicity. Thus, metabolite dynamics drive changes in protein abundance through diverse transcription and translation control mechanisms.

Upon entering new environmental conditions, the expression of new proteins can take several minutes, while the dilution of old proteins through cell growth can take several hours. Additionally, intrinsic noise in transcription and translation can create cell-to-cell differences

protein abundance which cannot be avoided (Kochanowski et al., 2015). Thus, microbes have also evolved fast responding mechanisms for controlling metabolic flux in response to metabolite changes (Kochanowski et al., 2013). Metabolites can affect flux through allosteric control mechanisms by binding directly to enzymes to affect their kinetic properties. A particularly striking example is in the control of TCA cycle anaplerosis (Xu et al., 2012). Here, phosphoenolpyruvate is accumulated by shutting down activity of PEP carboxylase through depletion of fructose-1,6-bisphosphate, which acts as an allosteric activator of PEP carboxylase. Disruption of this allosteric mechanism through point mutation disrupts growth when glucose availability oscillates (Xu et al., 2012), which demonstrates the necessity of these fast mechanisms for adaptation to fluctuating environments. Despite several well-known examples, systematic identification of allosteric metabolite-protein interactions with biological function is difficult due to their highly transient nature, and the current mapping of allosteric metabolite-protein interactions is likely far from completion (Ledezma-Tejeida et al., 2021). Nonetheless, recent advances in proteomic methods have enable the identification of hundreds of novel interactions between metabolites and enzymes (Li et al., 2010; Link et al., 2013; Feng et al., 2014; Diether et al., 2019).

In addition to direct interaction with proteins, metabolites can trigger post-translational modifications though enzyme phosphorylation and acetylation which alter the kinetic activity of metabolic enzymes (Kochanowski et al., 2015). Like direct allosteric interactions, post-translational modifications are rapid and reversable, but most often catalyzed by a metabolite sensor with kinase or acetyltransferase activity. A well-known example of this is the isocitrate dehydrogenase (ICD) kinase, AceK in *E. coli*, which directs isocitrate between the glyoxylate shunt, or the full TCA cycle through both phosphorylation/dephosphorylation of ICD (Walsh and

Koshland, 1985). AceK is thought to sense the abundance of ATP/ADP to switch between TCA cycle and glyoxylate shunt (Zheng and Jia, 2010), thus allowing a robust tuning of the rates of the two pathways (Shinar et al., 2009). Deactivation of AceK phosphatase activity causes growth arrest on acetate (LaPorte et al., 1985), showing that this control mechanism is necessary to correctly balance the activity of the two pathways. Until recently, only a small number of these post-translational control mechanisms have been identified, but recent work has shown that post-translational modification of enzymes is widespread in bacteria metabolism (Brunk et al., 2018; Schastnaya et al., 2021). Systematic identification of these control mechanisms, and the metabolites which drive them is likely to be an ongoing challenge. Altogether, these diverse and wide-spread metabolite sensing and control mechanisms demonstrate the importance of controlling metabolite dynamics to the growth and fitness of bacteria.

1.1.3 Metabolite Dynamics Affects Productivity of Engineered Microbes

Metabolite dynamics are also important to consider in industrial fermentations. Cells face two types of environmental variations during batch processes: slow global environmental changes due to process progression, and local environmental heterogeneity. Traditionally, cellular productivity is optimized for production in a single environment and at either exponential or stationary growth phase, which leads to sub-optimal productivity as the environment or cell growth phase changes during a production process (Gadkar et al., 2005; Anesiadis et al., 2008). Due to the difficulty in maintaining a homogenous environment in a large fermenter, cells can pass through regions with varied microenvironments, for instance different pH and different oxygen or substrate concentrations (Lara et al., 2006; Nadal-Rey et al., 2021). These disturbances result is changes in internal metabolite concentrations and affect bioproduction. Controlling metabolite dynamics can address these challenges by altering output of both natural and engineered metabolic

pathways in response to environmental changes, which has been done through the dynamic regulation of fatty acid ethyl ester and fatty acid producing pathways to achieve high productivity and yield (Zhang et al., 2012a; Xu et al., 2014; Liu et al., 2015).

Production of some chemicals through metabolic engineering can be suboptimal, or even infeasible without controlling metabolite dynamics, particularly if the engineered pathway significantly impacts cell growth. In some cases, a two-stage metabolic switch can be used to decouple the competing tasks of biomass accumulation and metabolite overproduction (Burg et al., 2016). In this mode of dynamic metabolic engineering, metabolism is optimized for biomass accumulation in the first stage, while product formation is optimized during the second stage. Early work showed that glycerol production in *E. coli* could be improved by 30% using this two-stage strategy (Gadkar et al., 2005). Continuous sensing and control of metabolite production pathways can also be used to balance metabolite production and cell toxicity for improved production metrics, as demonstrated in the production of pinene in *E. coli* (Dunlop et al., 2010; Siu et al., 2018). In this system, toxic pinene accumulation was sensed through a stress response TF MexR, which increased expression of pinene efflux pumps whenever pinene accumulated too much. This was shown to enhance tolerance to pinene production over a wide range of system parameter values (Siu et al., 2018). Thus, from both fundamental science and metabolic engineering perspectives, it is important to understand and have the ability to control metabolite dynamics.

1.2 Metabolite Heterogeneity in Natural and Engineered Microbes

1.2.1 Overview of Metabolite Heterogeneity

Genetically identical microbes display phenotypic heterogeneity even in identical environment, due to many inherent stochastic processes governing cell biology. For example, random segregation of molecules between daughter cells, stochastic gene expression, stochastic

translation machinery concentration, and stochastic enzyme catalysis are all sources of heterogeneity within a microbe. Because of the highly interconnected network of gene-protein-metabolite interactions, these sources of heterogeneity can propagate to cell-to-cell differences in metabolite concentrations. The extent and consequences of metabolite heterogeneity to microbial biology have only been recently revealed experimentally due to difficulties in analyzing metabolite concentrations at single cells, particularly during cell growth (Mustafi et al., 2012; Ibáñez et al., 2013; Zenobi, 2013; You et al., 2015).

The study of metabolite heterogeneity focuses on quantifying and modeling the shape of the distribution of metabolite concentrations across a population of cells. Important metrics are the mean and standard deviations of the population (Kiviet et al., 2014), the frequency of outliers with extremely altered metabolism (Hare et al., 2021), and the presence of multimodality (Guantes et al., 2016). Several methods for modeling and simulating metabolite heterogeneity have been put forward (Levine and Hwa, 2007; Thomas et al., 2011; Oyarzún et al., 2015; Ray et al., 2016). A popular starting point for modeling metabolite heterogeneity involves setting up a chemical master equation to keep track of the number and fluctuations of metabolites and other compounds over time, which can then be simulated by the Gillespie algorithm, or approximated used a tau-leaping method (Gillespie, 2007). However, this approach has difficulties due to the many timescales involved in production and consumption of intracellular metabolites (Tonn et al., 2019). Thus, frameworks for analyzing metabolite heterogeneity and its connection with gene-protein-metabolite network structures is an active field of research.

1.2.2 Metabolite Heterogeneity Affects Fitness of Natural Microbes

Variation of single cell metabolite concentration affects the collective behavior of a culture, even under constant environments. Flux balance analysis using experimentally measured single-

cell protein copy numbers (Taniguchi et al., 2010) predict that there is a large variation on single cell metabolic activities, that could lead to single cell growth rate variation as much as five-fold (Labhsetwar et al., 2013). Furthermore, experimentally measured coefficient of variation (CV) (standard deviation divided by mean) of single cell growth rate ranges from 0.2 to 0.4 (Kiviet et al., 2014). Both the size and the frequency of growth rate fluctuation is likely caused by fluctuations in the concentration of cellular components, including metabolites.

Metabolite heterogeneity can also play a larger role in fluctuating environments, especially in rapidly switching environments. Under these rapidly varying conditions, microbial populations may maintain multiple sub-populations with different metabolic pathways active, so that some cells are always optimized from growth upon environmental changes (Grimbergen et al., 2015). The potential benefit of this bet-hedging, or stochastic switching, strategy was demonstrated in galactose utilization network of *Saccharomyces cerevisiae,* where cells were engineered to randomly activate galactose pathways at different rates (Acar et al., 2008). It was found that populations which had frequent random switching grew faster under rapid fluctuations between galactose and glucose, as compared to populations with less frequent random switching. Phenotypic heterogeneity has also been observed upon diauxic shifts from glucose to many carbon sources in many microbial species (Boulineau et al., 2013; New et al., 2014; Solopova et al., 2014). For example, in *Lactococcus lactis* undergoing diauxic shift from glucose to cellobiose, only a small fraction of the population activated cellobiose consumption pathways once glucose was depleted, while the remaining fraction stopped growth (Solopova et al., 2014). Moreover, the size of fraction which transitioned to cellobiose was smaller if initial glucose concentrations were higher, which suggests cell's ability to adapt depends on their initial metabolic environment and potentially their initial metabolism. This phenomenon of responsive diversification, where a

population of adapted and non-adapted cells emerge from a single population, was also observed in *E. coli* during rapid nutrient shifts from glucose to fumarate (Kotte et al., 2014). Many factors potentially affect the size of the heterogeneity in switching times between nutrient sources including cell-to-cell differences in transcriptional activity, sensing components, or stochastic difference in metabolic pathways prior to switching (Schwabe and Bruggeman, 2014; Radzikowski et al., 2016; Chu, 2017; Barthe et al., 2020). For example, in the case of *L. lactis* transition to cellobiose, knockout of the stringent response gene *relA* increased the number of cells which transition (Solopova et al., 2014), implicating a role for the stringent response mechanisms and its key metabolite signal, (p)ppGpp (Magnusson et al., 2005), in governing switching times and frequency.

Metabolic heterogeneity has also been shown to underly some mechanisms bacterial persistence (Amato et al., 2014). Bacterial persistence allows a sub-population of bacteria to tolerate to antibiotic treatment (Balaban et al., 2019), which could be one mechanism that leads to recurrent infection in a clinical setting (Michiels et al., 2016). Persistence is a phenotype typically associated with transient metabolic dormancy (Wood et al., 2013) which slows the activity of many growth-related processes which are traditionally targeted by antibiotics. After persistence, cells can regrow and generate a new population, where again only a few cells are persisters, indicating that the persister phenotype is not inherited and that underlying stochastic process play a role in triggering persistence (Harms et al., 2016). Stochastic expression of toxin-antitoxin systems, which can trigger elevated levels of the signaling metabolite ppGpp are one mechanism by which cells enters persister state (Ronneau and Helaine, 2019). ppGpp shuts down transcription and translation, thus acting as a general signaling mechanism for cells to become dormant (Pacios et al., 2020). However, while knocking out genes responsible for ppGpp synthesis reduces persister

levels, it does not prevent persisters (Nguyen et al., 2011). Reduced ATP concentrations have also been associated with elevated persistence (Conlon et al., 2016; Manuse et al., 2021), independent of the formation of ppGpp (Shan et al., 2017). However, low ATP is also associated with slow growth, which may partially account for increased antibiotic tolerance, and therefore may not be a trigger of persistence (Pacios et al., 2020). Rapid nutrient shifts and diauxic shifts from glucose to fumarate, glycerol, and succinate also trigger elevated levels of persistence to multiple antibiotics (Amato et al., 2013; Amato and Brynildsen, 2014, 2015; Radzikowski et al., 2016). For example, in the case of glucose to fumarate shifts in *E. coli*, nearly all cells become persisters after the switch, and those cells activated several stress response genes which could give cells protection against antibiotics (Radzikowski et al., 2016). It was proposed that the ultimate cause of entry into persistence was a flux limitation in central metabolism, and cell-to-cell differences in the activity of fructose-1,6-bisphosphatase (Fbp) may explain why some cells adapt and others become persisters (Radzikowski et al., 2016). This view was later supported by observations of large heterogeneity in the expression of TCA cycle enzymes, where stochastically low TCA expression was associated with elevated tolerance to ciprofloxacin (Zalis et al., 2019). This evidence shows that, while there are likely many contributing factors to bacterial persistence, heterogeneity in metabolism is a central feature of persistence, which warrants further experiment into identifying the potential metabolite and metabolic triggers which explain cell-to-cell differences in entry and exit from the persistence phenotype.

1.2.3 Metabolite Heterogeneity Affects Cellular Productivity

While heterogeneity in bioreactor conditions has been shown to impact bioproduction, the importance of metabolite heterogeneity is only beginning to be recognized. Large cell-to-cell variation on productivity of engineered microbes was observed in the biosynthesis of 5’-

pyrophospate in *E. coli* (You et al., 2015), the production of free fatty acids (FFA) in *E. coli* (Xiao et al., 2016), and the production of L-valine, L-leucine, and L-isoleucine in *Corynebacterium glutamicum* (Mustafi et al., 2012). The size of metabolite variation was quantified in an engineered FFA-producing *E. coli* strain, where the mean FFA concentration between four isolated subpopulations was as large as ninefold (Xiao et al., 2016). This heterogeneity strongly affects the ensemble FFA titer and productivity as more than half of the FFA was produced from a subpopulation consisting of only 15% of the bacteria. The rest of the population consumed nutrient without producing a high concentration of FFA. Low producing cells probably devote more resources to growth, thus dominating the culture over time, leading to an overall decrease in productivity as demonstrated by bimodal L-valine production in *C. glutamicium* (Mustafi et al., 2014). On the other hand, single cell modeling of intracellular resource competition shows that the expression of competing metabolic pathways may be positively correlated at the single cell level (Han and Zhang, 2020). This would suggest that cells with higher expression of metabolite producing pathways could potentially be the faster growing cells in the population as well. Overall, these findings demonstrate that it is essential to understand the multifaceted contributions to metabolite heterogeneity and to develop methods to control it in engineered cells.

1.3 Metabolic Control Systems

Given the importance of metabolite concentrations to microbial metabolism, propagation, and survival, cells have evolved control mechanisms which shape the metabolite dynamics and heterogeneity to enhance their overall fitness in their environments (Chin et al., 2008). While metabolite concentrations are dependent on the whole gene-protein-metabolite network, smaller metabolic control systems are used to interact with metabolites directly. These metabolic control

systems require two main components. First, a sensing component is necessary to measure the intracellular concentration of a metabolite. Second, an actuating component is necessary to receive the information about metabolite concentration and affect cellular activity in response. These components can be within one molecule, for example in enzyme allostery, which senses metabolite concentration at the allosteric site and actuates a change in enzyme activity. The sensing and actuating can also rely on multiple molecular components, such as in transcriptional control of a gene by MRTFs.

The molecular control systems found in natural systems use a small number of recurrent functional motifs across a wide variety of pathways (Alon, 2007). These network motifs, or regulatory architectures, often have similar functional roles in the pathways in which they appear. System parameters, which are the strengths and rates of interactions between molecular species, also affect overall system performance. Regulatory architecture and parameters are evolved together to achieve optimal dynamic response to environmental changes (Zaslaver et al., 2004; Chubukov et al., 2012). Because these systems are used in disparate pathways, biologists are interested in the functional advantages these architectures give to microbes which drives the convergent evolution of these functional motifs. These insights are similarly important to engineers to endow newly designed metabolic pathways with these advantages. In the next section, we will review negative and positive feedback motifs, and their consequences to metabolite dynamics and heterogeneity.

1.3.1 Negative Feedback Control

Negative feedback is a critical control methodology across many engineering disciplines for increasing robustness and tuning response times (Vecchio et al., 2016) and is similarly found in the control of a number of natural metabolic pathways (Chubukov et al., 2014). For a negative

metabolic feedback system, the metabolite concentration acts as a signal, and actuates pathway activities to counteract changes in the metabolite concentrations. An example of a negative feedback architecture is in product feedback inhibition (PFI) where the final metabolite of a pathways allosterically inhibits the activity of the enzymes that produce it. Incorporating negative feedback architectures has been analyzed to enhance performance in several common problems faced by microbes with both natural and engineered metabolic networks.

A common task microbes face is to switch on transcriptional expression of pathway enzymes in response to a metabolite, through an MRTF. In both natural and engineered metabolic systems, rapid response to a switching metabolite concentration is desired because it allows microbes to quickly adapt to changing conditions or reach a productive metabolic state more rapidly. In controlling transcription, switching on pathway expression using an open loop (OL) architecture in response to an input metabolite is generally slow. It was found that for an OL architecture, it takes 2.48 cell cycles for the pathway metabolite concentration to rise to 50% of its steady-state concentration (defined as the metabolite rise-time) after addition of a signaling metabolite. Liu et al. built and studied three closed loop feedback systems of different architectures: a negative gene loop (NGL), a negative metabolic loop (NML), and a negative layered metabolic loop (NLML) (Liu and Zhang, 2018). While all three loops had some ability to decrease the rise-time for pathways metabolite concentrations compared to the OL, the NLML, where metabolite concentration is feedback through a genetic inverter then an enzyme controller, was capable of dramatically accelerating rise-times by 11.8-fold. However, this rapid increase in rise-time was accompanied by a large metabolite concentration overshoot, where metabolite concentration rises above the steady-state before settling. Through tuning the many parameters, it was found that for NLML, faster rise times were generally correlated with larger overshoots. Using

a high maximum promoter strength of the genetic inverter and a low threshold of the enzyme controller were found to be the most efficient for decreasing the rise-time. However, large overshoots may not be desirable for many microbes or engineers because pathway resources may be wasted on producing enzymes that are not being used. In these cases, an NML architecture could be more appropriate to accelerate metabolite dynamics (1.9-fold) without an accompanying overshoot.

A second kind of task for microbes is to be robust against microbial environmental perturbations and genetic perturbations (e.g. mutations) which affect metabolism. Environment perturbations can cause major concentration changes for metabolites necessary for growth (Kresnowati et al., 2006; Taymaz-Nikerel et al., 2013). Transcription-level metabolite feedback was shown to help make metabolite levels less sensitive to these metabolic fluctuations (Oyarzun and Stan, 2012; Oyarzún and Stan, 2013). Using strong, tight promoters allowed the system to further minimize the decrease in product concentration, however, strong promoters could also lead to oscillatory dynamics. Negative feedback in pathways also allows microbes to be more robust to both changes in the microbial environment and changes in system parameters due to mutation. For example, parameter sensitivity analysis of the pinene production-efflux system showed that including negative feedback system reduced the sensitivity of pinene production to system parameters variation (Dunlop et al., 2010; Harrison and Dunlop, 2012). This robustness was verified by constructing a library of pinene export feedback systems, which showed several members with enhanced pinene tolerance, despite having varying promoter strengths and number of TF binding sites in the promoter (Siu et al., 2018). These results highlight how incorporating negative feedback control into pathway design can make the system more robust to bother environmental and genetic perturbation.

Finally, negative feedback has been explored as a mechanism to reduce the amount of metabolite heterogeneity (Borri et al., 2015, 2016; Oyarzún et al., 2015). In these papers, a metabolic enzyme is continuously controlled by a promoter and the enzyme converts a substrate into a final product. Two main feedback loop architectures have been considered: enzyme autoregulation or end-product feedback. Compared to a constitutive system with an identical mean product level, both enzyme autoregulation and end-product feedback could always reduce metabolite noise, with stronger feedback leading to stronger noise reduction (Borri et al., 2015). Additionally, feedback sensitivity was identified as a critical parameter to achieve large noise reduction for a wide range of promoters and feedback strengths (Borri et al., 2015, 2016; Oyarzún et al., 2015).

These several advantages of incorporating negative feedback demonstrate their utility in enhancing the performance some metabolic pathways. However, these studies thus far have been limited to regulation of linear pathways, and primarily focus on control at the transcriptional level. Thus, more work is needed to understand the roles of negative feedback in pathways with branches and loops, and at the post-transcriptional level, which are also common in metabolism.

1.3.2 Positive Feedback Control

Biology makes extensive used of positive feedback in the control of a number of transcription, cell signaling and metabolic networks (Mitrophanov and Groisman, 2008; Tiwari et al., 2011). For positive feedback systems, changes in the metabolite's intracellular concentration work to promote further changes in the concentration. Thus, while negative feedback is associated with improving the stability of a network, positive feedback generally promotes instability (Cinquin and Demongeot, 2002). While this is typically considered problematic in the design of chemical engineering control system (Morud and Skogestad, 1994), biology uses this property to

ensure robust state switching (Freeman, 2000) and to maintain memory of past conditions (Acar et al., 2005), which is important in maintaining differentiated cells.

Positive feedback is necessary for systems to exhibit bistability, which is the existence of multiple steady states for a given parameter value or external metabolite concentration. Induction of the lactose catabolism system in *E. coli* has been shown to exhibit bistability when induced non-metabolizable inducers such as TMG (Novick and Weiner, 1957; Ozbudak et al., 2004). In this case, individual cells either fully activate lactose utilization networks or not, leading to large cell-to-cell differences in enzyme concentrations, and potentially metabolite concentrations. Thus, bistability can help to generate the multiple populations needed for metabolic bet-hedging, where different cells have different uptake rates of extracellular nutrients. Another general property of bistable systems is hysteresis, a memory-like property where the threshold of the signal output response curve is different depending on the recent history of the input signal (Ferrell, 2002). Hysteresis can allow the internal metabolite signal to be reduced without switching metabolic states. Additionally, hysteresis enables a slow response to metabolite concentrations signals that are near the switching threshold (Tiwari et al., 2011). This property allows bistable switches to filter out mild, transient changes in the metabolite concentrations which may be typical of a microbe's natural environment or of heterogenous bioreactors. Several positive feedback architectures for generating bistable metabolite uptake rate have been explored (Oyarzun and Chaves, 2015). It was found that using an activator-repressor topology, where the metabolite activates its own uptake and represses its consumption, had the largest parameter space for generating bistability.

While bistability is an interesting possibility for positive feedback systems, not all positive feedback systems are bistable. For example, while the *lac* operon can be bistable using non-

metabolizable inducer, bistability is has not been observed using the native inducer, lactose (Zander et al., 2017). Additionally, although activator-repressor topologies have the highest potential for bistability, no natural metabolic systems have been identified which use this topology (Krishna et al., 2007). In contrast, many cellular uptake systems, including the lactose system, have positive feedback in metabolite uptake, coupled with negative feedback in metabolite consumption. These systems have much smaller bistable parameter regions (Krishna et al., 2007; Oyarzun and Chaves, 2015), suggesting that the metabolite uptake systems may not benefit from bistability. Coupling positive feedback with negative feedback in metabolic systems without bistability may help efficiently allocate metabolic resources (Krishna et al., 2007; Zander et al., 2017) in response to extracellular environment nutrients, which can potentially explain its wide adoption.

1.4 Metabolic Control System for Fatty Acid Metabolism

Fatty acids (FAs) are critical metabolites in microbial metabolism and serve diverse functional roles. Fatty acids in phospholipids serve as the primary component of cellular membranes in both bacteria and eukaryotic domains (Lombard et al., 2012). The FA composition of those membranes plays an important role in surviving under different conditions, for example by increasing the ratio of cyclopropane FAs under stationary phase and acidic conditions (Cronan, 1968; Shabala and Ross, 2008) or by increasing unsaturated FA content under low temperature (Marr and Ingraham, 1962; de Mendoza et al., 1983). FAs also serve as a highly reduced, high energy carbon source, with an estimated ATP yield of ~100 per molecule, compared to ~30 ATP per molecule for glucose. Finally, it is becoming more evident that FAs and their catabolism play complex roles in regulating disease states, including both in promoting and inhibiting growth of

infectious bacteria (Gullett et al., 2019; Kengmo Tchoupa et al., 2022), in triggering inflammation and immune response (Hosomi et al., 2020), in microbial survival of antibiotic treatment (du Preez and Loots, 2012), and even in promoting proliferation of cancer cells (Carracedo et al., 2013). Given the many roles of FAs in biology, understanding how microbes regulate their dynamic response to exogenous FAs is a necessary step in unraveling how these processes contribute to microbial growth and disease.

1.4.1 FadR as Master Regulator of Fatty Acid Catabolism in E. coli

In aerobic conditions, *E. coli* can grow on long chain FAs as a sole carbon source. Catabolism of FA proceeds by primarily by the aerobic β-oxidation pathway, which yields two carbon units in the form of acetyl-CoA for use in central metabolism, and yields reduced NADH and flavoproteins (Nunn, 1986). Several TFs are involved in the transcriptional regulation of β-oxidation, including global regulators ArcA and CRP which coordinate FA degradation with the metabolic state of the cell (Cho et al., 2006). However, the primary transcriptional regulator of FA degradation is FadR, which represses transcription of the β-oxidation genes in the absence of exogenous FAs.

As a first step in sensing exogenous FAs, FAs must be transported intracellularly by FadL and FadD. FadL is responsible for transporting FAs across the outer membrane. FadD simultaneously transports fatty acids across the inner membrane, and activates FAs to acyl-CoA through ATP-dependent ligation to free coenzyme A (Weimar et al., 2002). FadR represses transcription of these genes through binding to operator sites to block transcription (Xu et al., 2001). However, binding of acyl-CoAs to FadR antagonizes its DNA binding activity (Henry and Cronan, 1992), thus allowing transcription of *fadl* and *fad*D. In this way, a positive feedback loop is formed, with acyl-CoAs activating *fadD* expression via FadR to promote further conversion of

FA to acyl-CoA. This regulatory logic of positive feedback in metabolite uptake is common in several *E. coli* systems, including the well-studied lactose uptake system. For a list of systems in *E. coli* displaying this regulatory logic, see Appendix A Table A.1.

Once FAs are activated to acyl-CoA, they are primarily degraded by the β-oxidation enzymes FadE, FadA, and FadB. Transcription of these enzymes is repressed by FadR when acyl-CoA concentration is low. The activity of these three enzymes removes two-carbon subunits from the acyl-chain, progressively shortening it. Assays of purified FadR show that FadR binding activity is not antagonized by acyl-CoAs shorter than 12 carbon units (DiRusso et al., 1992). Thus, these enzymes reduce the intracellular concentrations of the FadR-antagonizing acyl-CoAs, forming a negative feedback loop on acyl-CoA concentration. Overall, the regulation of the acyl-CoA concentration by FadR and the β-oxidation pathway forms a coupled positive and negative feedback loop which shares regulatory logic with other pathways, including the lactose degradation pathway. In contrast to the *lac* operon, transcription of the acyl-CoA forming (*fadD*) and degradation (*fadE*, *fadAB*) genes occurs from different operons, which allows for differential regulation of each of these pathways.

FadR also activates the expression of IclR, a TF which represses expression of the glyoxylate shunt operon *aceBAK* (Gui et al., 1996). Since degradation of FA produces only two carbon unit molecules of acetyl-CoA, bypass of the oxidation steps in the TCA cycle is required to direct carbon towards gluconeogenesis and biomass production, which is performed by the glyoxylate shunt enzymes AceB and AceA (Dolan and Welch, 2018). Acyl-CoAs activate expression of the glyoxylate shunt via FadR and IclR, which prepares the central metabolism for increased acetyl-CoA concentrations. Thus, FadR not only regulates FA degradation directly, but

also coordinates central metabolism for incorporation of FA into biomass (Clark and Cronan, 2005).

1.4.2 FadR as a Global Regulator in Response to Exogenous FA

As a transcriptional regulator, FadR has many unique regulatory activities beyond controlling expression of FA degradation pathways. First, FadR also acts global activator of FA biosynthesis (Campbell and Cronan, 2001). FA operator sites have been identified in all FA biosynthesis genes (My et al., 2015). FadR activation of these genes occurs when FadR is bound to the operator site, but this binding is again antagonized by acyl-CoAs. In this way, FadR acts as a global switch between FA biosynthesis in the absence of exogenous FAs, to FA degradation in the presence of FAs (Cronan and Subrahmanyam, 1998). Overexpression of FadR upregulates many FA biosynthesis genes, leading to an increase in total FA biosynthesis (Zhang et al., 2012b). Overexpression of FadR more strongly upregulates expression of *fabB* and *fabF*, which are involved in unsaturated FA biosynthesis, than other FA biosynthesis genes, leading to an increase in the fraction of unsaturated FAs in the cell membrane (Zhang et al., 2012b). Additionally, deletions of FadR strongly reduce the expression of *fabA*, another gene involved in unsaturated FA biosynthesis, and reduce the overall fraction of unsaturated FAs in the membrane (Nunn et al., 1983; Henry and Cronan, 1991). Thus, FadR also plays a role in regulating the ratio of saturated to unsaturated FAs in the membrane through its differential regulation of FA biosynthesis genes (DiRusso et al., 1999; My et al., 2015).

Interestingly, FadR has also been shown to repress the universal stress protein uspA (Farewell et al., 1996). While the function of UspA is unknown, it is strongly upregulated under stress conditions including starvation of nutrients and addition of toxic agents like heavy metals, oxidants, acids, and antibiotics (Nyström and Neidhardt, 1992). Addition of extracellular FA

increases *uspA* expression during exponential growth, but the role of UspA in FA metabolism is not known (Cronan and Subrahmanyam, 1998). But given this evidence, FadR may play a role in stress response through regulation of *uspA*.

More recently, FadR has been discovered as a regulator of pathogenicity genes in enterohemorrhagic *E. coli* (EHEC). EHEC rely on the a type III secretion system, encoded in the Locus of Enterocyte Effacement (LEE), to colonize the human intestine (Hartland et al., 2002). Screening a library of *E. coli* TF knockouts transformed with the LEE pathways revealed that FadR acts as a repressor of the LEE pathway, potentially through repression of LEE1 which is a activator of the other pathogenicity genes (Pifer et al., 2018). Further work on this pathway demonstrated that FadR more likely acts as an activator of LEE, not a repressor, and that expression from the LEE locus is reduced by the presence of exogenous FA (Ellermann et al., 2021). These regulations by FadR partially coordinate bacterial virulence in response to the host metabolism and to disease progression, establishing another major role of FadR regulation in *E. coli*.

These diverse regulatory roles of FadR make it a unique global regulator of FA degradation, biosynthesis, stress response, and virulence in *E. coli*. At the core of these regulations is the metabolite uptake positive feedback loop architecture, which allows coordination of these functions with the presence of exogenous FAs. Although this core architecture is similar to other pathways found in *E. coli*, the necessity of coordinating these multiple functions through a single regulatory may place unique constraints on the dynamics of the control system. Thus, understanding the control of metabolite dynamics and heterogeneity in the FA uptake and degradation system is a critical, yet unexplored, step in understanding the multi-pathway dynamic response of *E. coli* to FAs in its environment.

1.5 Dissertation Overview

This primary objective of this dissertation is to elucidate how the architecture and parameters of a MRTF-based metabolic control system impact the metabolite dynamics and heterogeneity in response to fluctuating and diverse metabolic environments. This dissertation focuses on the metabolite uptake positive feedback loop, a common architecture employed for the uptake of many metabolites in *E. coli*. The FA uptake system is studied as a representative example, due to its biological importance in controlling multiple beyond FA degradation, including FA biosynthesis, stress response, and *E. coli* virulence.

In Chapter 2, we examine how regulatory architecture and parameters of the FA uptake control system contribute to accelerating pathway recovery after extracellular FA is depleted. Fast recovery of nutrient degradation pathways after nutrient depletion is generally beneficial to cell survival by preventing waste of metabolic resources. We demonstrate that fast recovery can be achieved by rapid release of transcription factor from a metabolite-sequestered complex. This release depends on the rate of metabolite consumption and exposure time to FA. Further, we construct strains with re-wired architecture and demonstrate the benefits of negative autoregulation in controlling recovery time and overall resource usage.

In Chapter 3, we explore how changes in growth rate affect the minimum output, maximum output, and dynamic range of a MRTF-based biosensor. High dynamic range is a critical parameter in many biosensing applications to achieve good external control of metabolic pathways. We develop a kinetic model to explore how tuning the parameters of the biosensor impact the dynamic range growth rate dependence and find that there is strong coupling between the dynamic range

and its growth rate dependence. Additionally, we find that the transport and enzymatic catalysis mechanisms of the metabolite inducer shape the dynamic range-growth rate dependence.

In Chapter 4, we examine to role of positive feedback in the FA uptake control system in contributing to β-lactam tolerance in response to sudden nutrient shifts from gluconeogenic carbon to FA. Tolerance to antibiotics can be problematic in the treatment of microbial infections and can lead to the rise of antibiotic resistance. We find that cells exhibit a transient antibiotic tolerance after the switch and that the length of this transient tolerance is correlated with the time it takes to the accumulation of FadD enzymes. Thus, our results show that positive feedback in metabolism is not sufficient to trigger persistence but can instead controls the period of antibiotic tolerance after a nutrient shift.

Finally, in Chapter 5 the conclusions of this dissertation are summarized and possible future directions for research efforts in understanding and designing metabolic control systems are explored. Taken together, this dissertation provides a significant advance in understanding how microbes control metabolite dynamics and heterogeneity in the face of several kinds of environmental fluctuation. These advances expand our ability to design new metabolic control systems for use in metabolic engineering and synthetic biology applications, as well as deepen our knowledge of *E. coli* response to extracellular nutrients and FAs.

1.6 Chapter 1 References

Abu Kwaik, Y., and Bumann, D. (2013). Microbial quest for food in vivo : 'Nutritional virulence' as an emerging paradigm. *Cell. Microbiol.* 15, 882–890. doi:10.1111/cmi.12138.

Acar, M., Becskei, A., and van Oudenaarden, A. (2005). Enhancement of cellular memory by reducing stochastic transitions. *Nature* 435, 228–232. doi:10.1038/nature03524.

Acar, M., Mettetal, J. T., and van Oudenaarden, A. (2008). Stochastic switching as a survival strategy in fluctuating environments. *Nat. Genet.* 40, 471–475. doi:10.1038/ng.110.

Alon, U. (2007). Network motifs: Theory and experimental approaches. *Nat. Rev. Genet.* 8, 450–461. doi:10.1038/nrg2102.

Amato, S. M., and Brynildsen, M. P. (2014). Nutrient transitions are a source of persisters in *Escherichia coli* biofilms. *PLoS One* 9, e93110. doi:10.1371/journal.pone.0093110.

Amato, S. M., and Brynildsen, M. P. (2015). Persister heterogeneity arising from a single metabolic stress. *Curr. Biol.* 25, 2090–2098. doi:10.1016/j.cub.2015.06.034.

Amato, S. M., Fazen, C. H., Henry, T. C., Mok, W. W. K., Orman, M. A., Sandvik, E. L., et al. (2014). The role of metabolism in bacterial persistence. *Front. Microbiol.* 5, 70. doi:10.3389/fmicb.2014.00070.

Amato, S., Orman, M., and Brynildsen, M. (2013). Metabolic control of persister formation in *Escherichia coli*. *Mol. Cell* 50, 475–487. doi:10.1016/j.molcel.2013.04.002.

Anesiadis, N., Cluett, W. R., and Mahadevan, R. (2008). Dynamic metabolic engineering for increasing bioprocess productivity. *Metab. Eng.* 10, 255–266. doi:10.1016/j.ymben.2008.06.004.

Aoki, S. K., Lillacci, G., Gupta, A., Baumschlager, A., Schweingruber, D., and Khammash, M. (2019). A universal biomolecular integral feedback controller for robust perfect adaptation. *Nature* 570, 533–537. doi:10.1038/s41586-019-1321-1.

Bai, W., Geng, W., Wang, S., and Zhang, F. (2019). Biosynthesis, regulation, and engineering of microbially produced branched biofuels. *Biotechnol. Biofuels* 12, 1–12. doi:10.1186/s13068-019-1424-9.

Balaban, N. Q., Helaine, S., Lewis, K., Ackermann, M., Aldridge, B., Andersson, D. I., et al. (2019). Definitions and guidelines for research on antibiotic persistence. *Nat. Rev. Microbiol.* 17, 441–448. doi:10.1038/s41579-019-0196-3.

Barrick, J. E., Corbino, K. A., Winkler, W. C., Nahvi, A., Mandal, M., Collins, J., et al. (2004). New RNA motifs suggest an expanded scope for riboswitches in bacterial genetic control. *Proc. Natl. Acad. Sci.* 101, 6421–6426. doi:10.1073/pnas.0308014101.

Barthe, M., Tchouanti, J., Gomes, P. H., Bideaux, C., Lestrade, D., Graham, C., et al. (2020). Availability of the molecular switch XylR controls phenotypic heterogeneity and lag duration during Escherichia coli adaptation from glucose to xylose. *MBio* 11, e02938-20. doi:10.1128/mBio.02938-20.

Borri, A., Palumbo, P., and Singh, A. (2015). Metabolic noise reduction for enzymatic reactions: The role of a negative feedback. *Proc. IEEE Conf. Decis. Control* 54th IEEE, 2537–2542. doi:10.1109/CDC.2015.7402598.

Borri, A., Palumbo, P., and Singh, A. (2016). Impact of negative feedback in metabolic noise propagation. *IET Syst. Biol.* 10, 179–186. doi:10.1049/iet-syb.2016.0003.

Boulineau, S., Tostevin, F., Kiviet, D. J., ten Wolde, P. R., Nghe, P., and Tans, S. J. (2013). Single-cell dynamics reveals sustained growth during diauxic shifts. *PLoS One* 8, e61686. doi:10.1371/journal.pone.0061686.

Bowen, C. H., Bonin, J., Kogler, A., Barba-Ostria, C., and Zhang, F. (2016). Engineering *Escherichia coli* for conversion of glucose to medium-chain ω-hydroxy fatty acids and α,ω-dicarboxylic acids. *ACS Synth. Biol.* 5, 200–206. doi:10.1021/acssynbio.5b00201.

Brunk, E., Chang, R. L., Xia, J., Hefzi, H., Yurkovich, J. T., Kim, D., et al. (2018). Characterizing posttranslational modifications in prokaryotic metabolism using a multiscale workflow. *Proc. Natl. Acad. Sci.* 115, 11096–11101. doi:10.1073/pnas.1811971115.

Burg, J. M., Cooper, C. B., Ye, Z., Reed, B. R., Moreb, E. A., and Lynch, M. D. (2016). Large-scale bioprocess competitiveness: the potential of dynamic metabolic control in two-stage fermentations. *Curr. Opin. Chem. Eng.* 14, 121–136. doi:10.1016/j.coche.2016.09.008.

Campbell, J. W., and Cronan, J. E. (2001). *Escherichia coli* FadR positively regulates transcription of the *fabB* fatty acid biosynthetic gene. *J. Bacteriol.* 183, 5982–5990. doi: 10.1128/JB.183.20.5982-5990.2001

Carracedo, A., Cantley, L. C., and Pandolfi, P. P. (2013). Cancer metabolism: Fatty acid oxidation in the limelight. *Nat. Rev. Cancer* 13, 227–32. doi:10.1038/nrc3483.

Chen, X., Zhang, C., and Lindley, N. D. (2020). Metabolic engineering strategies for sustainable terpenoid flavor and fragrance synthesis. *J. Agric. Food Chem.* 68, 10252–10264. doi:10.1021/acs.jafc.9b06203.

Chin, C.-S., Chubukov, V., Jolly, E. R., DeRisi, J., and Li, H. (2008). Dynamics and design principles of a basic regulatory architecture controlling metabolic pathways. *PLoS Biol.* 6, e146. doi:10.1371/journal.pbio.0060146.

Cho, B.-K., Knight, E. M., and Palsson, B. Ø. (2006). Transcriptional regulation of the *fad* regulon genes of *Escherichia coli* by ArcA. *Microbiology* 152, 2207–2219. doi:10.1099/mic.0.28912-0.

Chu, D. (2017). Limited by sensing - a minimal stochastic model of the lag-phase during diauxic growth. *J. Theor. Biol.* 414, 137–146. doi:10.1016/j.jtbi.2016.10.019.

Chubukov, V., Gerosa, L., Kochanowski, K., and Sauer, U. (2014). Coordination of microbial metabolism. *Nat. Rev. Microbiol.* 12, 327–340. doi:10.1038/nrmicro3238.

Chubukov, V., Zuleta, I. A., and Li, H. (2012). Regulatory architecture determines optimal regulation of gene expression in metabolic pathways. *Proc. Natl. Acad. Sci.* 109, 5127–5132. doi:10.1073/pnas.1114235109.

Cinquin, O., and Demongeot, J. (2002). Positive and negative feedback: Striking a balance between necessary antagonists. *J. Theor. Biol.* 216, 229–241. doi:10.1006/jtbi.2002.2544.

Clark, D. P., and Cronan, J. E. (2005). Two-carbon compounds and fatty acids as carbon sources. *EcoSal Plus* 1, 2 doi:10.1128/ecosalplus.3.4.4.

Conlon, B. P., Rowe, S. E., Gandt, A. B., Nuxoll, A. S., Donegan, N. P., Zalis, E. A., et al. (2016). Persister formation in *Staphylococcus aureus* is associated with ATP depletion. *Nat. Microbiol.* 1, 16051. doi:10.1038/nmicrobiol.2016.51.

Cronan, J. E. (1968). Phospholipid alterations during growth of *Escherichia coli*. *J. Bacteriol.* 95, 2054–2061. doi:10.1128/jb.95.6.2054-2061.1968.

Cronan, J. E. J., and Subrahmanyam, S. (1998). FadR, transcriptional co-ordination of metabolic expediency. *Mol. Microbiol.* 29, 937–943. doi:10.1046/j.1365-2958.1998.00917.x.

Dayarian, A., Chaves, M., Sontag, E. D., and Sengupta, A. M. (2009). Shape, size, and robustness: Feasible regions in the parameter space of biochemical networks. *PLoS Comput. Biol.* 5, e1000256. doi:10.1371/journal.pcbi.1000256.

de Mendoza, D., Klages Ulrich, A., and Cronan, J. E. (1983). Thermal regulation of membrane fluidity in *Escherichia coli*. Effects of overproduction of beta-ketoacyl-acyl carrier protein synthase I. *J. Biol. Chem.* 258, 2098–2101. doi:10.1016/S0021-9258(18)32888-6.

Diether, M., Nikolaev, Y., Allain, F. H., and Sauer, U. (2019). Systematic mapping of protein-metabolite interactions in central metabolism of *Escherichia coli*. *Mol. Syst. Biol.* 15, e9008. doi:10.15252/msb.20199008.

DiRusso, C. C., Black, P. N., and Weimar, J. D. (1999). Molecular inroads into the regulation and metabolism of fatty acids, lessons from bacteria. *Prog. Lipid Res.* 38, 129–197. doi:10.1016/S0163-7827(98)00022-8.

DiRusso, C. C., Heimert, T. L., and Metzger, A. K. (1992). Characterization of FadR, a global transcriptional regulator of fatty acid metabolism in *Escherichia coli*. Interaction with the *fadB* promoter is prevented by long chain fatty acyl coenzyme A. *J. Biol. Chem.* 267, 8685–91. doi:10.1016/S0021-9258(18)42497-0

Dolan, S. K., and Welch, M. (2018). The glyoxylate shunt, 60 years on. *Annu. Rev. Microbiol.* 72, 309–330. doi:10.1146/annurev-micro-090817-062257.

du Preez, I., and Loots, D. T. (2012). Altered fatty acid metabolism due to rifampicin-resistance conferring mutations in the *rpoB* gene of *Mycobacterium tuberculosis*: Mapping the potential of pharmaco-metabolomics for global health and personalized medicine. *Omi. A J. Integr. Biol.* 16, 596–603. doi:10.1089/omi.2012.0028.

Dunlop, M. J., Keasling, J. D., and Mukhopadhyay, A. (2010). A model for improving microbial biofuel production using a synthetic feedback loop. *Syst. Synth. Biol.* 4, 95–104. doi:10.1007/s11693-010-9052-5.

Ellermann, M., Jimenez, A. G., Pifer, R., Ruiz, N., and Sperandio, V. (2021). The canonical long-chain fatty acid sensing machinery processes arachidonic acid to inhibit virulence in enterohemorrhagic *Escherichia coli*. *MBio* 12, e03247-20. doi:10.1128/mBio.03247-20.

Farewell, A., Diez, A. A., DiRusso, C. C., and Nyström, T. (1996). Role of the *Escherichia coli* FadR regulator in stasis survival and growth phase-dependent expression of the *uspA*, *fad*, and *fab* genes. *J. Bacteriol.* 178, 6443–6450. doi:10.1128/jb.178.22.6443-6450.1996.

Feng, Y., De Franceschi, G., Kahraman, A., Soste, M., Melnik, A., Boersema, P. J., et al. (2014). Global analysis of protein structural changes in complex proteomes. *Nat. Biotechnol.* 32, 1036–1044. doi:10.1038/nbt.2999.

Ferrell, J. E. (2002). Self-perpetuating states in signal transduction: Positive feedback, double-negative feedback and bistability. *Curr. Opin. Cell Biol.* 14, 140–148. doi:10.1016/S0955-0674(02)00314-9.

Freeman, M. (2000). Feedback control of intercellular signalling in development. *Nature* 408, 313–319. doi:10.1038/35042500.

Fung, E., Wong, W. W., Suen, J. K., Bulter, T., Lee, S.-G., and Liao, J. C. (2005). A synthetic gene – metabolic oscillator. *Nature* 435, 118–122. doi:10.1038/nature03503.1.

Gadkar, K. G., Doyle, F. J., Edwards, J. S., and Mahadevan, R. (2005). Estimating optimal profiles of genetic alterations using constraint-based models. *Biotechnol. Bioeng.* 89, 243–251. doi:10.1002/bit.20349.

Gerosa, L., and Sauer, U. (2011). Regulation and control of metabolic fluxes in microbes. *Curr. Opin. Biotechnol.* 22, 566–575. doi:10.1016/j.copbio.2011.04.016.

Gillespie, D. T. (2007). Stochastic simulation of chemical kinetics. *Annu. Rev. Phys. Chem.* 58, 35–55. doi:10.1146/annurev.physchem.58.032806.104637.

Grimbergen, A. J., Siebring, J., Solopova, A., and Kuipers, O. P. (2015). Microbial bet-hedging: The power of being different. *Curr. Opin. Microbiol.* 25, 67–72.

doi:10.1016/j.mib.2015.04.008.

Guantes, R., Benedetti, I., Silva-Rocha, R., and de Lorenzo, V. (2016). Transcription factor levels enable metabolic diversification of single cells of environmental bacteria. *ISME J.* 10, 1122–1133. doi:10.1038/ismej.2015.193.

Gui, L., Sunnarborg, A., and LaPorte, D. C. (1996). Regulated expression of a repressor protein: FadR activates *iclR*. *J. Bacteriol.* 178, 4704–4709. doi:10.1128/jb.178.15.4704-4709.1996.

Gullett, J. M., Cuypers, M. G., Frank, M. W., White, S. W., and Rock, C. O. (2019). A fatty acid-binding protein of *Streptococcus pneumoniae* facilitates the acquisition of host polyunsaturated fatty acids. *J. Biol. Chem.* 294, 16416–16428. doi:10.1074/jbc.RA119.010659.

Han, Y., and Zhang, F. (2020). Heterogeneity coordinates bacterial multi-gene expression in single cells. *PLoS Comput. Biol.* 16, e1007643. doi:10.1371/journal.pcbi.1007643.

Hare, P. J., LaGree, T. J., Byrd, B. A., DeMarco, A. M., and Mok, W. W. K. (2021). Single-cell technologies to study phenotypic heterogeneity and bacterial persisters. *Microorganisms* 9, 2277. doi:10.3390/microorganisms9112277.

Harms, A., Maisonneuve, E., and Gerdes, K. (2016). Mechanisms of bacterial persistence during stress and antibiotic exposure. *Science* 354, aaf4268. doi:10.1126/science.aaf4268.

Harrison, M. E., and Dunlop, M. J. (2012). Synthetic feedback loop model for increasing microbial biofuel production using a biosensor. *Front. Microbiol.* 3, 1–9. doi:10.3389/fmicb.2012.00360.

Hartland, E. L., Daniell, S. J., Delahay, R. M., Neves, B. C., Wallis, T., Shaw, R. K., et al. (2002). The type III protein translocation system of enteropathogenic *Escherichia coli* involves EspA-EspB protein interactions. *Mol. Microbiol.* 35, 1483–1492. doi:10.1046/j.1365-2958.2000.01814.x.

He, F., Murabito, E., and Westerhoff, H. V. (2016). Synthetic biology and regulatory networks: Where metabolic systems biology meets control engineering. *J. R. Soc. Interface* 13, 20151046. doi:10.1098/rsif.2015.1046.

Henry, M., and Cronan, J. E. (1992). A new mechanism of transcriptional regulation: Release of an activator triggered by small molecule binding. *Cell* 70, 671–679. doi:10.1016/0092-8674(92)90435-F.

Henry, M. F., and Cronan, J. E. (1991). *Escherichia coli* transcription factor that both activates fatty acid synthesis and represses fatty acid degradation. *J. Mol. Biol.* 222, 843–849. doi:10.1016/0022-2836(91)90574-P.

Hosomi, K., Kiyono, H., and Kunisawa, J. (2020). Fatty acid metabolism in the host and

commensal bacteria for the control of intestinal immune responses and diseases. *Gut Microbes* 11, 276–284. doi:10.1080/19490976.2019.1612662.

Ibáñez, A. J., Fagerer, S. R., Schmidt, A. M., Urban, P. L., Jefimovs, K., Geiger, P., et al. (2013). Mass spectrometry-based metabolomics of single yeast cells. *Proc. Natl. Acad. Sci.* 110, 8790–8794. doi:10.1073/pnas.1209302110.

Jiang, W., Gu, P., and Zhang, F. (2018). Steps towards 'drop-in' biofuels: Focusing on metabolic pathways. *Curr. Opin. Biotechnol.* 53, 26–32. doi:10.1016/j.copbio.2017.10.010.

Jiang, W., Qiao, J. B., Bentley, G. J., Liu, D., and Zhang, F. (2017). Modular pathway engineering for the microbial production of branched-chain fatty alcohols. *Biotechnol. Biofuels* 10, 1–15. doi:10.1186/s13068-017-0936-4.

Kelly, C. L., Harris, A. W. K., Steel, H., Hancock, E. J., Heap, J. T., and Papachristodoulou, A. (2018). Synthetic negative feedback circuits using engineered small RNAs. *Nucleic Acids Res.* 46, 9875–9889. doi:10.1093/nar/gky828.

Kengmo Tchoupa, A., Eijkelkamp, B. A., and Peschel, A. (2022). Bacterial adaptation strategies to host-derived fatty acids. *Trends Microbiol.* 30, 241–253. doi:10.1016/j.tim.2021.06.002.

Kiviet, D. J., Nghe, P., Walker, N., Boulineau, S., Sunderlikova, V., and Tans, S. J. (2014). Stochasticity of metabolism and growth at the single-cell level. *Nature* 514, 376–379. doi:10.1038/nature13582.

Kochanowski, K., Sauer, U., and Chubukov, V. (2013). Somewhat in control—the role of transcription in regulating microbial metabolic fluxes. *Curr. Opin. Biotechnol.* 24, 987–993. doi:10.1016/j.copbio.2013.03.014.

Kochanowski, K., Sauer, U., and Noor, E. (2015). Posttranslational regulation of microbial metabolism. *Curr. Opin. Microbiol.* 27, 10–17. doi:10.1016/j.mib.2015.05.007.

Kotte, O., Volkmer, B., Radzikowski, J. L., and Heinemann, M. (2014). Phenotypic bistability in *Escherichia coli*'s central carbon metabolism. *Mol. Syst. Biol.* 10, 736–736. doi:10.15252/msb.20135022.

Kresnowati, M. T. A. P., Van Winden, W. A., Almering, M. J. H., Ten Pierick, A., Ras, C., Knijnenburg, T. A., et al. (2006). When transcriptome meets metabolome: Fast cellular responses of yeast to sudden relief of glucose limitation. *Mol. Syst. Biol.* 2, 49. doi:10.1038/msb4100083.

Krishna, S., Semsey, S., and Sneppen, K. (2007). Combinatorics of feedback in cellular uptake and metabolism of small molecules. *Proc. Natl. Acad. Sci. U. S. A.* 104, 20815–20819. doi:10.1073/pnas.0706231105.

Labhsetwar, P., Cole, J. A., Roberts, E., Price, N. D., and Luthey-Schulten, Z. A. (2013).

Heterogeneity in protein expression induces metabolic variability in a modeled *Escherichia coli* population. *Proc. Natl. Acad. Sci. U. S. A.* 110, 14006–14011. doi:10.1073/pnas.1222569110.

LaPorte, D. C., Thorsness, P. E., and Koshland, D. E. (1985). Compensatory phosphorylation of isocitrate dehydrogenase. A mechanism for adaptation to the intracellular environment. *J. Biol. Chem.* 260, 10563–10568. doi:10.1016/S0021-9258(19)85122-0.

Lara, A. R., Galindo, E., Ramírez, O. T., and Palomares, L. A. (2006). Living with heterogeneities in bioreactors: Understanding the effects of environmental gradients on cells. *Mol. Biotechnol.* 34, 355–381. doi:10.1385/MB:34:3:355.

Ledezma-Tejeida, D., Schastnaya, E., and Sauer, U. (2021). Metabolism as a signal generator in bacteria. *Curr. Opin. Syst. Biol.* 28, 100404. doi:10.1016/j.coisb.2021.100404.

Levine, E., and Hwa, T. (2007). Stochastic fluctuations in metabolic pathways. *Proc. Natl. Acad. Sci.* 104, 9224–9229. doi:10.1073/pnas.0610987104.

Li, X., Gianoulis, T. A., Yip, K. Y., Gerstein, M., and Snyder, M. (2010). Extensive in vivo metabolite-protein interactions revealed by large-scale systematic analyses. *Cell* 143, 639–650. doi:10.1016/j.cell.2010.09.048.

Link, H., Kochanowski, K., and Sauer, U. (2013). Systematic identification of allosteric protein-metabolite interactions that control enzyme activity in vivo. *Nat. Biotechnol.* 31, 357–361. doi:10.1038/nbt.2489.

Liu, D., Xiao, Y., Evans, B. S., and Zhang, F. (2015). Negative feedback regulation of fatty acid production based on a Malonyl-CoA sensor–actuator. *ACS Synth. Biol.* 4, 132–140. doi:10.1021/sb400158w.

Liu, D., and Zhang, F. (2018). Metabolic feedback circuits provide rapid control of metabolite dynamics. *ACS Synth. Biol.* 7, 347–356. doi:10.1021/acssynbio.7b00342.

Lombard, J., López-García, P., and Moreira, D. (2012). The early evolution of lipid membranes and the three domains of life. *Nat. Rev. Microbiol.* 10, 507–515. doi:10.1038/nrmicro2815.

Madan Babu, M. (2003). Evolution of transcription factors and the gene regulatory network in *Escherichia coli*. *Nucleic Acids Res.* 31, 1234–1244. doi:10.1093/nar/gkg210.

Magnusson, L. U., Farewell, A., and Nyström, T. (2005). ppGpp: A global regulator in *Escherichia coli*. *Trends Microbiol.* 13, 236–242. doi:10.1016/j.tim.2005.03.008.

Mandal, M., Lee, M., Barrick, J. E., Weinberg, Z., Emilsson, G. M., Ruzzo, W. L., et al. (2004). A glycine-dependent riboswitch that uses cooperative binding to control gene expression. *Science* 306, 275–279. doi:10.1126/science.1100829.

Manuse, S., Shan, Y., Canas-Duarte, S. J., Bakshi, S., Sun, W.-S., Mori, H., et al. (2021).

Bacterial persisters are a stochastically formed subpopulation of low-energy cells. *PLOS Biol.* 19, e3001194. doi:10.1371/journal.pbio.3001194.

Marr, A. G., and Ingraham, J. L. (1962). Effect of temperature on the composition of fatty acids in *Escherichia coli*. *J. Bacteriol.* 84, 1260–1267. doi:10.1128/jb.84.6.1260-1267.1962.

Michiels, J. E., Van den Bergh, B., Verstraeten, N., and Michiels, J. (2016). Molecular mechanisms and clinical implications of bacterial persistence. *Drug Resist. Updat.* 29, 76–89. doi:10.1016/j.drup.2016.10.002.

Mitrophanov, A. Y., and Groisman, E. A. (2008). Positive feedback in cellular control systems. *BioEssays* 30, 542–555. doi:10.1002/bies.20769.

Morud, J., and Skogestad, S. (1994). Effects of recycle on dynamics and control of chemical processing plants. *Comput. Chem. Eng.* 18, S529–S534. doi:10.1016/0098-1354(94)80086-3.

Mustafi, N., Grünberger, A., Kohlheyer, D., Bott, M., and Frunzke, J. (2012). The development and application of a single-cell biosensor for the detection of L-methionine and branched-chain amino acids. *Metab. Eng.* 14, 449–457. doi:10.1016/j.ymben.2012.02.002.

Mustafi, N., Grünberger, A., Mahr, R., Helfrich, S., Nöh, K., Blombach, B., et al. (2014). Application of a genetically encoded biosensor for live cell imaging of L-Valine production in pyruvate dehydrogenase complex-deficient *Corynebacterium glutamicum* strains. *PLoS One* 9, e85731. doi:10.1371/journal.pone.0085731.

My, L., Ghandour Achkar, N., Viala, J. P., and Bouveret, E. (2015). Reassessment of the genetic regulation of fatty acid synthesis in *Escherichia coli*: Global positive control by the dual functional regulator FadR. *J. Bacteriol.* 197, 1862–1872. doi:10.1128/JB.00064-15.

Nadal-Rey, G., McClure, D. D., Kavanagh, J. M., Cornelissen, S., Fletcher, D. F., and Gernaey, K. V (2021). Understanding gradients in industrial bioreactors. *Biotechnol. Adv.* 46, 107660. doi:10.1016/j.biotechadv.2020.107660.

Nelson, J. W., Atilho, R. M., Sherlock, M. E., Stockbridge, R. B., and Breaker, R. R. (2017). Metabolism of free guanidine in bacteria is regulated by a widespread riboswitch class. *Mol. Cell* 65, 220–230. doi:10.1016/j.molcel.2016.11.019.

New, A. M., Cerulus, B., Govers, S. K., Perez-Samper, G., Zhu, B., Boogmans, S., et al. (2014). Different levels of catabolite repression optimize growth in stable and variable environments. *PLoS Biol.* 12, e1001764. doi:10.1371/journal.pbio.1001764.

Ng, C. S., and Stephanopoulos, G. (1996). Synthesis of control systems for chemical plants. *Comput. Chem. Eng.* 20, S999–S1004. doi:10.1016/0098-1354(96)00174-3.

Nguyen, D., Joshi-Datar, A., Lepine, F., Bauerle, E., Olakanmi, O., Beer, K., et al. (2011).

Active starvation responses mediate antibiotic tolerance in biofilms and nutrient-limited bacteria. *Science* 334, 982–986. doi:10.1126/science.1211037.

Nguyen, J., Lara-Gutiérrez, J., and Stocker, R. (2021). Environmental fluctuations and their effects on microbial communities, populations and individuals. *FEMS Microbiol. Rev.* 45, fuaa068. doi:10.1093/femsre/fuaa068.

Novák, B., and Tyson, J. J. (2008). Design principles of biochemical oscillators. *Nat. Rev. Mol. Cell Biol.* 9, 981–991. doi:10.1038/nrm2530.

Novick, A., and Weiner, M. (1957). Enzyme induction as an all-or-none phenomenon. *Proc. Natl. Acad. Sci.* 43, 553–566. doi:10.1073/pnas.43.7.553.

Nunn, W. D. (1986). A molecular view of fatty acid catabolism in *Escherichia coli*. *Microbiol. Rev.* 50, 179–92. doi:10.1128/mr.50.2.179-192.1986.

Nunn, W. D., Giffin, K., Clark, D., and Cronan, J. E. (1983). Role for *fadR* in unsaturated fatty acid biosynthesis in Escherichia coli. *J. Bacteriol.* 154, 554–560. doi:10.1128/jb.154.2.554-560.1983.

Nyström, T., and Neidhardt, F. C. (1992). Cloning, mapping and nucleotide sequencing of a gene encoding a universal stress protein in *Eschericha coli. Mol. Microbiol.* 6, 3187–3198. doi:10.1111/j.1365-2958.1992.tb01774.x.

O'Neill, J. (2016). Tackling drug-resistant infections globally: Final report and recommendations.

Oyarzun, D. A., and Chaves, M. (2015). Design of a bistable switch to control cellular uptake. *J. R. Soc. Interface* 12, 20150618. doi:10.1098/rsif.2015.0618.

Oyarzún, D. A., Lugagne, J. B., and Stan, G. B. V. (2015). Noise propagation in synthetic gene circuits for metabolic control. *ACS Synth. Biol.* 4, 116–125. doi:10.1021/sb400126a.

Oyarzún, D. A., and Stan, G. V (2012). Design tradeoffs in a synthetic gene control circuit for metabolic networks. *2012 American Control Conference (ACC)* (IEEE), 2743–2748. doi:10.1109/ACC.2012.6314705.

Oyarzún, D. A., and Stan, G. V (2013). Synthetic gene circuits for metabolic control: design trade-offs and constraints. *J. R. Soc. Interface* 10, 20120671. doi:10.1098/rsif.2012.0671.

Ozbudak, E. M., Thattai, M., Lim, H. N., Shraiman, B. I., and van Oudenaarden, A. (2004). Multistability in the lactose utilization network of *Escherichia coli*. *Nature* 427, 737–740. doi:10.1038/nature02298.

Pacios, O., Blasco, L., Bleriot, I., Fernandez-Garcia, L., Ambroa, A., López, M., et al. (2020). (p)ppGpp and its role in bacterial persistence: New challenges. *Antimicrob. Agents Chemother.* 64, e01283-20. doi:10.1128/AAC.01283-20.

Peng, B., Su, Y., Li, H., Han, Y., Guo, C., Tian, Y., et al. (2015). Exogenous alanine and/or glucose plus kanamycin kills antibiotic-resistant bacteria. *Cell Metab.* 21, 249–262. doi:10.1016/j.cmet.2015.01.008.

Pifer, R., Russell, R. M., Kumar, A., Curtis, M. M., and Sperandio, V. (2018). Redox, amino acid, and fatty acid metabolism intersect with bacterial virulence in the gut. *Proc. Natl. Acad. Sci.* 115, E10712–E10719. doi:10.1073/pnas.1813451115.

Radzikowski, J. L., Vedelaar, S., Siegel, D., Ortega, Á. D., Schmidt, A., and Heinemann, M. (2016). Bacterial persistence is an active σ^S stress response to metabolic flux limitation. *Mol. Syst. Biol.* 12, 882. doi:10.15252/msb.20166998.

Rahmat, E., and Kang, Y. (2020). Yeast metabolic engineering for the production of pharmaceutically important secondary metabolites. *Appl. Microbiol. Biotechnol.* 104, 4659–4674. doi:10.1007/s00253-020-10587-y.

Ray, J. C. J., Wickersheim, M. L., Jalihal, A. P., Adeshina, Y. O., Cooper, T. F., and Balázsi, G. (2016). Cellular growth arrest and persistence from enzyme saturation. *PLoS Comput. Biol.* 12, e1004825. doi:10.1371/journal.pcbi.1004825.

Reed, K. B., and Alper, H. S. (2018). Expanding beyond canonical metabolism: Interfacing alternative elements, synthetic biology, and metabolic engineering. *Synth. Syst. Biotechnol.* 3, 20–33. doi:10.1016/j.synbio.2017.12.002.

Ronneau, S., and Helaine, S. (2019). Clarifying the link between toxin–antitoxin modules and bacterial persistence. *J. Mol. Biol.* 431, 3462–3471. doi:10.1016/j.jmb.2019.03.019.

Schastnaya, E., Raguz Nakic, Z., Gruber, C. H., Doubleday, P. F., Krishnan, A., Johns, N. I., et al. (2021). Extensive regulation of enzyme activity by phosphorylation in *Escherichia coli*. *Nat. Commun.* 12, 5650. doi:10.1038/s41467-021-25988-4.

Schwabe, A., and Bruggeman, F. J. (2014). Single yeast cells vary in transcription activity not in delay time after a metabolic shift. *Nat. Commun.* 5, 4798. doi:10.1038/ncomms5798.

Serganov, A., Huang, L., and Patel, D. J. (2008). Structural insights into amino acid binding and gene control by a lysine riboswitch. *Nature* 455, 1263–1267. doi:10.1038/nature07326.

Shabala, L., and Ross, T. (2008). Cyclopropane fatty acids improve *Escherichia coli* survival in acidified minimal media by reducing membrane permeability to H+ and enhanced ability to extrude H+. *Res. Microbiol.* 159, 458–461. doi:10.1016/j.resmic.2008.04.011.

Shan, Y., Brown Gandt, A., Rowe, S. E., Deisinger, J. P., Conlon, B. P., and Lewis, K. (2017). ATP-dependent persister formation in *Escherichia coli*. *MBio* 8, e02267-16. doi:10.1128/mBio.02267-16.

Shinar, G., Rabinowitz, J. D., and Alon, U. (2009). Robustness in glyoxylate bypass regulation.

PLoS Comput. Biol. 5, e1000297. doi:10.1371/journal.pcbi.1000297.

Siu, Y., Fenno, J., Lindle, J. M., and Dunlop, M. J. (2018). Design and selection of a synthetic feedback loop for optimizing biofuel tolerance. *ACS Synth. Biol.* 7, 16–23. doi:10.1021/acssynbio.7b00260.

Smolen, P. (2000). Modeling transcriptional control in gene networks—methods, recent results, and future directions. *Bull. Math. Biol.* 62, 247–292. doi:10.1006/bulm.1999.0155.

Solopova, A., van Gestel, J., Weissing, F. J., Bachmann, H., Teusink, B., Kok, J., et al. (2014). Bet-hedging during bacterial diauxic shift. *Proc. Natl. Acad. Sci.* 111, 7427–7432. doi:10.1073/pnas.1320063111.

Stokes, J. M., Lopatkin, A. J., Lobritz, M. A., and Collins, J. J. (2019). Bacterial metabolism and antibiotic efficacy. *Cell Metab.* 30, 251–259. doi:10.1016/j.cmet.2019.06.009.

Tani, T. H., Khodursky, A., Blumenthal, R. M., Brown, P. O., and Matthews, R. G. (2002). Adaptation to famine: A family of stationary-phase genes revealed by microarray analysis. *Proc. Natl. Acad. Sci.* 99, 13471–6. doi:10.1073/pnas.212510999.

Taniguchi, Y., Choi, P. J., Li, G. W., Chen, H., Babu, M., Hearn, J., et al. (2010). Quantifying *E. coli* proteome and transcriptome with single-molecule sensitivity in single cells. *Science* 329, 533–538. doi:10.1126/science.1188308.

Taymaz-Nikerel, H., De Mey, M., Baart, G., Maertens, J., Heijnen, J. J., and van Gulik, W. (2013). Changes in substrate availability in *Escherichia coli* lead to rapid metabolite, flux and growth rate responses. *Metab. Eng.* 16, 115–129. doi:10.1016/j.ymben.2013.01.004.

Tegnér, J., Yeung, M. K. S., Hasty, J., and Collins, J. J. (2003). Reverse engineering gene networks: Integrating genetic perturbations with dynamical modeling. *Proc. Natl. Acad. Sci.* 100, 5944–5949. doi:10.1073/pnas.0933416100.

Theriault, N., Tillotson, G., and Sandrock, C. E. (2021). Global travel and gram-negative bacterial resistance; implications on clinical management. *Expert Rev. Anti. Infect. Ther.* 19, 181–196. doi:10.1080/14787210.2020.1813022.

Thomas, P., Straube, A. V., and Grima, R. (2011). Communication: Limitations of the stochastic quasi-steady-state approximation in open biochemical reaction networks. *J. Chem. Phys.* 135, 181103. doi:10.1063/1.3661156.

Tiwari, A., Ray, J. C. J., Narula, J., and Igoshin, O. A. (2011). Bistable responses in bacterial genetic networks: Designs and dynamical consequences. *Math. Biosci.* 231, 76–89. doi:10.1016/j.mbs.2011.03.004.

Tonn, M. K., Thomas, P., Barahona, M., and Oyarzún, D. A. (2019). Stochastic modelling reveals mechanisms of metabolic heterogeneity. *Commun. Biol.* 2, 1–9.

doi:10.1038/s42003-019-0347-0.

Tyson, J. J., and Novak, B. (2020). A dynamical paradigm for molecular cell biology. *Trends Cell Biol.* 30, 504–515. doi:10.1016/j.tcb.2020.04.002.

Vecchio, D. Del, Dy, A. J., and Qian, Y. (2016). Control theory meets system biology. *J. R. Soc. Interfac* 13, 20160380. doi:10.1098/rsif.2016.0380.

Venturelli, O. S., El-Samad, H., and Murray, R. M. (2012). Synergistic dual positive feedback loops established by molecular sequestration generate robust bimodal response. *Proc. Natl. Acad. Sci.* 109, E3324-E3333. doi:10.1073/pnas.1211902109.

Walsh, K., and Koshland, D. E. (1985). Branch point control by the phosphorylation state of isocitrate dehydrogenase. A quantitative examination of fluxes during a regulatory transition. *J. Biol. Chem.* 260, 8430–8437. doi:10.1016/S0021-9258(17)39492-9.

Wehrs, M., Tanjore, D., Eng, T., Lievense, J., Pray, T. R., and Mukhopadhyay, A. (2019). Engineering robust production microbes for large-scale cultivation. *Trends Microbiol.* 27, 524–537. doi:10.1016/j.tim.2019.01.006.

Weimar, J. D., DiRusso, C. C., Delio, R., and Black, P. N. (2002). Functional role of fatty acyl-coenzyme A synthetase in the transmembrane movement and activation of exogenous long-chain fatty acids: Amino acid residues within the ATP/AMP signature motif of *Escherichia coli fadD* are required for enzyme activity and fatty acid transport. *J. Biol. Chem.* 277, 29369–29376. doi:10.1074/jbc.M107022200.

Wood, T. K., Knabel, S. J., and Kwan, B. W. (2013). Bacterial persister cell formation and dormancy. *Appl. Environ. Microbiol.* 79, 7116–7121. doi:10.1128/AEM.02636-13.

Xiao, Y., Bowen, C. H., Liu, D., and Zhang, F. (2016). Exploiting nongenetic cell-to-cell variation for enhanced biosynthesis. *Nat. Chem. Biol.* 12, 339–344. doi:10.1038/nchembio.2046.

Xu, P., Li, L., Zhang, F., Stephanopoulos, G., and Koffas, M. (2014). (SI) Improving fatty acids production by engineering dynamic pathway regulation and metabolic control. *Proc. Natl. Acad. Sci.* 111, 11299–11304. doi:10.1073/pnas.1406401111.

Xu, Y.-F., Amador-Noguez, D., Reaves, M. L., Feng, X.-J., and Rabinowitz, J. D. (2012). Ultrasensitive regulation of anapleurosis via allosteric activation of PEP carboxylase. *Nat. Chem. Biol.* 8, 562–568. doi:10.1038/nchembio.941.

Xu, Y., Heath, R. J., Li, Z., Rock, C. O., and White, S. W. (2001). The FadR.DNA complex. Transcriptional control of fatty acid metabolism in *Escherichia coli*. *J. Biol. Chem.* 276, 17373–9. doi:10.1074/jbc.M100195200.

You, M., Litke, J. L., and Jaffrey, S. R. (2015). Imaging metabolite dynamics in living cells

using a Spinach-based riboswitch. *Proc. Natl. Acad. Sci.* 112, E2756-E2765. doi:10.1073/pnas.1504354112.

Yuan, S.-F., and Alper, H. S. (2019). Metabolic engineering of microbial cell factories for production of nutraceuticals. *Microb. Cell Fact.* 18, 1-11. doi:10.1186/s12934-019-1096-y.

Zalis, E. A., Nuxoll, A. S., Manuse, S., Clair, G., Radlinski, L. C., Conlon, B. P., et al. (2019). Stochastic variation in expression of the tricarboxylic acid cycle produces persister cells. *MBio* 10, e01930-19. doi:10.1128/mBio.01930-19.

Zander, D., Samaga, D., Straube, R., and Bettenbrock, K. (2017). Bistability and nonmonotonic induction of the *lac* operon in the natural lactose uptake system. *Biophys. J.* 112, 1984–1996. doi:10.1016/j.bpj.2017.03.038.

Zaslaver, A., Mayo, A., Rosenberg, R., Bashkin, P., Sberro, H., Tsalyuk, M., et al. (2004). Just-in-time transcription program in metabolic pathways. *Nat. Genet.* 36, 486–491. doi:10.1038/ng1348.

Zenobi, R. (2013). Single-cell metabolomics: Analytical and biological perspectives. *Science* 342, 1243259. doi:10.1126/science.1243259.

Zhang, F., Carothers, J. M., and Keasling, J. D. (2012a). Design of a dynamic sensor-regulator system for production of chemicals and fuels derived from fatty acids. *Nat. Biotechnol.* 30, 354–359. doi:10.1038/nbt.2149.

Zhang, F., Ouellet, M., Batth, T. S., Adams, P. D., Petzold, C. J., Mukhopadhyay, A., et al. (2012b). Enhancing fatty acid production by the expression of the regulatory transcription factor FadR. *Metab. Eng.* 14, 653–660. doi:10.1016/j.ymben.2012.08.009.

Zheng, J., and Jia, Z. (2010). Structure of the bifunctional isocitrate dehydrogenase kinase/phosphatase. *Nature* 465, 961–965. doi:10.1038/nature09088.

Zheng, Y., Chen, J. C., Ma, Y. M., and Chen, G. Q. (2020). Engineering biosynthesis of polyhydroxyalkanoates (PHA) for diversity and cost reduction. *Metab. Eng.* 58, 82–93. doi:10.1016/j.ymben.2019.07.004.

Chapter 2: Metabolite Sequestration Enables Rapid Recovery from Fatty Acid Depletion in *Escherichia coli*

This chapter contains text and figures published as:

Hartline, C.J.*, Mannan, A.A*, Liu, D., Zhang, F., and Oyarzún, D.A. (2020). Metabolite sequestration enables rapid recovery from fatty acid depletion in *Escherichia coli*. *MBio* 11, e03112-19. doi: 10.1128/mBio.03112-19.

Reprinted with permission.

*Authors contributed equally to work.

Chapter 2 Abstract

Microbes adapt their metabolism to take advantage of nutrients in their environment. Such adaptations control specific metabolic pathways to match energetic demands with nutrient availability. Upon depletion of nutrients, rapid pathway recovery is key to release cellular resources required for survival in the new nutritional condition. Yet little is known about the regulatory strategies that microbes employ to accelerate pathway recovery in response to nutrient depletion. Using the fatty acid catabolic pathway in *Escherichia coli*, here we show that fast recovery can be achieved by rapid release of a transcriptional regulator from a metabolite-sequestered complex. With a combination of mathematical modelling and experiments, we show that recovery dynamics depend critically on the rate of metabolite consumption and the exposure time to nutrient. We constructed strains with re-wired transcriptional regulatory architectures that highlight the metabolic benefits of negative autoregulation over constitutive and positive autoregulation. Our results have wide-ranging implications for our understanding dynamic

metabolic adaptations and guiding the design of gene circuitry for synthetic biology and metabolic engineering.

2.1 Introduction

Bacteria constantly adapt to changing environments by coordinating multiple levels of their intracellular machinery. Metabolic regulation provides a control layer that adapts catabolic activity to nutritional conditions. Such regulation relies on a complex interplay between gene expression and metabolic pathways (Piazza et al., 2018). In the case of catabolic pathways, genes for nutrient uptake and consumption need to be upregulated when the specific nutrient is available in the environment. Failure to quickly increase pathway capacity may result in missed metabolic resource opportunity and a potential cost on fitness (Lambert et al., 2014) and population survival (Amato et al., 2013; Kotte et al., 2014; Solopova et al., 2014). Conversely, upon nutrient depletion, the expression of catabolic enzymes is wasteful and leads to a suboptimal use of biosynthetic resources (Dekel and Alon, 2005; Kalisky et al., 2007).

Metabolite-responsive transcription factors are a widespread regulatory mechanism in microbes. Upon sensing nutrient availability, they trigger changes in enzyme expression and metabolic flux (Kotte et al., 2010). This strategy has been shown to control the dynamics of pathway upregulation in various ways (Alon, 2007; Chin et al., 2008; Chubukov et al., 2012). For example, negative autoregulation of transcription factors can speed the response time of gene expression (Rosenfeld et al., 2002) and feedback circuits based on metabolite-responsive transcription factors have been demonstrated to accelerate metabolite responses (Liu and Zhang, 2018). While much of the literature has focused on the control of activation dynamics upon nutrient

induction, little is known on how these regulatory mechanisms shape pathway recovery after depletion of nutrients.

Here we study a common regulatory architecture found in over a dozen bacterial nutrient uptake systems (Keseler et al., 2017) (Figure 2.1A; see also Appendix A, Table A.1). When a nutrient is absent from the environment, a metabolite-responsive transcription factor (MRTF) represses the expression of uptake and catabolic enzymes. When the nutrient is present, the nutrient is internalized and sequesters the transcription factor via reversible binding, thus preventing gene repression. This causes an upregulation of metabolic enzyme genes and an increase in the rate of nutrient import and utilization. A common feature of these control systems is the presence of negative autoregulation of the transcription factor (Appendix A, Table A.1). After nutrient depletion, the MRTF must recover its repressive activity on the catabolic pathway genes to rapidly shut down pathway activity, yet it is unclear what components of the regulatory system help to accelerate the recovery dynamics.

Using the *Escherichia coli* fatty acid catabolic pathway as a model system, we took a theoretical-experimental approach to study its recovery dynamics in response to a nutrient shift from an ON state to an OFF state. As illustrated in Figure 2.1B, these two states are defined as an environment with and without the presence of oleic acid as carbon source, respectively. In the ON state, oleic acid is imported as fatty acyl-Coenzyme A (acyl-CoA) which binds to the transcription factor FadR and sequesters it into a complex. This acyl-CoA sequestration releases FadR from its cognate DNA elements (Cronan, 1997), which relieves the repression of the uptake gene *fadD* and thus accelerates the import of oleic acid. We found that upon depletion of oleic acid, repression by FadR is recovered via its rapid release from the sequestered complex, which in turn is driven by consumption of acyl-CoA. We further found that the architecture of FadR autoregulation affects

the maintenance of a sequestered pool of FadR. In particular, negative autoregulation enables a large sequestered-transcription factor (TF) pool during the ON state and, at the same time, a reduced biosynthetic cost in the OFF state. Our results shed light on the regulatory mechanisms that allow cells to rapidly adapt to environmental shifts and provide insights for the design of gene circuits in synthetic biology and metabolic engineering, where strain performance is sensitive to nutrient fluctuations and inhomogeneities typical of large-scale fermentations.

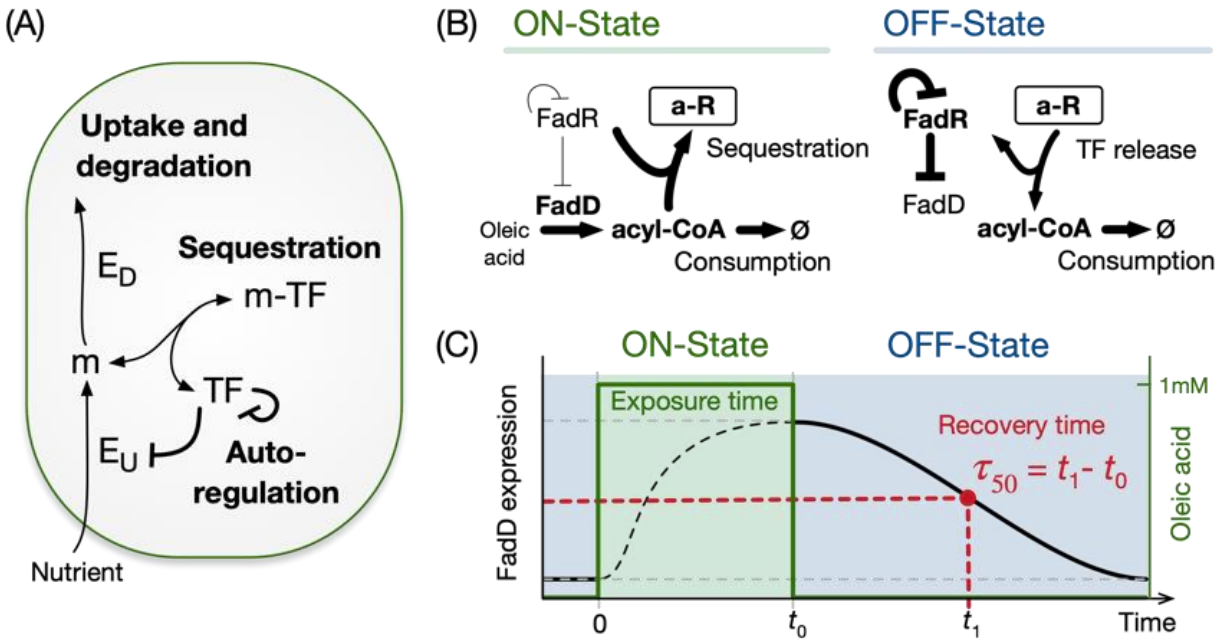

Figure 2.1. General architecture of a bacterial nutrient uptake system. (A) Regulation of nutrient uptake by a metabolite-responsive transcription factor, a ubiquitously observed control system in bacteria (Table A.1). **(B)** We use the *Escherichia coli* fatty acid uptake as a model system. The ON state is defined by induction at a constant level of oleic acid, which is imported as acyl-CoA by uptake enzyme FadD. Acyl-CoA sequesters the transcription factor FadR, which derepresses expression of the uptake enzyme. The OFF state is defined by the washout of oleic acid after some time (t_0) in the ON state. The release of sequestered FadR recovers its repression on FadD synthesis. FadR is also subject to negative autoregulation. **(C)** Schematic of the experiments and simulations in this work, with defined exposure time to oleic acid (green area) and with recovery time of FadD levels in the OFF state (τ_{50}) defined as the time to reach to halfway between the maximum and minimum concentrations.

2.2 Results

2.2.1 Recovery Dynamics in the Fatty Acid Uptake System

To study the recovery dynamics of fatty acid uptake, we built a kinetic model based on four core components of the regulatory system: FadD (*D*), free FadR (*R*), acyl-CoA (*A*) and sequestered FadR (*aR*). The model represents cells growing at a fixed growth rate with oleic acid at a fixed concentration in the media. We simulated the recovery dynamics by mimicking the three stages in our experimental setup: preculture without oleic acid, response to induction in the ON state, and recovery in the OFF state. During preculture, we ran the model to steady state in the absence of oleic acid and then initiated simulations of the ON state from the steady state achieved in preculture, with a fixed concentration of oleic acid for a defined exposure time. The concentrations achieved at the end of the ON state were used as initial conditions for the OFF state, which was simulated without oleic acid until the system recovers to the steady state in preculture (Figure 2.1C).

We defined two metrics to quantify the recovery dynamics after the switch from ON to OFF state (Figure 2.1C). First, we define the recovery time as the time taken for FadD to decrease to halfway between its maximum and minimum steady-state value after nutrient depletion (τ_{50}) (Figure 2.1C). Second, we defined the metric η as the proportion of free FadR released from the sequestered complex after one doubling time, shown in equation 2.1:

$$\eta = \frac{FadR_{DT} - FadR_{DT-new}}{FadR_{DT}} \qquad \text{(Eq. 2.1)}$$

where $FadR_{DT}$ and $FadR_{DT\text{-}new}$ are the concentrations of free FadR and newly expressed FadR in the OFF state after one doubling time (DT). This definition allows us to quantify the contribution of free FadR released from the sequestered pool to the recovery dynamics.

Since pathway recovery depends on the system state at the time of the ON to OFF switch, we used the kinetic model to study the relation between the initial conditions at the time of the switch and the recovery dynamics. To this end, we studied the impact of exposure time to oleic acid during the ON state, as well as the amount of acyl-CoA-consuming enzyme. We simulated the OFF-state dynamics for 2,500 combinations of 50 acyl-CoA-consuming enzyme concentrations and 50 exposure times, and calculated τ_{50} and η for each. The simulation results of the OFF-state dynamics (Figure 2.2A) suggest that the τ_{50} decreases with increasing concentrations of consuming enzyme, while the amount of released FadR (η) increases with both the consuming enzyme and the exposure time. Further simulations suggest that when exposure time increases, the pool of acyl-CoA accumulates further, with a rise time from 8.5 to 10 h, for levels of consuming enzyme from 100 μM and 6 μM (Appendix A, Figure A.2B). This larger pool takes a longer time to be consumed in the OFF state (Appendix A, Figure A.2A) and so delays the release of FadR from the complex. This results in a longer recovery time (details in Appendix A, Section A.3 and Figure A.2). Model simulations also reveal a strong inverse relation between τ_{50} and η (Figure 2.2B), indicating that the release of FadR from sequestration by acyl-CoA provides a mechanism for cells to achieve rapid recovery during nutrient depletion. Further, the sensitivity of this inverse relation increases when cells are exposed to a longer ON state. Simulations show that longer cell exposure times to oleic acid increase the pool of sequestered FadR (Appendix A, Figure A.2). Consequently, in the OFF state, more FadR can be released from sequestration than with new FadR synthesis, thus increasing the sensitivity of τ_{50} changes in the amount of released FadR.

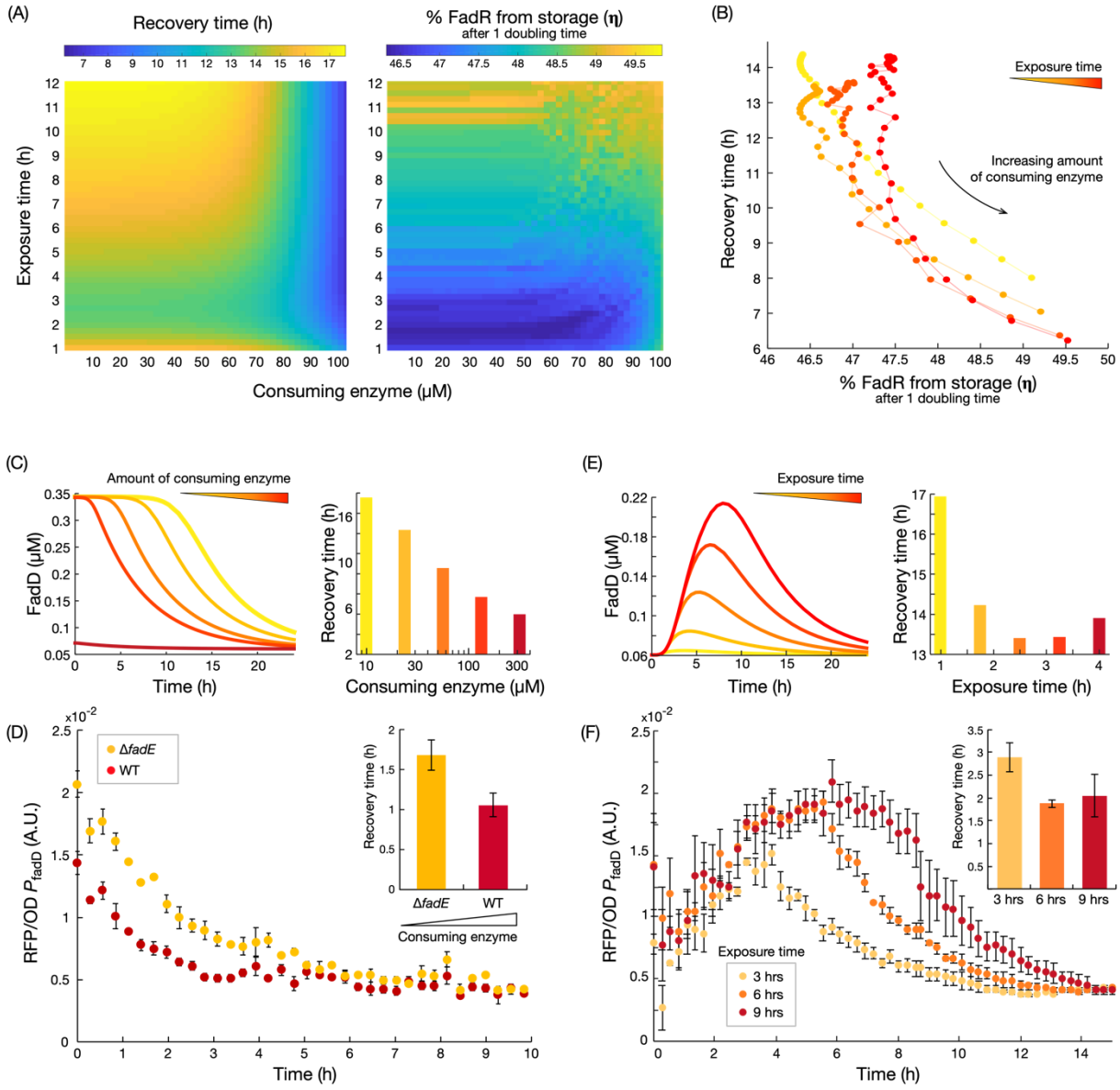

Figure 2.2. Nutrient exposure time and speed of metabolite consumption in the OFF state shape the recovery time. (A) Predicted recovery time (τ_{50}) and proportion of free FadR released from sequestration after one doubling time (η) for variations in the amount of consuming enzyme and nutrient exposure time. **(B)** Inverse relation between the proportion of released FadR (η) and predicted recovery time. **(C)** Simulated time course of FadD concentration in OFF state and predicted recovery times for increasing concentration of acyl-CoA consuming enzyme. **(D)** Measured time course of *fadD* expression when switching from ON to OFF state for strains with low (Δ*fadE* mutant reporter) and high (WT reporter) concentration of acyl-CoA consuming enzyme. Strains were switched from M9G plus 1 mM oleic acid to M9G media at time zero. Error

bars represent standard error of the mean (SEM) of the results from biological triplicates (n = 3). Recovery times were calculated from exponential fits to each of the triplicate time course data (inset). Error bars represent SEM of the results from biological triplicates (n = 3). **(E)** Time course simulations of FadD induction and recovery dynamics, and predicted recovery times, for increasing exposure times. **(F)** Measured time course of *fadD* expression from the WT reporter strain grown for 3, 6 and 9 hours of exposure to oleic acid (M9G plus 1 mM oleic acid) and then switched to an OFF state (M9G). Error bars represent the SEM of the results from biological triplicates (n = 3). Recovery times were again calculated from exponential fits, with error bars indicating the SEM of the results from triplicate (n = 3).

To verify the model predictions, we sought to experimentally perturb η through two complementary strategies, as follows: (i) by engineering strains with different amounts of acyl-CoA consuming enzymes, and (ii) by manipulating the exposure time to oleic acid. We first constructed a reporter strain with a decreased rate of consumption of acyl-CoA, the ΔfadE mutant reporter strains (see Appendix A, Table A.4 and Table A.5), where we deleted the *fadE* gene encoding the second step of the fatty acid β-oxidation pathway. This prevents metabolization of acyl-CoA by β-oxidation and leaves membrane incorporation (catalyzed by enzyme PlsB) as the only pathway for acyl-CoA consumption. We measured *fadD* expression dynamics after switching the strains from the ON state (M9G + 1mM oleic acid media) to OFF state (M9G media) using a red fluorescent protein (RFP) reporter fused downstream of the *fadD* promoter. The *fadE* knockout strain displayed a slower recovery than the wild type, with ~60% increase in recovery time (Figure 2.2D), confirming our theoretical prediction shown in Figure 2.2C. The measured increase in recovery time entails an increased expenditure of biosynthetic resources to import a metabolite that is no longer present in the environment.

Next, we measured the *fadD* recovery dynamics after switching the cultures from growth with 3, 6, and 9 hours of exposure time in the ON state. As predicted from the model in Figure

2.2E, the measured recovery time decreased for an increase in exposure time (Figure 2.2F). However, we observe that recovery time is not decreased further beyond 6 hours of exposure to oleic acid. We speculate that faster recovery is counteracted by the delay of having to consume a higher level of accumulated acyl-CoA, or because the maximum level of sequestered FadR may already have been achieved at 6 hours.

2.2.2 Impact of Autoregulatory Architecture on Recovery Dynamics

Among the uptake systems in *E. coli* with the architecture of Figure 2.1A, we found that the majority have a transcriptional regulator that represses its own expression, few systems have constitutive expression of the regulator, and no systems display positive autoregulation (see Appendix A, Table A.1). To better understand the salient features of each regulatory architecture and how they affect recovery dynamics, we built variants of our kinetic model with FadR under constitutive expression and positive or negative autoregulation (details in 2.4 Materials and Methods). Simulations of the recovery dynamics in the OFF state for varying exposure times in the ON state suggest that these architectures behave similarly for short exposure times (< 1 hour), quickly sequestering all the free FadR (Figure 2.3A, top). For longer exposure times (>1 hour), model simulations suggest important differences in the dynamics of sequestered FadR among the various modes of autoregulation. Negative autoregulation shows an accumulation of sequestered FadR, while positive autoregulation leads to an overall depletion of sequestered FadR. Constitutive expression causes the total level of FadR to be maintained at a constant level (Figure 2.3A).

To elucidate whether these predicted trends are a consequence of the model parameters or are inherently determined by the autoregulatory architecture, we analyzed the model and found relations for the change in steady-state concentrations of total FadR (ΔR_T) in each autoregulatory architecture (the details of derivation are in Appendix A, Section A.5), as follows: negative

autoregulation $\Delta R_T > 0$; positive autoregulation $\Delta R_T < 0$; constitutive expression, $\Delta R_T = 0$. These relationships are valid for any combination of positive parameters, and therefore, the long-term trends observed in Figure 2.3A are structural properties of the model.

To determine the effect of the three regulatory architectures on the recovery time, we simulated the recovery dynamics of each architecture for various exposure times and calculated the recovery time (Figure 2.3A, bottom). We observe that the overall relation between recovery time and exposure time is similar across the three architectures (Figure 2.3A bottom inset). However, for positive autoregulation, we found recovery to be significantly slower for a wide range of exposure times. To test this prediction, we engineered an *E. coli* strain with positively autoregulated FadR expression by replacing the native *fadR* promoter with one that activated by FadR (P_{fadRpo}) (see Appendix A, Section A.6, Table A.4), and a P_{fadD} reporter plasmid. The positively autoregulated reporter strain (PA reporter) (Appendix A, Section A.6, Tables A.5, A.6) was grown in the ON state (M9G medium plus 1 mM oleic acid) and then rapidly switched to the OFF state (M9G medium) after 3, 6 and 9 hours. We measured the *fadD* expression dynamics (see time course dynamics in Appendix A, Section A.6, Figure A.3), and calculated the respective recovery times (Figure 2.3B). Consistent with the trend predicted from the model, the recovery times for the positively autoregulated strain increased with the exposure time to oleic acid in the ON state (Figure 2.3C).

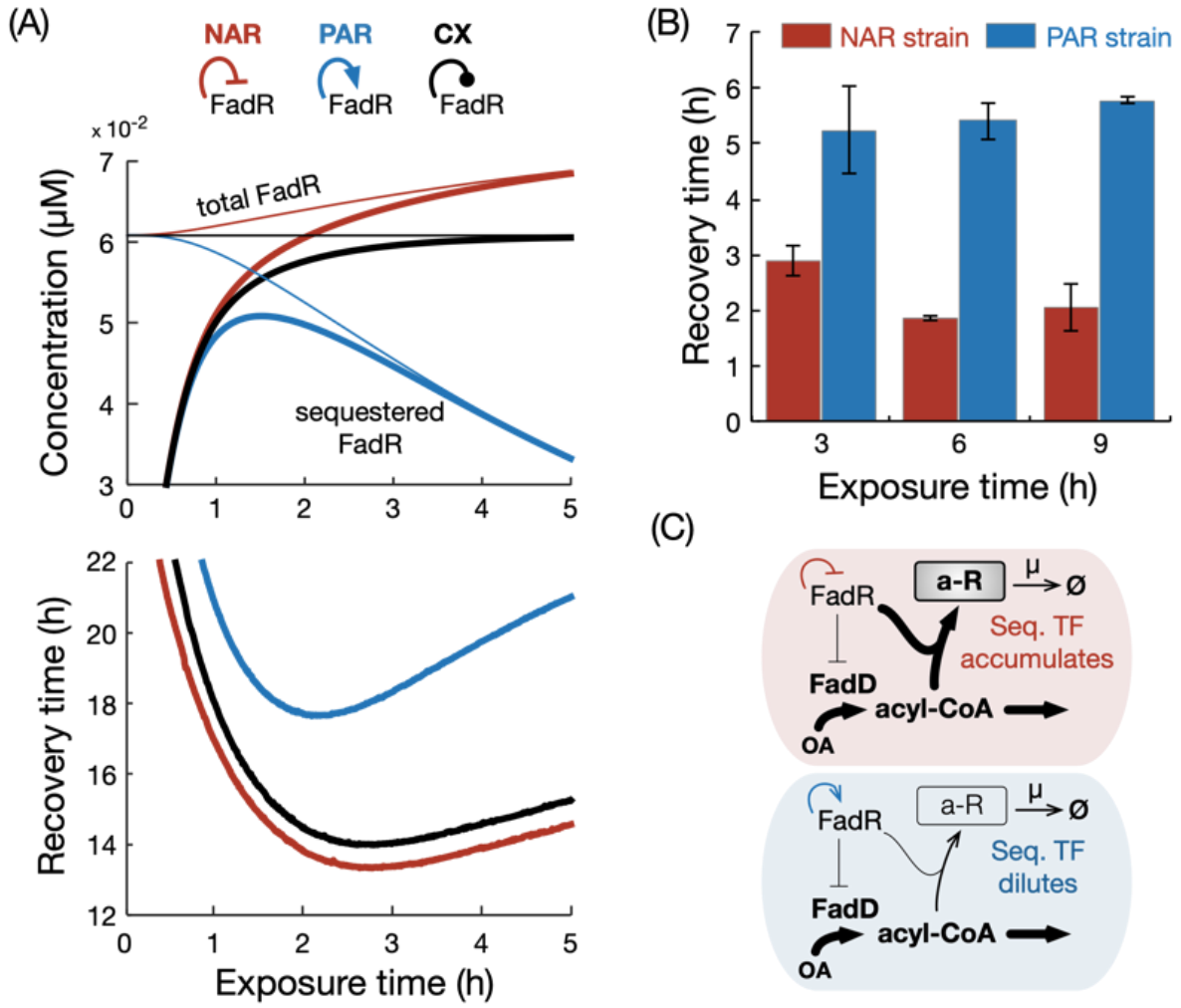

Figure 2.3. Impact of regulatory architecture on the recovery time after nutrient depletion. **(A)** Top, simulated steady-state concentrations of sequestered (thick line) and total (thin line) FadR for various times spent in the ON state for three regulatory architectures of FadR; constitutive expression (black line) is represented by a blunt line. Bottom, predicted recovery times for each architecture. **(B)** Measured recovery times in the WT (WT reporter) and positively autoregulated strain (PA reporter), (Appendix A, Tables A.3B and A.4) for 3, 6 and 9 hours of exposure in ON state. Recovery times were calculated from exponential fits to each of the triplicate time course data (see Appendix A, Section A.6 and Figure A.3), and error bars represent SEM of the calculated values (n=3). **(C)** Schematics illustrating how negative and positive autoregulation affect the build-up of sequestered FadR in the ON state.

2.2.3 Negative Autoregulation Provides a Resource-Saving Recovery Strategy

The results from the above-described autoregulation relationship suggest that constitutive expression and negative autoregulation can both maintain large amounts of sequestered FadR for

long exposure times to oleic acid. Our earlier results showed that longer exposure times lead to larger pool of sequestered FadR (Appendix A, Figure A.2D), which enables a faster recovery time (Figure 2.2E and 2.2F). We thus asked which system parameters influence the steady-state pool size of sequestered FadR in these two architectures. We found that for high concentrations of oleic acid, the steady-state concentration of sequestered FadR in the ON state is given by Equations 2.2 and 2.3 (details in Appendix A, Section A.7):

Negative autoregulation: $$\lim_{A\to\infty} \mathrm{aR} = \frac{a_n}{\mu} \quad \text{(Eq. 2.2)}$$

Constitutive expression: $$\lim_{A\to\infty} \mathrm{aR} = \frac{p_c}{\mu} \quad \text{(Eq. 2.3)}$$

where A and aR are the steady-state concentrations of acyl-CoA and sequestered FadR, respectively, and a_n and p_c are the promoter strengths in each case. These results suggest that at high oleic acid concentrations, the amount of sequestered FadR scales linearly with the strength of its own promoter. In simulations of both architectures in the ON state induced with high concentration of oleic acid (1 mM) and various promoter strengths, we found that increasing promoter strength both increases the amount of sequestered FadR in the ON state and decreases the recovery time (Figure 2.4A).

The results in Figure 2.4A also suggest that through tuning of *fadR* promoter strength, in principle, constitutive expression and negative autoregulation can produce the same recovery time. We thus sought to identify potential benefits of one architecture over the other in terms of the recovery dynamics in the OFF state. Since production of FadR entails a biosynthetic cost, we compared both regulatory architectures in terms of the cost of FadR synthesis. From time course simulations of FadR synthesis rates in the ON and OFF states (Figure 2.4B), we computed the total amount of synthesized FadR for increasing *fadR* promoter strengths by integrating the area under

the curves (Figure 2.4C). Our results show that both architectures require identical biosynthetic costs for FadR in the ON state, but negative autoregulation leads to a reduced biosynthetic cost for FadR in the OFF state compared to constitutive expression (Figure 2.4C).

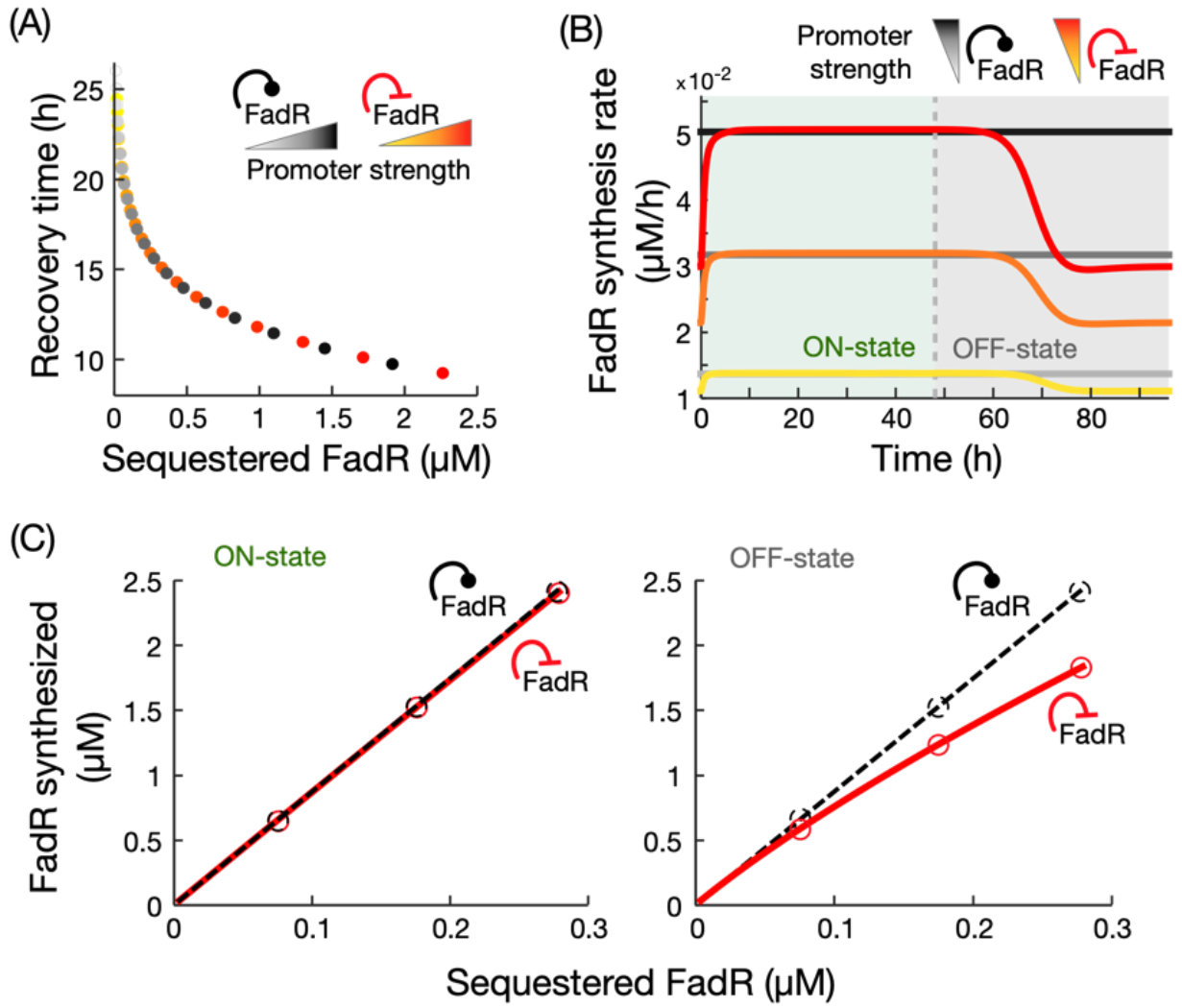

Figure 2.4. Comparison of recovery dynamics in constitutive expression and negative autoregulation. (A) Simulated recovery times for variations in the strength of FadR's own promoter, with the two architectures achieving the same recovery times. **(B)** Time course simulations of FadR synthesis rates for 48 hours in the ON state (1 mM oleic acid) and OFF state, for increasing promoter strengths; the yellow curve represents the response with the fitted promoter strength value (Appendix A, Table A.2). To ensure fair comparison, promoter strengths were

chosen to achieve the same recovery time in the two architectures. **(C)** Cost of FadR synthesis for increasing concentrations of sequestered FadR, modified by changes to *fadR* promoter strength. Circles correspond to costs associated to simulations shown in **(B)**. Details of the simulations are in Section 2.4 Materials and Methods.

2.3 Discussion

In this paper, we combined mathematical modelling and experiments to study metabolic pathway recovery upon depletion of a nutrient. Changes in nutrient conditions trigger transcriptional programs that adapt cell physiology (Chubukov et al., 2014) to meet the cellular energy budget (Weiße et al., 2015). We chose the regulation of fatty acid uptake in *E. coli* as our model system, as it was representative of a widely conserved transcriptional program for controlling the uptake of nutrients in bacteria (see Appendix A, Table A.1). We show that fast recovery after nutrient depletion can be achieved by rapid release of a transcriptional regulator from a metabolite-sequestered complex. In particular, a sizable contribution of FadR rapidly made available after oleic acid depletion came from its release from its sequestered complex form (aR), as opposed to new synthesis. The rapid availability of FadR quickly recovers its inhibition on the *fad* regulon and so shortens the recovery time. Furthermore, our model simulations and experiments have demonstrated that increasing the amount of FadR stored in complex form during nutrient exposure and fast consumption of acyl-CoA (the sequestering metabolite) facilitate a speedy recovery in the OFF state.

Our model simulations show that pathway recovery is delayed by high intracellular acyl-CoA concentrations, which slow the release of free FadR from stored complex until those high concentrations are reduced. This delay occurs because FadR is only able to sense the intracellular

metabolite concentrations, which can remain high even when extracellular metabolite concentrations are low. During this delay, wasteful expression of the uptake pathway continues despite the absence of oleic acid in the environment. Previous research has shown that upon nutrient induction, metabolite dynamics tend to lag behind slow upregulation of metabolic enzymes (Liu and Zhang, 2018). In contrast, here we find that after inducer depletion, the recovery of metabolic enzymes back to their downregulated state lags behind the metabolite dynamics. This has important implications for designing synthetic control circuits which utilize non-metabolizable inducers such as isopropyl-β-D-thiogalactopyranoside (IPTG) or methyl-β-D-thiogalactopyranoside (TMG). Without consumption of the inducer, the postinduction recovery response will be slow and may cause a dramatic drain of cellular resources. Our simulations of the relation between sequestered FadR and recovery time suggest that this inherent lag can be compensated for by storing and releasing higher amounts of TFs, which highlights the benefits of maintaining a sequestered pool of FadR.

Further mathematical analyses revealed principles that explain how autoregulation shapes the recovery time. We found that systems with only negative autoregulation and constitutive expression can maintain the pool of sequestered FadR needed for a rapid recovery. In contrast, we found that positive autoregulation loses this storage over time, resulting in a reduced availability of FadR after nutrient depletion and slower recovery times. We additionally found that negative autoregulation of the transcription factor reduces the total biosynthetic cost of for FadR in a full ON-OFF-state cycle as compared to using constitutive expression. This occurs because both systems need to maintain the same level of sequestered FadR in the ON state in order to achieve the same recovery time, but only negative autoregulation allows FadR synthesis to be downregulated in the OFF state. Thus, negative autoregulation provides a resource-saving strategy

for controlling the recovery dynamics compared to constitutive expression. We found that the transcriptional regulators in 13 out of 18 nutrient uptake systems have negative autoregulation (see Appendix A, Table A.1), suggesting an evolutionary pressure for a resource-saving control strategy. Past studies in the literature have found that expression under negative autoregulation can decrease response times in gene expression (Rosenfeld et al., 2002), linearize dose-response in responsive systems (Madar et al., 2011), and even speed up metabolic dynamics (Liu and Zhang, 2018). In addition to these properties, we find that negative autoregulation enables rapid and more resource-saving metabolic recovery to nutrient depletion.

Recent efforts in synthetic biology focus on engineering gene control circuits to manipulate microbial metabolism (Gupta et al., 2017a; Liu et al., 2018; Lv et al., 2019). One key goal of such control systems is to rapidly turn off metabolic pathways in response to metabolic signals (Gupta et al., 2017b; Harder et al., 2018; Moser et al., 2018). Our results provide core design principles for engineered metabolic systems with tunable response to nutrient depletions, which could be used as a pathway control tool in bioreactors. Our experiments and simulations reveal that the recovery time can be simply tuned through well-established promoter engineering techniques (Alper et al., 2005; Zhang et al., 2012; Mannan et al., 2017). Further, we identify regulatory architectures with differing dynamic responses to nutrient depletion, which provides further avenues for tuning system response to the highly dynamic and heterogeneous environments typical of large-scale fermenters. These design rules can be readily applied to mitigate against deleterious nutrient fluctuations found in metabolic engineering applications.

2.4 Materials and Methods

2.4.1 Materials

Phusion DNA polymerase, T4 DNA ligase, restriction enzymes, and Teknova 5x M9 minimal salts were purchased from Thermo Fisher Scientific (Waltham, MA, USA). Gel purification and plasmid miniprep kits were purchased from iNtRON Biotechnology (Lynnwood, WA, USA.). Oligonucleotides were synthesized by Integrated DNA Technologies (Coralville, IA, USA). All other reagents were purchased from Sigma-Aldrich (St. Louis, MO, USA.)

2.4.2 Plasmids, Strains, and Genome Modifications

A list of plasmids used along with promoter sequences in this study is provided in Appendix A, Section A.4, Tables A.4 and A.5). *E. coli* DH10β was used for plasmid construction. The plasmid pSfadDk-rfp was constructed by cloning the *fadD* promoter (500 bp upstream of its translation start site) into the 5' of a *rfp* gene in a BglBrick vector, pBbSk-rfp (Lee et al., 2011) using Golden Gate DNA Assembly (Engler et al., 2008). The positively autoregulated *fadR* strain was engineered by replacing *fadR*'s native promoter with a FadR-activated promoter P_{fadRpo} via CRISPR-Cas9 genome editing (Jiang et al., 2015). Detailed engineering methods and the characterization of the P_{fadRpo} promoter are described in Appendix A Section A.6.

Three reporter strains were created to measure expression dynamics from the *fadD* promoter. These strains were created by transforming plasmid pSfadDk-rfp into either the wild-type DH1 strain, DH1(Δ*fadE*), or an engineered strain with positively autoregulated *fadR*, resulting in wild-type (WT) reporter, Δ*fadE* mutant reporter, and PA reporter, respectively.

2.4.3 Media Conditions

All strains were grown from single colonies and cultivated overnight in Luria-Bertani (LB) medium before experiments. For OFF State culture conditions, cells were grown in M9 minimal

medium (Liu et al., 2015) supplemented with 1% glycerol and 0.5% Tergitol NP-40 solution (M9G). For ON state culture conditions, cells were grown in M9G plus 1 mM oleic acid (M9G+OA). All cultures were supplemented with appropriate antibiotic selection (50 mg/L kanamycin, 100 mg/L ampicillin).

2.4.4 Assays of fadD Expression Dynamics

To measure the recovery dynamics, reporter strains were grown in 3 mL M9G+OA for 24 to 48 hours at exponential-growth state. To rapidly switch nutrients, cells were centrifuged (5,500 relative centrifugal force [rcf], 2 minutes) and washed twice in M9G. Cultures were then diluted in M9G medium to an optical density at 600 nm (OD_{600}) of 0.08 and transferred to a Falcon 96-Well imaging microplate (Corning, NY, USA). The microplate was then incubated in an Infinite F200 Pro plate reader (Tecan, Männedorf, Switzerland) at 37°C with constant shaking. To maintain exponential growth during measurement, cultures were diluted by a factor of 5 for three times during incubation. Kinetic measurements of cell density (absorbance at 600 nm) and RFP fluorescence (excitation: 584 ± 9 nm, emission: 620 ± 20 nm) were taken every 900 seconds until all diluted cultures reached stationary phase. Fluorescence from water in the same 96-well plate was used as the background and was subtracted from all fluorescence measurements. The background-corrected fluorescence was later normalized by cell density. To calculate the recovery time, the average of three biological replicates were fitted to an exponential curve, shown in equation 2.4:

$$F = a \times e^{-b*t} + c \qquad \text{(Eq. 2.4)}$$

where F is the background-corrected, cell-density-normalized fluorescence. The recovery time was calculated as $\tau_{50} = \ln(2)/b$.

For switches after defined times in the ON state, cultures were first grown in exponential growth phase for 24 to 28 hours in M9G. Samples from these cultures were then centrifuged (5,500 rcf, 2 minutes) and suspended in M9G+OA with an initial OD_{600} of 0.08 and cultivated in 96-well plates for various amount of time as indicated.

2.4.5 Kinetic Model of Fatty Acid Uptake

To study the system dynamic response to oleic acid exposure (ON state) and its recovery (OFF state) (Figure 2.1C), we built a kinetic model of the fatty acid uptake system. We define the model as a system of ordinary differential equations (ODEs) describing the rate of change of each species, shown in equations 2.5 to 2.8:

$$\frac{dR}{dt} = P_R(R, p_r) - k_f \cdot R \cdot A^2 + k_r \cdot aR - \mu \cdot R \quad \text{(Eq. 2.5)}$$

$$\frac{dD}{dt} = b_D + \frac{a_D}{1 + (k_D \cdot R)^2} - \mu \cdot D \quad \text{(Eq. 2.6)}$$

$$\frac{dA}{dt} = \frac{k_{cat,D} \cdot OA}{K_{M,D} + OA} \cdot A \cdot D - \frac{k_{cat,B} \cdot A}{K_{M,B} + A} \cdot B - 2 \cdot \left(k_f \cdot R \cdot A^2 + k_r \cdot aR\right) - \mu \quad \text{(Eq. 2.7)}$$

$$\frac{daR}{dt} = k_f \cdot R \cdot A^2 - k_r \cdot aR - \mu \cdot aR \quad \text{(Eq. 2.8)}$$

where *R*, *D*, *A* and *aR* represent the concentrations of transcription factor FadR, uptake enzyme FadD, internalized fatty acid acyl-CoA, and sequestered complex acyl-CoA-FadR, respectively (Figure 2.1B). The reversible sequestering of one FadR dimer by two acyl-CoA molecules (stoichiometry as defined in (van Aalten et al., 2000)) is modeled as mass-action kinetics in the term $k_f RA^2 - k_r aR$. The term $P_R(R, p_r)$ represents the expression and autoregulation of the fadR promoter. To model FadR negative autoregulation for the wild-type strain, we use equation 2.9:

$$P_{R,n} = b_n + \frac{a_n}{1 + K_n \cdot R} \quad \text{(Eq. 2.9)}$$

To fit model parameters, we first extended the model to emulate batch culture experiments and then used least-squares fitting of simulations to time course measurements of RFP fluorescence expressed under an *fadD* promoter, from the *ΔfadE* mutant strain, in various concentrations of oleic acid (see details in Appendix A, Section A.2 and Table A.2). The fitting results are illustrated in Figure A.1, and the parameter values are reported in Table A.2B. These values were used throughout the study, unless otherwise stated. To understand the impact of model parameters on the recovery time, we performed global parameter sensitivity analysis (details in Appendix A, Section A.7 and Figure A.4). To model the strains with positive autoregulation and constitutive expression of FadR, we use equations 2.10 and 2.11:

$$P_{R,p} = b_p + \frac{a_p \cdot K_p \cdot R}{1 + K_p \cdot R} \quad \text{(Eq. 2.10)}$$

$$P_{R,c} = p_c \quad \text{(Eq. 2.11)}$$

2.4.6 Model Simulations

The model was solved with the MATLAB R2018a ODE solver suite. To simulate the ON state, simulations were initialized using the steady-state values achieved from simulations of the preculture (oleic acid [OA] concentration 0 µM), and a constant oleic acid concentration was set to 1,000 µM. Simulations were then run for a defined exposure time. To simulate the OFF state, the system was initialized from the state achieved at the end of the ON state, and the oleic acid concentration was set to 0 µM. Simulations were then run to steady state, and recovery times were calculated as the time from the start of the OFF state until FadD reached halfway between its initial

value and minimum steady-state value. To calculate the cost of FadR synthesis in the ON and OFF states (Figure 2.4C), we integrated simulations of the FadR synthesis rate over 48 hours in each state.

In Figure 2.3, for fair comparison, model parameters are set such that the steady-state concentration of FadR is the same for all three architectures prior to switching to the ON state. Likewise, in Figure 2.4B and 2.4C for fair comparison, *fadR* promoter strengths for both architectures were set to achieve same concentration of sequestered FadR in the ON state (and thus equal recovery times).

2.5 Supplemental Information

Table A.1- A.6, Figures A.1-A.4, and Appendix Sections A.1-A.9 can be found in Appendix A.

2.6 Chapter 2 References

Alon, U. (2007). Network motifs: Theory and experimental approaches. *Nat. Rev. Genet.* 8, 450–461. doi:10.1038/nrg2102.

Alper, H., Fischer, C., Nevoigt, E., and Stephanopoulos, G. (2005). Tuning genetic control through promoter engineering. *Proc. Natl. Acad. Sci.* 102, 12678–83. doi:10.1073/pnas.0504604102.

Amato, S., Orman, M., and Brynildsen, M. (2013). Metabolic control of persister formation in *Escherichia coli*. *Mol. Cell* 50, 475–487. doi:10.1016/j.molcel.2013.04.002.

Chin, C.-S., Chubukov, V., Jolly, E. R., DeRisi, J., and Li, H. (2008). Dynamics and design principles of a basic regulatory architecture controlling metabolic pathways. *PLoS Biol.* 6, e146. doi:10.1371/journal.pbio.0060146.

Chubukov, V., Gerosa, L., Kochanowski, K., and Sauer, U. (2014). Coordination of microbial metabolism. *Nat. Rev. Microbiol.* 12, 327–340. doi:10.1038/nrmicro3238.

Chubukov, V., Zuleta, I. A., and Li, H. (2012). Regulatory architecture determines optimal regulation of gene expression in metabolic pathways. *Proc. Natl. Acad. Sci.* 109, 5127–5132. doi:10.1073/pnas.1114235109.

Cronan, J. E. (1997). In vivo evidence that acyl coenzyme A regulates DNA binding by the *Escherichia coli* FadR global transcription factor. *J. Bacteriol.* 179, 1819–23. doi:10.1128/jb.179.5.1819-1823.1997.

Dekel, E., and Alon, U. (2005). Optimality and evolutionary tuning of the expression level of a protein. *Nature* 436, 588–92. doi:10.1038/nature03842.

Engler, C., Kandzia, R., and Marillonnet, S. (2008). A one pot, one step, precision cloning method with high throughput capability. *PLoS One* 3, e3647. doi:10.1371/journal.pone.0003647.

Gupta, A., Milias-Argeitis, A., and Khammash, M. (2017a). Dynamic disorder in simple enzymatic reactions induces stochastic amplification of substrate. *J. R. Soc. Interface* 14, 20170311. doi:10.1098/rsif.2017.0311.

Gupta, A., Reizman, I. M. B., Reisch, C. R., and Prather, K. L. J. (2017b). Dynamic regulation of metabolic flux in engineered bacteria using a pathway-independent quorum-sensing circuit. *Nat. Biotechnol.* 35, 273-279. doi:10.1038/nbt.3796.

Harder, B. J., Bettenbrock, K., and Klamt, S. (2018). Temperature-dependent dynamic control of the TCA cycle increases volumetric productivity of itaconic acid production by *Escherichia*

coli. *Biotechnol. Bioeng.* 115, 156–164. doi:10.1002/bit.26446.

Jiang, Y., Chen, B., Duan, C., Sun, B., Yang, J., and Yang, S. (2015). Multigene editing in the *Escherichia coli* genome via the CRISPR-Cas9 system. *Appl. Environ. Microbiol.* 81, 2506–2514. doi:10.1128/AEM.04023-14.

Kalisky, T., Dekel, E., and Alon, U. (2007). Cost-benefit theory and optimal design of gene regulation functions. *Phys. Biol.* 4, 229–45. doi:10.1088/1478-3975/4/4/001.

Keseler, I. M., Mackie, A., Santos-Zavaleta, A., Billington, R., Bonavides-Martínez, C., Caspi, R., et al. (2017). The EcoCyc database: Reflecting new knowledge about *Escherichia coli* K-12. *Nucleic Acids Res.* 45, D543–D550. doi:10.1093/nar/gkw1003.

Kotte, O., Volkmer, B., Radzikowski, J. L., and Heinemann, M. (2014). Phenotypic bistability in *Escherichia coli*'s central carbon metabolism. *Mol. Syst. Biol.* 10, 736–736. doi:10.15252/msb.20135022.

Kotte, O., Zaugg, J. B., and Heinemann, M. (2010). Bacterial adaptation through distributed sensing of metabolic fluxes. *Mol. Syst. Biol.* 6, 355. doi:10.1038/msb.2010.10.

Lambert, G., Kussell, E., and Kussel, E. (2014). Memory and fitness optimization of bacteria under fluctuating environments. *PLoS Genet.* 10, e1004556. doi:10.1371/journal.pgen.1004556.

Lee, T. S., Krupa, R. A., Zhang, F., Hajimorad, M., Holtz, W. J., Prasad, N., et al. (2011). BglBrick vectors and datasheets: A synthetic biology platform for gene expression. *J. Biol. Eng.* 5, 15–17. doi:10.1186/1754-1611-5-12.

Liu, D., Mannan, A. A., Han, Y., Oyarzún, D. A., and Zhang, F. (2018). Dynamic metabolic control: Towards precision engineering of metabolism. *J. Ind. Microbiol. Biotechnol.* 45, 535–543. doi:10.1007/s10295-018-2013-9.

Liu, D., Xiao, Y., Evans, B. S., and Zhang, F. (2015). Negative feedback regulation of fatty acid production based on a Malonyl-CoA sensor-actuator. *ACS Synth. Biol.* 4, 132–140. doi:10.1021/sb400158w.

Liu, D., and Zhang, F. (2018). Metabolic feedback circuits provide rapid control of metabolite dynamics. *ACS Synth. Biol.* 7, 347–356. doi:10.1021/acssynbio.7b00342.

Lv, Y., Qian, S., Du, G., Chen, J., Zhou, J., and Xu, P. (2019). Coupling feedback genetic circuits with growth phenotype for dynamic population control and intelligent bioproduction. *Metab. Eng.* 54, 109–116. doi:10.1016/j.ymben.2019.03.009.

Madar, D., Dekel, E., Bren, A., and Alon, U. (2011). Negative auto-regulation increases the input dynamic-range of the arabinose system of *Escherichia coli*. *BMC Syst. Biol.* 5, 1-9.

doi:10.1186/1752-0509-5-111.

Mannan, A. A., Liu, D., Zhang, F., and Oyarzún, D. A. (2017). Fundamental design principles for transcription-factor-based metabolite biosensors. *ACS Synth. Biol.* 6, 1851–1859. doi:10.1021/acssynbio.7b00172.

Moser, F., Espah Borujeni, A., Ghodasara, A. N., Cameron, E., Park, Y., and Voigt, C. A. (2018). Dynamic control of endogenous metabolism with combinatorial logic circuits. *Mol. Syst. Biol.* 14, 1–18. doi:10.15252/msb.20188605.

Piazza, I., Kochanowski, K., Cappelletti, V., Fuhrer, T., Noor, E., Sauer, U., et al. (2018). A map of protein-metabolite interactions reveals principles of chemical communication. *Cell* 172, 358-372. doi:10.1016/j.cell.2017.12.006.

Rosenfeld, N., Elowitz, M. B., and Alon, U. (2002). Negative autoregulation speeds the response times of transcription networks. *J. Mol. Biol.* 323, 785–793. doi:10.1016/S0022-2836(02)00994-4.

Solopova, A., van Gestel, J., Weissing, F. J., Bachmann, H., Teusink, B., Kok, J., et al. (2014). Bet-hedging during bacterial diauxic shift. *Proc. Natl. Acad. Sci.* 111, 7427–7432. doi:10.1073/pnas.1320063111.

van Aalten, D. M., DiRusso, C. C., Knudsen, J., and Wierenga, R. K. (2000). Crystal structure of FadR, a fatty acid-responsive transcription factor with a novel acyl coenzyme A-binding fold. *EMBO J.* 19, 5167–77. doi:10.1093/emboj/19.19.5167.

Weiße, A. Y., Oyarzún, D. A., Danos, V., and Swain, P. S. (2015). Mechanistic links between cellular trade-offs, gene expression, and growth. *Proc. Natl. Acad. Sci.* 112, E1038–E1047. doi:10.1073/pnas.1416533112.

Zhang, F., Carothers, J. M., and Keasling, J. D. (2012). Design of a dynamic sensor-regulator system for production of chemicals and fuels derived from fatty acids. *Nat. Biotechnol.* 30, 354–359. doi:10.1038/nbt.2149.

Chapter 3: The Growth Dependent Design Constraints of Transcription-Factor-Based Metabolite Biosensors

This chapter contains text and figures published as:

Hartline C.J., Zhang, F. (2022). The growth dependent design constraints of transcription-factor-based metabolite biosensors. *ACS Synth. Biol.* doi: 10.1021/acssynbio.2c00143

Chapter 3 Abstract

Metabolite biosensors based on metabolite-responsive transcription factors are key synthetic biology components for sensing and precisely controlling cellular metabolism. Biosensors are often designed under laboratory conditions but are deployed in applications where cellular growth rate differs drastically from its initial characterization. Here we asked how growth rate impacts the minimum and maximum biosensor outputs and the dynamic range, which are key metrics of biosensor performance. Using LacI, TetR, and FadR-based biosensors in *Escherichia coli* as models, we find that the dynamic range of different biosensors have different growth rate dependencies. We developed a kinetic model to explore how tuning biosensor parameters impact the dynamic range growth rate dependence. Our modeling and experimental results revealed that the effects to dynamic range and its growth rate dependence are often coupled, and the metabolite transport mechanisms shape the dynamic range-growth rate response. This work provides systematic understanding on biosensor's performance under different growth rates, which will be

useful for predicting biosensor's behavior in broad synthetic biology and metabolic engineering applications.

3.1 Introduction

Metabolite-responsive transcription factor (MRTF)-based biosensors have broad applications in synthetic biology and metabolic engineering, ranging from metabolic detection (Layton et al., 1998; Xu et al., 2013; Rogers and Church, 2016; Xiao et al., 2017) screening and selecting for high-metabolite-producing strains (Raman et al., 2014; Cheng et al., 2018; Bentley et al., 2020), dynamic metabolic control (Liu et al., 2015b; Schmitz et al., 2017; Liang et al., 2020; Wu et al., 2020; Hartline et al., 2021; Verma et al., 2022), to strain functional evolution (Chou and Keasling, 2013; Xiao et al., 2016). Nature has evolved various MRTFs that can be harnessed to create biosensors for a wide range of metabolites (Li et al., 2015; Liang et al., 2015; Liu et al., 2015a; Thompson et al., 2019; Hanko et al., 2020). Protein engineering and directed evolution of MRTF have further expanded the range of compounds which can be detected (Taylor et al., 2016; Koch et al., 2019; Flachbart et al., 2021). Additionally, promoters regulated by MRTFs can be engineered to tune sensitivity and dynamic range (Chen et al., 2018; Dabirian et al., 2019), enabling precise control of biosensor's performance (Mannan et al., 2017; Liu et al., 2018). These biosensors can be further layered to create complex circuits (Lo et al., 2016; Zhou et al., 2021), which require a well-defined performance for correct operation (Brophy and Voigt, 2014).

Most MRTF-based biosensors were designed and tested in well-defined laboratory conditions using rich growth media. These biosensors were often characterized using fluorescent proteins whose expression has little burden to growth and other cellular processes. However, during applications, biosensors are often deployed in different growth environments and used to control burdensome genes that affect cell growth rate. Changes in cell growth rate has been shown to impact several cellular parameters including plasmid copy numbers (Klumpp, 2011), ribosome concentration and mass fraction (Scott et al., 2014), transcription factor abundance and

concentration (Schmidt et al., 2016), and gene expression rate (Klumpp et al., 2009; Klumpp and Hwa, 2014), and average cellular volume (Volkmer and Heinemann, 2011; Taheri-Araghi et al., 2015). Biosensor operation relies on these shared cellular resources, so changes in cell growth rate will unavoidably affect the expression of MRTF and its regulated genes. Additionally, cell growth dilutes all molecular components as the volume of the cell increases (Figure 3.1A), so faster growth may lead to a net reduction in the concentration of molecules needed for biosensor operation (Klumpp et al., 2009; Hintsche and Klumpp, 2013). Thus, when cell growth rate changes, it may significantly alter a sensor's behavior, leading to undesirable performance. For example, in two-stage dynamic metabolic control, engineered microbial cells need to shift from a high-growth phase to a low-growth production phase (Hartline et al., 2021). Biosensors used in two-stage dynamic metabolic control have to be optimized to perform under both growth conditions (Qian et al., 2017; Moreb et al., 2020).

Many MRTF-based biosensors, use a repressed-repressor architecture (Canton et al., 2008; Lee et al., 2011). In this architecture, the MRTF represses gene expression from its cognate promoter in the absence of its target metabolite, but its expression repression activity is antagonized by the presence of a specific intracellular metabolite (Figure 3.1A). The output of a biosensor is the steady-state expression level of the controlled gene at a particular target metabolite concentration (Figure 3.1B). A sensor's behavior can be characterized by its minimum output in the absence of target metabolite, its maximum output under a saturating concentration of extracellular target metabolite, and its dynamic range (DR) which is defined as the ratio of the maximal increase in biosensor output relative to the its minimum output (Figure 3.1B) (Mannan et al., 2017). In real applications, it is often desirable to keep a low minimum output to prevent unwanted gene expression in the absence of target metabolite (Anthony et al., 2004), a high

maximum output to reach high signal-to-noise ratios (Nevoigt et al., 2007), and a large DR. Previous studies have shown how TF-repressed gene expression varies under different cell growth rates (Klumpp et al., 2009), yet, little is known about how growth rate affects a biosensor's behavior. Experimentally characterizing biosensor's behavior under a wide range of growth rates, for example by growing the biosensor in medium with different nutrient conditions both with and without the target metabolite, is labor intensive. Thus, it would be beneficial to develop quantitative models to understand how biosensor operation is impacted by growth rate to avoid undesirable sensor performance due to the change of growth rate.

In this work, we use three repressed-repressor type of biosensors to explore the effect of growth rate to sensor behavior. Interestingly, we found that while all sensors displayed both decreasing minimum and maximum outputs, the DR could have either a positive or negative growth rate dependence. By integrating experimental data with kinetic modeling, we provide a mathematical framework to reveal biosensor's behavior under changing growth conditions. We show how different parameters of the biosensor promoter and TF expression can lead to either a positive or negative dynamic range-growth rate (DR-μ) dependence. Additionally, our results show how growth rate-dependent membrane transport mechanisms of the target metabolite shape the overall DR-μ dependence. Our model and experimental results demonstrate a coupling between DR and sensitivity of DR to changes in growth rate for most biosensor designs, which implies a trade-off between high DR and low sensitivity objectives. Altogether our work provides a framework for tuning or predicting a biosensor's behavior under varying growth conditions, which will be useful for a wide range of biosensor applications in synthetic biology.

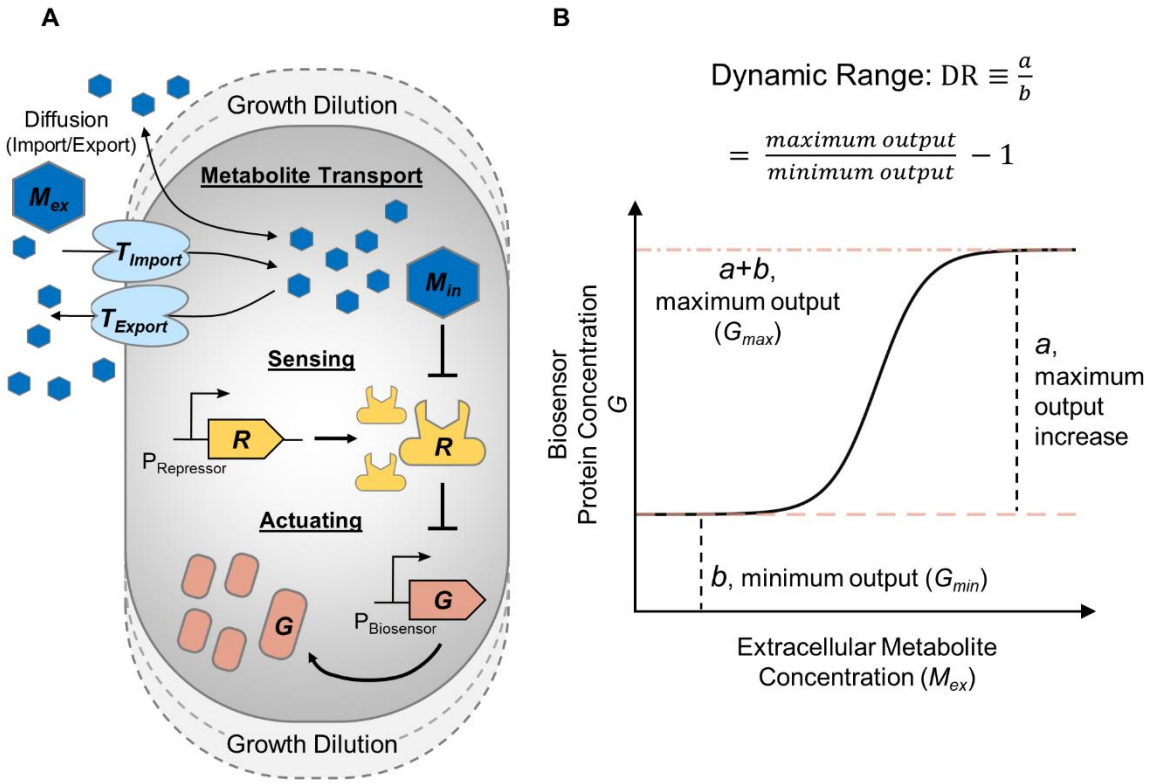

Figure 3.1. Molecular components contributing to the operation of a metabolite-responsive transcription factor (MRTF)-based biosensor. (A) Schematic of general components contributing to overall biosensor response. Extracellular metabolite enters the cell, becoming intracellular metabolite. Intracellular metabolite represses the DNA-binding activity of the MRTF. The MRTF represses the biosensor's promoter, which controls the expression of a reporter protein. All components are universally affected by growth rate through dilution as the cell volume expands. **(B)** Minimum output, maximum output, and dynamic range (DR) are critical parameters characterizing the dose-response curve of a MRTF-based biosensor.

3.2 Results

3.2.1 Growth Rate Dependence of Biosensor Dynamic Range

To study the relationship between sensor DR and cell growth rate of MRTF-based biosensors, we first tested three TF-promoter systems with a repressed-repressor architecture, TetR-P_{tet} (Figure 3.2A), LacI-P_{lacUV5} (Lee et al., 2011) (Figure 3.2B), and FadR-P_{AR} (Zhang et al., 2012a; Liu and Zhang, 2018; Hartline et al., 2020) (Figure 3.2C) that sense extracellular chemicals anhydrotetracycline (aTc), isopropyl β-D-1-thiogalactopyranoside (IPTG), and fatty acid (FA), respectively. All these three sensors have been commonly used for various applications (Lee et al., 2011; Zhang et al., 2012a). For each biosensor, we used a red fluorescent protein (RFP) as a reporter. Each biosensor construct was cloned into plasmids with the stringently regulated SC101 origin of replication to reduce copy number variation due to changes in growth rate (Klumpp, 2011; Jahn et al., 2016). Additionally, for the FA-sensor, native regulations of the *fadR* and *fadD* genes were removed, and *fadE* was knocked-out to prevent FA from being used as a carbon source for growth through β-oxidation (Hartline et al., 2020). Thus, all three target metabolites are primarily non-metabolizable activators of the biosensor output gene.

To manipulate cellular growth rate, biosensor cells were grown in minimal medium supplemented with different commonly-used carbon sources (You et al., 2013) including acetate, pyruvate, glycerol, sorbitol, succinate, glycerol with amino acids, and xylose. These differing media conditions supported a range of growth rates from 0.24-0.51 h^{-1} (see Appendix B, Table B.3 for a summary of media conditions and growth rates). To quantify the effect of growth rate on DR, sensor minimum and maximum outputs were measured under exponential growth phase under different media conditions either without or with high concentrations of the target metabolites, respectively. The target metabolite concentrations used for aTc (1000 nM) (Lee et al., 2011), IPTG

(1 mM) (Mannan et al., 2017), and FA (4 mM) (Zhang et al., 2012a) were previously shown to saturate the output of these biosensors. Our results show that both minimum and maximum outputs decreased with increasing growth rate for all three sensors (Figure 3.2D, 3.2E, 3.2F). At saturated target metabolite concentration (i.e. maximum output) a sensor's promoter is equivalent to a strong constitutive promoter, while in the absence of the target metabolite (i.e. minimum output), a sensor's promoter is equivalent to a repressor repressed promoter. Previous studies have shown that protein concentration under the control of either a constitutive promoter or a repressor controlled promoter decreases with increasing growth rates (Klumpp et al., 2009). Thus, our observations are consistent with previous studies. Additionally, we observe that cell growth rates in maximum output are always lower than in minimum output (Figure 3.2D, 3.2E, 3.2F), suggesting growth burden from activation of these sensors, even when they were only used to express an RFP reporter protein. These observations clearly demonstrated the influence of cell growth rate to sensor output as well as the effect of sensor's function to cell growth, which cannot be ignored during biotechnology applications (Han and Zhang, 2020a, 2020b).

We next calculated the DR of each biosensor under different growth rates. Interestingly, the aTc and IPTG sensors displayed an increasing DR with increasing growth rate (Figure 3.2G, 3.2H), while the FA sensor showed a decreased DR with increasing growth rate. Our results showed that for aTc and IPTG sensors, although both the minimum and maximum outputs decreased with growth rate, the minimum output decreased more rapidly than the maximum output, thus leading to a relative increase in the ratio of the two, as quantified by the DR. In contrast, the FA strain has a negative DR trend with increasing growth rate (Figure 3.2I) because the maximum output decreased more rapidly than the minimum output for this system. One major difference between the aTc/IPTG biosensors, and the FA biosensors is that FA transport requires

the protein FadD to enter the intracellular space, whereas aTc and IPTG can diffuse into the cell (Figure 3.2A, 3.2B, 3.2C). The concentration of these transport proteins is growth-dependent, particularly since FadD is expressed from a constitutive promoter (Klumpp et al., 2009), which may contribute to the rapid decline in maximum biosensor output at higher growth rates. Thus, these results suggest that although all three biosensors have the same general architecture, their DR-μ dependency are different and may be a tunable property of biosensors.

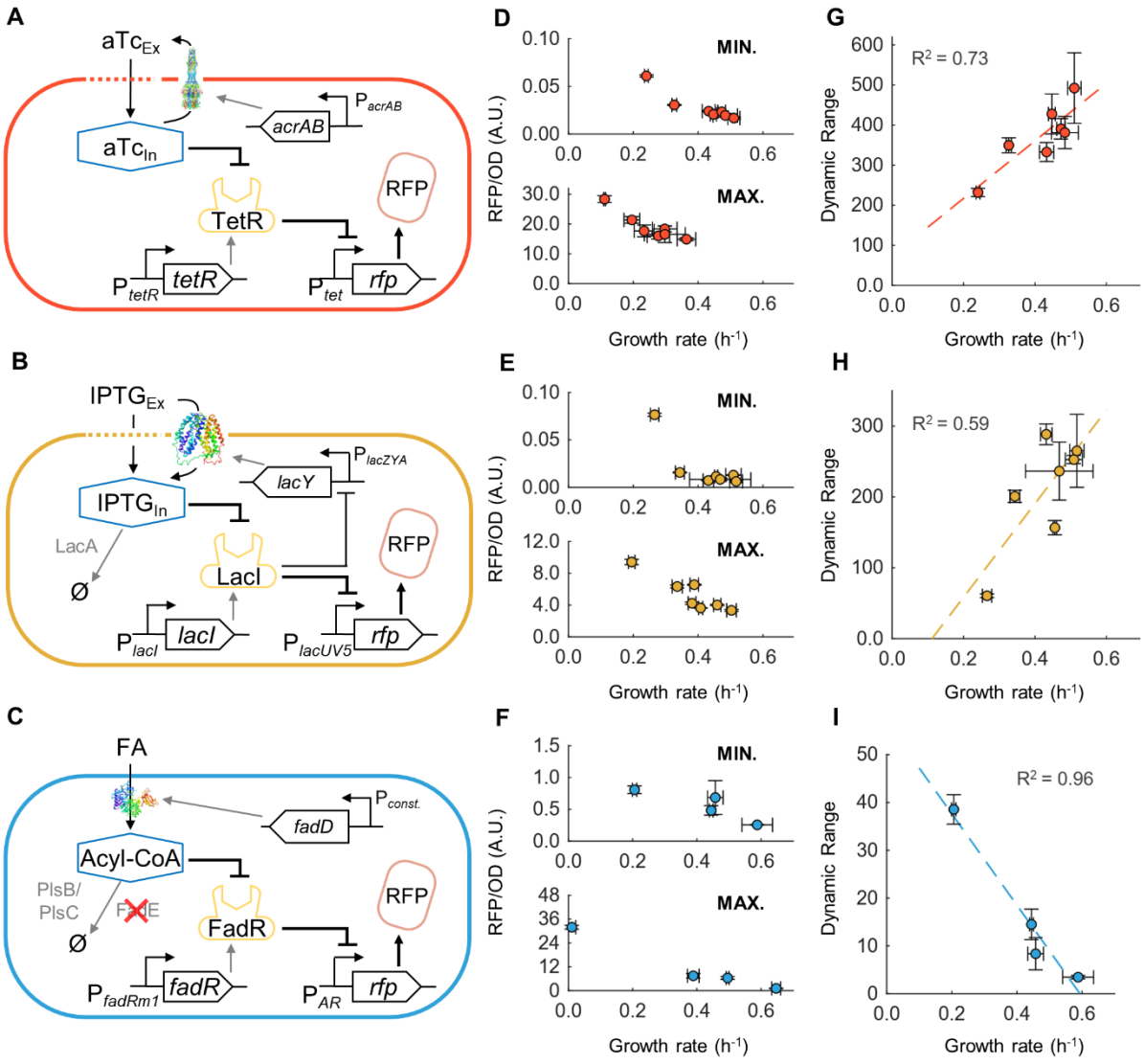

Figure 3.2. Minimum output, maximum output, and dynamic range of P_{tet}, P_{lacUV5}, and P_{AR} biosensors at different growth rates. (A-C) Schematic of cellular interactions for the **(A)** TetR-based biosensor, **(B)** LacI-based biosensor and **(C)** FadR-based biosensor. **(D-F)** Minimum (top) and maximum (bottom) output of the biosensor at different growth rates for **(D)** TetR, **(E)** LacI, and **(F)** FadR-based biosensors. **(G-I)** Calculated dynamic range of biosensor at different growth rates for **(G)** TetR, **(H)** LacI, and **(I)** FadR-based biosensors. Error bars are S.D. of biological replicates, n=3. Dashed line: Line of best fit.

To gain further insights into the different DR-μ dependencies, we developed a kinetic model to describe the intracellular concentration of the biosensor's output protein (G) and the intracellular concentrations of TF repressor (R) and target metabolite (M_{In}) at different growth rates. The volumetric production rate of each species is balanced by the dilution due to cellular volume expansion during cell growth. Additionally, transport of the target metabolite across cell membrane via either passive transport by diffusion or enzyme-facilitated active transport were also considered. For active transport, the concentration of protein transporters can also be affected by dilution due to cell growth. For a detailed description of the model, see Appendix B, Section B.1.

In the absence of the target metabolite, an analytical solution can be derived to describe the minimum output ($G_{\min}$) at steady state (see Appendix B, Section B.1.2 for details):

$$G_{min} = \frac{1}{\mu}\left(b_G + \frac{a_G}{1+\frac{b_R}{K_G\mu}}\right) \qquad \text{(Eq. 3.1)}$$

where μ represents cell growth rate. Parameters b_G, a_G, and K_G are intrinsic to the biosensor and describe the basal expression level, the strength of activated expression, and the MRTF-promoter dissociation constant, respectively. While the production rate of the MRTF is constant with growth, the total concentration of MRTF ($R = b_R / \mu$) is decreasing due to dilution by cell growth (see Appendix B, Section B.1.1 and B.1.2 for details). Because both the biosensor output protein (G) and its repressor (R) are being diluted by growth, we calculate the dependence of G_{min} on μ to understand the combined effect:

$$\frac{d}{d\mu}(G_{min}) = \frac{-1}{\mu^2}\left(b_G + \frac{a_G}{\left(1+\frac{b_R}{K_G\mu}\right)^2}\right) \qquad \text{(Eq 3.2)}$$

The dependence of G_{min} on μ is negative for all parameter values. Thus, $G_{\min}$ always decreases with growth rate, and is consistent with our experimental observation for all three biosensors (Figure 3.2D, 3.2E, 3.2F). The dependence of maximum output and DR on growth rate depend on sensor parameters and are not monotonic. A biosensor's DR can be described as:

$$DR = \frac{a_G b_R}{K_G \mu} \frac{M_{in}}{\left(a_G + b_G + \frac{b_G b_R}{K_G \mu}\right)\left(K_R + M_{In} + \frac{b_R K_R}{K_G \mu}\right)} \quad \text{(Eq. 3.3)}$$

where K_R represents the dissociation constant between the target metabolite and MRTF. Finally, M_{in} describes the intracellular target metabolite concentration which can also be a function of the growth rate, depending on the target metabolite's transport kinetics. To understand how the model parameters affect the DR-μ dependency, we next calculate the derivative of DR with respect to growth rate μ ($dDR/d\mu$):

$$\frac{d}{d\mu}(DR) = \frac{a_G b_R}{K_G} \frac{\mathrm{M}_{in}\left(\frac{b_G K_R {b_R}^2}{{K_G}^2 \mu^2} - (a_G + b_G)(K_R + M_{in})\right) + K_R \frac{dM_{in}}{d\mu}\left(a_G + b_G + \frac{b_G b_R}{K_G \mu}\right)\left(\mu + \frac{b_R}{K_G}\right)}{\mu^2\left(a_G + b_G + \frac{b_G b_R}{K_G \mu}\right)^2\left(K_R + M_{in} + \frac{b_R K_R}{K_G \mu}\right)^2} \quad \text{(Eq. 3.4)}$$

Our modeling result suggests that depending on the parameter values of a biosensor and its intracellular target metabolite concentration, $dDR/d\mu$ can be either positive (increasing with growth rate) or negative (decreasing with growth rate), depending on the sign of S:

$$S = M_{in}\left(\frac{b_G K_R {b_R}^2}{{K_G}^2 \mu^2} - (a_G + b_G)(K_R + M_{in})\right) + K_R \frac{dM_{in}}{d\mu}\left(a_G + b_G + \frac{b_G b_R}{K_G \mu}\right)\left(\mu + \frac{b_R}{K_G}\right) \quad \text{(Eq. 3.5)}$$

3.2.2 Tuning DR-μ Dependence Through TF Expression

To understand how sensor parameters affect the growth dependence of G_{min}, G_{max}, and DR (i.e. $dDR/d\mu$), we first targeted to the aTc-inducible sensor and tuned the production rate of the MRTF repressor TetR (i.e. b_R). According to our model, both G_{min} and $G_{\max}$ should decrease with b_R at a fixed growth rate, regardless of other parameters (see Equation 3.1 and Appendix B,

Equation B.12)). Experimentally, we placed TetR under the control of a constitutive promoter and a library of RBS with different strengths to vary the TetR production rate (Figure 3.3A), while not changing the promoter or RBS sequence of the biosensor output gene. When growing the library of cells at a fixed growth rate (in glycerol minimal medium), both G_{min} and G_{max} decreased with increasing TetR levels for 3.7- and 1.2-fold change across the library, respectively (Figure 3.3B, 3.3C), which matches our analytical model predictions (Figure 3.3E, 3.3F).Our model also shows that G_{min} is sensitive to changes in TetR production rate at low levels of TetR, while it becomes less sensitive at higher TetR levels (Figure 3.3E), which matches our observation of high sensitivity in G_{min} to TetR expression when TetR is low (Figure 3.3B). We further observe that under our experimental parameter regime, G_{min} is more sensitive to changes in TetR production rate than G_{max} (Figure 3.3B, 3.3C), thus affecting DR mostly by lowering the leaky expression level and leading to an increasing DR (Figure 3.3D), consistent with model prediction (Figure 3.3G). Additionally, we fit our model to the experimentally measured TetR expression, G_{min} and G_{max} (see Appendix B, Section B.2.2 for details). From the fitted model, we calculated the DR and observed a good agreement between the model and the observed DR-TetR expression trend (R^2 = 0.49). Overall, these experimental observations are qualitatively consistent with numerical simulations with increasing b_R values and with model fitting, thus validating our model.

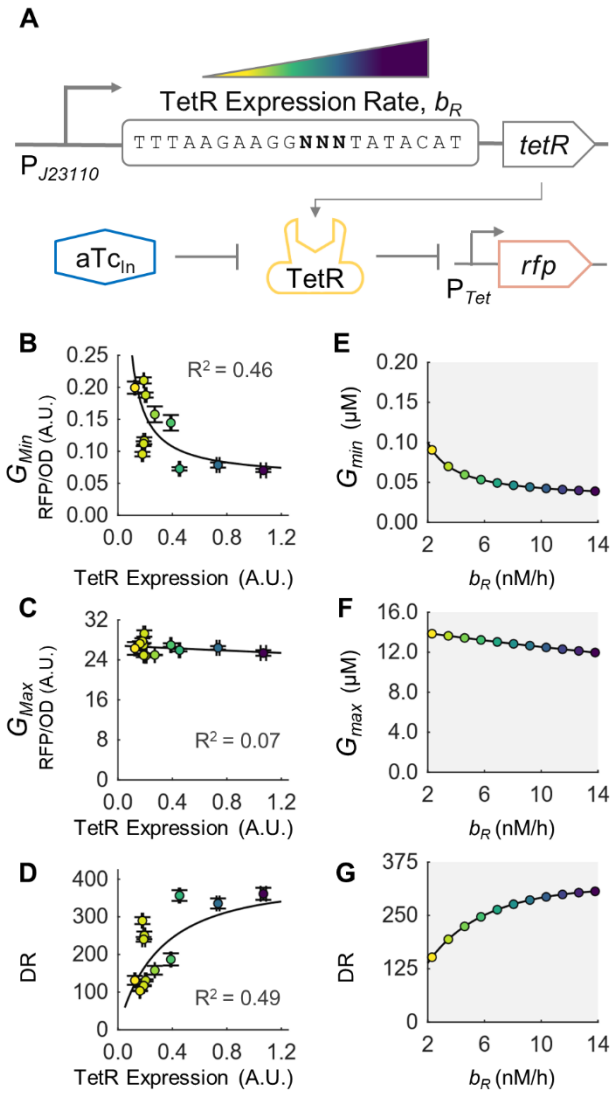

Figure 3.3. Tuning biosensor DR through changing TetR expression level at a constant growth rate. (A) Schematic of the TetR gene used to tune TetR expression level (b_R). The TetR level was varied by using a library of TetR genes with different RBS strengths. **(B-D)** Experimentally measured **(B)** minimum biosensor output, G_{min}, **(C)** maximum biosensor output G_{max}, and **(D)** dynamic range of TetR RBS library members with varying TetR expression levels. Error bars represent S.D., n=3. RBS sequences and their corresponding TetR expression levels, G_{min}, G_{max}, and DR are given in Appendix B, Table B.6. Solid line is fit of model to the experimental data (details in Appendix B, Section B.2.2) **(E-F)** Numerical model simulations of **(E)** minimum output, **(F)** maximum output, and **(G)** DR for different values of b_R. Parameter values and ranges are given in Appendix B, Table B.1.

We next measured how G_{min}, G_{max}, and DR change with growth rate under different TetR production rate (Figure 3.4A). According to Equation 3.2, as b_R increases, the dependence of G_{min} on μ is expected to be less negative. Experimentally, we indeed observed a less negative slope on the G_{min}-μ plot with a higher TetR expression (Figure 3.4B). This result indicates that when TetR production is insufficient (low TetR production), leaky expression becomes worse at lower growth rates, while a high TetR production rate can make the sensor less leaky across a wide growth rate range. The dependence of G_{max} on growth rate was negative and had similar slope for low and medium TetR production rates and a reduced slope at high TetR production rates (Figure 3.4C). This result indicates that at high TetR expression, maximal induction may not be achieved at lower growth rates. Finally, Equation 3.5 predicts that lowering the TetR production rate b_R should reduce the DR-μ dependence, changing it towards a negative regime. Our experimental results indeed showed a less positive $dDR/d\mu$ value at a lower TetR production rate (Figure 3.4D). Overall, our result showed that for aTc biosensor, a high TetR production rate provides high DR, however at a cost of higher growth dependence.

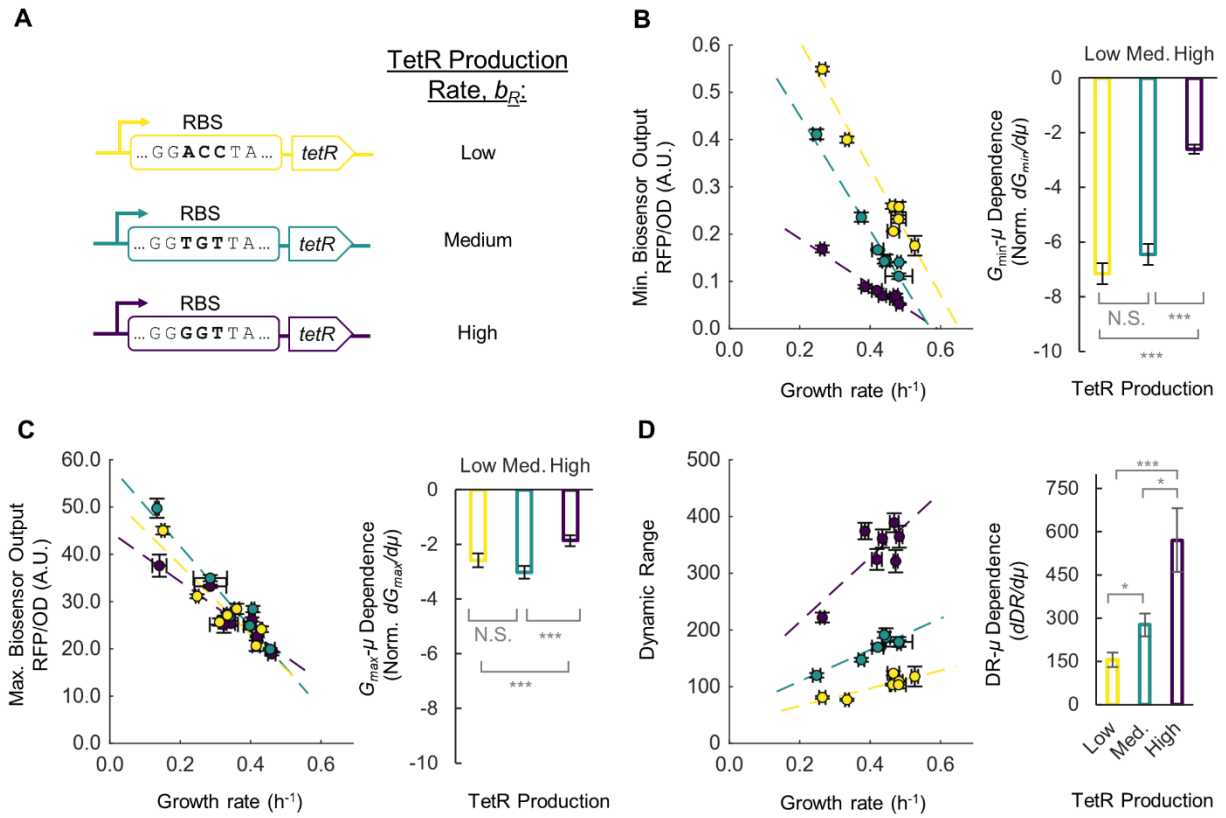

Figure 3.4. The growth rate dependence of DR for TetR-based biosensors with varying TetR production rates. (A) Three TetR operons with different RBS strength to produce TetR at low (yellow), medium (green), and high (purple) levels. **(B)** Minimum biosensor output at varying growth rate for each library member (left) and the dependence of minimum output on growth rate (right). **(C)** Maximum biosensor output at varying growth rate for each library member (left) and the dependence of the maximum output on growth rate (right). **(D)** DR at varying growth rate for each library member (left) and the dependence of DR on growth rate (right). $dG_{min}/d\mu$ and $dG_{max}/d\mu$ are normalized to the average G_{min} and G_{max}, respectively, from all data. Error bars of individual data points are S.D., n=3. Error bars for G_{min}, G_{max}, and DR-μ dependence are standard error of the slope. A Student's t-test was conducted between each pair of growth rate dependence data, stars indicate significant difference (N.S., not significant; * $p < 0.05$; ** $p < 0.01$; *** $p < 0.001$).

3.2.3 Metabolite Transport Affects DR-μ Dependence

Our experimental results on the aTc sensor showed that DR increased with both growth rate and TetR production rate. We next examine which parameter space can simultaneously support these trends and whether such trends can inform us on the parameters of the target metabolite transport mechanism. An extracellular target metabolite can enter or exit a cell via either passive transport (metabolite concentration gradient related) or protein-facilitated active transport (growth rate related), or a combination of both mechanisms. If passive transport is the only mechanism, the intracellular target metabolite concentration is mostly determined by extracellular target metabolite concentration and has little influence from growth rate. In this case, our mathematical analysis indicates that sensor DR cannot increase with both growth rate and MRTF production rate (see Appendix B, Section B.1.3). On the other hand, DR can increase with growth rate and MRTF production rate if intracellular aTc concentrations are also increasing with growth rate (see Appendix B, Section B.1.3). One way this could occur is when aTc membrane transport involves proteins whose steady state concentration is regulated by growth rate via cell dilution. Indeed, previous studies demonstrated that aTc can be exported by the AcrAB-TolC multi-drug efflux pump (Le et al., 2006), and demonstrate that the expression of *acrAB* is elevated at lower growth rates (Rand et al., 2002). Together, this may lead to reduced aTc concentrations at low growth rates due to elevated efflux. To elucidate this mechanism, we incorporated both passive transport and active export to our model (Figure 3.5A) and explored the parameter space that provides positive dependence of DR on both growth rate and TetR production rate. When active export is incorporated in the model, intracellular target metabolite becomes growth-dependent, which causes the gradient-dependent passive export to also be growth-dependent (Appendix B, Figure B.1A). Both passive and active transport rates were varied over 4-orders of magnitude to explore a large parameter space, starting from parameter settings where the target

metabolite's passive and active export rates are equal and considering different target metabolite concentration regimes ($M_{in} \gg K_{M,ex}$, $M_{in} = K_{M,ex}$, or $M_{in} \ll K_{M,ex}$, Appendix B, Figure B.1A). Our parameter space covers three modes of target metabolite export, where metabolite export is primarily through the active pathway, the passive pathway, or a mix of both active and passive pathways (Figure 3.5B). Modeling results show that sensor DR increased as passive transport rate increased and active export decreased (Figure 3.5C). This is because intracellular target metabolite concentration is high when the passive transport rate is higher than the active export rate (Appendix B, Figure B.1B). Interestingly, when active export rate is similar to or higher than passive transport rate, DR is more likely to positively correlate with growth (Figure 3.5D). And when active export rate is lower than passive transport rate, DR is more likely to positively correlate with TetR production rate (Figure 3.5E). As a result, DR can positively correlate with both cell growth and TetR production rate only when active export rate is similar to passive import (Figure 3.5F). Our modeling results further show that $dM_{in}/d\mu$ strongly increases when active export rate is similar to passive import (Appendix B, Figure B.1C), which is a necessary condition to observe simultaneous positive correlation for DR with cell growth and TetR production rate (see Appendix B, Section B.1.3). Thus, the aTc biosensor used in our experiments likely fall into this parameter range.

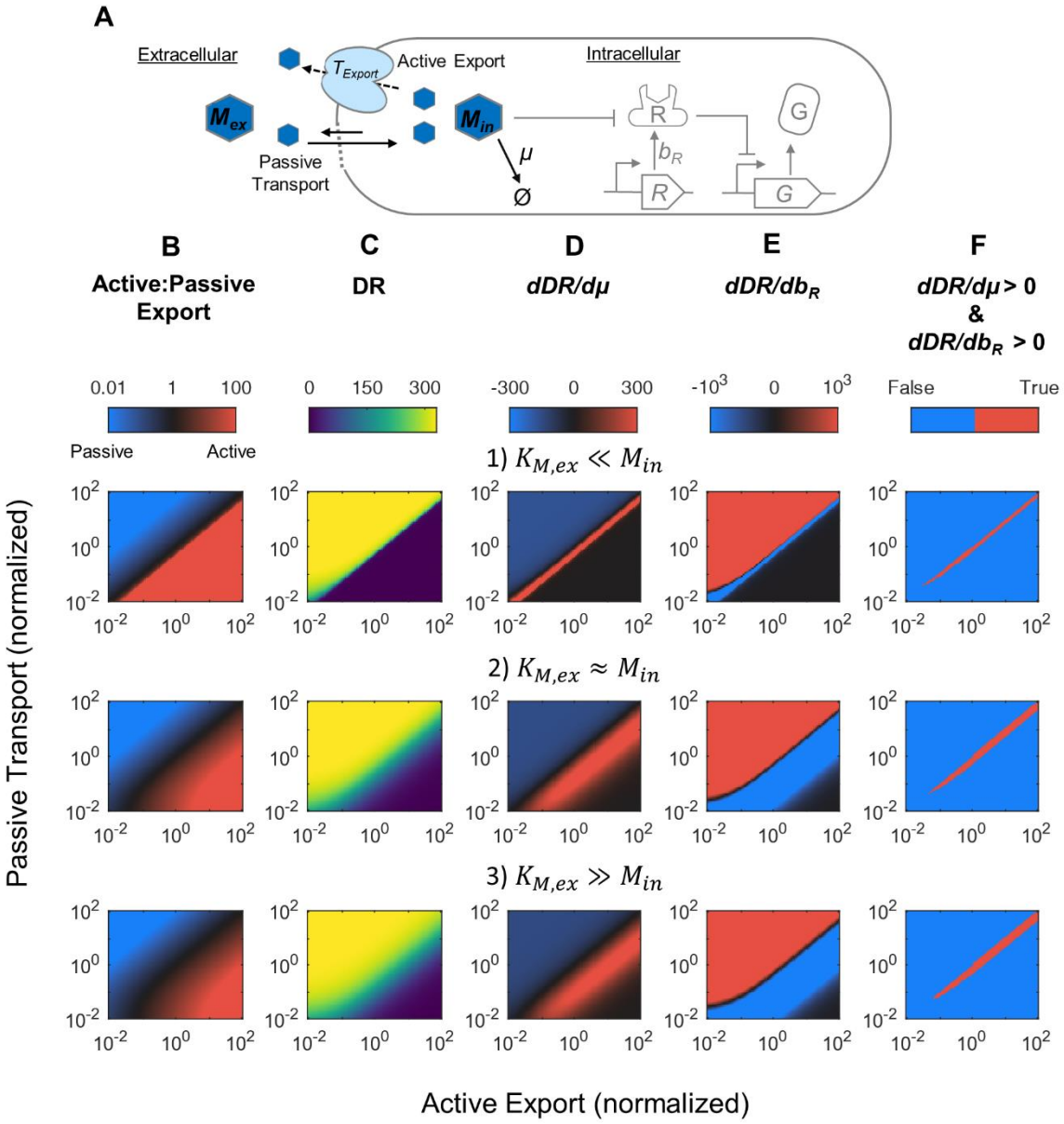

Figure 3.5. Modeling the impact of passive and active transport mechanism on DR-growth rate dependence for aTc-type biosensors. (A) Diagram of transport reactions including passive import of metabolite by diffusion and active export facilitated by a protein transporter. **(B)** Ratio of active to passive export rates, **(C)** Calculated DR, **(D)** $dDR/d\mu$, **(E)** dDR/db_R, and **(F)** Parameter region where both $dDR/d\mu$ and dDR/db_R, under different parameter space. The parameters k_{diff} and $k_{cat,ex}$ were increased to increase passive and active transport rate, respectively. $K_{M,ex}$ was varied to represent three scenarios where its value is either greater, similar, or smaller than the intracellular target metabolite concentration (M_{in}). See Appendix B, Figure B.1 and Section B.2.1 for details. Parameters values are given in Appendix B, Table B.1.

In contrast to the aTc sensor, many chemicals cannot diffuse across cell membrane passively, but solely rely to protein transporters and enzyme conversion to turn on the sensor. For example, the FA sensor requires a membrane-associated acyl-CoA synthase to convert extracellular FA into intracellular acyl-CoA, which binds to FadR, the MRTF, to turn on reporter expression. Thus, to understand the FA sensor, we modified our model to include both enzyme-based import and export mechanisms without passive transport (Figure 3.6A). Similar to the aTc model, DR increases when the active import rate is higher than export rate (Figure 3.6B), leading to higher intracellular target metabolite (acyl-CoA) concentration (Figure 3.6C). In contrast to aTc-type of sensors, the DR of FA-type of sensors has a negative dependence on cell growth when import rate is higher than export rate, which should occur under most cases since faster target metabolite import is necessary for high biosensor induction (Figure 3.6D). Thus, these modeling results are consistent with our experimental results. Additionally, when import is higher than export, the intracellular target metabolite growth dependence ($dM_{in}/d\mu$) is strongly negative (Figure 3.6E) indicating a large potential drop in the maximum biosensor output at higher growth rates, which is also consistent with experiments.

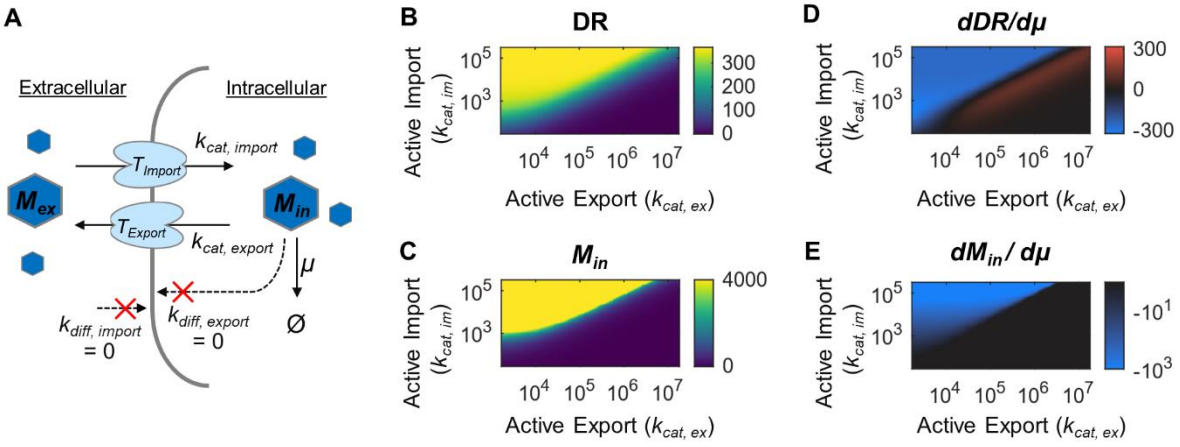

Figure 3.6. Modeling the impact of active transport mechanism on DR-growth rate dependence for FA-type biosensors. (A) Diagram of transport reactions. Target metabolite transport only occurs by protein-facilitated active mechanisms. **(B)** Model simulated DR under different import and export rates. All other parameters are held constant and are given in Appendix B, Table B.1. **(C)** Intracellular target metabolite concentration (M_{in}), **(D)** DR-μ dependence, and **(E)** intracellular metabolite-μ dependence, under different parameter space.

3.2.4 DR and DR-μ Are Sensitive to Similar Parameters

Thus far, our modeling and experimental results have shown good qualitative agreement and have predicted the effects of b_R and transport mechanisms on both DR and DR-μ dependence. In order to gain a deeper understanding of the other parameters effects on DR and DR-μ dependence, we conducted a global parameter sensitivity analysis, for a transport mechanism with both passive and active transport (Appendix B, Section B.3). Our results show that both the DR (Appendix B, Figure B.2A) and *dDR/dμ* (Appendix B, Figure B.2B) are most sensitive to parameters intrinsic to the biosensor (a_G, b_G, and K_G), the MRTF expression level, and parameters in MRTF-metabolite interaction (b_R, k_{sr}, k_{sf}). The similarity in parameter sets which strongly affect DR and *dDR/dμ* suggest both are tightly coupled. These results are consistent with our observation of the TetR system where increasing TetR production rate tuned both the DR and the DR-μ dependence in the same direction.

3.3 Discussion

Change in cellular growth rate often affects the performance of biosensors and cause problems when using biosensors in a different nutrient or environment (Cardinale and Arkin, 2012). In this work, we characterized the growth-rate dependent behavior of three commonly-used MRTF-based biosensors through changing the growth medium of the biosensors. Our results show that DR of the aTc-TetR and IPTG-LacI sensors have positive correlations with cell growth rate. In industrial-scale bioreactor settings where growth rates are typically lower than that in rich medium of lab settings, these sensors will have lower DRs and leakier expression before induction (Figure 3.2D, 3.2E) (Hollinshead et al., 2014; Nadal-Rey et al., 2021). Thus, these sensors may not be suitable for controlling toxic genes or burdensome pathways whose leaky expression can cause undesirable mutations to deactivate the strain's function. In contrast, DR of the FA-FadR biosensor has a negative correlation with cell growth rates. A higher DR at lower growth rate can benefit the sensor's application, although its leaky expression was also high at lower growth rate (Figure 3.2F).

In this work we used a simplified kinetic model for understanding the DR-μ dependency. The core modeling approach expands upon previous phenomenological models which were successful in capturing design constraints between various tunable molecular interactions and biosensor dose-response parameters (Mannan et al., 2017). We extended these phenological models with kinetic interactions between TF and intracellular target metabolite, as well as metabolite transport, which have been shown to capture key dynamic features of bacterial response to external metabolites (Hartline et al., 2020). Many of the model parameters are related to key biological processes that can be tuned experimentally to optimize a sensor's performance, such as the TF-operator interactions (Hao et al., 2014; Chen et al., 2019) and the presence of exporters

(Diao et al., 2016; De Paepe et al., 2017). Our model captures new design constraints for tuning DR across growth rates. For example, while the DR can be increased by reducing the minimum output through a stronger binding of the MRTF to the biosensor promoter, our model predicts this can result in a reduction of the maximum output at some growth rates, because there is a limit to how much the sensor promoter can be activated by the intracellular target metabolite. Thus, once model parameters are characterized at a single growth rate, the model can be used to predict the change in DR under different medium compositions by measuring the growth rate, allowing engineers to check for a potential loss of sensor performance without the need for lengthy experimental re-characterization of the biosensor at different growth rates or under different growth mediums. Additionally, while our results focus on biosensor's with a repressed-repressor architecture, previous phenomenological models (Mannan et al., 2017) can be similarly extended following our procedures to identify growth-dependent design constraints for other biosensor architectures, such as the commonly used activated-activator architecture.

Importantly, our model also highlights some fundamental couplings in biosensor's performance across varying growth rates, which are important when engineering a MRTF-based sensor. For both types of sensors explored in this study, strategies in increasing the DR always led to stronger growth rate dependence of DR (regardless of whether the dependence is positive or negative), thus making the DR more sensitive to changes in growth (Figure 3.4D, Figure 3.5, Figure 3.6). Therefore, there is a trade-off between high DR and low DR-μ sensitivity, which is important in applications when the value of the DR itself is critical. As an example, MRTF-based biosensors used for high-throughput screening usually require high DRs to reduce the identification of false-positive and false-negative strains (Lin et al., 2017; Dabirian et al., 2019). However, a sensor with too high of a DR also has high DR-μ sensitivity, which will lead to a high

false-hit rate when screening under different conditions. Thus, reducing DR in exchange for a less sensitive DR-μ dependence may present a better strategy in sensor design.

Additionally, our model suggests that transport of the target metabolite plays important roles in the growth rate dependence of DR. Different biosensors with similar underlying parameters can show different DR-μ dependencies. For biosensors the target metabolite's transport is controlled by passive diffusion and active export (e.g. aTc), there is a narrow parameter region where increasing TF expression can improve DR while also maintaining a positive DR-μ dependence (Figure 3.5E). In contrast, for biosensors where internal metabolite levels are controlled solely by enzymes (e.g. FA), the metabolite-μ dependence is negative over a large parameters space, so DR cannot be improved by increasing TF levels without leading to a more negative DR-μ dependence under these conditions. Thus, our model highlights metabolite transport or production as an important consideration for understanding the impact of growth on a sensor's DR.

MRTF-based biosensors are key components of synthetic biology systems and enable a diverse range of sensing applications. These applications require sensors with robust and predictable operation under a wide range of nutrient conditions and growth environments. Our work has uncovered new design considerations and trade-offs for metabolite biosensors under changing growth conditions, which will be found useful for a wide range of metabolic engineering and synthetic biology applications.

3.4 Methods

3.4.1 Materials

Phusion polymerase, restriction enzymes, and T4 ligase were purchased from Thermo Fisher Scientific (Waltham, MA, U.S.A.). DNA primers were synthesized by Integrated DNA Technologies (Coralville, IA, U.S.A.). DNA plasmid miniprep kits were purchased from iNtRON Biotechnology (Burlington, MA, U.S.A). All other reagents were purchased from Sigma-Aldrich (St. Louis, MO, U.S.A.)

3.4.2 Plasmids and Strains

E. coli MDS42pdu (Csörgő et al., 2012) was used to clone and isolate plasmids. *E. coli* MG1655 was used to host biosensor plasmids. All plasmids were constructed through PCR amplification and standard Golden-Gate DNA assembly techniques. Plasmids were transformed into electro-competent strains by electroporation and selected on LB agar plates with corresponding antibiotics (ampicillin, 100 mg/L; kanamycin, 50 mg/L; streptomycin 100 mg/L). Plasmids (Appendix B, Table B.4), strains (Appendix B, Table B.5), and sequences of constructed plasmids are given in Appendix B, Section B.5.

3.4.3 FA Biosensor Construction

The FA-FadR biosensor was created in strain MG1655 by modifying a previous FA sensor (Hartline et al., 2020). These modifications include the deletion of *fadE*, replacement of *fadD*'s native promoter with a constitutive promoter P_{pro4} to deactivate the positive feedback loop in FA transport (Hartline et al., 2020), and deletion of the negative autoregulation of FadR (Zhang et al., 2012b). These genome modifications were performed using CRISPR-Cas9 following previous methods (Jiang et al., 2015, 2017) using pTargetF plasmids as listed in Appendix B, Table B.4. The sequence of P_{pro4} was taken from a library of insulated constitutive promoters (Davis et al.,

2011) and constructed from PCR of overlapping primers. Deletion of the negative autoregulation of FadR was done by replacing *fadR*'s native promoter with the constitutive P_{fadRm1} (Appendix B, Section B.5.1). Additionally, the constitutively controlled *fadR* was cloned to the pA6a BglBrick plasmid, resulting in plasmid pAfadRm1a-fadR (Appendix B, Section B.5.1 for full sequence).

3.4.4 TetR RBS Library Construction

A library of plasmids with varying TetR RBS strength (namely pSk-P_{Tet}-rfp-P_{J23110}-RBSLibrary-tetR) was constructed by introducing a terminator, followed by the constitutive Bba_J23110 promoter, followed by an RBS 3' of pTetR promoter and 5' of the TetR coding sequence on a pS2k-rfp plasmid. Terminator and promoter were constructed from overlapping primers. The RBS library was then introduced by primers with degenerate nucleotide sequences. To evaluate the RBS strength, we constructed another plasmid library, namely pSk-P_{J23110}-RBSLibrary-rfp, by replacing the *tetR* gene of pSk-P_{J23110}-RBSLibrary-tetR with *rfp*. This library was constructed by individually amplifying the promoter, RBS sequence and first 30 codons of the TetR coding sequence from aTc-biosensor-TetR-RBS-library members which had characterized minimum and maximum outputs. These sequences were then individually cloned 5' of *rfp* and introduced to a BglBrick backbone with SC101 origin and kanamycin resistance. The final constructed sequences are shown in Appendix B, Section B.5.1. A list of the tested RBS sequences is given in Appendix B, Table B.6.

3.4.5 Cell Growth and Induction Conditions

Cells were cultivated in different growth media following previous protocols (Basan et al., 2020; Hartline et al., 2022). Specifically, single colonies from an overnight Luria-Bertani (LB) plate were cultivated for 3-5 hours in LB medium (225 rpm, 37 °C) supplemented with appropriate antibiotic. Cells were then washed twice by centrifugation (4500 rcf, 3 minutes) into M9 minimal

medium supplemented with 1% (w/v) glycerol and diluted to OD_{600} ~0.04 and grown overnight. Overnight cultures were again washed in M9 media without supplemented carbon. To achieve different growth rates, washed cells were transferred to M9 media supplemented with the following nutrient sources: 75 mM sodium acetate, 20 mM sodium pyruvate, 1% Glycerol, 20 mM sorbitol, 15 mM sodium succinate, 1% glycerol + 7 amino acids (0.8 mM Glycine, 0.2 mM Histidine, 0.4 mM isoleucine, 0.8 mM leucine, 0.4 mM lysine, 0.2 mM methionine, 0.4 mM phenylalanine), 20 mM xylose. For the FadR-based biosensor only, media was supplemented with 0.5% Tergitol NP-40 and the following nutrient sources were used: 75 mM sodium acetate, 1% glycerol, 1% glycerol+7 amino acids, and 0.4% glucose. A summary of growth rates achieved for each media condition is given in Appendix B, Table B.3. To induce biosensor activity, 1000 nM anhydrotetracycline (aTc), 1 mM isopropyl β-D-1-thiogalactopyranoside (IPTG), and 4 mM of sodium oleate, were added to the media for the aTc, IPTG, and FA sensors, respectively.

3.4.6 Biosensor Growth Rate, Minimum, Maximum, and Dynamic Range Assays

Cells growing in different carbon sources, with or without the sensor metabolite were diluted to OD_{600} at ~0.0007. Exponentially growing cells were transferred to a Falcon 96-Well Imaging Microplate (Corning, NY, U.S.A.). An Infinite F200PRO plate reader (TECAN, Männedorf, Switzerland) was used to take automated OD_{600} and red fluorescence measurements (Excitation: 584±9 nm, Emission: 620±20 nm) every 15 minutes with constant shaking at 37°C. Following previously established procedures for calculating growth rate (Basan et al., 2020; Hartline et al., 2022) and biosensor output (Mannan et al., 2017), growth rate was calculated as the slope of natural log(OD_{600}) from OD_{600} 0.1 to 0.4. RFP values were normalized by the OD_{600}, and the minimum and maximum RFP/OD values were calculated as the average of RFP/OD measurements

over the same OD_{600} range (0.1-0.4). The dynamic range was calculated from the minimum and maximum outputs measured from the same biological replicate (colony).

3.4.7 TetR RBS library characterization. Colonies of freshly transformed aTc-biosensor-TetR-RBS-library members were picked and grown following the cell growth and induction methods in M9 media supplemented with 1% glycerol. The minimum, maximum, and dynamic range of several colonies were measured, and colonies with different dynamic range were chosen for further characterization. The RBS sequence was determined by Sanger sequencing to confirm uniqueness of tested library members and duplicate members were combined. The minimum, maximum, and DR of the sequence verified library members were then re-measured with biological triplicates in 1% glycerol medium. To get the TetR expression level, TetR expression library members were individually constructed, and then also grown in M9 with 1% glycerol, and the growth rate and steady state RFP/OD were measured by plate reader. A summary of the RBS sequences characterized, and their TetR expression level, minimum and maximum outputs is provided in Appendix B, Table B.6.

3.4.8 Dynamic Range Modeling and Simulations

Details of the model development and parameterizations are given in supplementary information. Kinetic model simulations were performed using MATLAB 2020B ode15s (The Mathworks, Natick, MA, U.S.A.) from initial conditions where the concentration each species is zero. Simulations were run for 10^9 seconds to reach steady state, and the end point of each simulation was used as the model output. To obtain the model minimum and maximum outputs, the model was run with either 0 µM or 4000 µM extracellular target metabolite (M_{ex}), respectively. dDR/db_R was calculated directly from the simulations using Equation (S21), $dDR/d\mu$ was

calculated numerically using a 5-point central difference formula by running 5 simulations at nearby μ (equally spaced on the range μ ±0.0039).

3.5 Supplemental Information

Table B.1- B.6, Figures B.1-B.3, and Appendix Sections B.1-B.5 can be found in Appendix B.

3.5.1 Abbreviations

anhydrotetracycline, aTc; dynamic range, DR; Dynamic range-growth rate, DR-μ; fatty acid, FA; isopropyl β-D-1-thiogalactopyranoside, IPTG; metabolite-responsive transcription factor, MRTF.

3.6 Chapter 3 References

Anthony, L. C., Suzuki, H., and Filutowicz, M. (2004). Tightly regulated vectors for the cloning and expression of toxic genes. *J. Microbiol. Methods* 58, 243–250. doi:10.1016/j.mimet.2004.04.003.

Basan, M., Honda, T., Christodoulou, D., Hörl, M., Chang, Y. F., Leoncini, E., et al. (2020). A universal trade-off between growth and lag in fluctuating environments. *Nature* 584, 470–474. doi:10.1038/s41586-020-2505-4.

Bentley, G. J., Narayanan, N., Jha, R. K., Salvachúa, D., Elmore, J. R., Peabody, G. L., et al. (2020). Engineering glucose metabolism for enhanced muconic acid production in *Pseudomonas putida* KT2440. *Metab. Eng.* 59, 64–75. doi:10.1016/j.ymben.2020.01.001.

Brophy, J. A. N., and Voigt, C. A. (2014). Principles of genetic circuit design. *Nat. Methods* 11, 508–520. doi:10.1038/nmeth.2926.

Canton, B., Labno, A., and Endy, D. (2008). Refinement and standardization of synthetic biological parts and devices. *Nat. Biotechnol.* 26, 787–793. doi:10.1038/nbt1413.

Cardinale, S., and Arkin, A. P. (2012). Contextualizing context for synthetic biology - identifying causes of failure of synthetic biological systems. *Biotechnol. J.* 7, 856–866. doi:10.1002/biot.201200085.

Chen, S.-Y., Wei, W., Yin, B.-C., Tong, Y., Lu, J., and Ye, B.-C. (2019). Development of a highly sensitive whole-cell biosensor for arsenite detection through engineered promoter modifications. *ACS Synth. Biol.* 8, 2295–2302. doi:10.1021/acssynbio.9b00093.

Chen, Y., Ho, J. M. L., Shis, D. L., Gupta, C., Long, J., Wagner, D. S., et al. (2018). Tuning the dynamic range of bacterial promoters regulated by ligand-inducible transcription factors. *Nat. Commun.* 9, 64. doi:10.1038/s41467-017-02473-5.

Cheng, F., Tang, X.-L., and Kardashliev, T. (2018). Transcription factor-based biosensors in high-throughput screening: advances and applications. *Biotechnol. J.* 13, 1700648. doi:10.1002/biot.201700648.

Chou, H. H., and Keasling, J. D. (2013). Programming adaptive control to evolve increased metabolite production. *Nat. Commun.* 4, 1–8. doi:10.1038/ncomms3595.

Csörgő, B., Fehér, T., Tímár, E., Blattner, F. R., and Pósfai, G. (2012). Low-mutation-rate, reduced-genome *Escherichia coli*: An improved host for faithful maintenance of engineered genetic constructs. *Microb. Cell Fact.* 11, 11. doi:10.1186/1475-2859-11-11.

Dabirian, Y., Li, X., Chen, Y., David, F., Nielsen, J., and Siewers, V. (2019). Expanding the dynamic range of a transcription factor-based biosensor in *Saccharomyces cerevisiae*. *ACS*

Synth. Biol. 8, 1968–1975. doi:10.1021/acssynbio.9b00144.

Davis, J. H., Rubin, A. J., and Sauer, R. T. (2011). Design, construction and characterization of a set of insulated bacterial promoters. *Nucleic Acids Res.* 39, 1131–1141. doi:10.1093/nar/gkq810.

De Paepe, B., Peters, G., Coussement, P., Maertens, J., and De Mey, M. (2017). Tailor-made transcriptional biosensors for optimizing microbial cell factories. *J. Ind. Microbiol. Biotechnol.* 44, 623–645. doi:10.1007/s10295-016-1862-3.

Diao, J., Charlebois, D. A., Nevozhay, D., Bódi, Z., Pál, C., and Balázsi, G. (2016). Efflux pump control alters synthetic gene circuit function. *ACS Synth. Biol.* 5, 619–631. doi:10.1021/acssynbio.5b00154.

Flachbart, L. K., Gertzen, C. G. W., Gohlke, H., and Marienhagen, J. (2021). Development of a biosensor platform for phenolic compounds using a transition ligand strategy. *ACS Synth. Biol.* 10, 2002–2014. doi:10.1021/acssynbio.1c00165.

Han, Y., and Zhang, F. (2020a). Control strategies to manage trade-offs during microbial production. *Curr. Opin. Biotechnol.* 66, 158–164. doi:10.1016/j.copbio.2020.07.004.

Han, Y., and Zhang, F. (2020b). Heterogeneity coordinates bacterial multi-gene expression in single cells. *PLoS Comput. Biol.* 16, 1–17. doi:10.1371/journal.pcbi.1007643.

Hanko, E. K. R., Paiva, A. C., Jonczyk, M., Abbott, M., Minton, N. P., and Malys, N. (2020). A genome-wide approach for identification and characterisation of metabolite-inducible systems. *Nat. Commun.* 11, 1213. doi:10.1038/s41467-020-14941-6.

Hao, N., Krishna, S., Ahlgren-Berg, A., Cutts, E. E., Shearwin, K. E., and Dodd, I. B. (2014). Road rules for traffic on DNA-systematic analysis of transcriptional roadblocking in vivo. *Nucleic Acids Res.* 42, 8861–8872. doi:10.1093/nar/gku627.

Hartline, C. J., Mannan, A. A., Liu, D., Zhang, F., and Oyarzún, D. A. (2020). Metabolite sequestration enables rapid recovery from fatty acid depletion in *Escherichia coli*. *MBio* 11, e03112-19. doi:10.1128/mBio.03112-19.

Hartline, C. J., Schmitz, A. C., Han, Y., and Zhang, F. (2021). Dynamic control in metabolic engineering: Theories, tools, and applications. *Metab. Eng.* 63, 126–140. doi:10.1016/j.ymben.2020.08.015.

Hartline, C. J., Zhang, R., and Zhang, F. (2022). Transient antibiotic tolerance triggered by nutrient shifts from gluconeogenic carbon sources to fatty acid. *Front. Microbiol.* 13, 854272. doi:10.3389/fmicb.2022.854272.

Hintsche, M., and Klumpp, S. (2013). Dilution and the theoretical description of growth-rate dependent gene expression. *J. Biol. Eng.* 7, 22. doi:10.1186/1754-1611-7-22.

Hollinshead, W., He, L., and Tang, Y. J. (2014). Biofuel production: An odyssey from metabolic engineering to fermentation scale-up. *Front. Microbiol.* 5, 334. doi:10.3389/fmicb.2014.00344.

Jahn, M., Vorpahl, C., Hübschmann, T., Harms, H., and Müller, S. (2016). Copy number variability of expression plasmids determined by cell sorting and Droplet Digital PCR. *Microb. Cell Fact.* 15, 211. doi:10.1186/s12934-016-0610-8.

Jiang, W., Qiao, J. B., Bentley, G. J., Liu, D., and Zhang, F. (2017). Modular pathway engineering for the microbial production of branched-chain fatty alcohols. *Biotechnol. Biofuels* 10, 1–15. doi:10.1186/s13068-017-0936-4.

Jiang, Y., Chen, B., Duan, C., Sun, B., Yang, J., and Yang, S. (2015). Multigene editing in the *Escherichia coli* genome via the CRISPR-Cas9 system. *Appl. Environ. Microbiol.* 81, 2506–2514. doi:10.1128/AEM.04023-14.

Klumpp, S. (2011). Growth-rate dependence reveals design principles of plasmid copy number control. *PLoS One* 6, e20403. doi:10.1371/journal.pone.0020403.

Klumpp, S., and Hwa, T. (2014). Bacterial growth: Global effects on gene expression, growth feedback and proteome partition. *Curr. Opin. Biotechnol.* 28, 96–102. doi:10.1016/j.copbio.2014.01.001.

Klumpp, S., Zhang, Z., and Hwa, T. (2009). Growth rate-dependent global effects on gene expression in bacteria. *Cell* 139, 1366–1375. doi:10.1016/j.cell.2009.12.001.

Koch, M., Pandi, A., Borkowski, O., Cardoso Batista, A., and Faulon, J. L. (2019). Custom-made transcriptional biosensors for metabolic engineering. *Curr. Opin. Biotechnol.* 59, 78–84. doi:10.1016/j.copbio.2019.02.016.

Layton, A. C., Muccini, M., Ghosh, M. M., and Sayler, G. S. (1998). Construction of a bioluminescent reporter strain to detect polychlorinated biphenyls. *Appl. Environ. Microbiol.* 64, 5023–5026. doi:10.1128/aem.64.12.5023-5026.1998.

Le, T. T., Emonet, T., Harlepp, S., Guet, C. C., and Cluzel, P. (2006). Dynamical determinants of drug-inducible gene expression in a single bacterium. *Biophys. J.* 90, 3315–3321. doi:10.1529/biophysj.105.073353.

Lee, T. S., Krupa, R. A., Zhang, F., Hajimorad, M., Holtz, W. J., Prasad, N., et al. (2011). BglBrick vectors and datasheets: A synthetic biology platform for gene expression. *J. Biol. Eng.* 5, 15–17. doi:10.1186/1754-1611-5-12.

Li, S., Si, T., Wang, M., and Zhao, H. (2015). Development of a synthetic malonyl-CoA sensor in *Saccharomyces cerevisiae* for intracellular metabolite monitoring and genetic screening. *ACS Synth. Biol.* 4, 1308–1315. doi:10.1021/acssynbio.5b00069.

Liang, C., Xiong, D., Zhang, Y., Mu, S., and Tang, S. Y. (2015). Development of a novel uric-acid-responsive regulatory system in *Escherichia coli*. *Appl. Microbiol. Biotechnol.* 99, 2267–2275. doi:10.1007/s00253-014-6290-6.

Liang, C., Zhang, X., Wu, J., Mu, S., Wu, Z., Jin, J.-M., et al. (2020). Dynamic control of toxic natural product biosynthesis by an artificial regulatory circuit. *Metab. Eng.* 57, 239–246. doi:10.1016/j.ymben.2019.12.002.

Lin, J.-L., Wagner, J. M., and Alper, H. S. (2017). Enabling tools for high-throughput detection of metabolites: Metabolic engineering and directed evolution applications. *Biotechnol. Adv.* 35, 950–970. doi:10.1016/j.biotechadv.2017.07.005.

Liu, D., Evans, T., and Zhang, F. (2015a). Applications and advances of metabolite biosensors for metabolic engineering. *Metab. Eng.* 31, 35–43. doi:10.1016/j.ymben.2015.06.008.

Liu, D., Mannan, A. A., Han, Y., Oyarzún, D. A., and Zhang, F. (2018). Dynamic metabolic control: Towards precision engineering of metabolism. *J. Ind. Microbiol. Biotechnol.* 45, 535–543. doi:10.1007/s10295-018-2013-9.

Liu, D., Xiao, Y., Evans, B. S., and Zhang, F. (2015b). Negative feedback regulation of fatty acid production based on a malonyl-CoA sensor-actuator. *ACS Synth. Biol.* 4, 132–140. doi:10.1021/sb400158w.

Liu, D., and Zhang, F. (2018). Metabolic feedback circuits provide rapid control of metabolite dynamics. *ACS Synth. Biol.* 7, 347–356. doi:10.1021/acssynbio.7b00342.

Lo, T. M., Chng, S. H., Teo, W. S., Cho, H. S., and Chang, M. W. (2016). A two-layer gene circuit for decoupling cell growth from metabolite production. *Cell Syst.* 3, 133–143. doi:10.1016/j.cels.2016.07.012.

Mannan, A. A., Liu, D., Zhang, F., and Oyarzún, D. A. (2017). Fundamental design principles for transcription-factor-based metabolite biosensors. *ACS Synth. Biol.* 6, 1851–1859. doi:10.1021/acssynbio.7b00172.

Moreb, E. A., Ye, Z., Efromson, J. P., Hennigan, J. N., Menacho-Melgar, R., and Lynch, M. D. (2020). Media robustness and scalability of phosphate regulated promoters useful for two-stage autoinduction in *E. coli*. *ACS Synth. Biol.* 9, 1483–1486. doi:10.1021/acssynbio.0c00182.

Nadal-Rey, G., McClure, D. D., Kavanagh, J. M., Cornelissen, S., Fletcher, D. F., and Gernaey, K. V (2021). Understanding gradients in industrial bioreactors. *Biotechnol. Adv.* 46, 107660. doi:10.1016/j.biotechadv.2020.107660.

Nevoigt, E., Fischer, C., Mucha, O., Matthäus, F., Stahl, U., and Stephanopoulos, G. (2007). Engineering promoter regulation. *Biotechnol. Bioeng.* 96, 550–558. doi:10.1002/bit.21129.

Qian, Y., Huang, H.-H., Jiménez, J. I., and Del Vecchio, D. (2017). Resource competition shapes the response of genetic circuits. *ACS Synth. Biol.* 6, 1263–1272. doi:10.1021/acssynbio.6b00361.

Raman, S., Rogers, J. K., Taylor, N. D., and Church, G. M. (2014). Evolution-guided optimization of biosynthetic pathways. *Proc. Natl. Acad. Sci.* 111, 17803–17808. doi:10.1073/pnas.1409523111.

Rand, J. D., Danby, S. G., Greenway, D. L. A., and England, R. R. (2002). Increased expression of the multidrug efflux genes *acrAB* occurs during slow growth of *Escherichia coli*. *FEMS Microbiol. Lett.* 207, 91–95. doi:10.1111/j.1574-6968.2002.tb11034.x.

Rogers, J. K., and Church, G. M. (2016). Genetically encoded sensors enable real-time observation of metabolite production. *Proc. Natl. Acad. Sci.* 113, 2388–2393. doi:10.1073/pnas.1600375113.

Schmidt, A., Kochanowski, K., Vedelaar, S., Ahrné, E., Volkmer, B., Callipo, L., et al. (2016). The quantitative and condition-dependent *Escherichia coli* proteome. *Nat. Biotechnol.* 34, 104–110. doi:10.1038/nbt.3418.

Schmitz, A. C., Hartline, C. J., and Zhang, F. (2017). Engineering microbial metabolite dynamics and heterogeneity. *Biotechnol. J.* 12, 1700422. doi:10.1002/biot.201700422.

Scott, M., Klumpp, S., Mateescu, E. M., and Hwa, T. (2014). Emergence of robust growth laws from optimal regulation of ribosome synthesis. *Mol. Syst. Biol.* 10, 747. doi:10.15252/msb.20145379.

Taheri-Araghi, S., Bradde, S., Sauls, J. T., Hill, N. S., Levin, P. A., Paulsson, J., et al. (2015). Cell-size control and homeostasis in bacteria. *Curr. Biol.* 25, 385–391. doi:10.1016/j.cub.2014.12.009.

Taylor, N. D., Garruss, A. S., Moretti, R., Chan, S., Arbing, M. A., Cascio, D., et al. (2016). Engineering an allosteric transcription factor to respond to new ligands. *Nat. Methods* 13, 177–183. doi:10.1038/nmeth.3696.

Thompson, M. G., Costello, Z., Hummel, N. F. C., Cruz-Morales, P., Blake-Hedges, J. M., Krishna, R. N., et al. (2019). Robust characterization of two distinct glutarate sensing transcription factors of *Pseudomonas putida* L-lysine metabolism. *ACS Synth. Biol.* 8, 2385–2396. doi:10.1021/acssynbio.9b00255.

Verma, B. K., Mannan, A. A., Zhang, F., and Oyarzún, D. A. (2022). Trade-offs in biosensor optimization for dynamic pathway engineering. *ACS Synth. Biol.* 11, 228–240. doi:10.1021/acssynbio.1c00391.

Volkmer, B., and Heinemann, M. (2011). Condition-dependent cell volume and concentration of *Escherichia coli* to facilitate data conversion for systems biology modeling. *PLoS One* 6,

e23126. doi:10.1371/journal.pone.0023126.

Wu, Y., Chen, T., Liu, Y., Tian, R., Lv, X., Li, J., et al. (2020). Design of a programmable biosensor-CRISPRi genetic circuits for dynamic and autonomous dual-control of metabolic flux in *Bacillus subtilis*. *Nucleic Acids Res.* 48, 996–1009. doi:10.1093/nar/gkz1123.

Xiao, Y., Bowen, C. H., Liu, D., and Zhang, F. (2016). Exploiting nongenetic cell-to-cell variation for enhanced biosynthesis. *Nat. Chem. Biol.* 12, 339–344. doi:10.1038/nchembio.2046.

Xiao, Y., Jiang, W., and Zhang, F. (2017). Developing a genetically encoded, cross-species biosensor for detecting ammonium and regulating biosynthesis of cyanophycin. *ACS Synth. Biol.* 6, 1807–1815. doi:10.1021/acssynbio.7b00069.

Xu, T., Close, D. M., Sayler, G. S., and Ripp, S. (2013). Genetically modified whole-cell bioreporters for environmental assessment. *Ecol. Indic.* 28, 125–141. doi:10.1016/j.ecolind.2012.01.020.

You, C., Okano, H., Hui, S., Zhang, Z., Kim, M., Gunderson, C. W., et al. (2013). Coordination of bacterial proteome with metabolism by cyclic AMP signalling. *Nature* 500, 301–306. doi:10.1038/nature12446.

Zhang, F., Carothers, J. M., and Keasling, J. D. (2012a). Design of a dynamic sensor-regulator system for production of chemicals and fuels derived from fatty acids. *Nat. Biotechnol.* 30, 354–359. doi:10.1038/nbt.2149.

Zhang, F., Ouellet, M., Batth, T. S., Adams, P. D., Petzold, C. J., Mukhopadhyay, A., et al. (2012b). Enhancing fatty acid production by the expression of the regulatory transcription factor FadR. *Metab. Eng.* 14, 653–660. doi:10.1016/j.ymben.2012.08.009.

Zhou, S., Yuan, S.-F., Nair, P. H., Alper, H. S., Deng, Y., and Zhou, J. (2021). Development of a growth coupled and multi-layered dynamic regulation network balancing malonyl-CoA node to enhance (2S)-naringenin biosynthesis in *Escherichia coli*. *Metab. Eng.* 67, 41–52. doi:10.1016/j.ymben.2021.05.007.

Chapter 4: Transient Antibiotic Tolerance Triggered by Nutrient Shifts from Gluconeogenic Carbon Sources to Fatty Acid

This chapter contains text and figures published as:

Hartline, C.J., Zhang, R. and Zhang, F. (2022). Transient antibiotic tolerance triggered by nutrient shifts from gluconeogenic carbon sources to fatty acid. *Front. Microbiol.* 13, 854272. doi: 10.3389/fmicb.2022.854272.

Reprinted with permission.

Chapter 4 Abstract

Nutrient shifts from glycolytic to gluconeogenic carbon sources can create large sub-populations of extremely antibiotic tolerant bacteria, called persisters. Positive feedback in *Escherichia coli* central metabolism was believed to play a key role in the formation of persister cells. To examine whether positive feedback in nutrient transport can also support high persistence to β-lactams, we performed nutrient shifts for *E. coli* from gluconeogenic carbon sources to fatty acid (FA). We observed tri-phasic antibiotic killing kinetics characterized by a transient period of high antibiotic tolerance, followed by rapid killing then a slower persister-killing phase. The duration of transient tolerance (3-44 hours) varies with pre-shift carbon source and correlates strongly with the time needed to accumulate the FA degradation enzyme FadD after the shift. Additionally, FadD accumulation time and thus transient tolerance time can be reduced by induction of the glyoxylate bypass prior to switching, highlighting that two interacting feedback loops simultaneously control the length of transient tolerance. Our results demonstrate that nutrient switches along with positive feedback are not sufficient to trigger persistence in a majority of the population, but instead triggers only a temporary tolerance. Additionally, our results demonstrate that the pre-shift metabolic state

determines the duration of transient tolerance and that supplying glyoxylate can facilitate antibiotic killing of bacteria.

4.1 Introduction

Antibiotic tolerance describes the ability of bacteria to survive longer periods of antibiotic treatment while remaining genetically susceptible to antibiotic killing (Meylan et al., 2018). Heterotolerance, or persistence, is a special case of antibiotic tolerance where only a sub-population of an isogenic culture displays antibiotic tolerance, leading to a biphasic antibiotic killing kinetics—a rapid killing phase for the susceptible subpopulation followed by a slow killing phase for the tolerant population. Tolerance and persistence have been suspected as an important cause of recurrent and recalcitrant bacterial infections, particularly when the disease-causing bacterium appears to remain susceptible to antibiotic killing during *in vitro* assays (Ojha et al., 2008; Mulcahy et al., 2010; Fauvart et al., 2011; Morrison et al., 2020). Further, tolerance can promote the ability of bacteria to acquire antibiotic resistance (Levin-Reisman et al., 2017; Windels et al., 2019; Liu et al., 2020), which reduces antibiotic efficacy in clinical settings and is contributing to an impending global public health crisis (Aslam et al., 2018; Talebi Bezmin Abadi et al., 2019). These public health problems have led to increased interest in understanding antibiotic tolerance mechanisms in microbes.

The degree of metabolic activity has been deeply explored as a central feature of antibiotic tolerance and persistence (Shah et al., 2006; Amato et al., 2014; Lopatkin et al., 2019). Increased antibiotic tolerance is observed in metabolic environments where cells are slowly growing or non-growing, including in stationary phase and biofilms (Gilbert et al., 1990; Jõers et al., 2010; Orman

and Brynildsen, 2015). Genomic screens for antibiotic tolerance genes have identified several mutations in metabolic pathways which vary the frequency of antibiotic tolerant cells (De Groote et al., 2009; Bernier et al., 2013). These mutations affecting metabolic genes may contribute to antibiotic resistance under repeated antibiotic selection (Zampieri et al., 2017; Lopatkin et al., 2021). Additionally, antibiotic tolerant cells were shown to have lower levels of ATP (Shan et al., 2017; Manuse et al., 2021), increased levels of alarmones (Hauryliuk et al., 2015; Svenningsen et al., 2019), and reduced translation (Gefen et al., 2008). These metabolic mechanisms alter the efficacy of antibiotics, leading to the prolonged survival of antibiotic tolerant cells (Stokes et al., 2019). Persistence has an additional requirement of maintaining a sub-population of tolerant cells while the remainder of the population is antibiotic susceptible (Balaban et al., 2019). Thus, several stochastic mechanisms for generating and maintaining low metabolic activity, particularly stochastic induction of toxin-antitoxin pairs and stochastic accumulation of (p)ppGpp, have been explored in connection with persistence (Balaban, 2004; Germain et al., 2015; Schmitz et al., 2017; Svenningsen et al., 2019; Evans and Zhang, 2020).

Nutrient shifts are one of the mechanisms that has been shown to produce increased sub-populations of antibiotic tolerant cells (Radzikowski et al., 2017). During a nutrient shift, bacteria need to adjust their metabolic activities for different nutrient sources. The ability to generate tolerant subpopulation during metabolic adjustment may have evolutionary benefits to the entire population (Van Boxtel et al., 2017). Diauxic shifts from glucose to fumarate, glycerol, and succinate have been shown to result in bi-phasic killing kinetics with elevated levels of *Escherichia coli* persisters to both ofloxacin (Amato et al., 2013; Amato and Brynildsen, 2014) and ampicillin (Amato and Brynildsen, 2015) antibiotics. Similarly, complete shifts from glucose to fumarate resulted in an apparent mono-phasic killing kinetics with a large population of extremely slow

growing *E. coli* cells that were tolerant to many antibiotics with diverse mechanisms of action (Radzikowski et al., 2016), while only a small fraction of cells were able to resume growth on fumarate (Kotte et al., 2014). It was proposed that bistability in a positive feedback loop involving a phosphoenolpyruvate (PEP) flux sensor and the enzyme fructose-1,6-bisphosphatase (Fbp) was responsible for creating a two-population response to nutrient shifts. Positive feedback has been highlighted for its ability to increase cell-to-cell variability in gene networks and produce bistability, and can be an important mechanism in maintaining cells in the persister state (Eldar and Elowitz, 2010). Many metabolic regulatory networks are also controlled by positive feedback loops, particularly in the uptake of carbon sources such as carbohydrates (e.g. lactose, arabinose, xylose, glycerol) and fatty acids (FAs) from the environment (Weissenborn et al., 1992; Song and Park, 1997; Cronan and Subrahmanyam, 1998; Ferrández et al., 2000; Ozbudak et al., 2004; Megerle et al., 2008; Hartline et al., 2020). However, it is not known whether the prevalent feedback loops in nutrient uptake can commonly lead to elevated levels of persistence during nutrient shifts.

In this work, we studied *E. coli* nutrient transition to FA because both FA transport and catabolic pathways are regulated by a positive feedback loop. Recent work in pathogenic bacteria has highlighted that utilization of exogenous FAs from the host environment plays a central role in regulating virulence factors in a broad-range of gram-negative pathogens, including *E. coli* (Pifer et al., 2018; Pan et al., 2020; Ellermann et al., 2021). Thus, nutrient transitions to FA catabolism are associated with increased pathogenicity, but these transitions remain an understudied mechanism with respect to its effect on antibiotic tolerance. To avoid complication from the Fbp regulatory loop that may form bistability (Kotte et al., 2014), we focus on shifts from gluconeogenic carbon sources such as glycerol. Because both glycerol and FA require Fbp for

growth (Fraenkel and Horecker, 1965), switching between gluconeogenic carbon sources should avoid triggering major changes in the activity of the Fbp loop. Distinct from the mono-phasic and bi-phasic killing kinetics previously reported during glycolytic-to-gluconeogenic switches, we observed a transient tolerance phase, where the population displays nearly universal tolerance to ampicillin during the first 8 hours right after glycerol-to-FA shift. The transient tolerant phase was followed by a rapid killing phase for 98% of cells, followed by a persister phase with slower killing kinetics. This three-phase killing kinetics was observed when switching from at least 5 different gluconeogenic carbon sources (i.e. glycerol, pyruvate, malate, succinate, and acetate) tested in this study. We genetically fused the FA transport gene *fadD* (encodes the acyl-CoA ligase FadD) to a yellow fluorescent protein (YFP) and tracked transport expression kinetics after the nutrient shift. The results showed that the period of transient tolerance correlates well ($R^2 = 0.82$ in the absence of glyoxylate and $R^2 = 0.98$ in the presence of glyoxylate) with the time needed for FadD to accumulate to a threshold before resuming growth. We demonstrate that the activity of the positive feedback loop in the glyoxylate bypass modulates the timing of both transient tolerance and FadD production on shifts to FA. These results demonstrate a fundamental difference in *E. coli* response to gluconeogenic-to-FA nutrient shifts compared to previously reported glycolytic-to-gluconeogenic switches. Overall, our results have broad implications for the relation between metabolic regulations, nutrient shifts, and β-lactam antibiotic tolerance.

4.2 Results

4.2.1 Nutrient Shifts to Fatty Acid Stimulate Transient Ampicillin Tolerance

Similar to many other nutrients, FA uptake in *E. coli* is regulated by a positive feedback loop (Figure 4.1A). In this loop, the fatty acyl-CoA ligase FadD controls the uptake and activation of extracellular free FAs to acyl-CoAs, which are then catabolized by a series of FA degradation

(Fad) enzymes to acetyl-CoA for use in central metabolism. Expression of *fadD* and the *fad* regulon is repressed by the transcriptional regulator FadR, whose DNA-binding activity is further inhibited by acyl-CoAs, forming a simple positive feedback loop. Modeling of this FA uptake loop shows that bistability in FA uptake can appear under some parameters and the parameters for *E. coli* may be near the bistable regime (Mannan and Bates, 2021). In the bistable regime, a subpopulation of cells would have low FadD expression due to FadR repression, thus low FA uptake rate to activate FadR and to support rapid cell growth. Another subpopulation would maintain a high FadD expression level, thus can keep high intracellular acyl-CoA level to both antagonizes FadR's DNA binding activity and to support cell growth. If bistability in FA uptake does occur, the rapid growing subpopulation will be killed by ampicillin whereas cells with slow-growing cells may display tolerance ampicillin which only targets growing cells.

To test the possible presence of bistability in FA uptake, we transformed *E. coli* cells with an engineered FadR-based acyl-CoA biosensor (Zhang et al., 2012) that reports intracellular acyl-CoA level (Xiao et al., 2016; Liu and Zhang, 2018), and indirectly reports expression of *fad* genes. To characterize the acyl-CoA biosensor activity under different conditions, the strain was grown to steady state in defined media containing mixtures of glycerol and oleate at different ratios. Flow cytometry showed that the mean activity of the acyl-CoA biosensor increased as the ratio of FA-to-glycerol increased (Figure 4.1B), consistent with the biosensor's behavior in glucose/FA media (Liu and Zhang, 2018). At single-cell level, the biosensor activity showed unimodal distribution under all conditions (Figure 4.1C), without a distinctive subpopulation above the detection limit of the method (~1% of the population). These results suggest that although positive FA uptake loop can support bimodality/bistability under some parameters (Mannan and Bates, 2021), the

actual parameters for this strain of *E. coli* do not support a large bimodal population. Even so, a much smaller bimodal population may exist below the detection limit of flow cytometry.

Thus, to more sensitively determine whether two distinct subpopulations exist with different killing kinetics, we next conducted nutrient shifting experiments (Radzikowski et al., 2016) from different ratios of glycerol/FA mixtures to pure FA accompanied by ampicillin treatment (Figure 4.1D). When pure FA was used in the pre-culture as a negative control without nutrient switching (FA-to-FA), a typical biphasic killing kinetics was observed (Figure 4.1E): nearly-immediate and rapid killing followed by a small population (0.008%) of antibiotic tolerant cells, close to previously reported levels of persistent cells in active cultures (Balaban et al., 2019). Although we observe a short period without killing (less than 1 hour), which may be caused by starvation and cold stress from the washing procedures to provide temporary tolerance to ampicillin (Heinemann et al., 2020), this tolerance is not maintained for a large fraction of the population. Overall, this result proves that the switching procedure used in this study did not generate an elevated level of persisters. In contrast, when switching from glycerol to FA, the killing curve displayed much longer initial tolerant period, where nearly all cells survived ampicillin treatment during the first 8 hours. This transient tolerance period is followed by a rapid killing where 98% of the transiently tolerant cells were killed. Finally, the rate of killing reduced with ~2% population having elevated antibiotic tolerance. When mixtures of glycerol and FA were used in the pre-culture, the killing curves also displayed an initial transient tolerant period followed by rapid killing. The length of this tolerance period increased as the amount of FA in the pre-culture decreased (Figure 4.1E). These results further confirm that the long transient tolerance to ampicillin was caused by specifically by nutrient shifting rather than the washing procedure used

in this study and suggests a connection between the prior acyl-CoA activity with the tolerance period.

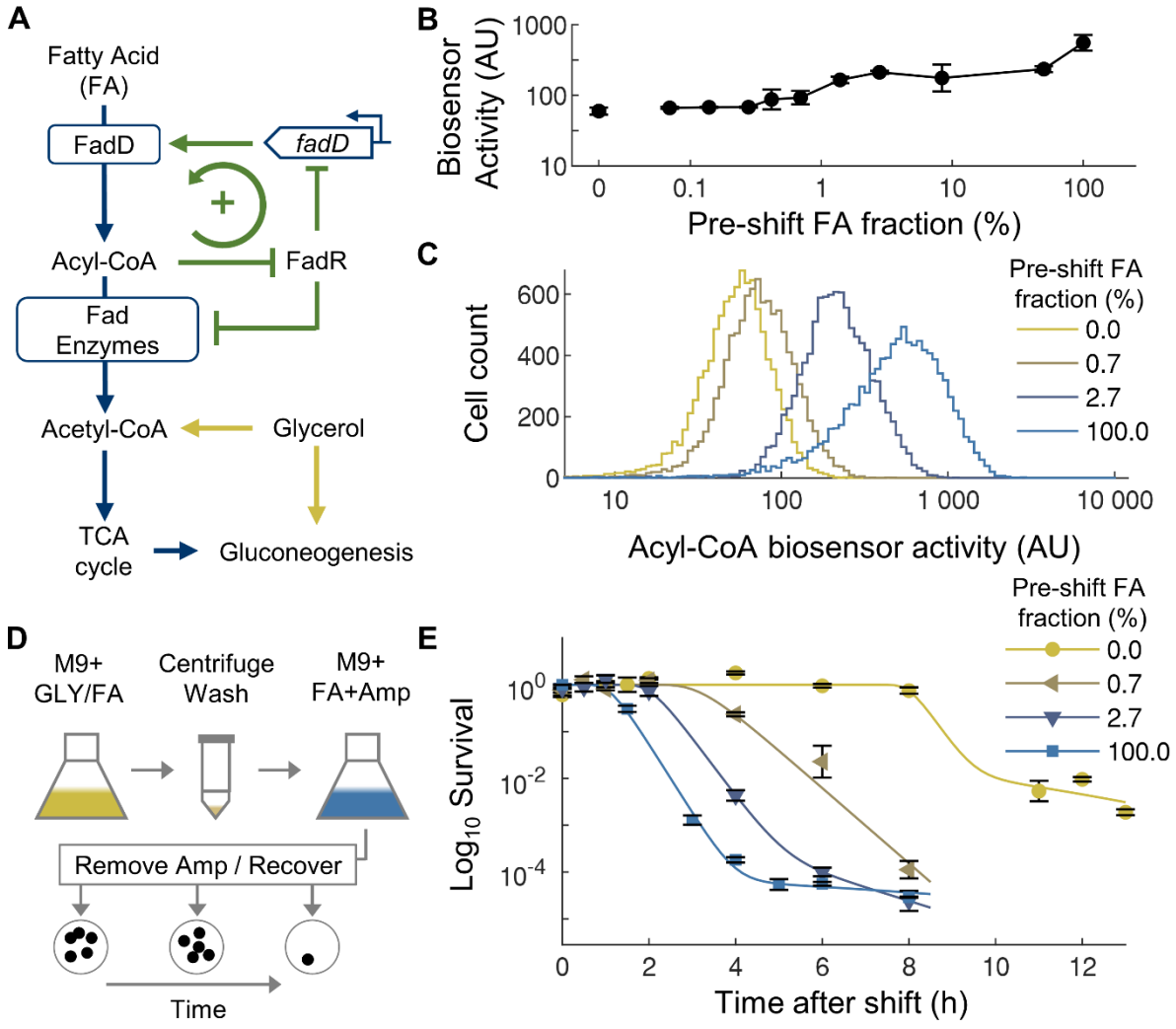

Figure 4.1. Transitions from glycerol to fatty acid (FA) generates transient ampicillin tolerance. (A) Simplified metabolic and regulatory network for FA and glycerol utilization. **(B)** Average acyl-CoA biosensor activity during co-utilization of FA and glycerol at different ratios. Across all conditions, the total concentration of carbon is constant at 72 mM. **(C)** Single-cell distribution of acyl-CoA biosensor activity during co-utilization of FA and glycerol at different ratios. A single representative distribution is shown per condition, n = 10,000 per distribution. All distributions are unimodal, with the mean shifting higher for higher fractions of FA. **(D)** Illustration of media switching and antibiotic killing experimental protocol. Abbreviations: GLY, glycerol; Amp, Ampicillin; FA, Fatty acid. **(E)** Time course survival curves of cells after nutrient

shifts from mixtures of glycerol and FA to 100% FA with 100 µg/mL ampicillin. The glycerol/oleate fraction in the pre-switch correspond with the conditions displayed for the distributions in Fig 1C. Average of biological replicates, n=3, Error Bars represent SEM. Curves are fitting of the Gompertz model to experimental data.

4.2.2 Transient Tolerance Correlates with Lag Phase During Nutrient Shift

To examine whether the transient tolerant exists when switching from other gluconeogenic carbons, we performed additional switching experiments by replacing glycerol with 4 other carbon sources: acetate, pyruvate, malate, and succinate. These carbon sources represent different entry points into the central metabolism (Figure 4.2A), thus would allow us to compare how different metabolic state of cells in the pre-culture affect transient tolerance. All transitions displayed similar tri-phasic killing kinetics with an initial transient tolerance followed by rapid killing of susceptible cells and a slow killing of persistent cells. The period of transient tolerance varied significantly with different carbon sources (Figure 4.2B). While transitions from acetate had a relatively short transient tolerance time (3.3 ± 0.4 hours, 95% confidence interval (C.I.)), transitions from pyruvate displayed extremely long tolerance (44 ± 3 hours, 95% C.I.). However, despite great variability in the timing, all conditions showed that majority of cells were eventually killed by ampicillin, indicating that the initial antibiotic tolerance is only temporary after gluconeogenic to FA nutrient shifts.

Shifts from glycolytic to gluconeogenic carbon sources have been shown to produce lag phase during which cell halts growth transiently (Basan et al., 2020). Since ampicillin is only effective on growing cells, cessation of growth after a nutrient shift offers a simple mechanism for transient tolerance. To test this, we measured growth kinetics of cultures switching from each gluconeogenic carbon source to FA without antibiotic (Figure 4.2C). The lag time of each shift was found to

correlate well (R^2 = 0.82) with the transient tolerance time (Figure 4.2D). These results suggest that non-growing cells in the lag phase after a nutrient shift cause transient tolerance to ampicillin.

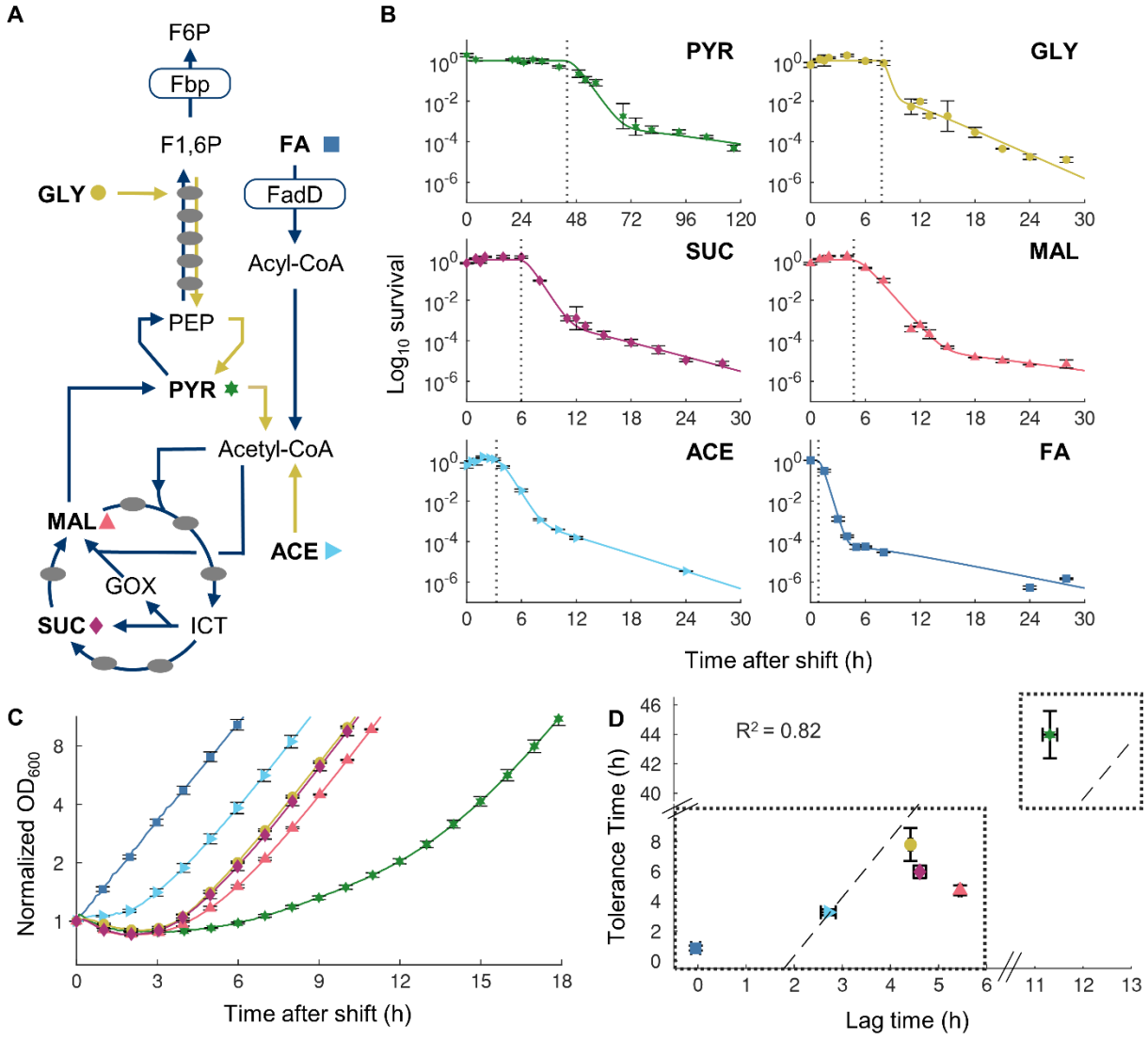

Figure 4.2. Tolerance time correlates with lag time on transitions from gluconeogenic carbon sources to oleate. (A) Simplified metabolic network for gluconeogenic carbon source utilization. Pre-shift carbon sources used are in bold with a corresponding symbol indicating that carbon source: (FA, square; Acetate, right-pointing triangle; Pyruvate, star; Glycerol, Circle; Malate, up-pointing triangle; Succinate, kite). Dark arrows indicate pathways necessary for FA utilization. Names of key metabolite intermediates and enzymes are shown. **(B)** Time course survival curves of cells after shifts from gluconeogenic carbon sources to FA with 100 µg/mL ampicillin. Data points are averaged values from biological replicates, n = 3. Curves are fitting of a two-population Gompertz model to experimental data. Vertical dashed line indicates tolerance time determined by fitting the Gompetz model. **(C)** Time course OD_{600} after shift from gluconeogenic carbon to FA

without ampicillin, normalized to time point t = 0. Average of biological replicates, n=3, SEM Error Bars. **(D)** Correlation between measured tolerance time and lag time after switch to FA. Dashed line is least-squares linear fit to the data with equal weighting.

4.2.3 Time for FadD Accumulation Correlates with Transient Tolerance

Since the lag time and transient tolerance period after the nutrient shift are well correlated, we sought to understand the molecular mechanisms which govern both phenomena. Growth rate in pre-culture conditions was shown to predict lag time for glycolytic to gluconeogenic switches (Basan et al., 2020) and therefore may also predict tolerance time on nutrient shifts from gluconeogenic carbons to FA. We measured pre-culture growth rates and found a weak negative correlation ($R^2 = 0.35$) between pre-culture growth rate and tolerance time (Figure 4.3A). Although the direction of correlation is consistent with previous studies (Basan et al., 2020), nutrient shifts from pyruvate to FA presents a clear outlier, suggesting the presence of other mechanisms that control tolerance time more directly.

Previous studies illustrated that β-oxidation enzymes are essential for growth when FA is the sole carbon source (DiRusso et al., 1999), suggesting a possible role for β-oxidation enzymes in tolerance time during nutrient shifts to FA. Because FadD is a key component of the positive feedback loop controlling transport and activation of FAs for β-oxidation, we genetically fused a YFP to FadD to monitor activity of FA degradation during the nutrient shift. The FadD-YFP strain was grown in different gluconeogenic carbon sources and switched to FA in the absence of ampicillin. Cell growth and YFP fluorescence were simultaneously monitored after the nutrient shift. After shifting from different gluconeogenic carbon sources, the initial FadD levels were different and all lower than that without carbon shift (i.e. from FA to FA, Figure 4.3B), suggesting that the β-oxidation enzymes were not highly expressed in gluconeogenic carbons. The FadD concentration gradually increased over time during the lag phase. When cells resume steady state growth, FadD concentration from all switches reached the same threshold level (Figure 4.3C).

Without carbon shift (from FA to FA), the FadD level remained above this threshold level, and the cells continued to grow without a lag phase. We measured the time needed to reach this threshold FadD level and found that it has a good correlation with the tolerance time (R^2 = 0.82, Figure 4.3D). Since the timing of accumulating FadD correlates well with transient tolerance, we wondered whether this timing of each phenomenon is simply determined by the amount of FadD initially present immediately after the nutrient shift. Although FadD accumulation time appears to decrease with increasing initial FadD concentrations (R^2 = 0.57, Figure 4.3E), transitions from pyruvate again provide a strong outlier with cells taking much longer to accumulate FadD to a threshold.

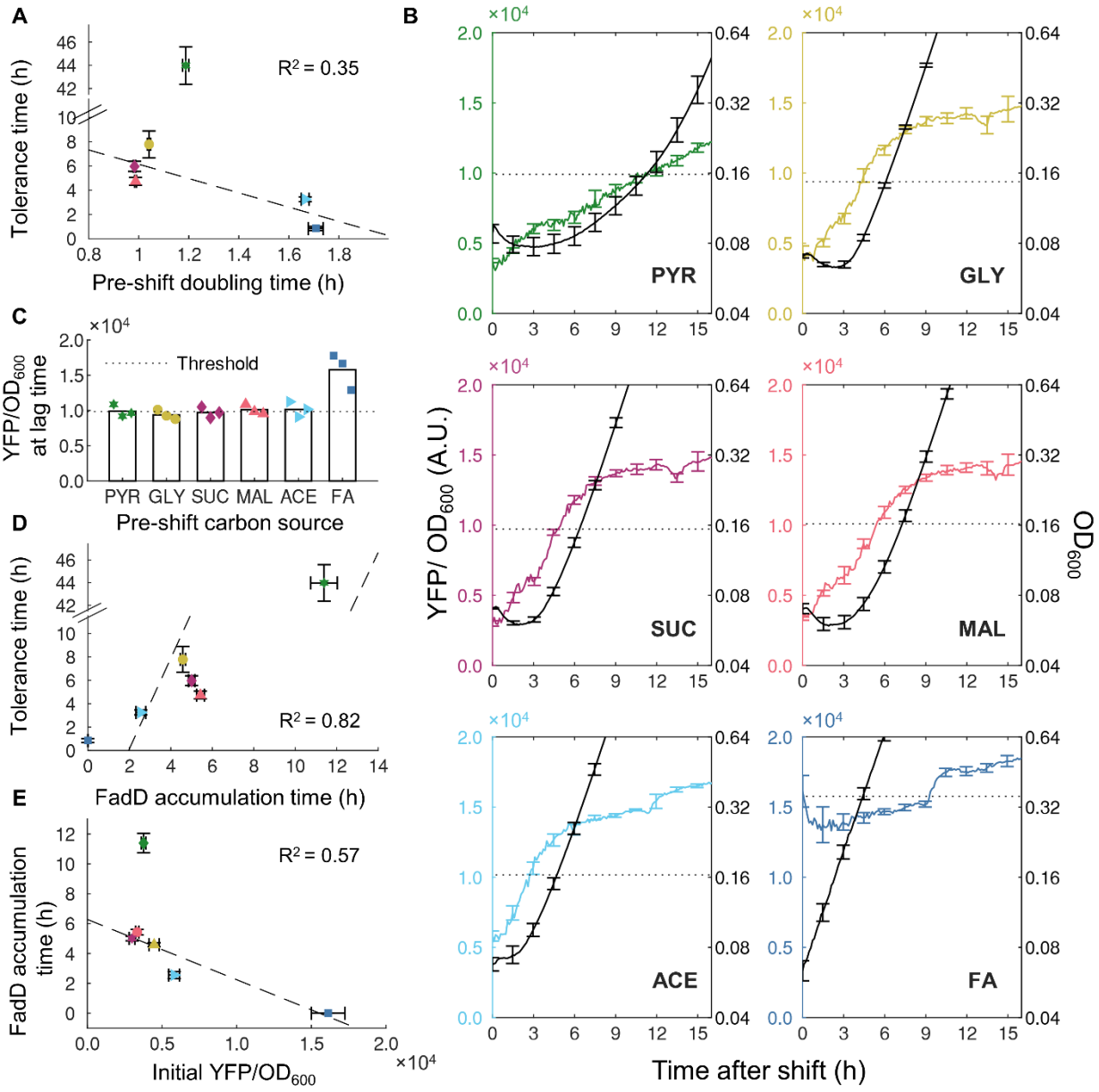

Figure 4.3. Timing of FadD accumulation associated with transient tolerance time. (A) Correlation between measured tolerance time and growth rate in pre-switch carbon source. Dashed line is least-squares linear fit to data with bisquare weighting. **(B)** Time course of YFP/OD_{600} from FadD-YFP fusion (colored line, left axis) and OD_{600} (black line, right axis) after shifts from a gluconeogenic carbon source to FA, n = 3, Error Bars represent SEM. The dotted line indicates the YFP/OD_{600} level when cells resume steady state growth. **(C)** Average YFP/OD_{600} from FadD-YFP fusion at the end of the lag phase, n = 3. Values from individual replicates shown as points. The dashed line (namely the FadD threshold) shows the average FadD concentration at the end of lag phase across all pre-shift conditions except FA. **(D)** Correlation between tolerance time and FadD accumulation time (time for FadD to reach the threshold level). Tolerance time was obtained from data in Fig 2B. Dashed line is a linear fit. **(E)** Correlation between YFP/OD_{600} value at the

steady state of pre-culture and FadD accumulation time. Dashed line is a least-squares linear fit with bisquare weighting.

To verify whether these FadD dynamics are representative of the nutrient shifts in the presence of antibiotics, we performed similar experiments using the FadD-YFP fusion strain in the presence of ampicillin. Across all switching conditions, OD_{600} initially decreased slightly followed by a leveling off period (Appendix C, Figure C.1A). Because this slight decrease is also observed in the absence of antibiotic, this decrease more likely represents reductive division of cells, which has been previously reported for cells under starvation conditions (Nyström, 2004), rather than killing by antibiotics. After this relatively level period (transient tolerance), the OD decreases substantially, corresponding to rapid killing of susceptible cells. In all switching conditions, the FadD level continued to increase during the transient tolerance period, indicating active transcription and translation. The time needed to reach a threshold FadD level still correlated well with the tolerance time ($R^2 = 0.79$, Appendix C, Figure C.1B). Additionally, the timing of FadD accumulation in the absence and presence of ampicillin correlated extremely well ($R^2 = 0.997$, Appendix C, Figure C.1C), indicating that the FadD dynamics during the nutrient shift are nearly the same prior to reaching the FadD threshold, regardless of the presence of ampicillin. Overall, these results suggest that FA metabolic activity was low during lag phase, resulting in slow cell growth and transient tolerance to ampicillin. A key level of FadD is needed to resume cell growth and active metabolism in FA medium.

Finally, we evaluated the single-cell behavior of FA metabolism using the acyl-CoA biosensor during nutrient transitions from pyruvate to FA, which has the longest transient tolerance time. We characterized the acyl-CoA biosensor activity under mixtures of pyruvate and FA and found that the population has a monomodal distribution of acyl-CoA biosensor activity under all conditions

(Appendix C, Figure C.2A), consistent with the biosensor activity on glycerol/FA mixtures (Figure 4.1C). We then conducted nutrient switches from pyruvate to FA with ampicillin and measured the acyl-CoA biosensor activity at time points during the transient tolerance phase. Again, we observed monomodal populations at all time points, with the biosensor activity of the whole population increasing sharply by 4 hours after the shift, and then more gradually after 21 hours (Appendix C, Figure C.2B). Thus, these results suggest that there is a single, large majority population before the shift and this whole population gradually transitions toward active FA metabolism after the shift, leading to growth and sudden killing by ampicillin for a large population at the end of the transient tolerance.

4.2.4 Multiple Metabolic Regulations Control the Transient Tolerance Time

Given that the time for FadD to reach its threshold concentration correlates well with transient tolerance, we wondered what controls FadD accumulation. Particularly, shifts from pyruvate to FA produced the longest transient tolerance times from the above experiment. We searched the literature and did not find direct regulatory effects of pyruvate on *fadD* expression in *E. coli*. However, pyruvate activates the IlcR transcription factor (Lorca et al., 2007) which represses expression the glyoxylate bypass operon *aceBAK* (Figure 4.4A). The glyoxylate bypass is necessary for FA utilization because β-oxidation produces only two-carbon metabolite precursors in the form of acetyl-CoA (Dolan and Welch, 2018). To examine whether pyruvate impacts the glyoxylate bypass or β-oxidation gene expression, we evaluated the expression level of the *aceB* and *fadD* genes via RT-qPCR for cells growing in glycerol, pyruvate, and FA (Appendix C, Figure C.3). In pyruvate, *aceB* expression is 1.7-fold lower compared to that in glycerol, however, *fadD* expression is not significantly different between glycerol and pyruvate conditions, indicating that the glyoxylate bypass rather than the FA transport genes is more blocked in pyruvate. During

growth on FA, both *aceB* and *fadD* expression are significantly increased (13.7-fold and 5.0-fold increase respectively), which indicates that the expression of both *aceB* and *fadD* genes needs to be increased for cells to grow on FA, in agreement with previous literature (Clark and Cronan, 2005).

In addition to pyruvate regulation, IclR activity is antagonized by glyoxylate (Lorca et al., 2007), an intermediate in the glyoxylate bypass (Figure 4.4A), thus forming a positive feedback loop which also governs FA utilization. Therefore, when cells are growing in pyruvate, accumulation of glyoxylate is slow, and the glyoxylate bypass enzymes remain at low levels. We hypothesize that switching from pyruvate to FA requires a gradual increase in the metabolic flux through the glyoxylate bypass to produce central metabolites (e.g. amino acids) for synthesizing β-oxidation enzymes. To test this hypothesis, we added glyoxylate to the pre-shift medium to activate the glyoxylate bypass enzymes, thus alleviating the bottleneck in the glyoxylate bypass enzymes. New nutrient shift experiments with glyoxylate displayed decreased lag phase as well as FadD accumulation times for pyruvate, succinate, and malate (Figure 4.4B, 4.4C). Among them, pyruvate exhibited the most drastically change, its FadD accumulation time decreased from 11.4±1.3 hours to 3.4±0.5 hours (95% C.I.) (Figure 4.4C). Additionally, we performed similar growth kinetic experiments during nutrient shift to FA with ampicillin and observed similar reductions in the transient tolerance time measured by OD_{600} (Appendix C, Figure C.4). The transient tolerant time shifting from pyruvate with glyoxylate supplement to FA decreased from >16 hours without glyoxylate to 3.1±0.5 hours (95% C.I.). With the presence of glyoxylate in the pre-shift medium, the highest correlation between the transient tolerance period and FadD accumulation time was obtained (R^2 = 0.98, Figure 4.4D), demonstrating that both FadD accumulation and transient tolerance are accelerated by the removal of the glyoxylate bottleneck.

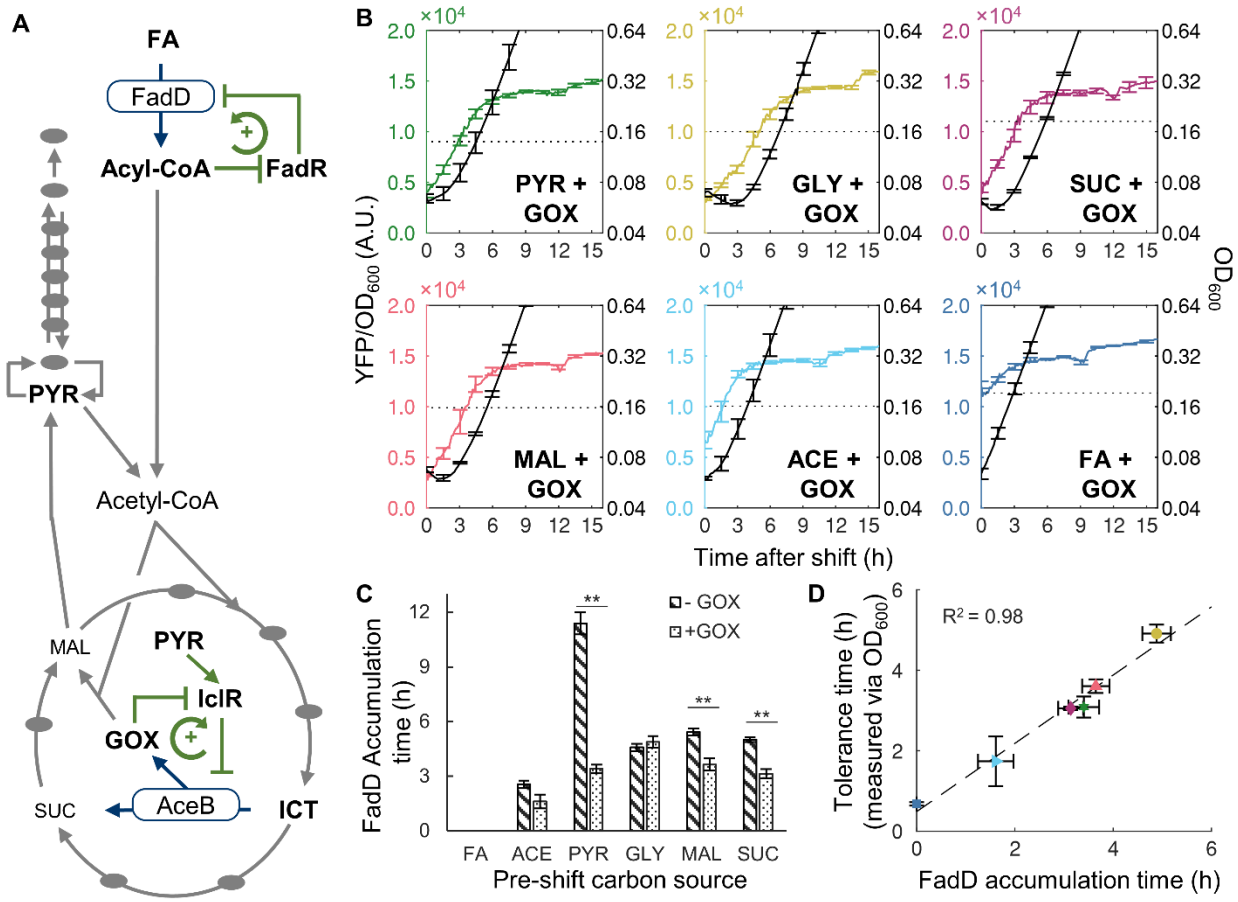

Figure 4.4. Activity of glyoxylate shunt affects tolerance time. (A) Simplified metabolic network with key positive-feedback regulatory interactions for FA utilization. Metabolic enzymes (FadD/AceB) convert a precursor into a regulatory metabolite intermediate (acyl-CoA/glyoxylate). The regulatory intermediate represses the activity of a transcription factor (FadR/IclR) which alleviates the repression of the metabolic enzyme. IclR activity is also activated by pyruvate. **(B)** Time course of YFP/OD_{600} from FadD-YFP fusion (colored line, left axis) and OD_{600} (black line, right axis) after shifts from a glyoxylate supplemented gluconeogenic carbon source to FA (not supplemented with glyoxylate). Error Bars represent SEM with n = 3 for FA, ACE, MAL, and SUC, n = 4 for PYR, and n= 5 for GLY. The dotted line indicates the YFP/OD_{600} level when cells resume steady state growth. **(C)** FadD accumulation time for nutrient shifts from carbon source without glyoxylate (stripes) or with glyoxylate (dotted). Stars indicate significant change in accumulation time, two-tailed t-test (**, $p < 0.01$) **(D)** Correlation between tolerance time and FadD accumulation time for shifts from carbon with glyoxylate to FA. Tolerance timed determined by time course optical density measurements (Appendix C, Figure C.4). Dashed line is a least-squares linear fit.

4.3 Discussion

In this study, we sought to elucidate the role of nutrient shifts and positive metabolic feedback architecture in producing antibiotic tolerant cells. In doing so, we discovered that nutrient shifts from gluconeogenic carbon source to FA produce tri-phasic antibiotic killing kinetics which depend on the initial metabolic state of the cells. These killing kinetics are defined by an initial period of nearly universal antibiotic survival, followed by a sudden increase in antibiotic killing for over 98% of the population, followed by a slower, persister killing rate. Our results outline a clear mechanism for this behavior. First, before switching to FA, cells are in single population of low Fad activity. After shifting to FA, the bulk of the population is in a metabolically mal-adapted state which causes the cells to cease growth, producing a lag phase. In this metabolically reduced stated, ampicillin, which targets actively dividing cells, is rendered ineffective. This tolerance continues until the cells adapt their metabolism by increasing the concentration of key metabolic enzymes such as the FA degradation and glyoxylate bypass pathways to restore metabolism and growth. Further, the timing of the recovery depends on its initial metabolic state and on specific regulatory mechanisms for enzyme induction.

The connection between lag phase and antibiotic tolerance has been demonstrated previously (Fridman et al., 2014) when shifting from stationary phase media to rich media. In the so-called “tolerance by lag” (TBL) phenotype, mutant strains of *E. coli* have a population of cells with a wide distribution of lag times when shifting back to rich media, which allows the population to be more tolerant to ampicillin killing. While TBL and transient tolerance can both be attributed to the growth-arrest of cells in a lag phase, there are several important distinctions between these phenomena. First, the shapes of the killing curves are different. In transient tolerance, the killing curve is initially flat followed by a sharp decline which suggests that transient tolerant populations

shift from high tolerance to low tolerance over time. In contrast, the TBL killing curves gradually decrease at a constant slope without distinct phases which suggests that tolerance from TBL is more constant in time. Second, TBL is caused by mutations in genes which are selected for by the length of antibiotic treatments. In contrast, transient tolerance is caused by a major disruption of the metabolic network due to nutrient shift which forces cells to halt growth. Finally, although transient tolerance is correlated with lag, we show that transient tolerance is more fundamentally affected by the time is takes to readjust the metabolic network by accumulating pathway enzymes. Because nutrient shifts can often leave cells in a metabolically mal-adapted state, transient tolerance is likely to be a general tolerance mechanism to ampicillin for cell populations.

Since the FA utilization and β-lactam tolerance mechanisms in *E. coli* are well-known, the connection between adaptation of the FA pathways and transient tolerance may seem apparent at first. However, the tri-phasic shape of the antibiotic killing curves shed important insights and raise new questions about how *E. coli* responds to nutrient shifts in general. In particular, it has previously been demonstrated that on glucose-to-fumarate transitions cells adopt a responsive diversification strategy where only a small minority of cells are capable of adaptation and the vast majority becoming persisters (Kotte et al., 2014; Radzikowski et al., 2016). From these experiments, it has been suggested then that prolonged cold shock and flux limitation are triggers of persistence (Heinemann et al., 2020). Our results show that cold shock and flux-limitation on nutrient shifts does not necessarily trigger persistence but can instead induce only a temporary tolerance. The correlation of transient tolerance with adaptation to FA utilization and the sudden killing of at least 98% of the population suggests that a majority of cells adapt to utilizing FA after a gluconeogenic-to-FA transitions with very few cells entering a long-lived persister state. Therefore, our results demonstrate that despite both being regulated by positive feedback,

glycolytic-to-gluconeogenic and gluconeogenic-to-FA transitions follow fundamentally different adaptation strategies. These contrasting results highlight the need for a deeper understanding of how the underlying molecular mechanisms contribute to the choice of adaptation strategies in response to nutrient transitions.

More generally, our results elucidate the role of metabolic positive feedback loops in nutrient shift and β-lactam tolerance. For example, the positive feedback loop in the glyoxylate bypass causes cells to maintain transient tolerance for up to 44 hours when switching from pyruvate to FA. Adding glyoxylate to the pre-shift medium accelerated both transient tolerance and FadD accumulation, indicating that a bottleneck in the glyoxylate bypass has a global effect on the metabolic network, beyond its own regulatory loop. Previous studies of antibiotic persistence have demonstrated the possibility of potentiating antibiotic killing by introducing key metabolites (Allison et al., 2011). Our results demonstrate that glyoxylate can act as a key regulatory metabolite to prime the metabolic network to adapt to certain nutrient shifts, thus reducing transient tolerance to β-lactams. Because of the presence of these specific metabolic regulations, cells maintain a memory of their pre-shift nutrient conditions, causing large differences in tolerance time despite having identical post-shift nutrient environments. Additionally, although we mainly focus on understanding the transient tolerance period, we note that shifts from different carbon sources also have different rates of antibiotic killing and different persister fractions (Figure 4.2B, Appendix C, Table C.1). These observations suggest a more profound impact of metabolism on persistence, which are worth further studies. Altogether, our findings show how the pre-shift metabolic conditions can have long lasting effects on the metabolism and antibiotic tolerance of cells after a nutrient shift.

4.4 Materials and Methods

4.4.1 Strains, Plasmids, and Construction

All strains were derived from *Escherichia coli* NCM3722, which was obtained from the Coli Genetic Stock Center (Yale, USA). All strains, plasmids, and primers used are given in Appendix C, Table C.2 and the plasmid sequences are given in Table C.3. Phusion DNA polymerase, restriction enzymes, and T4 ligase used in plasmid construction were purchased from Thermo Fisher Scientific (Waltham, MA, U.S.A.). Primers were synthesized by Integrated DNA Technologies (Coralville, IA, U.S.A).

Acyl-CoA Biosensor Strain. The Acyl-coA biosensor plasmid pSARk-yemGFP was constructed from three parts following standard enzyme digestion and ligation protocols. The bglBrick vector pS5k-rfp (Lee et al., 2011) was digested by *AatII* and *XhoI*. The pAR promoter was obtained by digesting pBARk-rfp (Xiao et al., 2016) with *AatII* and *BglII*. The yemGFP sequence was amplified by polymerase chain reaction (PCR) yemGFP_F and yemGFP_R (Appendix C, Table C.2) and digested with *BglII* and *XhoI*. Parts were ligated and transformed into *E. coli* NCM3722 to make the Acyl-CoA Biosensor Strain.

FadD-YFP Strain. The FadD-YFP strain was constructed by following the pTarget-pCas homologous recombination system protocol as described previously (Jiang et al., 2015, 2017). Homology arms with 200-300 base pairs upstream and downstream of FadD were amplified from *E. coli* NCM3722 genomic DNA by PCR. The YFP gene was amplified from a codon optimized plasmid (Cox et al., 2010). The *fadD* and YFP genes were separated by a flexible glycine-serine-rich linker constructed on primers (Bai et al., 2019). A guide RNA with the following sequence was synthesized on primers and amplified along with the pTarget backbone: TGACGACTGACTTAACGCTC. PCR products were then assembled via Golden Gate Cloning

to form pTargetF-FadD-YFP. The pTarget plasmid was then used to integrate YFP into the genome of *E. coli* NCM3722 transformed with pCas. Genome integration was verified by colony PCR and sequencing, and the genome integrated strain was cured of the pTarget and pCas plasmids. The final sequence of the FadD-YFP strain in the genome region of *fadD* is given in Appendix C, Table C.3.

4.4.2 Growth Media

Cell growth and nutrient shift experiments were performed in M9 minimal media with corresponding carbon source (M9 minimal salts supplemented with 75 mM MOPS at pH 7.4, 2 mM magnesium sulfate, 1 mg/L thiamine hydrochloride, 10 μM iron(II) sulfate, 100 μM calcium chloride, 3 μM ammonium heptamolybdate, 0.4 mM boric acid, 30 μM cobalt(II) chloride, 15 μM copper(II) chloride, 80 μM Manganese(II) chloride, and 10 μM Zinc sulfate). Media was supplemented with sodium salts of each carbon source at a 72 mM carbon: 4mM oleate, 36 mM acetate, 24 mM pyruvate, 24 mM glycerol, 18 mM (S)-malate, 18 mM succinate. For experiments with co-utilization of glycerol and FA, the ratios of glycerol and oleate were adjusted to maintain a total of 72 mM carbon atoms in the media. For experiments with co-utilization of carbon and glyoxylate, 9 mM glyoxylate was used in all conditions, along with following concentrations of each carbon source such that 72 mM of carbon atoms was maintained: 3 mM oleate, 24 mM acetate, 18 mM pyruvate, 18 mM glycerol, 13.5 mM (S)-malate, 13.5 mM succinate. All cultures were supplemented with appropriate antibiotic for selection (Ampicillin, 100 μg/mL; Kanamycin, 50 μg/mL).

4.4.3 Acyl-CoA Biosensor Activity

Single colonies of the acyl-CoA biosensor strain were grown in 3 mL LB media for 2-3 hours, then washed twice in M9 without a carbon source. Cultures were shifted into 3 mL M9

media supplemented with specified glycerol and oleate concentration and grown for an additional 3-5 hours. Cells were again washed twice in M9 without a carbon source and were transferred M9 media supplemented with the specified glycerol/oleate ratios in a 96-well plate. Cells were diluted to a density of ~2 cells/μL so that the glycerol/oleate ratio does not significantly change during cell growth. Cells were grown for 9 hours, then growth was halted by addition of 100 μg/mL of rifampicin and incubated on ice for at least 15 minutes prior to measurement. Samples were analyzed with a Guava easyCyte HT5 flow cytometer (Luminex Corporation, Austin, TX, U.S.A.) with blue 488 nm excitation laser and the green 525 nm emission filter.

4.4.4 Nutrient Shifting and Colony Counting Assays

All nutrient shifts were performed following previous methods (Radzikowski et al., 2016). Specifically, cells were cultivated in a pre-shift medium at 37°C and were kept in exponential growth phase for 14-17 hours. Cells were then collected and centrifuged in a pre-chilled centrifuge (4 °C) at 4500 rcf for 10 minutes. Supernatant was discarded and cells were resuspended in chilled M9 without carbon source. Three washes were performed. Finally, cell density (OD_{600}) was normalized to 0.5 in M9 without carbon, and then diluted 1:5 into pre-warmed oleate media so that the final cell density was 0.1, and the final oleate and ampicillin concentrations were 4 mM and 100 μg/mL respectively, and with a final culture volume of 25 mL. At times indicated, 1 mL culture was transferred to centrifuge tubes pre-filled with 200 μL of phosphate buffered saline (PBS, pH 7.4). Cells are centrifuged at 4500 rcf, 4 °C, and washed 4 times in PBS. Finally, cell pellets were resuspended to a final volume of 1 mL, and serial dilutions were also performed in PBS. For each diluted culture, 10 μL was transferred onto LB agar plates and incubated for 12 hours at 37°C. Colonies were counted to determine the colony forming units per mL of culture (CFU/mL).

4.4.5 Transient Tolerance Time Determination

To quantify the length of time where the cells are transiently tolerant to ampicillin, we fit the colony counting data to a modified two-population Gompertz model, which has been widely used to describe kinetics of bacterial growth (Zwietering et al., 1990) and mortality (Kirkwood, 2015):

$$Survival = \left((1-p) \times \left(1 - exp\left(-exp\left(1 + \mu_{TT} \times e \times (t - \tau_{TT})\right)\right)\right)\right) + \left((p) \times \left(1 - exp\left(-exp\left(1 + \mu_{PER} \times e \times (t - \tau_{PER})\right)\right)\right)\right)$$

where p is the persister fraction, μ_{TT} and μ_{PER} are the maximum killing rates of the transient tolerant and persister population, respectively, τ_{TT} and τ_{PER} are the transient tolerance times of the transient tolerant and persister fractions, respectively. Next, we assume that the tolerance time of the transient tolerant fraction and persister fraction are equal, i.e. $\tau_{TT} = \tau_{PER} = \tau$. Thus, only the maximum rate of killing distinguishes the transient tolerant and persister populations.

To fit the data, CFU/mL counts were first normalized to the CFU/mL from time point zero and converted to a $\log_{10}$ scale. All data from replicates of each shifting experiment was fit to the two-population Gompertz model using the MATLAB R2020B curve fitting tool (cftool). An initial transient tolerance time was determined; the data was then re-normalized to the average CFU/mL counts prior to the tolerance time for each replicate. The re-normalized data was fit again, and the parameters along with their 95% confidence intervals and SEM were determined.

4.4.6 FadD-YFP Kinetic Assays

Cells were grown in different pre-shift carbon sources at steady state as described for Colony Counting Assays. Cells were centrifuged and washed in M9 without carbon source for 4 times. Washed cells were then transferred to a Falcon 96-Well Imaging Microplate (Corning, NY,

USA) and diluted to an initial OD_{600} of 0.08 in oleate media with or without ampicillin, with a final volume of 150 µL. An Infinite F200PRO plate reader (TECAN, Männedorf, Switzerland) was used to make automated OD_{600} and fluorescence measurements (Excitation: 514 nm, Emission: 552 nm) every 6 minutes with constant shaking and 37 °C temperature control. Fluorescence measurements are normalized by OD_{600} to give an estimate of FadD concentration.

4.4.7 Lag Phase, Threshold, and Accumulation Time Calculations

Lag phase was determined by a similar protocol as described previously (Basan et al., 2020). The steady state growth rate after nutrient shift was first calculated by fitting a line to the natural log of the OD_{600} for the first hour after the culture density increases 8-fold from its initial density. The time point where this line intersects the initial culture density is the end of the lag phase. The fluorescence measurement at the closest measured time point is used as YFP/OD_{600} at the lag time. The FadD threshold was determined by taking the average YFP/OD level at the end of the lag phase across all nutrient shift conditions without glyoxylate. The accumulation time was determined as the first time point where the YFP/OD_{600} was above this threshold and the YFP/OD_{600} at all subsequent time points also exceeded the threshold.

4.4.8 Tolerance Time via OD_{600} Calculation and YFP Normalization

For kinetic optical density measurements in the presence of ampicillin, the transient tolerance time was calculated as the last local maximum in the log of the OD for each time series. To determine this, a moving window slope of 11 time points was used twice to calculate the first and second derivatives of the log OD. The last time point where the first derivative was closest to zero, and where the second derivative was negative was taken as the tolerance time measured by OD_{600}. Additionally, all fluorescence measurements after the measured tolerance time were

normalized by the OD_{600} at the tolerance time to give an estimate of the FadD concentration which is unbiased by the reduction in OD due to cell death.

4.4.9 Transcription Analysis by Reverse Transcription-qPCR

Cells were cultivated to steady state growth to an OD_{600} of 0.2 and 2 mL of cells were collected and stored in RNA/DNA Shield (Zymo Research, Irvine, CA, USA). Total RNA was extracted from cells using the Quick-RNA Miniprep Plus Kit (Zymo Research) following manufactures protocols. Contaminating genomic DNA was removed by DNase I treatment of RNA on collection column, following the Quick-RNA Miniprep Kit protocol. cDNA was synthesized using Revert Aid First strand cDNA Synthesis (Thermo Fischer Scientific) with random hexamer primers following the manufactures protocol. Negative control reactions without the use of reverse transcriptase were preformed to evaluate the potential presence of contaminating genomic DNA. 2 µL of cDNA was amplified using Power SYBR green PCR Master Mix (Thermo Fischer Scientific) and gene specific primers (Appendix C, Table C.2). qPCR reactions for each biological replicate, gene, and growth condition were performed in triplicate. qPCR assays were performed on a QuantStudio3 (Thermo Fischer Scientific) following standard thermal cycling conditions recommended by the manufacturer. Expression levels of the condition invariant gene *gyrA* were used as a control for normalization between samples (Said-Salman et al., 2019). Fold changes of each gene of interest were calculated following the $2\text{-}\Delta\Delta C_T$ method.

4.5 Supplemental Information

Tables C.1- C.3, Figures C.1-C.4, and Appendix Sections C.1-C.2 can be found in Appendix C.

4.5.1 Abbreviations

ACE, Acetate; Amp, Ampicillin; FA, Fatty Acid; F1,6P, fructose-1,6-bisphosphate; F6P, fructose 6-phosphate; GLY, glycerol; GOX, Glyoxylyate; ICT, Isocitrate; MAL, Malate; PEP, phosphoenolpyruvate; PYR, pyruvate; SUC, Succinate; TBL, tolerance by lag

4.6 Chapter 4 References

Allison, K. R., Brynildsen, M. P., and Collins, J. J. (2011). Metabolite-enabled eradication of bacterial persisters by aminoglycosides. *Nature* 473, 216–220. doi:10.1038/nature10069.

Amato, S. M., and Brynildsen, M. P. (2014). Nutrient transitions are a source of persisters in *Escherichia coli* biofilms. *PLoS One* 9, e93110. doi:10.1371/journal.pone.0093110.

Amato, S. M., and Brynildsen, M. P. (2015). Persister heterogeneity arising from a single metabolic stress. *Curr. Biol.* 25, 2090–2098. doi:10.1016/j.cub.2015.06.034.

Amato, S. M., Fazen, C. H., Henry, T. C., Mok, W. W. K., Orman, M. A., Sandvik, E. L., et al. (2014). The role of metabolism in bacterial persistence. *Front. Microbiol.* 5, 70. doi:10.3389/fmicb.2014.00070.

Amato, S., Orman, M., and Brynildsen, M. (2013). Metabolic control of persister formation in *Escherichia coli*. *Mol. Cell* 50, 475–487. doi:10.1016/j.molcel.2013.04.002.

Aslam, B., Wang, W., Arshad, M. I., Khurshid, M., Muzammil, S., Rasool, M. H., et al. (2018). Antibiotic resistance: A rundown of a global crisis. *Infect. Drug Resist.* Volume 11, 1645–1658. doi:10.2147/IDR.S173867.

Bai, W., Sargent, C. J., Choi, J.-M., Pappu, R. V., and Zhang, F. (2019). Covalently-assembled single-chain protein nanostructures with ultra-high stability. *Nat. Commun.* 10, 3317. doi:10.1038/s41467-019-11285-8.

Balaban, N. Q. (2004). Bacterial Persistence as a Phenotypic Switch. *Science* 305, 1622–1625. doi:10.1126/science.1099390.

Balaban, N. Q., Helaine, S., Lewis, K., Ackermann, M., Aldridge, B., Andersson, D. I., et al. (2019). Definitions and guidelines for research on antibiotic persistence. *Nat. Rev. Microbiol.* 17, 441–448. doi:10.1038/s41579-019-0196-3.

Basan, M., Honda, T., Christodoulou, D., Hörl, M., Chang, Y. F., Leoncini, E., et al. (2020). A universal trade-off between growth and lag in fluctuating environments. *Nature* 584, 470–474. doi:10.1038/s41586-020-2505-4.

Bernier, S. P., Lebeaux, D., DeFrancesco, A. S., Valomon, A., Soubigou, G., Coppée, J.-Y., et al. (2013). Starvation, together with the SOS response, mediates high biofilm-specific tolerance to the fluoroquinolone ofloxacin. *PLoS Genet.* 9, e1003144. doi:10.1371/journal.pgen.1003144.

Clark, D. P., and Cronan, J. E. (2005). Two-carbon compounds and fatty acids as carbon sources. *EcoSal Plus* 1, 2. doi:10.1128/ecosalplus.3.4.4.

Cox, R. S., Dunlop, M. J., and Elowitz, M. B. (2010). A synthetic three-color scaffold for

monitoring genetic regulation and noise. *J. Biol. Eng.* 4, 10. doi:10.1186/1754-1611-4-10.

Cronan, J. E. J., and Subrahmanyam, S. (1998). FadR, transcriptional co-ordination of metabolic expediency. *Mol. Microbiol.* 29, 937–943. doi:10.1046/j.1365-2958.1998.00917.x.

De Groote, V. N., Verstraeten, N., Fauvart, M., Kint, C. I., Verbeeck, A. M., Beullens, S., et al. (2009). Novel persistence genes in *Pseudomonas aeruginosa* identified by high-throughput screening. *FEMS Microbiol. Lett.* 297, 73–79. doi:10.1111/j.1574-6968.2009.01657.x.

DiRusso, C. C., Black, P. N., and Weimar, J. D. (1999). Molecular inroads into the regulation and metabolism of fatty acids, lessons from bacteria. *Prog. Lipid Res.* 38, 129–197. doi:10.1016/S0163-7827(98)00022-8.

Dolan, S. K., and Welch, M. (2018). The glyoxylate shunt, 60 years on. *Annu. Rev. Microbiol.* 72, 309–330. doi:10.1146/annurev-micro-090817-062257.

Eldar, A., and Elowitz, M. B. (2010). Functional roles for noise in genetic circuits. *Nature* 467, 167–173. doi:10.1038/nature09326.

Ellermann, M., Jimenez, A. G., Pifer, R., Ruiz, N., and Sperandio, V. (2021). The canonical long-chain fatty acid sensing machinery processes arachidonic acid to inhibit virulence in enterohemorrhagic *Escherichia coli*. *MBio* 12, e03247-20. doi:10.1128/mBio.03247-20.

Evans, T. D., and Zhang, F. (2020). Bacterial metabolic heterogeneity: Origins and applications in engineering and infectious disease. *Curr. Opin. Biotechnol.* 64, 183–189. doi:https://doi.org/10.1016/j.copbio.2020.04.007.

Fauvart, M., de Groote, V. N., and Michiels, J. (2011). Role of persister cells in chronic infections: Clinical relevance and perspectives on anti-persister therapies. *J. Med. Microbiol.* 60, 699–709. doi:10.1099/jmm.0.030932-0.

Ferrández, A., García, J. L., and Díaz, E. (2000). Transcriptional regulation of the divergent *paa* catabolic operons for phenylacetic acid degradation in *Escherichia coli*. *J. Biol. Chem.* 275, 12214–12222. doi:10.1074/jbc.275.16.12214.

Fraenkel, D. G., and Horecker, B. L. (1965). Fructose-1, 6-diphosphatase and acid hexose phosphatase of *Escherichia coli*. *J. Bacteriol.* 90, 837–842. doi:10.1128/JB.90.4.837-842.1965.

Fridman, O., Goldberg, A., Ronin, I., Shoresh, N., and Balaban, N. Q. (2014). Optimization of lag time underlies antibiotic tolerance in evolved bacterial populations. *Nature* 513, 418–421. doi:10.1038/nature13469.

Gefen, O., Gabay, C., Mumcuoglu, M., Engel, G., and Balaban, N. Q. (2008). Single-cell protein induction dynamics reveals a period of vulnerability to antibiotics in persister bacteria. *Proc. Natl. Acad. Sci.* 105, 6145–6149. doi:10.1073/pnas.0711712105.

Germain, E., Roghanian, M., Gerdes, K., and Maisonneuve, E. (2015). Stochastic induction of persister cells by HipA through (p)ppGpp-mediated activation of mRNA endonucleases. *Proc. Natl. Acad. Sci.* 112, 5171–5176. doi:10.1073/pnas.1423536112.

Gilbert, P., Collier, P. J., and Brown, M. R. (1990). Influence of growth rate on susceptibility to antimicrobial agents: Biofilms, cell cycle, dormancy, and stringent response. *Antimicrob. Agents Chemother.* 34, 1865–1868. doi:10.1128/AAC.34.10.1865.

Hartline, C. J., Mannan, A. A., Liu, D., Zhang, F., and Oyarzún, D. A. (2020). Metabolite sequestration enables rapid recovery from fatty acid depletion in *Escherichia coli*. *MBio* 11, e03112-19. doi:10.1128/mBio.03112-19.

Hauryliuk, V., Atkinson, G. C., Murakami, K. S., Tenson, T., and Gerdes, K. (2015). Recent functional insights into the role of (p)ppGpp in bacterial physiology. *Nat. Rev. Microbiol.* 13, 298–309. doi:10.1038/nrmicro3448.

Heinemann, M., Basan, M., and Sauer, U. (2020). Implications of initial physiological conditions for bacterial adaptation to changing environments. *Mol. Syst. Biol.* 16, e9965. doi:10.15252/msb.20209965.

Jiang, W., Qiao, J. B., Bentley, G. J., Liu, D., and Zhang, F. (2017). Modular pathway engineering for the microbial production of branched-chain fatty alcohols. *Biotechnol. Biofuels* 10, 1–15. doi:10.1186/s13068-017-0936-4.

Jiang, Y., Chen, B., Duan, C., Sun, B., Yang, J., and Yang, S. (2015). Multigene editing in the *Escherichia coli* genome via the CRISPR-Cas9 system. *Appl. Environ. Microbiol.* 81, 2506–2514. doi:10.1128/AEM.04023-14.

Jõers, A., Kaldalu, N., and Tenson, T. (2010). The frequency of persisters in *Escherichia coli* reflects the kinetics of awakening from dormancy. *J. Bacteriol.* 192, 3379–3384. doi:10.1128/JB.00056-10.

Kirkwood, T. B. L. (2015). Deciphering death: A commentary on Gompertz (1825) 'On the nature of the function expressive of the law of human mortality, and on a new mode of determining the value of life contingencies.' *Philos. Trans. R. Soc. B Biol. Sci.* 370, 20140379. doi:10.1098/rstb.2014.0379.

Kotte, O., Volkmer, B., Radzikowski, J. L., and Heinemann, M. (2014). Phenotypic bistability in *Escherichia coli*'s central carbon metabolism. *Mol. Syst. Biol.* 10, 736. doi:10.15252/msb.20135022.

Lee, T. S., Krupa, R. A., Zhang, F., Hajimorad, M., Holtz, W. J., Prasad, N., et al. (2011). BglBrick vectors and datasheets: A synthetic biology platform for gene expression. *J. Biol. Eng.* 5, 15–17. doi:10.1186/1754-1611-5-12.

Levin-Reisman, I., Ronin, I., Gefen, O., Braniss, I., Shoresh, N., and Balaban, N. Q. (2017).

Antibiotic tolerance facilitates the evolution of resistance. *Science* 355, 826–830. doi:10.1126/science.aaj2191.

Liu, D., and Zhang, F. (2018). Metabolic feedback circuits provide rapid control of metabolite dynamics. *ACS Synth. Biol.* 7, 347–356. doi:10.1021/acssynbio.7b00342.

Liu, J., Gefen, O., Ronin, I., Bar-Meir, M., and Balaban, N. Q. (2020). Effect of tolerance on the evolution of antibiotic resistance under drug combinations. *Science* 367, 200–204. doi:10.1126/science.aay3041.

Lopatkin, A. J., Bening, S. C., Manson, A. L., Stokes, J. M., Kohanski, M. A., Badran, A. H., et al. (2021). Clinically relevant mutations in core metabolic genes confer antibiotic resistance. *Science* 371, eaba0862. doi:10.1126/science.aba0862.

Lopatkin, A. J., Stokes, J. M., Zheng, E. J., Yang, J. H., Takahashi, M. K., You, L., et al. (2019). Bacterial metabolic state more accurately predicts antibiotic lethality than growth rate. *Nat. Microbiol.* 4, 2109–2117. doi:10.1038/s41564-019-0536-0.

Lorca, G. L., Ezersky, A., Lunin, V. V., Walker, J. R., Altamentova, S., Evdokimova, E., et al. (2007). Glyoxylate and pyruvate are antagonistic effectors of the *Escherichia coli* IclR transcriptional regulator. *J. Biol. Chem.* 282, 16476–16491. doi:10.1074/jbc.M610838200.

Mannan, A. A., and Bates, D. G. (2021). Designing an irreversible metabolic switch for scalable induction of microbial chemical production. *Nat. Commun.* 12, 3419. doi:10.1038/s41467-021-23606-x.

Manuse, S., Shan, Y., Canas-Duarte, S. J., Bakshi, S., Sun, W.-S., Mori, H., et al. (2021). Bacterial persisters are a stochastically formed subpopulation of low-energy cells. *PLOS Biol.* 19, e3001194. doi:10.1371/journal.pbio.3001194.

Megerle, J. A., Fritz, G., Gerland, U., Jung, K., and Rädler, J. O. (2008). Timing and dynamics of single cell gene expression in the arabinose utilization system. *Biophys. J.* 95, 2103–2115. doi: 10.1529/biophysj.107.127191.

Meylan, S., Andrews, I. W., and Collins, J. J. (2018). Targeting antibiotic tolerance, pathogen by pathogen. *Cell* 172, 1228–1238. doi:10.1016/j.cell.2018.01.037.

Morrison, J. M., Chojnacki, M., Fadrowski, J. J., Bauza, C., Dunman, P. M., Dudas, R. A., et al. (2020). Serum-associated antibiotic tolerance in pediatric clinical isolates of *Pseudomonas aeruginosa*. *J. Pediatric Infect. Dis. Soc.* 9, 671–679. doi:10.1093/jpids/piz094.

Mulcahy, L. R., Burns, J. L., Lory, S., and Lewis, K. (2010). Emergence of *Pseudomonas aeruginosa* strains producing high levels of persister cells in patients with cystic fibrosis. *J. Bacteriol.* 192, 6191–6199. doi:10.1128/JB.01651-09.

Nyström, T. (2004). Stationary-phase physiology. *Annu. Rev. Microbiol.* 58, 161–181.

doi:10.1146/annurev.micro.58.030603.123818.

Ojha, A. K., Baughn, A. D., Sambandan, D., Hsu, T., Trivelli, X., Guerardel, Y., et al. (2008). Growth of *Mycobacterium tuberculosis* biofilms containing free mycolic acids and harbouring drug-tolerant bacteria. *Mol. Microbiol.* 69, 164–174. doi:10.1111/j.1365-2958.2008.06274.x.

Orman, M. A., and Brynildsen, M. P. (2015). Inhibition of stationary phase respiration impairs persister formation in *E. coli*. *Nat. Commun.* 6, 7983. doi:10.1038/ncomms8983.

Ozbudak, E. M., Thattai, M., Lim, H. N., Shraiman, B. I., and van Oudenaarden, A. (2004). Multistability in the lactose utilization network of *Escherichia coli*. *Nature* 427, 737–740. doi:10.1038/nature02298.

Pan, X., Fan, Z., Chen, L., Liu, C., Bai, F., Wei, Y., et al. (2020). PvrA is a novel regulator that contributes to *Pseudomonas aeruginosa* pathogenesis by controlling bacterial utilization of long chain fatty acids. *Nucleic Acids Res.* 48, 5967–5985. doi:10.1093/nar/gkaa377.

Pifer, R., Russell, R. M., Kumar, A., Curtis, M. M., and Sperandio, V. (2018). Redox, amino acid, and fatty acid metabolism intersect with bacterial virulence in the gut. *Proc. Natl. Acad. Sci.* 115, E10712–E10719. doi:10.1073/pnas.1813451115.

Radzikowski, J. L., Schramke, H., and Heinemann, M. (2017). Bacterial persistence from a system-level perspective. *Curr. Opin. Biotechnol.* 46, 98–105. doi:10.1016/j.copbio.2017.02.012.

Radzikowski, J. L., Vedelaar, S., Siegel, D., Ortega, Á. D., Schmidt, A., and Heinemann, M. (2016). Bacterial persistence is an active σ^S stress response to metabolic flux limitation. *Mol. Syst. Biol.* 12, 882. doi:10.15252/msb.20166998.

Said-Salman, I. H., Jebaii, F. A., Yusef, H. H., and Moustafa, M. E. (2019). Global gene expression analysis of *Escherichia coli* K-12 DH5α after exposure to 2.4 GHz wireless fidelity radiation. *Sci. Rep.* 9, 14425. doi:10.1038/s41598-019-51046-7.

Schmitz, A. C., Hartline, C. J., and Zhang, F. (2017). Engineering microbial metabolite dynamics and heterogeneity. *Biotechnol. J.* 12, 1700422. doi:10.1002/biot.201700422.

Shah, D., Zhang, Z., Khodursky, A. B., Kaldalu, N., Kurg, K., and Lewis, K. (2006). Persisters: A distinct physiological state of *E. coli*. *BMC Microbiol.* 6, 53. doi:10.1186/1471-2180-6-53.

Shan, Y., Brown Gandt, A., Rowe, S. E., Deisinger, J. P., Conlon, B. P., and Lewis, K. (2017). ATP-Dependent Persister Formation in Escherichia coli. *MBio* 8, e02267-16. doi:10.1128/mBio.02267-16.

Song, S., and Park, C. (1997). Organization and regulation of the D-xylose operons in

Escherichia coli K-12: XylR acts as a transcriptional activator. *J. Bacteriol.* 179, 7025–7032. doi:10.1128/jb.179.22.7025-7032.1997.

Stokes, J. M., Lopatkin, A. J., Lobritz, M. A., and Collins, J. J. (2019). Bacterial metabolism and antibiotic efficacy. *Cell Metab.* 30, 251–259. doi:10.1016/j.cmet.2019.06.009.

Svenningsen, M. S., Veress, A., Harms, A., Mitarai, N., and Semsey, S. (2019). Birth and resuscitation of (p)ppGpp induced antibiotic tolerant persister cells. *Sci. Rep.* 9, 6056. doi:10.1038/s41598-019-42403-7.

Talebi Bezmin Abadi, A., Rizvanov, A. A., Haertlé, T., and Blatt, N. L. (2019). World Health Organization report: Current crisis of antibiotic resistance. *Bionanoscience* 9, 778–788. doi:10.1007/s12668-019-00658-4.

Van Boxtel, C., Van Heerden, J. H., Nordholt, N., Schmidt, P., and Bruggeman, F. J. (2017). Taking chances and making mistakes: Non-genetic phenotypic heterogeneity and its consequences for surviving in dynamic environments. *J. R. Soc. Interface* 14, 20170141. doi:10.1098/rsif.2017.0141.

Weissenborn, D. L., Wittekindt, N., and Larson, T. J. (1992). Structure and regulation of the *glpFK* operon encoding glycerol diffusion facilitator and glycerol kinase of *Escherichia coli* K-12. *J. Biol. Chem.* 267, 6122–6131. doi:10.1016/S0021-9258(18)42670-1.

Windels, E. M., Michiels, J. E., Fauvart, M., Wenseleers, T., Van den Bergh, B., and Michiels, J. (2019). Bacterial persistence promotes the evolution of antibiotic resistance by increasing survival and mutation rates. *ISME J.* 13, 1239–1251. doi:10.1038/s41396-019-0344-9.

Xiao, Y., Bowen, C. H., Liu, D., and Zhang, F. (2016). Exploiting nongenetic cell-to-cell variation for enhanced biosynthesis. *Nat. Chem. Biol.* 12, 339–344. doi:10.1038/nchembio.2046.

Zampieri, M., Enke, T., Chubukov, V., Ricci, V., Piddock, L., and Sauer, U. (2017). Metabolic constraints on the evolution of antibiotic resistance. *Mol. Syst. Biol.* 13, 917. doi:10.15252/msb.20167028.

Zhang, F., Carothers, J. M., and Keasling, J. D. (2012). Design of a dynamic sensor-regulator system for production of chemicals and fuels derived from fatty acids. *Nat. Biotechnol.* 30, 354–359. doi:10.1038/nbt.2149.

Zwietering, M. H., Jongenburger, I., Rombouts, F. M., and van 't Riet, K. (1990). Modeling of the Bacterial Growth Curve. *Appl. Environ. Microbiol.* 56, 1875–1881. doi:10.1128/aem.56.6.1875-1881.1990.

Chapter 5: Conclusions and Future Directions

5.1 Conclusions

Metabolite dynamics and heterogeneity are two concepts which are gaining acceptance as critical considerations in the design of engineered metabolic systems for producing commodity chemicals (Schmitz et al., 2017; Hartline et al., 2021). Microbiologists have long understood the significance of metabolic control systems in natural microbes, since the discovery of the lactose inducible promoter in *E. coli* (Jacob and Monod, 1961). Despite this long history of deciphering the molecular interactions involved in the control of metabolism, our ability to quantitatively characterize systemic features arising from these interactions and to design new systems has been limited. As such, only 53 examples of engineered dynamic control in metabolic engineering were identified from the year 2000 to 2020 (Hartline et al., 2021). This dissertation expands the details of how the regulatory architectures and parameters of metabolic control systems combine to affect metabolite dynamics and heterogeneity, with a particular focus on the FA system in *E. coli*.

In Chapter 2, we dissected the role of regulatory architecture and parameters on recovering pathway shutdown after a nutrient becomes depleted. Based on modeling and experimental results, we uncovered the importance of maintaining and releasing a pool of sequestered TF in actuating recovery. Our results show that negative autoregulation is a superior architecture for achieving fast recovery with lower overall resource usage. This suggests a potential reason why many metabolites uptake positive feedback loops incorporate negative autoregulation of the TF. The work elucidates the tunable parameters and the constraints of regulatory architecture for controlling pathway recovery in the design of metabolite uptake systems, which can be used in metabolic engineering and metabolite sensing applications.

In Chapter 3, we explored how changes in cell growth rate due to changing nutrient conditions affect the minimum, maximum, and dynamic range (DR) of MRTF-based biosensors. Our modeling results show how the growth dependence of DR is related to the biosensor's parameters, and to the transport mechanism of the sensed metabolite. Our results show that dynamic range and its growth rate sensitivity are deeply coupled in due to their parameters, which is a previously unknown design constrain in the engineering of MRTF-based biosensors. Since MRTF-based biosensors are a critical component of engineered metabolic control systems, these results highlight new considerations, and provide quantitative modeling approaches in the design of such systems for use in different nutrient and growth environments.

Finally, in Chapter 4, we explored how positive feedback in nutrient uptake contributes to β-lactam antibiotic tolerance after rapid nutrient shifts to FA. Our results show that both before and after shifts to FA, there is apparently only a single population of cells which adapts to FA utilization. During the adaptation period, cells are tolerant to killing by β-lactams. This tolerance disappears for a majority of the population after the transient tolerance time, which is strongly correlated with the timing of FadD production in the positive feedback loop. This study revealed that positive feedback loops can control the timing of adaptation to nutrient sources and antibiotic tolerance, without necessarily triggering persistence in these cells. These results shed new light on persistence mechanisms during switching nutrient environments and suggests potential treatment methods.

5.2 Future Directions

This dissertation uncovers several new design principles for controlling metabolite dynamics and heterogeneity at the transcription level through MRTFs. To uncover these design principles, we took a combination of synthetic biology methods and modeling. These results highlight new research directions which can be addressed to expand the applicability of this work to new systems.

5.2.1 Synthetic Biology Parts Design for Enhanced Metabolic Control Systems

From synthetic biology perspective, we were able to tune the architecture of the system by replacing native promoters with engineered promoters with different regulatory logic to experimentally test the impact on metabolite dynamics, for example in Chapter 2. These parts with altered logic were derived from native FadR-regulated promoters, such as FabA, or from random rearmament of FadR-regulatory sites to inactivate them. Although this approach successfully changes the regulatory logic, the parameters of the system were also significantly altered, thus requiring more tuning to get the parameters to be comparable between systems. This was particularly noticeable in Chapters 2 and 3, where replacement of the native FadR promoter with a positive autoregulation (Chapter 2) or constitutive regulation (Chapter 3) lead to a significant loss of repression on controlled promoters (P_{FadD} and P_{AR}). In both cases, we solved the problem by introducing extra copies of the re-wired *fadR* on a plasmid to increase FadR levels, which added further complexity to the experiments. Additionally in Chapter 4, it would be interesting to tune the system into the bistable region by replacing the FadD promoter. This experiment was attempted, but ultimately failed because a promoter with suitable parameters could not be easily found. Advancements in methods to predict promoter strength (Zhao et al., 2022) and RBS strength (Salis et al., 2009) directly from sequence are being explored, but current methods often make inaccurate predictions for native promoters, and fail to capture the impact of regulators. The use

of libraries with a range of parameter strengths could be useful but selecting out the correct ones from the library is labor intensive. Thus, having the ability to quickly engineer novel promoters with appropriate and tunable parameters would significantly accelerate research in the control of metabolite dynamics and heterogeneity. Additionally, fine tuning the parameters of a control system is necessary for their function in metabolic engineering (Stevens and Carothers, 2015; Liu et al., 2018), so rapid parameter tuning will be a critical advancement for this field.

In these studies, we took advantage of the fact that FadR acts as both a positive and negative regulator of gene expression in some contexts. However, few TF have this capability without extensive engineering, and many TF act repressively in the absence of a metabolite (Brautaset et al., 2009; Shong et al., 2013). While our work shows that negative autoregulation is beneficial for rapid pathway shutdown (Chapter 2), our results along with more recent modeling also shows that positive autoregulation can be useful for purposely generating a slow response in for metabolic engineering applications (Mannan and Bates, 2021). In these cases, a positively autoregulating transcription factor needs to be identified. Thus, more research into protein engineering to turn negative regulators into positive regulators can benefit the design of metabolic control systems with appropriate dynamics.

5.2.2 Quantitative Design Algorithms for Metabolic Control Systems

In this work, we used mathematical modeling to elucidate design constraints and advantages of regulatory architecture and parameters. These models where generally small in scale, containing only a few differential equations with limited interactions between components. This approach helped to abstract molecular details of the system and yet still provided good agreement in trends between experiment and data. However, future models of metabolic control systems will benefit by incorporating more interactions between the control system and

metabolism, for example by modeling the effects of burden on control system components and the role of the sensed metabolite as a carbon and energy source in the metabolic network. Incorporating these interactions may help models to achieve better numerical accuracy to experimental data, which will be very important in both the design of novel control systems and in understanding the advantages of different control systems. Thus, algorithms which both capture these details, yet maintain the simplicity and abstraction of small-scale models should enable better designs and understanding of metabolic control.

For the FadR system, our work focused primarily on the interactions between FadR, acyl-CoA and FadD in the metabolite uptake positive feedback loop. However, FadR has many interesting regulatory roles including in central metabolism, FA biosynthesis, stress response, and virulence. Additionally, other regulations play an important role in regulating FA catabolism dynamics. For example, experiments in Chapter 4 revealed that the IclR-*aceB*-glyoxylate positive feedback loop affected the dynamics of the FadR-*fadD*-acyl-CoA feedback loop though some global coordinating mechanism. Additionally, although the kinetics of nutrient switches could be broadly captured with a single transient tolerance time, many cells maintain tolerance for a much longer duration. Understanding these persister cells will require modeling of heterogeneity in the system. Thus, there remains much research to understand the dynamics and heterogeneity of FadR and FAs in the context of these many global interactions, and more complex models will be necessary to capture these dynamics.

5.2.3 Metabolic Control Systems in Control of Antibiotic Persistence

This dissertation revealed that transitions from gluconeogenic carbon to FA produce a transient tolerance to β-lactam antibiotics. These results raise several questions about the role of metabolism in persistence. First, a prevalent view of metabolic persistence holds that carbon

starvation and flux limitation in central metabolism triggers ppGpp synthesis (Gaca et al., 2015), which can further trigger persistence in cells (Radzikowski et al., 2017; Wood and Song, 2020). The transient tolerant cells similarly face a strong metabolic perturbation, which is sufficient to cease cell wall biosynthesis (the primary target of β-lactam activity) yet is insufficient to completely inhibit transcription and translation. Given these results, it would be interesting to understand the role of ppGpp and other stress response mechanisms in transient tolerance, and its relation to the metabolic signals necessary to generate "*bona fide* persistence" (Radzikowski et al., 2016; Song and Wood, 2021). Second, previous reports claim bistability is an important mechanism in maintenance of persistence after a flux limitation. We did not observe bistability in FA metabolism, instead seeing only a single population before and after the switch. Thus, bistability may still paly a role in the difference between transient tolerance and persistence. Methods for quickly tuning the control system in the appropriate range can help tune bistability and potentially the length of transient tolerance or degree of persistence, which could have use in synthetic biology or metabolic engineering. Finally, this dissertation focused on β-lactam antibiotics in transient tolerance. Our results show that transcription and translation are active during FA nutrient shifts, which suggests these could be targeted by antibiotics. It would be interesting to see if different classes of antibiotic generate different killing kinetics, which would provide a useful tool in understanding the coordinated control of different biosynthetic and catabolic pathways during nutrient shifts. The work in this dissertation highlights the many avenues for research in understand the connection between metabolite dynamics, heterogeneity, and antibiotic tolerance.

5.3 Chapter 5 References

Brautaset, T., Lale, R., and Valla, S. (2009). Positively regulated bacterial expression systems. *Microb. Biotechnol.* 2, 15–30. doi:10.1111/j.1751-7915.2008.00048.x.

Gaca, A. O., Colomer-Winter, C., and Lemos, J. A. (2015). Many means to a common end: The intricacies of (p)ppGpp metabolism and its control of bacterial homeostasis. *J. Bacteriol.* 197, 1146–1156. doi:10.1128/JB.02577-14.

Hartline, C. J., Schmitz, A. C., Han, Y., and Zhang, F. (2021). Dynamic control in metabolic engineering: Theories, tools, and applications. *Metab. Eng.* 63, 126–140. doi:10.1016/j.ymben.2020.08.015.

Jacob, F., and Monod, J. (1961). Genetic regulatory mechanisms in the synthesis of proteins. *J. Mol. Biol.* 3, 318–356.

Liu, D., Mannan, A. A., Han, Y., Oyarzún, D. A., and Zhang, F. (2018). Dynamic metabolic control: Towards precision engineering of metabolism. *J. Ind. Microbiol. Biotechnol.* 45, 535–543. doi:10.1007/s10295-018-2013-9.

Mannan, A. A., and Bates, D. G. (2021). Designing an irreversible metabolic switch for scalable induction of microbial chemical production. *Nat. Commun.* 12, 3419. doi:10.1038/s41467-021-23606-x.

Radzikowski, J. L., Schramke, H., and Heinemann, M. (2017). Bacterial persistence from a system-level perspective. *Curr. Opin. Biotechnol.* 46, 98–105. doi:10.1016/j.copbio.2017.02.012.

Radzikowski, J. L., Vedelaar, S., Siegel, D., Ortega, Á. D., Schmidt, A., and Heinemann, M. (2016). Bacterial persistence is an active σ^S stress response to metabolic flux limitation. *Mol. Syst. Biol.* 12, 882. doi:10.15252/msb.20166998.

Salis, H. M., Mirsky, E. A., and Voigt, C. A. (2009). Automated design of synthetic ribosome binding sites to control protein expression. *Nat. Biotechnol.* 27, 946–950. doi:10.1038/nbt.1568.

Schmitz, A. C., Hartline, C. J., and Zhang, F. (2017). Engineering microbial metabolite dynamics and heterogeneity. *Biotechnol. J.* 12, 1700422. doi:10.1002/biot.201700422.

Shong, J., Huang, Y.-M., Bystroff, C., and Collins, C. H. (2013). Directed evolution of the quorum-sensing regulator esar for increased signal sensitivity. *ACS Chem. Biol.* 8, 789–795. doi:10.1021/cb3006402.

Song, S., and Wood, T. K. (2021). Are we really studying persister cells? *Environ. Microbiol. Rep.* 13, 3–7. doi:10.1111/1758-2229.12849.

Stevens, J. T., and Carothers, J. M. (2015). Designing RNA-based genetic control systems for efficient production from engineered metabolic pathways. *ACS Synth. Biol.* 4, 107–115. doi:10.1021/sb400201u.

Wood, T. K., and Song, S. (2020). Forming and waking dormant cells: The ppGpp ribosome

dimerization persister model. *Biofilm* 2, 100018. doi:10.1016/j.bioflm.2019.100018.

Zhao, M., Yuan, Z., Wu, L., Zhou, S., and Deng, Y. (2022). Precise prediction of promoter strength based on a de novo synthetic promoter library coupled with machine learning. *ACS Synth. Biol.* 11, 92–102. doi:10.1021/acssynbio.1c00117.

Appendix A: Supplemental Information for "Metabolite sequestration enables rapid recovery from fatty acid depletion in *Escherichia coli*"

Appendix A contains supplemental information for Chapter 2.

A.1. Nutrient Uptake Systems in *Escherichia coli*

Table A.1. Nutrient uptake systems in *Escherichia coli*. List of metabolite-responsive transcription factors (TF) that control expression of nutrient uptake enzymes in *Escherichia coli*, taken from EcoCyc (Keseler et al., 2017). All these systems follow the schematic in Figure. 2.1A.

TF	Name	TF autoregulation	Operon inhibited by TF	Sequestering metabolite
ArsR	Arsenate inducibility regulator	Negative	arsB, from arsRBC operon	Arsenite / Antimonite ion
AlsR	Allose utilization regulator	Negative	alsABC, from alsRBACE operon	D-allose
BetI	Betaine Inhibitor	Negative	betT	Choline
ChbR	Chitobiose regulator	Negative	chbBCA from chbBCARFG operon	N,N'-diacetylchitobiose 6-phosphate
CytR	Cytidine regulator	Negative	nupC and nupG	Cytidine
FadR	Fatty acid degradation regulon	Negative	fadD	Acyl-CoA
GntR	Gluconate repressor	None, constitutive	gntT, gntU	D-Gluconate
LacI	Lactose inhibitor	None, constitutive	lacZYA	Allolactose
LldR	Lactate regulator	Negative	lldP, from lldPRD operon	S-lactate

LsrR	Quorum sensing system	Negative	lsrACDB operon	AI-2 (autoinducer)
NagC	N-acetylglucosamine transcriptional regulator	Negative	chbF, from chbBCARFG operon	Acetyl-D-glucosamine 6-phosphate
NanR	N-acetyl-neuraminic acid regulator	None, constitutive	nanT, from nanATEK-yhcH operon	N-acetylneuraminate
PaaX	Phenylacetic acid regulator	Negative	paaK, from paa operon	Phenylacetyl-CoA
PuuR	Putrescine utilization and transport regulator	Negative	puuP, from puuAP operon	Putrescine
RbsR	Ribose repressor	Negative	rbsACB, from rbs operon	D-ribose
SrlR	Glucitol Repressor	Negative	srlAEB, from srlAEBD-gutM-slrR-gutQ operon	D-sorbitol
TreR	Trehalose repressor	None, constitutive	treB, from treBC operon	Trehalose 6-phosphate
UlaR	Utilization of l-ascorbic acid repressor	None, constitutive	ulaABC, from ulaABCDEF operon	L-ascorbate 6-phosphate

A.2. Kinetic Model of Fatty Acid Uptake

To model the system in Figure 2.1B, we use the kinetic model:

$$\frac{dR}{dt} = P_R(R, p_r) - S - \mu \cdot R, \quad \text{(Eq. A1)}$$

$$\frac{dD}{dt} = b_D + \frac{a_D}{1+(K_D \cdot R)^{n_D}} - \mu \cdot D, \quad \text{(Eq. A2)}$$

$$\frac{dA}{dt} = \frac{k_{cat,D} \cdot \mathrm{OA}}{K_{m,D}+\mathrm{OA}} \cdot D - \frac{k_{cat,B} \cdot A}{K_{m,B}+A} \cdot B - 2 \cdot S - \mu \cdot A, \quad \text{(Eq. A3)}$$

$$\frac{d\,\mathrm{sR}}{dt} = S - \mu \cdot \mathrm{sR}, \quad \text{(Eq. A4)}$$

$$S = k_f \cdot R \cdot A^2 - k_r \cdot \mathrm{sR}, \quad \text{(Eq. A5)}$$

where *R, D, A* and *sR* represent the concentrations of transcription factor FadR, uptake enzyme FadD, internalized fatty acyl-CoA and sequestered acyl-CoA-FadR complex, respectively (Figure 2.1B). During inducting, two molecules of acyl-CoA bind to sequester 1 dimer of FadR (van Aalten et al., 2000). We model this reversible binding as mass-action kinetics (Eq. A5). The term $P_R(R, p_r)$ represents the expression and autoregulation of the *fadR* promoter. To model TF expression when under negative autoregulation (*n*), positive autoregulation (*p*) or constitutive expression (*c*), we write

$$P_{R,n} = b_n + \frac{a_n}{1+(K_n \cdot R)^{n_R}}, \quad \text{(Eq. A6)}$$

$$P_{R,p} = b_p + \frac{a_p \cdot (K_p \cdot R)^{n_R}}{1+(K_p \cdot R)^{n_R}}, \quad \text{(Eq. A7)}$$

$$P_{R,c} = p_c, \quad \text{(Eq. A8)}$$

respectively. We can use the model to simulate growth in continuous culture by fixing oleic acid concentration (OA) in Eq. A3. Model parameters can be found in Table A.2.

Table A.2. Model parameters for kinetic model of fatty acid uptake.

Parameter	b_R	a_R	K_R	n_R
Description	fadR basal exp. rate Units = $\mu M/h$ *(Fitted)*	fadR promoter strength Units = $\mu M/h$ *(Fitted)*	Affinity of FadR for its own promoter Units = $1/\mu M$ *(Fitted)*	Hill coefficient Units = N/A *(Fixed = 1)*
Parameter	b_D	a_D	K_D	n_D
Description	fadD basal exp. rate Units = $\mu M/h$ *(Fitted)*	fadD promoter strength Units = $\mu M/h$ *(Fitted)*	Affinity of FadR for fadD promoter Units = $1/\mu M$ *(Fitted)*	Hill coefficient Units = N/A *(Fixed = 2)*
Parameter	$k_{cat,D}$	$K_{m,D}$	$k_{cat,B}$	$K_{m,B}$
Description	Turnover rate of FadD Units = $1/h$ *(Fitted)*	Michaelis const. for FadD Units = μM *(Fitted)*	Turnover rate of PlsB enzyme Units = $1/h$ *(Fitted)*	Michaelis const. Units = μM *(Fitted)*
Parameter	B	k_f	k_r	μ
Description	Conc. of PlsB enzyme Units = μM *(Fixed = 0.1369)*	Fwd rate of sequestering Units = $1/h$ *(Fitted)*	Reverse rate of sequestering Units = $1/h$ *(Fitted)*	Cell growth rate Units = h^{-1} *(Fitted)*

To fit model parameters, we use time course data from batch cultures induced with titrations of oleic acid, shown in Figure A.1B. We used a red fluorescent protein (RFP) gene placed at 3' of the *fadD* promoter on a low copy number plasmid (pSfadDk-RFP). The plasmid was incorporated to a *fadE* knockout strain to make *ΔfadE*-reporter. The *fadE* knockout strain was chosen to reduce the consumption rate of intracellular acyl-CoA and to simplify the metabolite dynamics for this parameterization purpose. Cells were cultivated in M9 glycerol (M9G) medium, in flasks, to exponential growth phase and induced with varying concentrations of oleic acid. Time

course measurements of cell density (Figure A.1A) and RFP fluorescence (Figure. A.1B) were recorded.

For model fitting we extended the Eqs. (A1) - (A8) with population growth in batch culture:

$$\frac{dX}{dt} = \mu \cdot X, \qquad \text{(Eq. A9)}$$

$$\frac{d\,\mathrm{OA}}{dt} = -\frac{k_{cat,D} \cdot \mathrm{OA}}{K_{m,D} + \mathrm{OA}} \cdot D \cdot X, \qquad \text{(Eq. A10)}$$

with parameters defined in Table S2. We first converted fluorescence values to units of concentration (μM) by assuming that the average fluorescence value in the absence of inducer (dark blue points, Figure A.1B) represents the steady state concentration of FadD reported in, measured in (Schmidt et al., 2016), where cells were grown in the same media as ours (M9G). This gives a conversion factor of 1.12×10^{-4} μM per unit of fluorescence, which was then applied to all fluorescence values; results are in Figure A.1B.

We then performed a weighted least-squares fitting of simulations to the data. We define $D_i(t,p)$ and $\bar{d}_i(t)$ as the simulated and average measured FadD concentration (from three biological replicates), at time t, from the i^{th} time series. The index $i = 1, \ldots, 9$ refers to the time course when induced with oleic acid = 0, 0.4, 1, 4, 10, 40, 100, 400, and 1000 μM respectively. Fitting was performed to find optimal values of model parameters (p) that minimize the cost function

$$C = \sum_{i=1}^{9} \sum_{t=0}^{t_{\text{end}}} \left(\frac{\bar{d}_i(t)}{d_i^{\text{SEM}}(t)} \right) \cdot \left(\frac{D_i(t,p) - \bar{d}_i(t)}{\max_t(\bar{d}_i(t))} \right)^2, \qquad \text{(Eq. A11)}$$

given constraints

$$\mathrm{LB} \leq p \leq \mathrm{UB}, \qquad \text{(Eq. A12)}$$

where LB and UB are lower and upper bounds on the parameter search space. The term $d_{i,t}^{\mathrm{SEM}}$ is the standard error measured from triplicate data. The term $\frac{\bar{d}_i(t)}{d_i^{\mathrm{SEM}}(t)}$ in Eq. A11 ensures that the difference between simulation and data at each time point is weighted by the inverse of the relative standard error. This increases the weight of those contributions to the cost where data has a lower measured error. We optimized parameters with a two-step approach. We first used a genetic algorithm (GA) from the Global Optimization toolbox in MATLAB 2018a to find a candidate for a global minimum (using 200 generations of the GA), and then to initialize the solver fmincon and perform a local optimization using the same cost function (Eq. A11). Fitting was performed independently 100 times; results are shown in Figure A.1B, and summary statistics of parameter values are given in Table A.3.

Growth rates (μ) were estimated through a least-squares fitting of the measured optical densities in Figure A.1A to the exponential function:

$$h(t) = h_0 \cdot e^{\mu t}. \qquad \text{(Eq. A13)}$$

To understand the impact of each model parameter on the recovery time, we conducted global parameter sensitivity analysis; see Appendix A.8 for details.

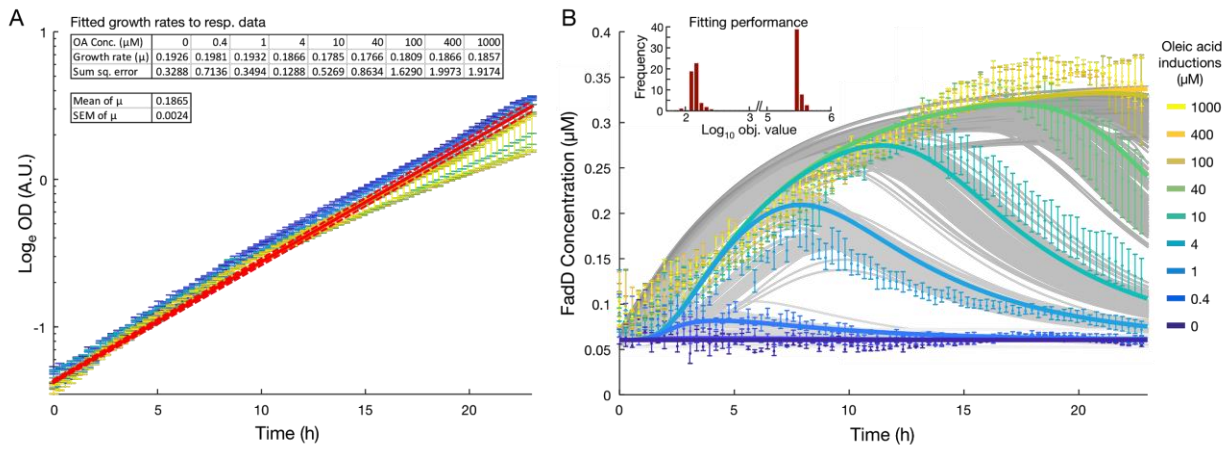

Figure A.1. Fitting model to data. (A) Plot of time series data of measured optical density (OD), in log scale, during growth in media induced with titrations of oleic acid. Values of the fitted growth rate to each data series is given inset, including average growth rate (based on all data series) used to in the model; modelled growth shown in red line, ± SEM in red dashed lines. **(B)** Ensemble of 100 independent fits (grey curves) and the optimal fit (coloured curves) of simulations to time course data (point with error bars), after converting fluorescence values to concentration. Error bars in data represent SEM from biological triplicates (n = 3). Fitting performance in inset.

Table A.3. Results of parameter fitting. Optimal parameter values together with search bounds and summary statistics for 100 independent fits. The bounds on growth rate, μ, are based on ± two times the SEM from data (shown in Figure A.1A, inset). Hill coefficients are fixed to n_R=1 and n_D=2, based on the number of FadR binding sites on the fadR and fadD promoters. Concentration of PlsB is fixed to 0.1369 μM, as taken from (Schmidt et al., 2016).

Parameters	Optimal	Bounds of GA		Summary Statistics			
		Lower bound	Upper bound	Average	Median	SD	CV
μ	0.1818	0.1817	0.1913	0.1854	0.1840	0.0036	1.9172%
b_R	0.0007	1.00E-06	0.0600	0.0210	0.0173	0.0140	66.7954%
a_R	0.0131	1.00E-06	0.1500	0.0414	0.0343	0.0343	82.8857%
K_R	4.3222	1.00E-03	100.0000	27.1436	22.9710	21.3182	78.5385%
n_R	1.0000	-	-	-	-	-	-
b_D	0.0108	1.00E-06	0.1000	0.0108	0.0112	0.0015	13.5842%
a_D	0.0517	1.00E-06	0.1000	0.0486	0.0484	0.0021	4.4003%
K_D	305.9500	1.00E-03	750.0000	267.2850	215.9050	201.6395	75.4399%
n_D	2.0000	-	-	-	-	-	-
k_{catD}	49.0000	1.00E-06	27,000.0	12,364.4	12,817.5	7,610.1	61.5483%
Km_D	0.0672	1.00E-02	650.0000	173.6743	149.1950	128.8831	74.2096%
k_{catB}	192.9100	1.00E-06	620.0000	235.0742	214.5650	160.4516	68.2557%
Km_B	45,429.0	1.00E-02	50,000.0	29,547.0	31,923.5	12,371.9	41.8719%
PlsB	0.1369	-	-	-	-	-	-
k_f	612.5500	1.00E-06	625.0000	409.3018	446.6350	174.9435	42.7419%
k_r	900.7300	1.00E-06	3,200.0	844.9572	515.6600	928.0828	109.8378%
Init. Biomass	0.1648	1.00E-02	2.0000	0.2308	0.1521	0.2567	111.2037%
Obj Value	82.0500	-	-	160,209.7	150,475.6	161,591.8	100.8627%

A.3. Impact of the Exposure Time to Nutrient

As seen in Figure A.2, simulations suggest that for small increases in exposure time to oleic acid cause a decrease in recovery time, but for longer times recovery time is increased again. Further analysis of the simulations indicates that for exposure times, acyl-CoA accumulates to higher levels. In the OFF state larger pools of accumulated acyl-CoA take longer to consume, which causes delays in the release of free FadR in the OFF state. We infer that this delays the recovery of FadD, increasing recovery time. We hypothesized that the bottleneck lies in the consumption rate of acyl-CoA, as it is limited by the effective v_{max} of the consuming enzyme kinetics (in our system $v_{max} = k_{cat,B}$PlsB). To computationally test this hypothesis, we increased the concentration of consuming enzyme (PlsB) in the model and found a faster release of free FadR which, in turn, reduced recovery time. Since longer exposure times increase the level of FadR stored in complex (a-R), we also found a general decrease in recovery time.

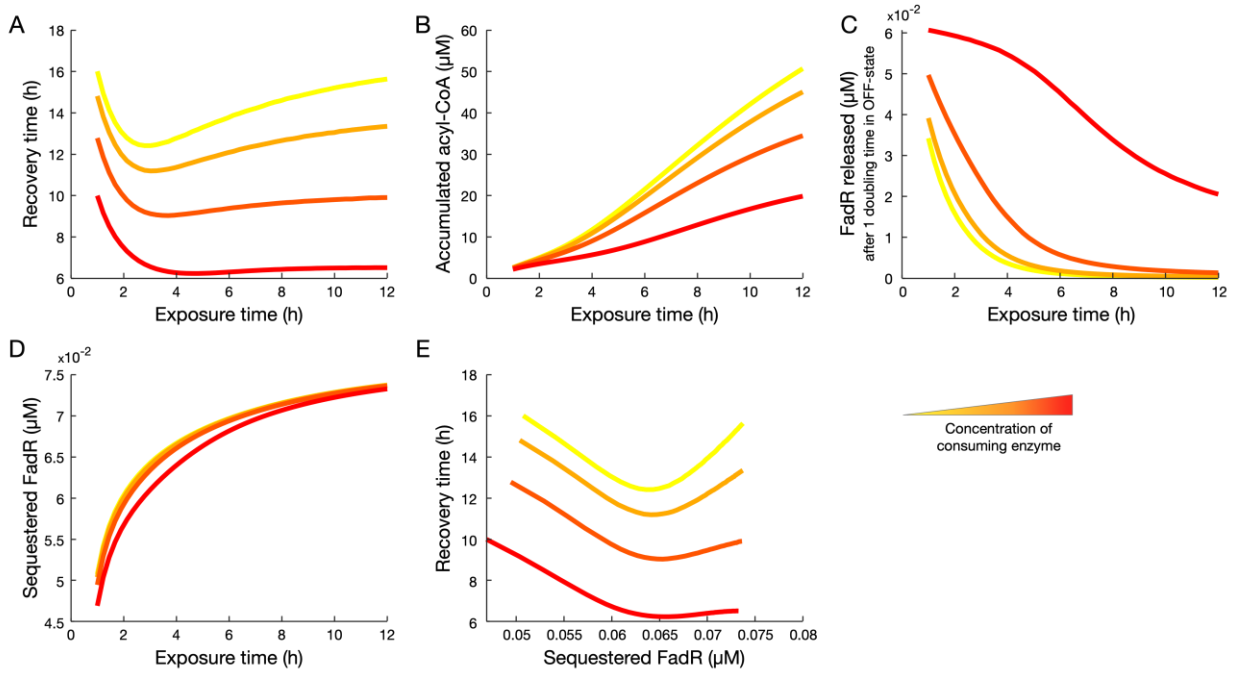

Figure A.2. Exposure time to oleic acid affects accumulated acyl-CoA and recovery time. Colored curves show how the respective relations are affected by increases in the concentration of consuming enzyme.

A.4. Plasmids and Strains Used in This Study

Table A.4. Plasmids used in this study.

Plasmids	Replication Origin	Operon	Resistance	Reference
pSfadDk-RFP	SC101**	P_{fadD}-*rfp*	Kan^R	This Study
pEfadRpoa-fadR	colE1	P_{fadRpo}-*fadR*	Amp^R	This Study
pSfadRpok-rfp	SC101**	P_{fadRpo}-*rfp*	Kan^R	This Study

Table A.5. Strains used in this study.

Strains	Relevant Genotype	Reference
E. coli DH1	F- λ- *supE44 hsdR17 recA1 endA1 gyrA96 thi-1 relA1*	Hanahan 1983
DH1(ΔfadE)	DH1, Δ*fadE*	Steen 2010
WT-reporter	DH1, pSfadDk-RFP	This Study
ΔfadE-reporter	DH1, Δ*fadE*, pSfadDk-RFP	This Study
PA-reporter	*DH1, fadR::*P_{fadRpo}-*fadR*, pSfadDk-RFP, pEfadRpoa-fadR	This Study
PA-FadR reporter	DH1, *fadR::*P_{fadRpo}-*fadR*, pSfadRpok-RFP, pEfadRpoa-fadR	This Study

A.5. Steady State Analysis: Autoregulation Affects FadR Levels During Induction

Here, we ask how the mode of FadR autoregulation affects how the pool of total FadR changes for long exposure times. To quantify this change, we look at the difference in the steady state $\Delta R_{T,ss} = R_{T,ss}^{(I)} - R_{T,ss}^{(0)}$ between the concentration of total FadR achieved in the ON-state ($R_{T,ss}^{(I)}$) to that achieved before induction ($R_{T,ss}^{(0)}$) for each of the three systems (negative autoregulation, positive autoregulation and constitutive expression).

To derive the expression for $\Delta R_{T,ss}$, we define total FadR as $R_{\mathrm{T}} = R + sR$, which from Eq. A1 and A4 follows

$$\frac{dR_{\mathrm{T}}}{dt} = p_R(R,p) - \mu \cdot R_{\mathrm{T}}, \qquad \text{(Eq. A14)}$$

where $p_R(R,p)$ is the FadR synthesis rate as a function of free FadR and parameters, p, defined in Eqs. A6-A8 for each architecture. μ is growth rate and assumed constant before and during the ON state. At steady state Eq. A14 gives

$$R_{T,ss} = \frac{p_R(R_{ss},p)}{\mu}. \qquad \text{(Eq. A15)}$$

We can now write down an expression for $\Delta R_{T,ss}$ as

$$\Delta R_{T,ss} = R_{T,ss}^{(I)} - R_{T,ss}^{(0)} = \frac{p_R(R_{ss}^{(I)},p)}{\mu} - \frac{p_R(R_{ss}^{(0)},p)}{\mu}, \qquad \text{(Eq. A16)}$$

where $R_{ss}^{(0)}$ and $R_{ss}^{(I)}$ are free FadR before induction and during the ON-state, respectively. In general, Eq. A1 at steady state gives

$$0 = p_R(R_{ss}, p) - \mu \cdot R_{ss} - k_f \cdot A_{ss}^2 \cdot R_{ss} + k_r \cdot \mathrm{sR}_{ss}, \qquad \text{(Eq. A17)}$$

where R_{ss}, A_{ss} and sR_{ss} are steady state concentrations of free FadR, acyl-CoA and sequestered FadR, respectively. Before induction, we have that $A_{ss} = 0$ and $\mathrm{sR}_{ss} = 0$ for the three architectures. Substitution into Eq. A17 leads to

$$0 = p_R(R_{ss}^{(0)}, p) - \mu \cdot R_{ss}^{(0)}. \qquad \text{(Eq. A18)}$$

We now substitute Eqs. A6-A8 into Eq. A18 for each mode of autoregulation, to get:

$$R_{ss,c}^{(0)} = \frac{p_c}{\mu} \qquad \text{(Eq. A19)}$$

(constitutive expression)

$$R_{ss,n}^{(0)} = \frac{\left(\frac{K_n b_n}{\mu} - 1\right) + \sqrt{\left(\frac{K_n b_n}{\mu} - 1\right)^2 + 4\frac{K_n}{\mu}(a_n + b_n)}}{2K_n} \qquad \text{(Eq. A20)}$$

(negative autoregulation)

$$R_{ss,p}^{(0)} = \frac{\left(\frac{K_a(a_a + b_a)}{\mu} - 1\right) + \sqrt{\left(\frac{K_a(a_a + b_a)}{\mu} - 1\right)^2 + 4\frac{K_a}{\mu} b_a}}{2K_a} \qquad \text{(Eq. A21)}$$

(positive autoregulation)

To compute the steady state during the ON state, we first solve for *sR* in steady state from Eq. A4 to obtain $\mathrm{sR}_{ss} = \frac{k_f A_{ss}^2 R_{ss}}{k_r + \mu}$, and then substitute into Eq. A17:

$$0 = p_R(R_{ss}, p) - \lambda(A_{ss}) \cdot R_{ss}, \quad \text{(Eq. A22)}$$

where we have defined

$$\lambda = \mu \cdot \left(1 + \frac{k_f A_{ss}^2}{k_r + \mu}\right), \quad \text{(Eq. A23)}$$

We now substitute Eqs. A6-A8 into Eq. A2 for each mode of autoregulation, to get the steady state concentration of $R^{(I)}_{ss}$ for each mode of autoregulation:

$$R^{(I)}_{ss,c} = \frac{p_c}{\lambda} \quad \text{(Eq. A24)}$$

(constitutive expression)

$$R^{(I)}_{ss,n} = \frac{\left(\frac{K_n b_n}{\lambda} - 1\right) + \sqrt{\left(\frac{K_n b_n}{\lambda} - 1\right)^2 + 4\frac{K_n}{\lambda}(a_n + b_n)}}{2K_n} \quad \text{(Eq. A25)}$$

(negative autoregulation)

$$R^{(I)}_{ss,p} = \frac{\left(\frac{K_a(a_a + b_a)}{\lambda} - 1\right) + \sqrt{\left(\frac{K_a(a_a + b_a)}{\lambda} - 1\right)^2 + 4\frac{K_a}{\lambda} b_a}}{2K_a} \quad \text{(Eq. A26)}$$

(positive autoregulation)

We now use the expressions for $R^{(I)}_{ss}$ in Eqs. A19-A21 and for $R^{(0)}_{ss}$ in Eqs. A24-A26 to compute the direction of change in steady state concentration of free FadR. From Eq. A23 we have that $\lambda \geq \mu$ for positive parameters, and therefore:

$$R^{(I)}_{ss,c} - R^{(0)}_{ss,c} \leq 0, \quad \text{(Eq. A27)}$$

$$R^{(I)}_{ss,n} - R^{(0)}_{ss,n} \leq 0, \quad \text{(Eq. A28)}$$

$$R_{ss,p}^{(I)} - R_{ss,p}^{(0)} \leq 0. \quad \text{(Eq. A29)}$$

Therefore, irrespective of the mode of autoregulation, the steady state level of free FadR is always lower in the ON state relative to its steady state level before induction.

We can now return to Eq. A16 to compute the change in total FadR levels for each mode of autoregulation. **For constitutive expression**, substituting Eq. A8 into A16 we get

$$\Delta R_{T,ss,c} = \frac{p_c}{\mu} - \frac{p_c}{\mu} = 0, \quad \text{(Eq. A30)}$$

and therefore, there is no change in the level of total FadR in the ON state, relative to its level before induction.

For negative autoregulation, substitution of Eq. E6 into E16 gives

$$\Delta R_{T,ss,n} = \frac{a_n}{\mu(1+K_n R_{ss,n}^{(I)})} - \frac{a_n}{\mu(1+K_n R_{ss,n}^{(0)})}. \quad \text{(Eq. A31)}$$

Using the relation in Eq. A28, it can be shown that $\Delta R_{T,ss,n} \geq 0$ and therefore the level of total FadR is increased in the ON state, relative to its level before induction.

For positive autoregulation, substitution of Eq. A7 into A16 leads to

$$\Delta R_{T,ss,p} = \frac{a_p K_p R_{ss,p}^{(I)}}{\mu(1+K_p R_{ss,p}^{(I)})} - \frac{a_p K_p R_{ss,p}^{(0)}}{\mu(1+K_p R_{ss,p}^{(0)})}. \quad \text{(Eq. A32)}$$

Using the relation in Eq. A29, it can be shown that $\Delta R_{T,ss,p} \leq 0$ and therefore level of total FadR is decreased in the ON-state, relative to its level before induction.

In summary, we conclude that:

- For constitutive expression there is no change in total FadR and thus the system maintains the level of sequestered FadR during induction.
- For negative autoregulation, total FadR increases and thus the system builds up a larger pool of sequestered FadR during induction.
- For positive autoregulation, total FadR decreases and thus the system loses sequestered FadR during induction.

A.6. Construction and Characterization of Strain with Positively Autoregulated *fadR*

To engineer a strain with a self-activating architecture, a portion of the *fadR* promoter sequence, including the -10, -35 and the *fadR* operator sites were replaced with a sequence originating from the promoter of the *fabA* gene, which is positively regulated by FadR. To alter the genome sequence, we utilized pTarget-pCas genome editing system. The original promoter sequence and the engineered promoter (P_{fadRpo}) sequence are show in Table A.6. To enhance the expression of the FadR, we placed a plasmid copy of the positively regulated *fadR*, P_{fadRpo}-fadR, in a ColE1 origin plasmid. The positively autoregulated reporter strain (named "PA reporter") was then created by transforming the pSfadDk-RFP reporter plasmid (Table A4, Table A5).

To confirm the self-activation of *fadR*, we measured the dose-response of the engineered P_{fadRpo} promoter. A *rfp* gene with a strong ribosome binding site (RBS) was cloned to the 3' of the P_{fadRpo} promoter in a BglBrick plasmid (pSfadRpok-rfp). The engineered promoter and RBS sequences are shown in Table A.6. To measure dose-response output, PA-FadR reporter strain was grown in M9G with oleic acid concentrations = 0, 0.4, 1, 4, 10, 40, 100, 400 and 1000 μM. Cells were grown in a plate reader. Cell culture absorbance and RFP fluorescence were measured. Cultures were initially started at OD_{600} = 0.001 and were allowed to reach steady state. Measurements for each culture condition were made in triplicate. Induction with high concentration of oleic acid reduces the output expression from the P_{fadRpo} promoter (Figure A.3A), confirming P_{fadRpo} as a positively autoregulated promoter.

Table A.6. Sequences of engineered promoter with positively autoregulated *fadR*. (A) Native *fadR* promoter sequence, P_{fadR}. Bold lettering indicates FadR operator site, blue lettering indicates coding sequence. **(B)** Positively autoregulated *fadR* promoter, P_{fadRpo}, engineered in this work. The underlined sequence is derived from the *fabA* promoter region of *E. coli* DH1 genome. **(C)** Engineered P_{fadRpo} used to control *rfp* expression.

(A)	CCCTTTTTCTTCTTTTTGTCTGCTATCAGCGTAGTTAGCC**CTCTGGTATGATGAGTCC**AACTTTGTTTT GCTGTGTTATGGAAATCTCACTATGGTCATTAAGGCG
(B)	CCCTTTTTCTTCTTTTTATTCCG**AACTGATCGGACTTGTT**CAGCGTACACGTGTTAGCT ATCCTGCGTCAACTTTGTTTTGCTGTGTTATGGAAATCTCACTATGGTCATTAAGGCG
(C)	CCCTTTTTCTTCTTTTTATTCCG**AACTGATCGGACTTGTT**CAGCGTACACGTGTTAGCTATCCTGCGTCA ACTTTGTTTTGCAGGTTTGTAAATAAAGGAGGGAGAAAGGGTATATGGCGAGTAGCGAA

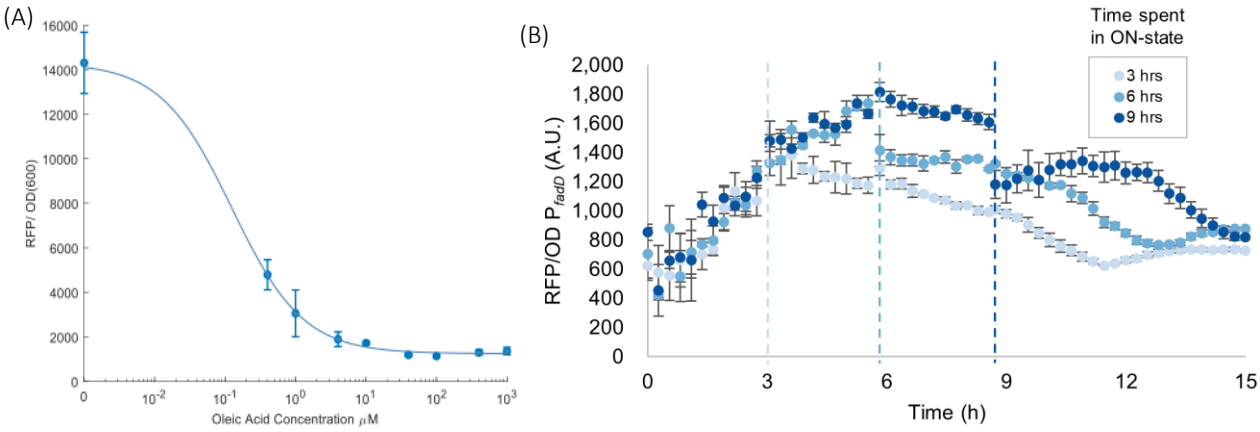

Figure A.3. Characterization and use of PA reporter strain. (A) Dose-response of P_{fadRpo}-rfp indicates FadR activated, and OA inhibited P_{fadRpo} expression. Error bars are SEM for biological replicates (n=3) and blue curve is fit of a hill equation to the mean oleic acid concentrations. **(B)** Time course fluorescence data for the switching experiment of the PA-reporter strain. Cells were induced by 1mM oleic acid at time zero, and grown for three different exposure times, 3, 6, and 9 hours (dashed vertical lines), after which cultures were rapidly switched to fresh media lacking oleic acid (OFF state). Error bars represent the SEM from biological triplicates.

A.7. Steady State Analysis: Promoter Strength Affects Level of Sequestered FadR

For long exposure times, in Section A.4 we have shown that constitutive expression and negative autoregulation can maintain or even build up the concentration of sequestered FadR. Here we study how the mode of autoregulation and parameters shape the steady state level of sR (sR_{ss}) achieved for long exposure times. We recall from the previous section that the steady state of sequestered FadR in the ON state is

$$\mathrm{sR}_{ss} = \frac{k_f \cdot R_{ss} \cdot A_{ss}^2}{k_r+\mu}, \qquad \text{(Eq. A33)}$$

where R_{ss} is given by the formulae in Eq. A24 and A25 for constitutive and negative autoregulation

$$R_{ss,c} = \frac{p_c}{\mu \cdot \left(1+\frac{k_f A_{ss,c}^2}{k_r+\mu}\right)}, \qquad \text{(Eq. A34)}$$

$$R_{ss,n} = \frac{\left(\frac{K_n b_n}{\mu \cdot \left(1+\frac{k_f A_{ss,n}^2}{k_r+\mu}\right)} - 1\right) + \sqrt{\left(\frac{K_n b_n}{\mu \cdot \left(1+\frac{k_f A_{ss,n}^2}{k_r+\mu}\right)} - 1\right)^2 + 4\frac{K_n}{\mu \cdot \left(1+\frac{k_f A_{ss,n}^2}{k_r+\mu}\right)}(a_n+b_n)}}{2K_n}, \qquad \text{(Eq. A35)}$$

respectively. Note that in Eqs. (A34)-(A35) we have substituted the expression for λ given by Eq. A23. Substituting both expressions back into Eq. A33 we get

$$\mathrm{sR}_{ss,c} = \frac{p_c}{\mu} \cdot \frac{k_f A_{ss,c}^2}{k_f A_{ss,c}^2 + k_r + \mu}, \qquad \text{(Eq. A36)}$$

$$\mathrm{sR}_{ss,n} = \frac{k_f}{k_r+\mu} \cdot \frac{1}{2K_n} \cdot \left(\left(\frac{K_n b_n}{\mu\left(\frac{1}{A_{ss,n}^2}+\frac{k_f}{k_r+\mu}\right)} - A_{ss,n}^2 \right) + \sqrt{\left(\frac{K_n b_n}{\mu\left(\frac{1}{A_{ss,n}^2}+\frac{k_f}{k_r+\mu}\right)} - A_{ss,n}^2 \right)^2 + \frac{4A_{ss,n}^2 K_n (a_n+b_n)}{\mu\left(\frac{1}{A_{ss,n}^2}+\frac{k_f}{k_r+\mu}\right)}} \right), \qquad \text{(Eq. A37)}$$

for constitutive expression and negative autoregulation, respectively. To explore how parameters affect sR_{ss} for long exposure time, we consider the scenario when there is a large accumulation of acyl-CoA from high levels of inducer in the media. We therefore approximate sR_{ss} for each system by evaluating Eq. A36 and A37 in the limit $A_{ss} \to \infty$. For constitutive expression we get

$$\lim_{A_{ss,c}\to\infty} \mathrm{sR}_{ss,c} = \frac{p_c}{\mu}. \qquad \text{(Eq. A38)}$$

For negative autoregulation, we further assume that the basal expression of *fadR* promoter is negligible ($b_n = 0$), so that Eq. A37 simplifies to

$$\mathrm{sR}_{ss,n} = \frac{k_f}{k_r+\mu} \cdot \frac{1}{2K_n} \cdot \left(-A_{ss,n}^2 + \sqrt{A_{ss,n}^4 + \frac{4A_{ss,n}^2 K_n a_n}{\mu\left(\frac{1}{A_{ss,n}^2} + \frac{k_f}{k_r+\mu}\right)}} \right), \qquad \text{(Eq. A39)}$$

and thus we obtain

$$\lim_{A_{ss,n}\to\infty} \mathrm{sR}_{ss,n} = \frac{a_n}{\mu}. \qquad \text{(Eq. A40)}$$

In summary, from Eq. A38 and A40 we conclude that in both architectures, sequestered FadR is scaled by the *fadR* promoter strength.

A.8. Sensitivity Analysis of Kinetic Model

We used global sensitivity analysis (GSA) to quantify the impact of model parameters on the recovery time. We performed GSA using the method of extended Fourier amplitude sensitivity test (eFAST) (Saltelli et al., 1999; Marino et al., 2008) . We adapted the MATLAB code reported in (Marino et al., 2008) and implemented eFAST to calculate the first-order and total-order sensitivity indices (Figure A.4). We assumed that each parameter could vary from 0.1- to 10-fold its fitted value, and model output was defined as the recovery time of FadD for the given input parameters. To enable us to determine which parameters the recovery time was statistically and significantly more sensitive to, we adopted the method of adding a dummy parameter to the model (details in (Marino et al., 2008)). This was used to compare to the sensitivities of other model parameters and a 2-tailed *t*-test was performed to test for significance. The parameters with significantly higher sensitivities are highlighted with an asterisk in Figure A.4. The results suggest that recovery time is more sensitive to parameters associated with the sequestering kinetics of FadR by acyl-CoA and the promoter strength of *fadR* promoter. It is also sensitive to the parameters representing the expression and regulation of FadD, but this is expected as it directly affects recovery time.

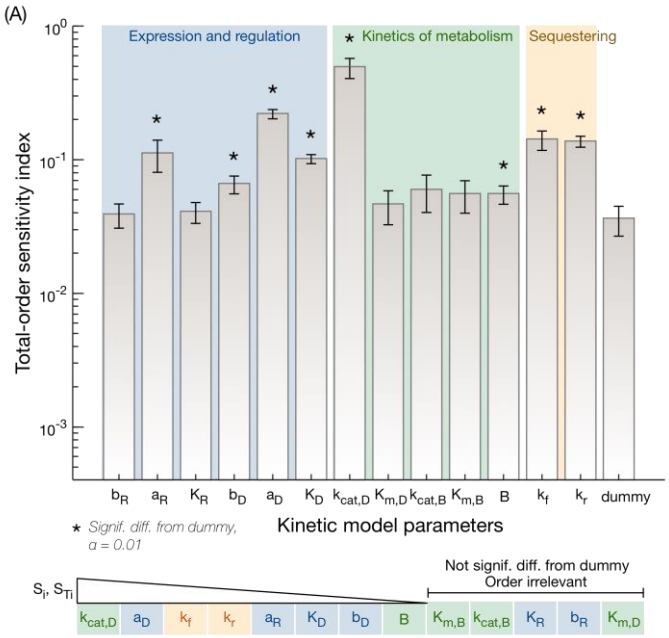

Figure A.4. Global sensitivity analysis of recovery time to model parameters. Bar plot of the total-order sensitivity indices calculated from global sensitivity analysis (GSA) with eFAST. Sensitivities were calculated from 257 samples per search curve (set of parameters), and this sampling was repeated 7 times to ensure coverage of parameter values. Bars and error-bars show the average and 1 standard deviation of sensitivities over the 7 repeated sampling. eFAST assigns a dummy parameter a small, non-zero sensitivity (last bar). This was exploited to perform a two-tailed *t*-test to calculate whether the sensitivity of each parameter was significantly greater than that of the dummy parameter (asterisk, using a significance $\alpha=0.01$). Parameters are listed in descending order of sensitivity (bottom).

A.9 Appendix A References

Keseler, I. M., Mackie, A., Santos-Zavaleta, A., Billington, R., Bonavides-Martínez, C., Caspi, R., et al. (2017). The EcoCyc database: Reflecting new knowledge about *Escherichia coli* K-12. *Nucleic Acids Res.* 45, D543–D550. doi:10.1093/nar/gkw1003.

Marino, S., Hogue, I. B., Ray, C. J., and Kirschner, D. E. (2008). A methodology for performing global uncertainty and sensitivity analysis in systems biology. *J. Theor. Biol.* 254, 178–196. doi:10.1016/j.jtbi.2008.04.011.

Saltelli, A., Tarantola, S., and Chan, K. P.-S. (1999). A quantitative model-independent method for global sensitivity analysis of model output. *Technometrics* 41, 39–56. doi:10.1080/00401706.1999.10485594.

Schmidt, A., Kochanowski, K., Vedelaar, S., Ahrné, E., Volkmer, B., Callipo, L., et al. (2016). The quantitative and condition-dependent *Escherichia coli* proteome. *Nat. Biotechnol.* 34, 104–110. doi:10.1038/nbt.3418.

van Aalten, D. M., DiRusso, C. C., Knudsen, J., and Wierenga, R. K. (2000). Crystal structure of FadR, a fatty acid-responsive transcription factor with a novel acyl coenzyme A-binding fold. *EMBO J.* 19, 5167–77. doi:10.1093/emboj/19.19.5167.

Appendix B: Supplemental Information for "The Growth Dependent Design Constraints of Transcription-Factor-Based Metabolite Biosensors"

Appendix B contains supplemental information for Chapter 3.

B.1. Kinetic Model of MRTF-Based Biosensor with Repressed-Repressor Architecture

B.1.1 Description of Kinetic Model

Motivated by the reactions shown in Figure 3.1A and recent simplified kinetic modeling of biosensors (Mannan et al., 2017; Hartline et al., 2020), we develop the following kinetic model for the operation of a biosensor.

Biosensor Expression

Hill-equations have been successful in describing the rate of protein production from a biosensor promoter as a function of the amount of transcription factor (TF) (Mannan et al., 2017), so we use the repressed-repressor hill-equation to describe protein production rate. These biosensor reporter proteins (G) are diluted by growth only, and the effects of proteases are ignored due to being much slower than cell growth under most conditions. Thus, we get the following kinetic equation for the concentration of the biosensor output protein:

$$\frac{\mathrm{d}G}{\mathrm{d}t} = b_G + \frac{a_G}{1+\frac{R_F}{K_G}} - \mu G \qquad \text{(Eq. B.1)}$$

Where b_g is the basal promoter expression rate, a_g is the promoter strength, and K_G is the TF-operator dissociation constant. R_F is the amount of free repressor TF, described below. The effects of co-operativity in TF binding are ignored.

Transcription Factor Expression and Metabolite-TF Sequestration

Free repressor (R_f) is produced at a constitutive rate. Based on previous modeling (Hartline et al., 2020), free repressors can bind to intracellular target metabolite (M_{in}) with mass-action kinetics to produce metabolite-bound repressors (R_s), which cannot bind to DNA. This reaction is reversable with first order kinetics as represented by the following reaction scheme:

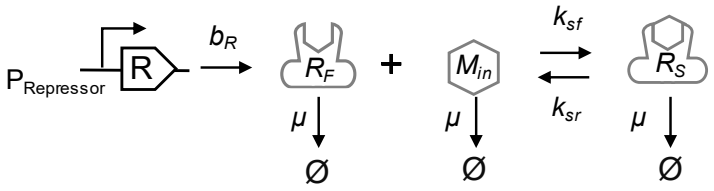

This gives the following kinetic equations for the intracellular concentration of free repressor (R_f) and metabolite-bound repressor intracellular (R_s):

$$\frac{\mathrm{d}R_F}{\mathrm{dt}} = b_R - k_{sf}R_F\mathrm{M}_{in} + k_{sr}R_S - \mu R_F \qquad \text{(Eq. B.2)}$$

$$\frac{\mathrm{d}R_S}{\mathrm{dt}} = k_{sf}R_f M_{in} - k_{sr}R_S - \mu R_S \qquad \text{(Eq. B.3)}$$

where b_R is the constitutive repressor production rate, and k_{sf} and k_{sr} are the forward and reverse binding rates between metabolite and MRTF. The total concentration of TF is $R_T = R_F + R_S$.

Metabolite transport mechanisms

We provide a general mechanism to describe intracellular metabolite dynamics which can be reduced to more specific mechanism by setting appropriate rates or concentrations to zero. First, metabolite diffusion cross cell membrane is bi-directional with an identical diffusion rate constant in each direction. Second, a metabolite can either be transported from extracellular environment

or catalytically created/destroyed by an enzyme following Michaelis-Menten kinetics. The enzyme transporters are constitutively expressed and are diluted by cell growth, which gives growth rate dependence. Third, the metabolite binds to the repressor TF. Finally, the metabolite is also diluted by growth. These give the following kinetic equations for the intracellular target metabolite concentrations:

$$\frac{\mathrm{dI_{in}}}{\mathrm{dt}} = k_{diff}(M_{ex} - M_{in}) + \frac{k_{cat,im}T_{im}}{K_{M,im}+\mathrm{M}_{ex}}M_{ex} - \frac{k_{cat,ex}T_{ex}}{K_{M,ex}+M_{in}}M_{in}$$

$$- k_{sf}R_F M_{in} + k_{sr}R_S - \mu M_{in} \qquad \text{(Eq. B4)}$$

$$\frac{dT_{im}}{dt} = b_{T,im} - \mu T_{im} \qquad \text{(Eq. B5)}$$

$$\frac{\mathrm{d}T_{ex}}{\mathrm{dt}} = b_{T,ex} - \mu T_{ex} \qquad \text{(Eq. B6)}$$

Where M_{ex} is the extracellular metabolite concentration, and T_{im} and T_{ex} are the concentrations of importer and exporter enzymes, respectively. The parameter values and descriptions of the other parameters are given in Table B.1.

B.1.2 Analytical Solutions for Minimum Output, Maximum Output, and Dynamic Range

The steady-state value for the output protein concentration can be solved by setting Eq. B1-B6 to zero and solving for *G*.

Minimum Output

For a repressed-repressor architecture, the minimum output (G_{min}) occurs when extracellular target metabolite concentration is zero (M_{ex} = 0), so that maximum repression of the biosensor is achieved.

Thus, the amount of free repressor is:

$$R_{F,min} = \frac{b_R}{\mu} \quad \text{(Eq. B7)}$$

and G_{min} can be calculated as:

$$G_{min} = \frac{1}{\mu}\left(b_G + \frac{a_G}{1+\frac{b_R}{K_G\mu}}\right) \quad \text{(Eq. B8)}$$

To understand the effect of growth rate on the minimum output, we take the derivative with respect to growth:

$$\frac{d}{d\mu}(R_F) = \frac{-b_R}{\mu^2} \quad \text{(Eq. B9)}$$

$$\frac{d}{d\mu}(G_{min}) = \frac{-1}{\mu^2}\left(b_G + \frac{a_G}{\left(1+\frac{b_R}{K_G\mu}\right)^2}\right) \quad \text{(Eq. B10)}$$

From Eq B.9-B.10, we observe that the minimum is always decreasing with growth for all positive parameters. Additionally, based on Eq. B9, the overall repression of the biosensor is decreasing since the repressor is diluted at higher growth rates.

Maximum Output

The maximum output depends on the amount of free repressor. From Eqs. B2-B3, we can find the fraction of free repressors available at steady-state:

$$F_{Rf} \equiv \frac{R_F}{R_F+R_S} = \frac{1}{1+\frac{k_{sf}M_{in}}{k_{sr}+\mu}} = \frac{K_R}{M_{in}+K_R} \qquad \text{(Eq. B11)}$$

Because the metabolite-MRTF binding rate k_{sr} is much faster than cell growth rate (i.e. $k_{sr} >> \mu$), we can set $k_{sr}+\mu \approx k_{sr}$, and let $K_R \equiv k_{sr}/k_{sf}$ be the TF-metabolite dissociation constant. Solving for M_{in} is generally difficult, so we write G_{max} in terms of M_{in}:

$$G_{max} = \frac{1}{\mu}\left(b_G + \frac{a_G}{1+\frac{b_R K_R}{K_G \mu (M_{in}+K_R)}}\right) \qquad \text{(Eq. B12)}$$

$$\frac{d}{d\mu}(G_{max}) = \frac{-1}{\mu^2}\left(b_G + \frac{a_G\left(1-\frac{dM_{in}}{d\mu}*\frac{b_r K_R}{K_G(M_{in}+K_R)^2}\right)}{\left(1+\frac{b_R K_R}{K_G \mu (M_{in}+K_R)}\right)^2}\right) \qquad \text{(Eq. B13)}$$

From this equation, it can be determined that the maximum output decreases with growth if $\frac{dM_{in}}{d\mu} \leq 0$, and increases with growth rate if $\frac{dM_{in}}{d\mu} > 0$.

Often, models allow M_{in} to reach infinity to describe the maximum output of a biosensor. However, in experimental scenarios, the intracellular or extracellular metabolite cannot be made arbitrarily high due to limitations in solubility, toxicity to cells, or transport limitations into the intracellular environment. Thus, in our models, M_{ex} takes on a large, but not infinite, value so that the potential effects of these realistic experimental limitations can be captured by the model.

Dynamic Range

Finally, the DR can be calculated as

$$DR = \frac{G_{max}}{G_{min}} - 1 = \frac{a_G b_R}{K_G \mu} \frac{M_{in}}{\left(a_G + b_G + \frac{b_G b_R}{K_G \mu}\right)\left(K_R + M_{in} + \frac{b_R K_R}{K_G \mu}\right)} \quad \text{(Eq. B14)}$$

and its derivative:

$$\frac{d}{d\mu}(DR) = \frac{a_G b_R}{K_G} \frac{M_{in}\left(\frac{b_G K_R {b_R}^2}{{K_G}^2 \mu^2} - (a_G + b_G)(K_R + M_{in})\right) + K_R \frac{dM_{in}}{d\mu}\left(a_G + b_G + \frac{b_G b_R}{K_G \mu}\right)\left(\mu + \frac{b_R}{K_G}\right)}{\mu^2\left(a_G + b_G + \frac{b_G b_R}{K_G \mu}\right)^2\left(K_R + M_{in} + \frac{b_R K_R}{K_G \mu}\right)^2}$$

(Eq. B15)

which can be either positive or negative depending on the sign of:

$$S = M_{in}\left(\frac{b_G K_R {b_R}^2}{{K_G}^2 \mu^2} - (a_G + b_G)(K_R + M_{in})\right) + K_R \frac{dM_{in}}{d\mu}\left(a_G + b_G + \frac{b_G b_R}{K_G \mu}\right)\left(\mu + \frac{b_R}{K_G}\right)$$

(Eq. B16)

B.1.3 Analytical Solution for Parameter Space with dDR/dμ and dDR/dbR Both Positive

dDR/dμ positive for passive-only metabolite transport

If diffusion is the only process by which metabolite can enter the cell, a simplified relation between DR and μ can be obtained. From Eq S4, the active import and export rates can be set to zero. Additionally, since $k_{sr} >> \mu$, then Eq S3 can be used to eliminate the sequestration terms from Eq S4. Then at steady state, Eq S4 can be solved for the internal metabolite concentration:

$$M_{in} = \frac{k_{diff}}{(k_{diff}+\mu)} M_{ex} \approx M_{ex} \; if \; k_{diff} >> \mu \qquad \text{(Eq. B17)}$$

Generally, diffusion happens on the order of a few minutes (Reuter et al., 2020), with a diffusion rate of 8.4 h^{-1} estimated for the lacI inducer TMG (Noel et al., 2009), while the growth rate of a cell is 0.69 h^{-1} for a cell with a 1-hour doubling time. Thus, the intracellular target metabolite concentration becomes approximately independent of growth rate, (i.e. $dM_{in}/d\mu = 0$). If growth dilution cannot be ignored, the metabolite-μ dependence becomes negative for all positive diffusion rates as evident by equation S16:

$$\frac{d}{d\mu}(M_{in}) = -\frac{k_{diff}}{(k_{diff}+\mu)^2} M_{ex} \qquad \text{(Eq. B18)}$$

If $dM_{in}/d\mu = 0$ then the DR-μ dependence becomes

$$\frac{d}{d\mu}(DR) = \frac{a_G b_R}{K_G} \frac{M_{in}\left(\frac{b_G K_R {b_R}^2}{{K_G}^2 \mu^2} - (a_G+b_G)(K_R+M_{in})\right)}{\mu^2\left(a_G+b_G+\frac{b_G b_R}{K_G \mu}\right)^2\left(K_R+M_{in}+\frac{b_R K_R}{K_G \mu}\right)^2} \qquad \text{(Eq. B19)}$$

And a simplified condition for where $dDR/d\mu$ is positive is found:

$$S_{passive-only} = \left(\frac{b_G K_R {b_R}^2}{{K_G}^2 \mu^2} - (a_G+b_G)(K_R+M_{in})\right) > 0 \qquad \text{(Eq. B20)}$$

Analytical solution for dDR/dbR positive

dDR/db$_R$ can be calculated directly from Eq. B13:

$$\frac{dDR}{db_r} = \frac{a_G M_{in}}{K_G \mu} \frac{(a_G+b_G)(K_R+M_{in})-\frac{b_G K_R {b_R}^2}{{K_G}^2 \mu^2}}{\left(a_G+b_G+\frac{b_G b_R}{K_G \mu}\right)^2 \left(K_R+M_{in}+\frac{b_R K_R}{K_G \mu}\right)^2} \qquad \text{(Eq. B21)}$$

Which is positive under the condition:

$$S_{dDR/dbR} = \left((a_G+b_G)(K_R+M_{in}) - \frac{b_G K_R {b_R}^2}{{K_G}^2 \mu^2} \right) > 0 \qquad \text{(Eq. B22)}$$

Comparing Eq B20 and Eq B22, it can be seen that $S_{dDR/dbR} = -S_{passive-only}$. Thus, there is no parameter space where both *dDR/dμ* and *dDR/db*$_R$ are positive for a passive diffusion only mechanism. Examining Eq B16, if $S_{dDR/dbR}$ is positive, the sign of *dDR/dμ* is only positive when $\frac{dM_{in}}{d\mu} > 0$, which motivates the examination active transport mechanisms to identify parameter spaces where both Eq B16 and Eq B22 are positive.

B.2. Model Parameterization and Fitting

B.2.1 Model Parameterization for Simulations

The model is parameterized to biologically relevant values to explore the effects of parameters and transport mechanisms. For growth rate, a doubling time between 1-8 hours was measured, so the average of these corresponding growth rates (~1.8 hour doubling time) was used. To parameterize the biosensor, parameters were chosen from previous literature values (Rosenfeld et al., 2002; Hooshangi et al., 2005; Hartline et al., 2020), and then some parameters were further tuned to match experimental results from our study. In particular, we observed that the maximum DR range

from our library was ~500. So, $a_{g,}$ b_G, and K_G, were tuned to give a maximum dynamic range of 500, while keeping the minimum output constant to match previous literature.

To model the appropriate transport dynamics, we assumed the TetR system had the mechanism outlined in Figure 3.5. The diffusion rate was chosen to be 10-times the maximum growth rate observed so that diffusion is much faster than growth. This value is on the same order of magnitude as the diffusion rate observed for the lac inducer TMG (Noel et al., 2009). Next, as a starting point for our analysis, we desired a set of parameters where the transport of the intracellular metabolite through active and passive mechanisms are equal (for more detail, see Figure B.1A) which will allow us to observe the effect of moving away from this balanced point on DR and $dDR/d\mu$. To identify this initial balance point, the literature values for k_{sf}, $k_{cat,ex}$, and $K_{M,ex}$ were fine-tuned to match the following constraint:

$$\frac{k_{cat,ex}T_{ex}}{K_{M,ex}+M_{in}}M_{in} - (k_{diff} + \mu)\,M_{in} = 0 \qquad \text{(Eq. B23)}$$

To explore the effect of tuning the K_M values, K_M values were chosen to be K_M =1000 M_{in}, K_M = M_{in}, and K_M =0.001M_{in} for K_M << M_{in}, K_M = M_{in} and K_M >> $M_{in,}$ respectively. Parameter-fine tuning was performed using Matlab 2020b optimization toolbox fmincon.

Finally, when exploring the catalytic import/export mechanism, as many parameters were maintained between the systems as possible, instead of re-tuning to match the FA-FadR sensor. To enable a fair comparison between mechanisms, the center $k_{cat,im}$ value was chosen so that M_{in} = $K_{M,ex}$. A summary of parameters used is given in Table B.1.

Table B.1. Model Parameters and Values for Biosensor Model.

Parameter	Description	Value (units)
Parameters used across all simulations		
μ_0	Growth Rate	0.3899 (h^{-1})
M_{ex}	External metabolite	4000 (µM)
b_G	Biosensor basal expression rate	1.113E-2 (µM h^{-1})
a_G	Biosensor promoter strength	5.565E0 (µM h^{-1})
K_G	TF Dissociation constant	2.573E-5; (µM)
b_R	TF constitutive expression rate	1.380E-2 (µM h^{-1})
k_{sr}	TF-M reverse sequestration rate	900.7 (h^{-1})
Parameters Tuning b_R at constant growth (Figure 3)		
b_R	TF constitutive expression rate	Range: Min: 2.30E-3 (µM h^{-1}) Max: 1.38E-2 (µM h^{-1})
k_{sf}	TF-M forward sequestration rate	3.345E3 (μM^{-1} h^{-1})
M_{in}	Internal metabolite	1.894E3 (µM)
Parameters: passive transport/active export mechanism (aTc-type: Figure 5, Figure S2)		
k_{diff}	Metabolite diffusive rate	Center value: 6.931E1 (h^{-1})
$b_{T,ex}$	Met. transporter (export) constitutive expression rate	0.0625 (µM h^{-1})
$k_{cat,ex}$	Active export turnover rate	Center values: K_M Low: 8.657E4 (h^{-1}) K_M Med: 1.730E5 (h^{-1}) K_M High:8.657E7 (h^{-1})
$K_{M,ex}$	Active export Michaelis constant	K_M Low: 1.894E0 (µM) K_M Med: 1.894E3 (µM) K_M High:1.894E6 (µM)
k_{sf}	TF-M forward sequestration rate	K_M Low: 4.117E3 (μM^{-1} h^{-1}) K_M Med: 3.345E3 (μM^{-1} h^{-1}) K_M High:2.958E3 (μM^{-1} h^{-1})
Parameters: active import/export mechanism (FA-type, Figure 6)		

$b_{T,ex}$	Met. transporter (export) constitutive expression rate	0.0625 (μM h^{-1})
$k_{cat,ex}$	Active export turnover rate	Center value: 1.730E5 (h^{-1})
$K_{M,ex}$	Active export Michaelis constant	1.894E3 (μM)
$b_{T,im}$	Met. transporter (import) constitutive expression rate	0.0625 (μM h^{-1})
$k_{cat,im,0}$	Active export turnover rate	Center value: 2.923E4 (h^{-1})
$K_{M,im}$	Active import Michaelis constant	49.00 (μM)
k_{sf}	TF-M forward sequestration rate	3.345E3 (μM^{-1} h^{-1})

B.2.2 Model Fitting to RBS Library Data

To determine how well the model works at a single-growth rate, we fit the model to the data collected from the aTc sensors with a library of RBS strengths controlling TetR expression (Figure 3.3B, 3.3C, Appendix B, Table B.6). To do so we fit equations Eq B.8 and Eq B.12 representing G_{min} and G_{max} respectively, to the data. To fit the data, the measured G_{min} and G_{max} were first multiplied by the average growth rate from all strains in the minimum and maximum output conditions respectively. This operations converts the measured RFP concentration (RFP/OD) into units of expression rate (RFP/OD/h). The measured TetR expression level was corrected for G_{max} to account for the change in growth rate. Finally, M_{in} is assumed to be the same for all library members and is taken to be 1 at the maximum and 0 at the minimum, for the purposes of fitting. Four parameters were converted into log space and fitted, b_G, a_G, K_G, and K_R. The minimum and maximum expression rates were fit simultaneously using Matlab R2020b surface fitting tool (cftool) with two inputs (TetR expression and aTc concentration), and one output (biosensor protein expression rate). A summary of the fitted parameters is given in Table B.2. The measured DR data was not used directly during fitting. Instead, the model prediction for DR was calculated from the minimum and maximum outputs of the model and plotted directly for Figure 3.3D.

To determine whether the model fitting is statistically significant for the relation between minimum output and TetR expression rate (Figure 3.3B), we refit the G_{min} versus TetR expression data with the average value for all the G_{min} data (i.e. G_{min} is not correlated with TetR expression). We conducted an F-test of the residuals and found that our fitted model (Eq S8) provides a statistically significant better description of G_{min} versus TetR, as compared to a no-correlation model (F-Statistic: 12.14; degrees of freedom no-correlation model: 11, degrees of freedom Eq. B8: 9, p-value 4.1×10^{-4}). This supports that our model can correctly capture the relation between G_{min} and TetR expression rate (b_R).

Table B.2. Model parameters and fitting to aTc-biosensor, TetR-RBS-library.

Model (Adapted from Eq B8 and Eq B12)		
$$\mu \cdot G = b_G + \frac{a_G}{\left(1 + \left(\frac{\mu_{min} \cdot TetR}{\mu \cdot K_G}\right) \cdot \left(\frac{K_R}{K_R + M}\right)\right)}$$		
Input Parameters	Description	Value from experiment (units)
μ_{min}	Average Growth Rate of TetR-RBS-Library at G_{min}	0.4627 (h^{-1})
μ_{max}	Average Growth Rate of TetR-RBS-Library at G_{max}	0.3410 (h^{-1})
M_{min}	Internal Target Metabolite Concentration at G_{min}	0 (Concentration)
M_{max}	Internal Target Metabolite Concentration at G_{max}	1 (Concentration)
$TetR$	TetR Expression Strength from TetR Expression Strength Library	See Table b.6
G	Biosensor output	See Table S6
Fitted Parameters	Description	Fitted Value (units)
b_G	Biosensor basal expression rate	10^(-1.5729) (RFP/(OD h))
a_G	Biosensor promoter strength	10^(0.9604) (RFP/(OD h))
K_G	TF Dissociation constant	10^(-2.9963) (RFP/OD)
K_R	TF-metabolite dissociation constant	10^(-4.4500) (Concentration)

B.3. Sensitivity Analysis of Kinetic Model

We used global sensitivity analysis (GSA) to quantify the impact of model parameters on the DR and DR-μ dependence ($dDR/d\mu$). We performed GSA by extended Fourier amplitude sensitivity test (eFAST) using MATLAB code adapted from previous works (Marino et al., 2008; Hartline et al., 2020), to calculate the total-order sensitivity indices for each parameter. Parameter values were varied from 0.1- to 10- fold from the parametrized values (with the intermediate value for $K_{M,ex}$) and DR and $dDR/d\mu$ were calculated as model outputs. A dummy parameter was incorporated into the model which has no effect on output. The sensitivities of each parameter were compared against the dummy parameter for significance testing (2-tailed t-test, $\alpha = 0.01$). The results suggest that both DR and $dDR/d\mu$ are sensitive to the actuating parameters intrinsic to the biosensor promoter (a_G, b_G, K_G) and the sensing parameters related to repressor expression and activity (b_R, k_{sf}, k_{sr}) but are less sensitive to metabolite transport kinetic parameters (Figure B.2). Overall, both DR and $dDR/d\mu$ share the same significant parameters, suggesting that tuning DR will also impact the DR-growth rate dependence and vice versa.

B.4. Effect of Time-Varying Target Metabolite Concentration on Dynamic Range-Growth Rate Dependence

For our model and experiments, it was assumed that the extracellular environment and target metabolite concentrations are constant and saturating for the biosensors, so that the biosensor output could reach a steady-state. These assumptions are valid for several reasons. First, the addition of extracellular inducer is very high, at concentrations at or beyond what are typically used to achieve full induction. Under these conditions, small reductions in target metabolite are unlikely to significantly impact the output of the biosensor. Second, data was collected at early exponential growth (O.D. 600 < 0.4), so that the distribution of the target metabolite to each cell

remains high over that period. Third, the inducers used are non-metabolizable so their extracellular concentration would not be significantly impacted by cells.

In some cases, the growth of the cell population can impact the extracellular concentration. This can happen because the target metabolite is degraded by the cell, or because when cell density is high, the relative amount of target metabolite per cell is reduced. In these cases, the DR-μ dependence could be affected by changes in the availability of extracellular target metabolite. To understand this scenario, we use the model to explore how the DR-μ dependence changes for a linearly decreasing extracellular target metabolite concentrations (Figure B.3A). Although the extracellular target metabolite concentration is unlikely to change in this way, the biosensor outputs G_{min} and G_{max} are defined as the steady-state protein concentration of the biosensor. Thus, the dynamics of the extracellular concentration can be ignored when calculating DR. We model biosensor with an aTc-type transport mechanism for extracellular inducer and calculate how the DR-μ dependence changes as the target metabolite concentration decreases (Figure B.3B). Our model shows that initially as the target metabolite concentration decreases, the DR-μ dependence increases, indicating that the DR become more sensitive to growth. Then as the target metabolite concentration approaches zero, the DR-μ dependence also goes to zero. To explain this behavior, we focus on how G_{max} changes over time, since G_{min} does not depend on target metabolite concentration (Eq S8). Our model shows that G_{max} does not decay linearly with time and the rate of G_{max} decay depends on the growth rate of the cell (Figure B.3C). At low growth rates, G_{max} is more sensitive to falling extracellular target metabolite concentrations. Because of this, the G_{max} levels cross, and the DR becomes highly sensitive to growth rate, mostly due to a high G_{min}-μ dependence. Once the extracellular target metabolite concentrations reach zero, the G_{max}, and DR become zero, so there is no more DR-μ sensitivity. These results demonstrate a non-linear

relationship between DR-μ dependence and extracellular target metabolite concentration, which could be important in applications requiring high cell densities or when sensing degradable metabolites.

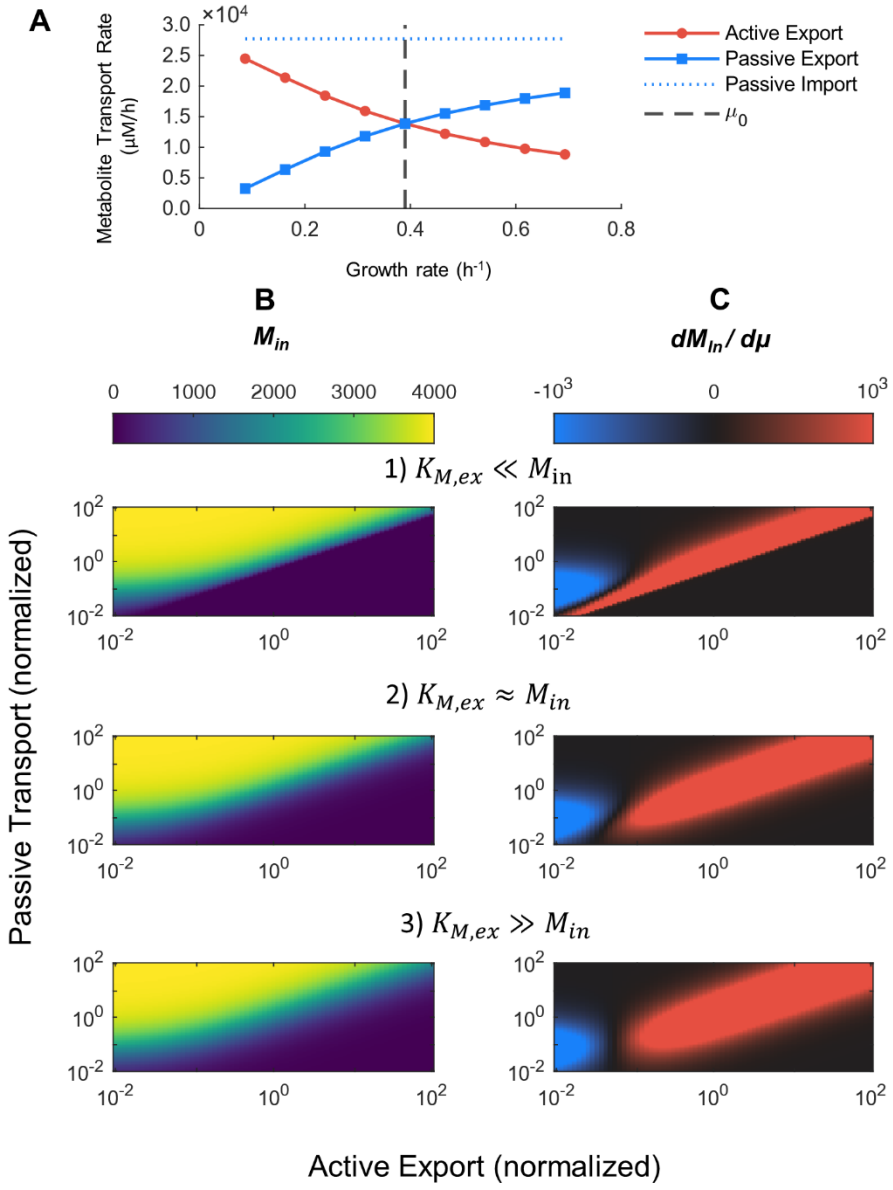

Figure B.1. Modeling the impact of passive transport/active export (aTc-like) transport on intracellular target metabolite concentration and M_{in}-μ dependence. (A) Total active (red) and passive (blue) transport rates at different growth rates at center k_{diff} and $k_{cat,ex}$ values for intermediate $K_{M,ex}$ (i.e. $K_{M,ex} \approx M_{in}$). The dotted line shows the growth rate μ_0, at which the passive and active transport rates are equal. **(B)** Intracellular target metabolite concentration and. **(C)** M_{in}-μ dependence under different parameter space.

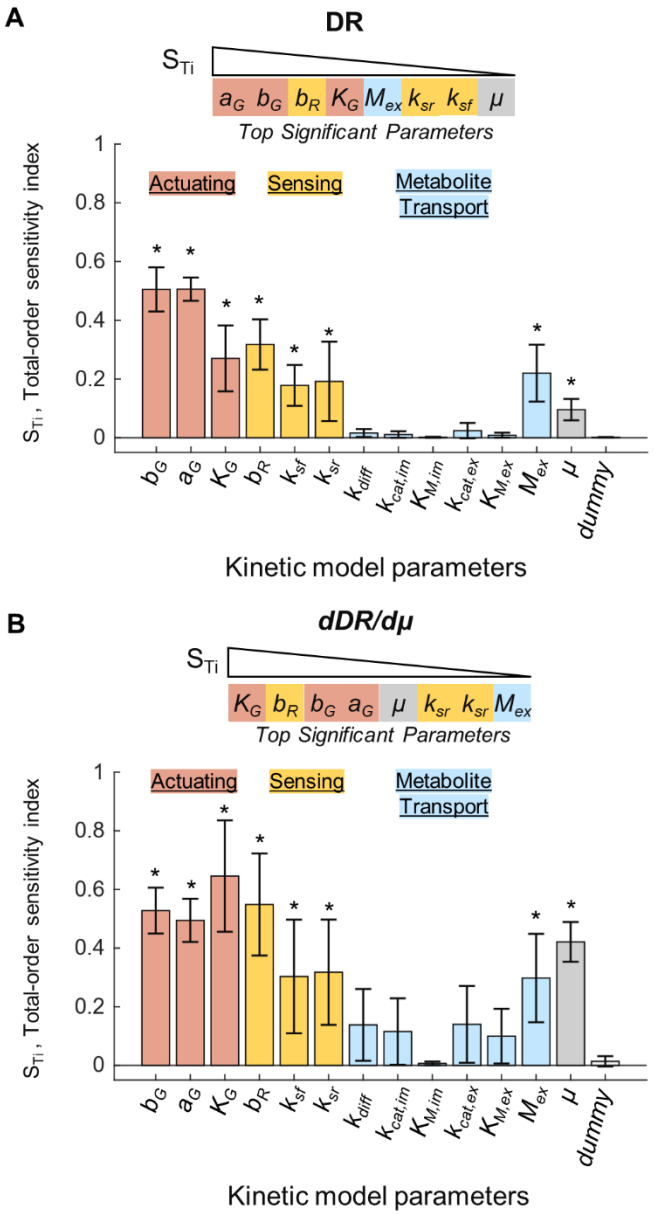

Figure B.2. Global sensitivity analysis of DR and *dDR/dμ* to model parameters. Bar plot of the total-order sensitivity indices calculated from GSA by eFAST for the **(A)** Dynamic Range, **(B)** *dDR/Dμ*. Sensitivities were calculated from 600 samples per search curve over the parameter space, and each sampling was repeated 9 times for a high coverage of the parameter space. Bars and error-bars represent the average and 1 standard deviation of the total-order sensitivity over the 9 repeated samplings. The significance of each model parameter was tested against a dummy variable by a two-tailed t-test, (*, $p < 0.01$). Significant parameters are listed in descending order of sensitivity.

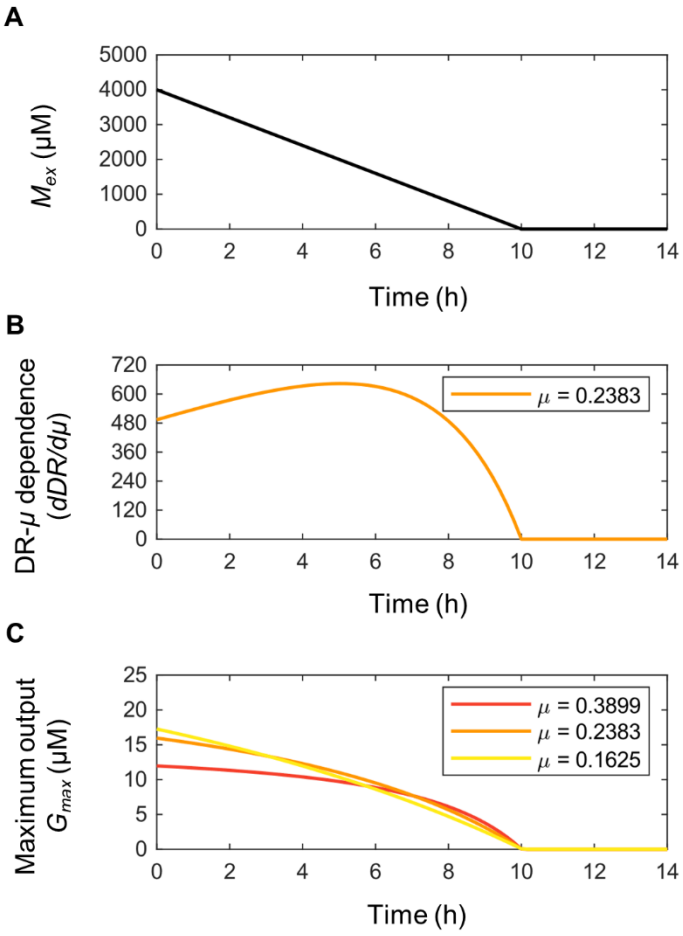

Figure B.3. Effect of time-varying extracellular target metabolite concentration on DR-μ dependence. Model represents an biosensor with an aTc-like transport mechansim. **(A)** Extracellular target metabolite concentration is decrasing over time due to significant consumption by the cells. **(B)** DR-μ dependence over time at an intermediate growth rate as extraceullar target metabolite concentrations fall. **(C)** Maximum biosensor output (G_{max}) over time at a slow, intermediate, and fast growth rate during decreasing extracellular target metabolite concentrations. Parameters used are given in Table B.1 for aTc-type biosensor with a medium K_M value.

B.5. Growth Conditions, Plasmids, Strains, and Sequences Used in This Study

Table B.3. Medium conditions and growth rates used in this study.

Medium Condition	Growth rate [a] at minimum output	Growth rate at maximum output		
		aTc biosensor	IPTG biosensor	FA biosensor
75 mM Acetate	0.24 ± 0.02 h^{-1}	0.111 ± 0.001 h^{-1}	0.20 ± 0.01 h^{-1}	0.01 ± 0.01 h^{-1}
20 mM Pyruvate	0.34 ± 0.01 h^{-1}	0.20 ± 0.01 h^{-1}	0.34 ± 0.02 h^{-1}	N.D.
1% (v/v) Glycerol	0.43 ± 0.02 h^{-1}	0.28 ± 0.02 h^{-1}	0.38 ± 0.01 h^{-1}	0.40 ± 0.02 h^{-1}
20 mM Sorbitol	0.45 ± 0.01 h^{-1}	0.23 ± 0.02 h^{-1}	0.41 ± 0.01 h^{-1}	N.D.
15 mM Succinate	0.49 ± 0.03 h^{-1}	0.29 ± 0.02 h^{-1}	0.39 ± 0.01 h^{-1}	N.D.
1% Glycerol + 7 Amino Acids	0.50 ± 0.03 h^{-1}	0.36 ± 0.02 h^{-1}	0.50 ± 0.01 h^{-1}	0.49 ± 0.02 h^{-1}
20 mM Xylose	0.51 ± 0.02 h^{-1}	0.29 ± 0.02 h^{-1}	0.45 ± 0.01 h^{-1}	N.D.
0.4 % (w/v) Glucose	0.59 ± 0.05 h^{-1} [b]	N.D.	N.D.	0.65 ± 0.01 h^{-1}

N.D. Not determined

[a] Growth rate at minimum output are averages from all three sensors

[b] Glucose medium growth rate at minimum output is from FA-sensor only

Table B.4. Plasmids used in this study.

Plasmid	Description	Replication Origin	Operon	Resistance marker	References
pS2k-rfp	aTc biosensor	SC101	**P_{tet}**-*rfp* **P_{tetR}**-*tetR*	**KanR**	(Lee et al., 2011)
pS5k-rfp	IPTG biosensor	SC101	**P_{lacUV5}**-*rfp* **P_{lacI}**-*lacI*	**KanR**	(Lee et al., 2011)
pSARk-rfp	FA biosensor	SC101	**P_{AR}**-*rfp*	**KanR**	(Zhang et al., 2012)
pAfadRm1a-fadR	*fadR* over-expression	p15A	**P_{fadRm1}**-*fadR*	**AmpR**	This Study
pTargetF-P_{fadRm1}	Genome Editing: constitutive *fadR* promoter	ColE1	**P_{J23119}** -*fadR* gRNA, targeting *fadR* promoter, P_{fadRm1}-fadR homology arms	**SpecR**	This Study
pTargetF-ΔfadE	Genome Editing: *fadE* knockout	ColE1	**P_{J23119}** -*fadE* gRNA, targeting *fadE* coding sequence, FadE 5' and 3' homology arms	**SpecR**	This Study
pTargetF-Ppro4::fadD	Genome Editing: constitutive *fadD* promoter	ColE1	**P_{J23119}** -*fadD* gRNA, targeting *fadD* promoter sequence, FadD 5' and 3' homology arms, P_{pro4} upstream of FadD	**SpecR**	This Study
pSk-P_{Tet}-rfp-P_{J23110}-RBSLibrary-tetR	aTc biosensor with Library of TetR RBS	SC101	**P_{tet}**-*rfp* **P_{J23110}**-*tetR*	**KanR**	This Study
pSk-P_{J23110}-RBSLibrary-rfp	Library of TetR RBS controlling RFP	SC101	**P_{J23110}**-*rfp*	**KanR**	This Study

Table B.5. Strains used in this study.

Strains	Genotype	references
E. coli MG1655	K-12 F^- λ^- *ilvG*$^-$ *rfb-50 rph-1*	This study
aTc biosensor strain	MG1655 pS2k-rfp	This study
IPTG biosensor strain	MG1655 pS5k-rfp	This Study
FA biosensor strain	MG1655 Δ*fadE* P_{fadRm1}::*fadR* P_{pro4}::*fadD* pSARk-rfp pAfadRm1a-fadR	This Study
TetR-RBS-Library	MG1655 pSk-P_{Tet}-rfp-P_{J23110}-RBSLibrary-tetR	This Study
TetR Expression Strength Library	MG1655 pSk-P_{J23110}-RBSLibrary-rfp	This Study

Table B.6. aTc biosensor-TetR RBS library members used in this study.

RBS Sequence	TetR Expression Strength (RFP/OD) [a]	G_{Min} (RFP/OD) [b]	G_{Max} (RFP/OD) [c]	DR
GGT	1.07 ± 0.02	0.070 ± 0.002	25.4 ± 0.6	361 ± 16
ATG	0.74 ± 0.01	0.078 ± 0.004	26.4 ± 0.3	335 ± 13
GTT	0.452 ± 0.005	0.072 ± 0.003	25.9 ± 0.2	356 ±14
TGT	0.388 ± 0.005	0.14 ± 0.01	27.0 ± 0.3	186 ±16
TTC	0.270 ± 0.001	0.16 ± 0.01	25.0 ± 0.1	158 ± 11
CAC	0.203 ± 0.006	0.187 ± 0.003	24.8 ± 0.1	131 ± 2
ACT	0.193 ± 0.007	0.116 ± 0.005	29.3 ± 0.6	250 ± 10
CCC	0.189 ± 0.002	0.210 ± 0.005	24.9 ±0.4	117 ± 1
CGC	0.19 ± 0.01	0.112 ± 0.004	27.0 ± 0.4	240 ± 6
CGT	0.180 ± 0.005	0.095 ± 0.004	27.7 ± 0.6	289 ± 9
ACC	0.161 ± 0.003	0.261 ± 0.004	27.3 ± 0.4	103 ± 1
ACA	0.124 ± 0.004	0.20 ± 0.01	26.3 ± 1.3	131 ± 11

[a] Measured from TetR Expression Strength Library Strains
[b] Measured from TetR-RBS-Library Strains at 0 nM aTc
[c] Measured from TetR-RBS-Library Strains at 1000 nM aTc
* Colors correspond to those low (yellow), medium (green), and high (purple) TetR expression sensors displayed in Figure 3.4.

B.5.1 DNA Sequences of Plasmids Constructed in This Study.

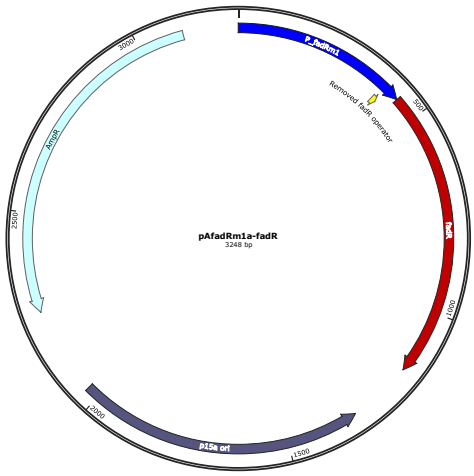

pAfadRm1a-fadR. Features: Promoter P_{fadRm1}, blue; Removed FadR operator site, highlight; *fadR*, dark red;

cttcgatagccaacagaccaccggggagcagcgggtagcatttcagggccatcgccagagtgaaaataaattccgctaccagcaaccagcccgcgac
gaaagggctgatgaggaaaattaacgggtttacgattaagaaaatgatgagggcgagtttgtaccagtcgggggactggcccaaaaaattgcgccat
agcgcgcggccccaggagatctccatgatggtttcccttaccttacaaataatcaatgatgtttttatgtttaaacgcaaagcttaacggtcaggca
ggagtgaggcaagtcttgatagtcaaggggaaagagatgcggaaaatgaagccttgatccctttttcttcttttgtctgctatcagcgtagttagc
cctaatttatgatactgccaactttgttttgctgtgttatggaaatctcactatggtcattaaggcgcaaagcccggcgggtttcgcggaagagtac
attattgaaagtatctggaataaccgcttccctcccgggactattttgcccgcagaacgtgaactttcagaattaattggcgtaacgcgtactacgt
tacgtgaagtgttacagcgtctggcacgagatggctggttgaccattcaacatggcaagccgacgaaggtgaataatttctgggaaacttccggttt
aaatatccttgaaacactggcgcgactggatcacgaaagtgtgccgcagcttattgataatttgctgtcggtgcgtaccaatatttccactatttttt
attcgcaccgcgtttcgtcagcatcccgataaagcgcaggaagtgctggctaccgctaatgaagtggccgatcacgccgatgcctttgccgagctgg
attacaacatattccgcggcctggcgtttgcttccggcaacccgatttacggtctgattcttaacgggatgaaagggctgtatacgcgtattggtcg
tcactatttcgccaatccggaagcgcgcagtctggcgctgggcttctaccacaaactgtcggcgttgtgcagtgaaggcgcgcacgatcaggtgtac
gaaacagtgcgtcgctatgggcatgagagtggcgagatttggcaccggatgcagaaaaatctgccgggtgatttagccattcaggggcgataaggat
ccaaactcgagtaaggatctccaggcatcaaataaaacgaaaggctcagtcgaaagactgggcctttcgttttatctgttgtttgtcggtgaacgct
ctctactagagtcacactggctcaccttcgggtgggcctttctgcgtttatacctagggatatattccgcttcctcgctcactgactcgctacgctc
ggtcgttcgactgcggcgagcggaaatggcttacgaacggggcggagatttcctggaagatgccaggaagatacttaacagggaagtgagagggccg
cggcaaagccgtttttccataggctccgcccccctgacaagcatcacgaaatctgacgctcaaatcagtggtggcgaaacccgacaggactataaag
ataccaggcgtttcccccctggcggctccctcgtgcgctctcctgttcctgccttcggtttaccggtgtcattccgctgttatggccgcgtttgtct
cattccacgcctgacactcagttccgggtaggcagttcgctccaagctggactgtatgcacgaacccccgttcagtccgaccgctgcgccttatcc
ggtaactatcgtcttgagtccaacccggaaagacatgcaaaagcaccactggcagcagccactggtaattgatttagaggagttagtcttgaagtca
tgcgccggttaaggctaaactgaaaggacaagttttggtgactgcgctcctccaagccagttacctcggttcaaagagttggtagctcagagaacct
tcgaaaaaccgccctgcaaggcggtttttcgttttcagagcaagagattacgcgcagaccaaaacgatctcaagaagatcatcttattaatcagat
aaaatatttctagatttcagtgcaatttatctcttcaaatgtagcacctgaagtcagccccatacgatataagttgttactagtgcttggattctca
ccaataaaaaacgcccggcggcaaccgagcgttctgaacaaatccagatggagttctgaggtcattactggatctatcaacaggagtccaagcgagc
tcgtaaacttggtctgacagttaccaatgcttaatcagtgaggcacctatctcagcgatctgtctatttcgttcatccatagttgcctgactccccg
tcgtgtagataactacgatacgggagggcttaccatctggccccagtgctgcaatgataccgcgtgaaccacgctcaccggctccagatttatcagc
aataaaccagccagccggaagggccgagcgcagaagtggtcctgcaactttatccgcctccatccagtctattaattgttgccgggaagctagagta
agtagttcgccagttaatagtttgcgcaacgttgttgccattgctacaggcatcgtggtgtcacgctcgtcgtttggtatggcttcattcagctccg
gttcccaacgatcaaggcgagttacatgatcccccatgttgtgcaaaaaagcggttagctccttcggtcctccgatcgttgtcagaagtaagttggc
cgcagtgttatcactcatggttatggcagcactgcataattctcttactgtcatgccatccgtaagatgcttttctgtgactggtgagtactcaacc
aagtcattctgagaatagtgtatgcggcgaccgagttgctcttgcccggcgtcaatacgggataataccgcgccacatagcagaactttaaaagtgc
tcatcattggaaaacgttcttcggggcgaaaactctcaaggatcttaccgctgttgagatccagttcgatgtaacccactcgtgcacccaactgatc
ttcagcatcttttactttcaccagcgtttctgggtgagcaaaaacaggaaggcaaaatgccgcaaaaaagggaataagggcgacacggaaatgttga
atactcatactcttcctttttcaatattattgaagcatttatcagggttattgtctcatgagcggatacatatttgaatgtatttagaaaaataaac
aaatagggttccgcgcacatttccccgaaaagtgccacctgacgtc

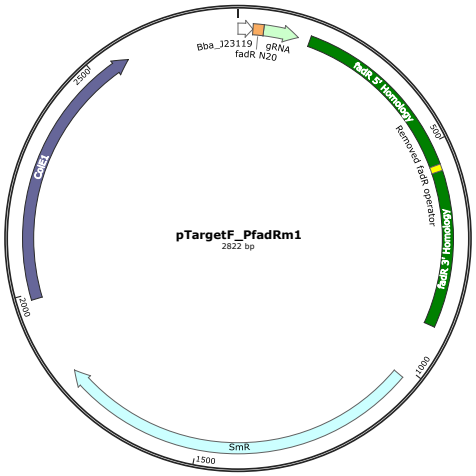

pTargetF-P$_{fadRm1}$. Features: *fadR* N20, orange; Homology arms, green; Removed FadR operator site, highlight

ttgacagctagctcagtcctaggtataatacttatcagcgtagttagccctctgggttttagagctagaaatagcaagttaaaataaggctagtccg
ttatcaacttgaaaaagtggcaccgagtcggtgctttttttgaattctctagagtcgaccttcgatagccaacagaccaccggggagcagcgggtag
catttcagggccatcgccagagtgaaaataaattccgctaccagcaaccagcccgcgacgaaagggctgatgaggaaaattaacgggtttacgatta
agaaaatgatgagggcgagtttgtaccagtcgggggactggcccaaaaaattgcgccatagcgcgcggccccaggagatctccatgatggtttccct
taccttacaaataatcaatgatgtttttatgtttaaacgcaaagcttaacggtcaggcaggagtgaggcaagtcttgatagtcaaggggaaagagat
gcggaaaatgaagccttgatccctttttcttcttttgtctgctatcagcgtagttagccctaatttatgatactgccaactttgttttgctgtgtt
atggaaatctcactatggtcattaaggcgcaaagcccggcgggtttcgcggaagagtacattattgaaagtatctggaataaccgcttccctcccgg
gactattttgcccgcagaacgtgaactttcagaattaattggcgtaacgcgtactacgttacgtgaagtgttacagcgtctggcacgagatggctgg
ttgaccattcaacatggcaagccgacgaaggtgaataatttctgggaaacttccggtttaaatatccttgaaacactggcgcgactggatcacgaaa
gtgtgccgcagcttattgataatctcgagttcatgtgcagctccatcagcaaaaggggatgataagtttatcaccaccgactatttgcaacagtgcc
gttgatcgtgctatgatcgactgatgtcatcagcggtggagtgcaatgtcatgagggaagcggtgatcgccgaagtatcgactcaactatcagaggt
agttggcgtcatcgagcgccatctcgaaccgacgttgctggccgtacatttgtacggctccgcagtggatggcggcctgaagccacacagtgatatt
gatttgctggttacggtgaccgtaaggcttgatgaaacaacgcggcgagctttgatcaacgacctttttggaaacttcggcttcccctggagagagcg
agattctccgcgctgtagaagtcaccattgttgtgcacgacgacatcattccgtggcgttatccagctaagcgcgaactgcaatttggagaatggca
gcgcaatgacattcttgcaggtatcttcgagccagccacgatcgacattgatctggctatcttgctgacaaaagcaagagaacatagcgttgccttg
gtaggtccagcggcggaggaactctttgatccggttcctgaacaggatctatttgaggcgctaaatgaaaccttaacgctatggaactcgccgcccg
actgggctggcgatgagcgaaatgtagtgcttacgttgtcccgcatttggtacagcgcagtaaccggcaaaatcgcgccgaaggatgtcgctgccga
ctgggcaatggagcgcctgccggcccagtatcagcccgtcatacttgaagctagacaggcttatcttggacaagaagaagatcgcttggcctcgcgc
gcagatcagttggaagaatttgtccactacgtgaaaggcgagatcaccaaggtagtcggcaaataagatgccgctcgccagtcgattggctgagctc
atgaagttcctattccgaagttccgcgaacgcgtaaaggatctaggtgaagatccttttgataatctcatgaccaaaatcccttaacgtgagtttt
cgttccactgagcgtcagaccccgtagaaaagatcaaaggatcttcttgagatcctttttttctgcgcgtaatctgctgcttgcaaacaaaaaaacc
accgctaccagcggtggtttgtttgccggatcaagagctaccaactctttttccgaaggtaactggcttcagcagagcgcagataccaaatactgtc
cttctagtgtagccgtagttaggccaccacttcaagaactctgtagcaccgcctacatacctcgctctgctaatcctgttaccagtggctgctgcca
gtggcgataagtcgtgtcttaccgggttggactcaagacgatagttaccggataaggcgcagcggtcgggctgaacgggggttcgtgcacacagcc
cagcttggagcgaacgacctacaccgaactgagatacctacagcgtgagctatgagaaagcgccacgcttcccgaagggagaaaggcggacaggtat
ccggtaagcggcagggtcggaacaggagagcgcacgagggagcttccagggggaaacgcctggtatctttatagtcctgtcgggtttcgccacctct
gacttgagcgtcgatttttgtgatgctcgtcaggggggcggagcctatggaaaaacgccagcaacgcggcctttttacggttcctggccttttgctg
gccttttgctcacatgttctttcctgcgttatcccctgattctgtggataaccgtattaccgcctttgagtgagctgataccgctcgccgcagccga
acgaccgagcgcagcgagtcagtgagcgaggaagcggaagagcgcctgatgcggtattttctccttacgcatctgtgcggtatttcacaccgcatat
gctggatcc

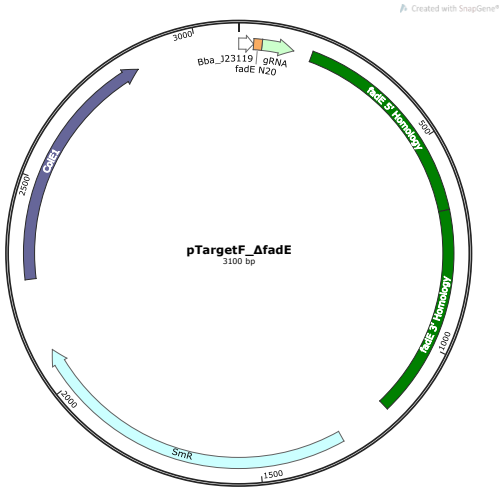

pTargetF-ΔfadE. Features: *fadE* N20, orange; Homology arms, green;

ttgacagctagctcagtcctaggtataatactagtgatgctggtggagtgcctcttgttttagagctagaaatagcaagttaaaataaggctagtccg
ttatcaacttgaaaaagtggcaccgagtcggtgctttttttgaattctctagagtcgacctgcagaagcttagatctcgggaggaatgatgtttaag
gcaataacgacagtcgccgctctggtcatcgccaccagtgcaatggcgcaggatgatttaaccattagcagccttgcaaagggcgaaaccaccaaag
ctgcatttaatcagatggtacaagggcataagctgcctgcctgggtgatgaaaggcggtacttatactcccgcacaaaccgtaacgttgggagatga
gacgtatcaggtgatgagcgcgtgcaaaccgcatgactgtggctcgcaacgtatcgctgtgatgtggtccgagaaatctaatcagatgacggggctg
ttctcgactattgatgagaaaacgtcgcaagagaaactcacctggctgaatgtgaacgatgcgctttcgattgatggtaaaacggtgttgttcgcgg
cgttgaccggcagcctggaaaaccatccggatggctttaattttaaataattagcggataaagaaacggagcctttcggctccgttattcatagcac
ctgcccgtacttctcgcttttggcggtatccggtacactgcattttgtctattacatttatgctgaaggatatcctcatgtaccaggatcttattcg
taacgaactgaacgaagcggcggaaacgctggctaacttttttaaaagatgacgccaatattcacgccattcagcgcgcggcggtcctgttagcagac
agctttaaagccggtggcaaagtgctttcctgcggcaacggcggttcccattgcgacgctatgcactttgccgaagagttgaccggtcgctaccgtg
aaaaccgtccgggctacccggcgattgctatttctgacgttagtcatatttcctgcgtcggtaatgatttcggtttcaatgatattttctcccgcta
cgttgaagcggtaggtcgcgaaggcgatgtactgctggggatctccacctccggtaactctgcaaacgtgatcaaagcgatcgcagcggcgcgtgag
aagggaatgactcgagttcatgtgcagctccatcagcaaaaggggatgataagtttatcaccaccgactatttgcaacagtgccgttgatcgtgcta
tgatcgactgatgtcatcagcggtggagtgcaatgtcatgagggaagcggtgatcgccgaagtatcgactcaactatcagaggtagttggcgtcatc
gagcgccatctcgaaccgacgttgctggccgtacatttgtacggctccgcagtggatggcggcctgaagccacacagtgatattgatttgctggtta
cggtgaccgtaaggcttgatgaaacaacgcggcgagctttgatcaacgacctttttggaaacttcggcttcccctggagagagcgagattctccgcgc
tgtagaagtcaccattgttgtgcacgacgacatcattccgtggcgttatccagctaagcgcgaactgcaatttggagaatggcagcgcaatgacatt
cttgcaggtatcttcgagccagccacgatcgacattgatctggctatcttgctgacaaaagcaagagaacatagcgttgccttggtaggtccagcgg
cggaggaactctttgatccggttcctgaacaggatctatttgaggcgctaaatgaaaccttaacgctatggaactcgccgcccgactgggctggcga
tgagcgaaatgtagtgcttacgttgtcccgcatttggtacagcgcagtaaccggcaaaatcgcgccgaaggatgtcgctgccgactgggcaatggag
cgcctgccggcccagtatcagcccgtcatacttgaagctagacaggcttatcttggacaagaagaagatcgcttggcctcgcgcgcagatcagttgg
aagaatttgtccactacgtgaaaggcgagatcaccaaggtagtcggcaaataagatgccgctcgccagtcgattggctgagctcatgaagttcctat
tccgaagttccgcgaacgcgtaaaggatctaggtgaagatccttttttgataatctcatgaccaaaatcccttaacgtgagttttcgttccactgagc
gtcagaccccgtagaaaagatcaaaggatcttcttgagatcctttttttctgcgcgtaatctgctgcttgcaaacaaaaaaaccaccgctaccagcg
gtggtttgtttgccggatcaagagctaccaactctttttccgaaggtaactggcttcagcagagcgcagataccaaatactgtccttctagtgtagc
cgtagttaggccaccacttcaagaactctgtagcaccgcctacatacctcgctctgctaatcctgttaccagtggctgctgccagtggcgataagtc
gtgtcttaccgggttggactcaagacgatagttaccggataaggcgcagcggtcgggctgaacgggggggttcgtgcacacagcccagcttggagcga
acgacctacaccgaactgagatacctacagcgtgagctatgagaaagcgccacgcttcccgaagggagaaaggcggacaggtatccggtaagcggca
gggtcggaacaggagagcgcacgagggagcttccagggggaaacgcctggtatctttatagtcctgtcgggtttcgccacctctgacttgagcgtcg
atttttgtgatgctcgtcaggggggcggagcctatggaaaaacgccagcaacgcggcctttttacggttcctggccttttgctggccttttgctcac
atgttctttcctgcgttatcccctgattctgtggataaccgtattaccgcctttgagtgagctgataccgctcgccgcagccgaacgaccgagcgca
gcgagtcagtgagcgaggaagcggaagagcgcctgatgcggtattttctccttacgcatctgtgcggtatttcacaccgcatatgctggatcc

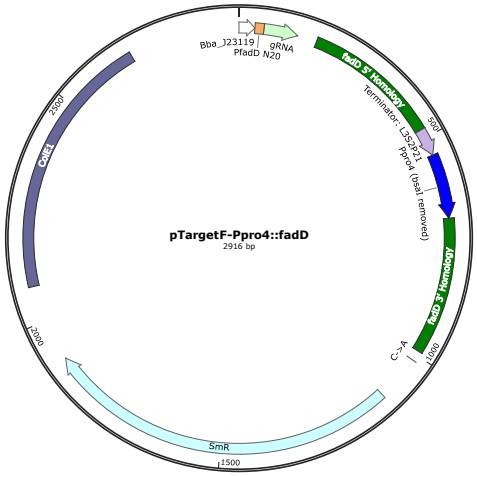

pTargetF-P$_{pro4}$::fadD. Features: *fadD* N20, orange; Homology arms, green; Terminator L3S2P21, purple; Promoter Ppro4, blue;

ttgacagctagctcagtcctaggtataatactagtccgctgtttctgcattcttagttttagagctagaaatagcaagttaaaataaggctagtccg
ttatcaacttgaaaaagtggcaccgagtcggtgctttttttgaattctctagagtcgacctgcagaagcttagatctcggttttctggacccggtgg
atttccgtggacaactggttacggtagtcgggccaatcactggtgcggttgacggcaaaatcggcaatacgccctataaatttatggtgatgcaagt
aacgggttacaaacgttggcatttaacccagcaggtgattatgccgcctcagccgattgatccatggtttatggcggtcgtggctggccctatggc
tacggcggatggggctggtataatcccggccccgcgagagtacaaacagttgtaactgaataattgcttgtttttaaagaaaaagaaacagcctcgg
taccaaattccagaaaagaggcctcccgaaaggggggccttttttcgttttggtcccacagctaacaccacgtcgtccctatctgctgccctaggtc
tatgagtggttgctggataactttacgggcatgcataaggctcggatgatatattcagggagtcgacaacggtttccctctacaaataattttgttt
aactttaacggcatgtatatcatttggggttgcgatgacgacgaacacgcattttagaggtgaagaattgaagaaggtttggcttaaccgttatccc
gcggacgttccgacggagatcaaccctgaccgttatcaatctctggtagatatgtttgagcagtcggtcgcgcgctacgccgatcaacctgcgtttg
tgaatatgggggaggtaatgaccttccgcaagctggaagaacgcagtcgcgcgtttgccgcttatttgcaacaagggttggggctgaagaaaggcga
tcgcgttgcgttgatgatgcctcgagttcatgtgcagctccatcagcaaaaggggatgataagtttatcaccaccgactatttgcaacagtgccgtt
gatcgtgctatgatcgactgatgtcatcagcggtggagtgcaatgtcatgagggaagcggtgatcgccgaagtatcgactcaactatcagaggtagt
tggcgtcatcgagcgccatctcgaaccgacgttgctggccgtacatttgtacggctccgcagtggatggcggcctgaagccacacagtgatattgat
ttgctggttacggtgaccgtaaggcttgatgaaacaacgcggcgagctttgatcaacgacctttttggaaacttcggcttcccctggagagagcgaga
ttctccgcgctgtagaagtcaccattgttgtgcacgacgacatcattccgtggcgttatccagctaagcgcgaactgcaatttggagaatggcagcg
caatgacattcttgcaggtatcttcgagccagccacgatcgacattgatctggctatcttgctgacaaaagcaagagaacatagcgttgccttggta
ggtccagcggcggaggaactctttgatccggttcctgaacaggatctatttgaggcgctaaatgaaaccttaacgctatggaactcgccgcccgact
gggctggcgatgagcgaaatgtagtgcttacgttgtcccgcatttggtacagcgcagtaaccggcaaaatcgcgccgaaggatgtcgctgccgactg
ggcaatggagcgcctgccggcccagtatcagcccgtcatacttgaagctagacaggcttatcttggacaagaagaagatcgcttggcctcgcgcgca
gatcagttggaagaatttgtccactacgtgaaaggcgagatcaccaaggtagtcggcaaataagatgccgctcgccagtcgattggctgagctcatg
aagttcctattccgaagttccgcgaacgcgtaaaggatctaggtgaagatccttttgataatctcatgaccaaaatcccttaacgtgagttttcgt
tccactgagcgtcagaccccgtagaaaagatcaaaggatcttcttgagatcctttttttctgcgcgtaatctgctgcttgcaaacaaaaaaaccacc
gctaccagcggtggtttgtttgccggatcaagagctaccaactctttttccgaaggtaactggcttcagcagagcgcagataccaaatactgtcctt
ctagtgtagccgtagttaggccaccacttcaagaactctgtagcaccgcctacatacctcgctctgctaatcctgttaccagtggctgctgccagtg
gcgataagtcgtgtcttaccgggttggactcaagacgatagttaccggataaggcgcagcggtcgggctgaacgggggttcgtgcacacagcccag
cttggagcgaacgacctacaccgaactgagatacctacagcgtgagctatgagaaagcgccacgcttcccgaagggagaaaggcggacaggtatccg
gtaagcggcagggtcggaacaggagagcgcacgagggagcttccagggggaaacgcctggtatctttatagtcctgtcgggtttcgccacctctgac
ttgagcgtcgatttttgtgatgctcgtcaggggggcggagcctatggaaaaacgccagcaacgcggcctttttacggttcctggccttttgctggcc
ttttgctcacatgttctttcctgcgttatcccctgattctgtggataaccgtattaccgcctttgagtgagctgataccgctcgccgcagccgaacg
accgagcgcagcgagtcagtgagcgaggaagcggaagagcgcctgatgcggtattttctccttacgcatctgtgcggtatttcacaccgcatatgct
ggatcc

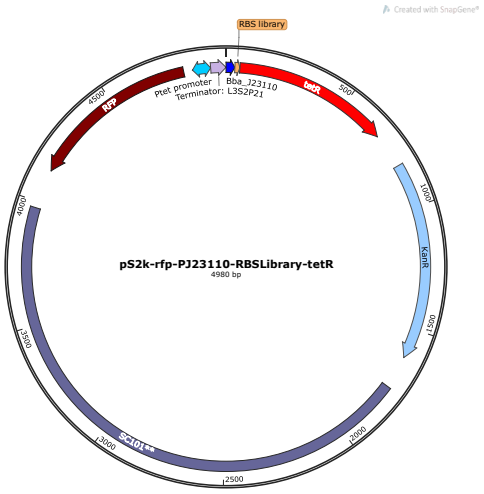

pSk-P$_{Tet}$-rfp-P$_{J23110}$-RBSLibrary-tetR. Features: Terminator L3S2P21, purple; Promoter Bba_J23110, blue; RBS Library, orange; *tetR*, red; *rfp*, dark red; P$_{tet}$ bi-directional promoter, light blue.

ctcggtaccaaattccagaaaagaggcctcccgaaaggggggccttttttcgttttggtcctttacggctagctcagtcctacgtacaatgctagct
ttaagaaggNNNtatacatatgatgtctagattagataaaagtaaagtgattaacagcgcattagagctgcttaatgaggtcggaatcgaaggttta
acaacccgtaaactcgcccagaagctaggtgtagagcagcctacattgtattggcatgtaaaaaataagcgggctttgctcgacgccttagccattg
agatgttagataggcaccatactcacttttgccctttagaaggggaaagctggcaagatttttacgtaataacgctaaaagttttagatgtgcttt
actaagtcatcgcgatggagcaaaagtacatttaggtacacggcctacagaaaaacagtatgaaactctcgaaaatcaattagccttttttatgccaa
caaggtttttcactagagaatgcattatatgcactcagcgctgtggggcattttactttaggttgcgtattggaagatcaagagcatcaagtcgcta
aagaagaaagggaaacacctactactgatagtatgccgccattattacgacaagctatcgaattatttgatcaccaaggtgcagagccagccttctt
attcggccttgaattgatcatatgcggattagaaaaacaacttaaatgtgaaagtgggtcttaagacgtcggaattgccagctggggcgccctctgg
taaggttgggaagccctgcaaagtaaactggatggctttcttgccgccaaggatctgatggcgcaggggatcatgatctgatcaagagacaggatga
ggatcgtttcgcatgattgaacaagatggattgcacgcaggttctccggccgcttgggtggagaggctattcggctatgactgggcacaacagacaa
tcggctgctctgatgccgccgtgttccggctgtcagcgcaggggcgcccggttctttttgtcaagaccgacctgtccggtgccctgaatgaactgca
ggacgaggcagcgcggctatcgtggctggccacgacgggcgttccttgcgcagctgtgctcgacgttgtcactgaagcgggaagggactggctgcta
ttgggcgaagtgccggggcaggatctcctgtcatctcaccttgctcctgccgagaaagtatccatcatggctgatgcaatgcggcggctgcatacgc
ttgatccggctacctgcccattcgaccaccaagcgaaacatcgcatcgagcgagcacgtactcggatggaagccggtcttgtcgatcaggatgatct
ggacgaagagcatcaggggctcgcgccagccgaactgttcgccaggctcaaggcgcgcatgcccgacggcgaggatctcgtcgtgacccatggcgat
gcctgcttgccgaatatcatggtggaaaatggccgcttttctggattcatcgactgtggccggctgggtgtggcggaccgctatcaggacatagcgt
tggctacccgtgatattgctgaagagcttggcggcgaatgggctgaccgcttcctcgtgctttacggtatcgccgctcccgattcgcagcgcatcgc
cttctatcgccttcttgacgagttcttctgagcgggactctggggttcgagagctcgcttggactcctgttgatagatccagtaatgacctcagaac
tccatctggatttgttcagaacgctcggttgccgccgggcgtttttttattggtgagaatccaagcactagggacagtaagacgggtaagcctgttga
tgataccgctgccttactgggtgcattagccagtctgaatgacctgtcacgggataatccgaagtggtcagactggaaaatcagagggcaggaactg
ctgaacagcaaaaagtcagatagcaccacatagcagacccgccataaaacgccctgagaagcccgtgacgggcttttcttgtattatgggtagtttc
cttgcatgaatccataaaaggcgcctgtagtgccatttacccccattcactgccagagccgtgagcgcagcgaactgaatgtcacgaaaaagacagc
gactcaggtgcctgatggtcggagacaaaaggaatattcagcgatttgcccgagcttgcgagggtgctacttaagcctttagggttttaaggtctgt
tttgtagaggagcaaacagcgtttgcgacatccttttgtaatactgcggaactgactaaagtagtgagttatacacagggctgggatctattctttt
tatcttttttattctttctttattctataaattataaccacttgaatataaacaaaaaaaacacacaaaggtctagcggaatttacagagggtcta
gcagaatttacaagttttccagcaaaggtctagcagaatttacagatacccagatcaccgggaaaaggactagtaattatcattgactagcccatc
tcaattggtatagtgattaaaatcacctagaccaattgagatgtatgtctgaattagttgttttcaaagcaaatgaactagcgattagtcgctatga
cttaacggagcatgaaaccaagctaatttttatgctgtgtggcactactcaaccccacgattgaaaaccctacaaggaaagaacggacggtatcgttc
acttataaccaatacgctcagatgatgaacatcagtagggaaaatgcttatggtgtattagctaaagcaaccagagagctgatgacgagaactgtgg
aaatcaggaatcctttggttaaaggctttgagattttccagtggacaaactatgccaagttctcaagcgaaaaattagaattagtttttagtgaaga
gatattgccttatcttttccagttaaaaaaattcataaaatataatctggaacatgttaagtcttttgaaaacaaatactctatgaggatttatgag
tggttattaaaagaactaacacaaaagaaaactcacaaggcaaatatagagattagccttgatgaatttaagttcatgttaatgcttgaaaataact
accatgagtttaaaaggcttaaccaatgggttttgaaaccaataagtaaagatttaaacacttacagcaatatgaaattggtggttgataagcgagg
ccgcccgactgatacgttgattttccaagttgaactagatagacaaatggatctcgtaaccgaacttgagaacaaccagataaaaatgaatggtgac
aaaatacaacaaccattacatcagattcctacctacataacggactaagaaaaacactacacgatgctttaactgcaaaaattcagctcaccagtt
ttgaggcaaaatttttgagtgacatgcaaagtaagtatgatctcaatggttcgttctcatggctcacgcaaaaacaacgaaccacactagagaacat
actggctaaatacggaaggatctgaggttcttatggctcttgtatctatcagtgaagcatcaagactaacaaacaaaagtagaacaactgttcaccg
ttacatatcaaagggaaaactgtccatatgcacagatgaaaacggtgtaaaaaagatagatacatcagagctttacgagttttggtgcattcaaa
gctgttcaccatgaacagatcgacaatgtaacagatgaacagcatgtaacacctaatagaacaggtgaaaccagtaaaacaaagcaactagaacatg
aaattgaacacctgagacaacttgttacagctcaacagtcacacatagacagcctgaaacaggcgatgctgcttatcgaatcaaagctgccgacaac
acgggagccagtgacgcctcccgtggggaaaaaatcatggcaattctggaagaaatagcgctttcagccggcaaaccggctgaagccggatctgcga

ttctgataacaaactagcaacaccagaacagcccgtttgcgggcagcaaaaccctaccctaggtataaacgcagaaaggcccaccgaaggtgagc
cagtgtgactctagtagagagcgttcaccgacaaacaacagataaaacgaaaggcccagtctttcgactgagcctttcgttttatttgatgcctgga
gatccttactcgagtttggatccttaagcaccggtggagtgacgaccttcagcacgttcgtactgttcaacgatggtgtagtcttcgttgtgggagg
tgatgtccagtttgatgtcggttttgtaagcacccggcagctgaaccggtttttttagccatgtaggtggttttaacttcagcgtcgtagtgaccacc
gtctttcagtttcagacgcattttgatttcacctttcagagcaccgtcttccgggtacatacgttcggtggaagcttcccaacccatggtttttttc
tgcataaccggaccgtcggacgggaagttggtaccacgcagtttaactttgtagatgaactcaccgtcttgcagggaggagtcctgggtaacggtaa
caacaccaccgtcttcgaagttcataacacgttcccatttgaaaccttccgggaaggacagtttcaggtagtccgggatgtcagccgggtgtttaac
gtaagctttggaaccgtactggaactgcggggacaggatgtcccaagcgaacggcagcggaccacctttggtaactttcagtttagcggtctgggta
ccttcgtacggacgaccttcaccttcaccttcgatttcgaactcgtgaccgttaacggaaccttccatacgaactttgaaacgcatgaactctttga
taacgtcttcgctactcgccatatgtatatctccttcttaaaagatcttttgaattcttttctctatcactgatagggagtggtaaaataactctat
caacgatagagtgtcaacaaaaattaggaatta

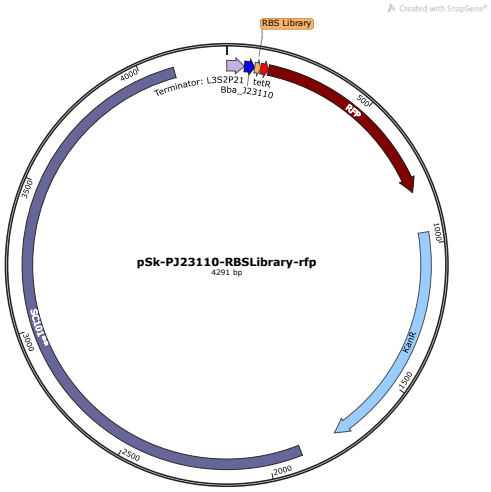

pSk-P$_{J23110}$-RBSLibrary-rfp. Features: Terminator L3S2P21, purple; Promoter Bba_J23110, blue; RBS Library, orange; *tetR* first 9 codons, red; *rfp*, dark red.

ctcggtaccaaattccagaaaagaggcctcccgaaagggggggccttttttcgttttggtcctttacggctagctcagtcctacgtacaatgctagct
ttaagaaggNNNtatacatatgatgtctagattagataaaagtaaagcgagtagcgaagacgttatcaaagagttcatgcgtttcaaagttcgtatg
gaaggttccgttaacggtcacgagttcgaaatcgaaggtgaaggtgaaggtcgtccgtacgaaggtacccagaccgctaaactgaaagttaccaaag
gtggtccgctgccgttcgcttgggacatcctgtccccgcagttccagtacggttccaaagcttacgttaaacacccggctgacatcccggactacct
gaaactgtccttcccggaaggtttcaaatgggaacgtgttatgaacttcgaagacggtggtgttgttaccgttacccaggactcctccctgcaagac
ggtgagttcatctacaaagttaaactgcgtggtaccaacttcccgtccgacggtccggttatgcagaaaaaaaccatgggttgggaagcttccaccg
aacgtatgtacccggaagacggtgctctgaaaggtgaaatcaaaatgcgtctgaaactgaaagacggtggtcactacgacgctgaagttaaaaccac
ctacatggctaaaaaaccggttcagctgccgggtgcttacaaaaccgacatcaaactggacatcacctcccacaacgaagactacaccatcgttgaa
cagtacgaacgtgctgaaggtcgtcactccaccggtgcttaagacgtcggaattgccagctggggcgccctctggtaaggttgggaagccctgcaaa
gtaaactggatggctttcttgccgccaaggatctgatggcgcaggggatcatgatctgatcaagagacaggatgaggatcgtttcgcatgattgaac
aagatggattgcacgcaggttctccggccgcttgggtggagaggctattcggctatgactgggcacaacagacaatcggctgctctgatgccgccgt
gttccggctgtcagcgcaggggcgcccggttctttttgtcaagaccgacctgtccggtgccctgaatgaactgcaggacgaggcagcgcggctatcg
tggctggccacgacgggcgttccttgcgcagctgtgctcgacgttgtcactgaagcgggaagggactggctgctattgggcgaagtgccggggcagg
atctcctgtcatctcaccttgctcctgccgagaaagtatccatcatggctgatgcaatgcggcggctgcatacgcttgatccggctacctgcccatt
cgaccaccaagcgaaacatcgcatcgagcgagcacgtactcggatggaagccggtcttgtcgatcaggatgatctggacgaagagcatcaggggctc
gcgccagccgaactgttcgccaggctcaaggcgcgcatgcccgacggcgaggatctcgtcgtgacccatggcgatgcctgcttgccgaatatcatgg
tggaaaatggccgcttttctggattcatcgactgtggccggctgggtgtggcggaccgctatcaggacatagcgttggctacccgtgatattgctga
agagcttggcggcgaatgggctgaccgcttcctcgtgctttacggtatcgccgctcccgattcgcagcgcatcgccttctatcgccttcttgacgag
ttcttctgagcgggactctggggttcgagagctcgcttggactcctgttgatagatccagtaatgacctcagaactccatctggatttgttcagaac
gctcggttgccgccgggcgtttttttattggtgagaatccaagcactagggacagtaagacgggtaagcctgttgatgataccgctgccttactgggt
gcattagccagtctgaatgacctgtcacgggataatccgaagtggtcagactggaaaatcagagggcaggaactgctgaacagcaaaaagtcagata
gcaccacatagcagacccgccatagaaacgccctgagaagcccgtgacgggcttttcttgtattatgggtagtttccttgcatgaatccataaaaggc
gcctgtagtgccatttaccccccattcactgccagagccgtgagcgcagcgaactgaatgtcacgaaaaagacagcgactcaggtgcctgatggtcgg
agacaaaaggaatattcagcgatttgcccgagcttgcgagggtgctacttaagcctttagggttttaaggtctgttttgtagaggagcaaacagcgt
ttgcgacatccttttgtaatactgcggaactgactaaagtagtgagttatacacagggctgggatctattcttttttatcttttttattctttcttt
attctataaattataaccacttgaatataaacaaaaaaaacacacaaaggtctagcggaatttacagagggtctagcagaatttacaagttttccag

caaaggtctagcagaatttacagatacccagatcacccgggaaaaggactagtaattatcattgactagcccatctcaattggtatagtgattaaaa
tcacctagaccaattgagatgtatgtctgaattagttgttttcaaagcaaatgaactagcgattagtcgctatgacttaacggagcatgaaaccaag
ctaattttatgctgtgtggcactactcaacccccacgattgaaaaccctacaaggaaagaacggacggtatcgttcacttataaccaatacgctcaga
tgatgaacatcagtagggaaaatgcttatggtgtattagctaaagcaaccagagagctgatgacgagaactgtggaaatcaggaatcctttggttaa
aggctttgagattttccagtggacaaactatgccaagttctcaagcgaaaaattagaattagtttttagtgaagagatattgccttatcttttccag
ttaaaaaaattcataaaatataatctggaacatgttaagtcttttgaaaacaaatactctatgaggatttatgagtggttattaaaagaactaacac
aaaagaaaactcacaaggcaaatatagagattagccttgatgaatttaagttcatgttaatgcttgaaaataactaccatgagtttaaaaggcttaa
ccaatgggttttgaaaccaataagtaaagatttaaacacttacagcaatatgaaattggtggttgataagcgaggccgcccgactgatacgttgatt
ttccaagttgaactagatagacaaatggatctcgtaaccgaacttgagaacaaccagataaaaatgaatggtgacaaaataccaacaaccattacat
cagattcctacctacataacggactaagaaaaacactacacgatgctttaactgcaaaaattcagctcaccagttttgaggcaaaatttttgagtga
catgcaaagtaagtatgatctcaatggttcgttctcatggctcacgcaaaaacaacgaaccacactagagaacatactggctaaatacggaaggatc
tgaggttcttatggctcttgtatctatcagtgaagcatcaagactaacaaacaaaagtagaacaactgttcaccgttacatatcaaagggaaaactg
tccatatgcacagatgaaaacggtgtaaaaaagatagatacatcagagcttttacgagtttttggtgcattcaaagctgttcaccatgaacagatcg
acaatgtaacagatgaacagcatgtaacacctaatagaacaggtgaaaccagtaaaacaaagcaactagaacatgaaattgaacacctgagacaact
tgttacagctcaacagtcacacatagacagcctgaaacaggcgatgctgcttatcgaatcaaagctgccgacaacacgggagccagtgacgcctccc
gtggggaaaaaatcatggcaattctggaagaaatagcgctttcagccggcaaaccggctgaagccggatctgcgattctgataacaaactagcaaca
ccagaacagcccgtttgcgggcagcaaaacccgtaccctaggtataaacgcagaaaggcccacccgaaggtgagccagtgtgactctagtagagagc
gttcaccgacaaacaacagataaaacgaaaggcccagtctttcgactgagcctttcgttttatttgatgcctggagatccttactcgagtttggatc
cgtcaacaaaaattaggaatta

B.6 Appendix B References

Hartline, C. J., Mannan, A. A., Liu, D., Zhang, F., and Oyarzún, D. A. (2020). Metabolite sequestration enables rapid recovery from fatty acid depletion in *Escherichia coli*. *MBio* 11, e03112-19. doi:10.1128/mBio.03112-19.

Hooshangi, S., Thiberge, S., and Weiss, R. (2005). Ultrasensitivity and noise propagation in a synthetic transcriptional cascade. *Proc. Natl. Acad. Sci.* 102, 3581–3586. doi:10.1073/pnas.0408507102.

Lee, T. S., Krupa, R. A., Zhang, F., Hajimorad, M., Holtz, W. J., Prasad, N., et al. (2011). BglBrick vectors and datasheets: A synthetic biology platform for gene expression. *J. Biol. Eng.* 5, 15–17. doi:10.1186/1754-1611-5-12.

Mannan, A. A., Liu, D., Zhang, F., and Oyarzún, D. A. (2017). Fundamental design principles for transcription-factor-based metabolite biosensors. *ACS Synth. Biol.* 6, 1851–1859. doi:10.1021/acssynbio.7b00172.

Marino, S., Hogue, I. B., Ray, C. J., and Kirschner, D. E. (2008). A methodology for performing global uncertainty and sensitivity analysis in systems biology. *J. Theor. Biol.* 254, 178–196. doi:10.1016/j.jtbi.2008.04.011.

Noel, J. T., Pilyugin, S. S., and Narang, A. (2009). The diffusive influx and carrier efflux have a strong effect on the bistability of the lac operon in *Escherichia coli*. *J. Theor. Biol.* 256, 14–28. doi:10.1016/j.jtbi.2008.09.003.

Reuter, A., Virolle, C., Goldlust, K., Berne-Dedieu, A., Nolivos, S., and Lesterlin, C. (2020). Direct visualisation of drug-efflux in live *Escherichia coli* cells. *FEMS Microbiol. Rev.* 44, 782–792. doi:10.1093/femsre/fuaa031.

Rosenfeld, N., Elowitz, M. B., and Alon, U. (2002). Negative autoregulation speeds the response times of transcription networks. *J. Mol. Biol.* 323, 785–793. doi:10.1016/S0022-2836(02)00994-4.

Zhang, F., Carothers, J. M., and Keasling, J. D. (2012). Design of a dynamic sensor-regulator system for production of chemicals and fuels derived from fatty acids. *Nat. Biotechnol.* 30, 354–359. doi:10.1038/nbt.2149.

Appendix C: Supplemental Information for "Transient Antibiotic Tolerance Triggered by Nutrient Shifts from Gluconeogenic Carbon Sources to Fatty Acid"

Appendix C contains supplemental information for Chapter 4.

C.1 Chapter 4 Supplemental Figures

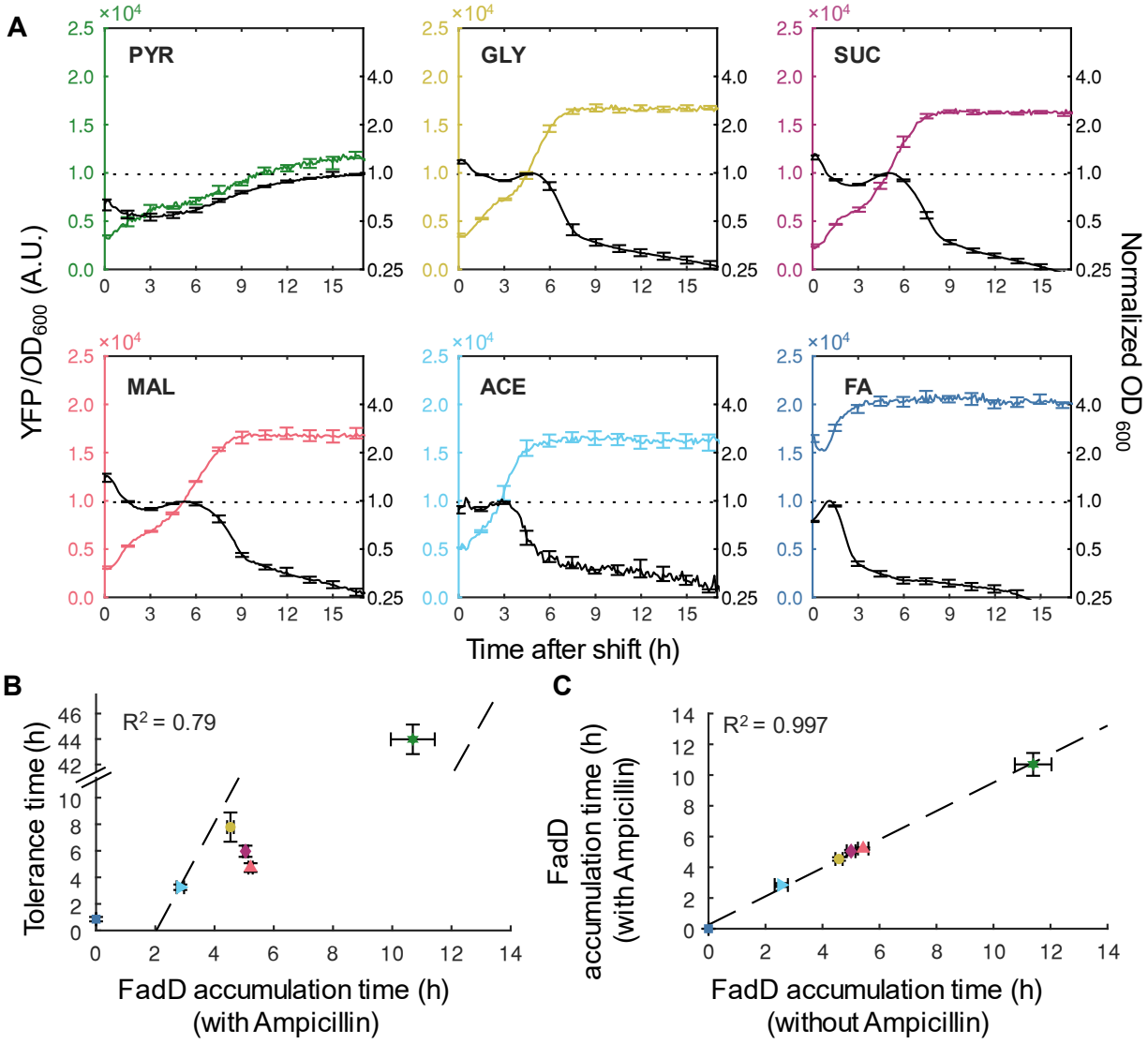

Figure C.1. FadD accumulation dynamics in the presence of ampicillin after nutrient shift. **(A)** Time course of YFP/OD_{600} from FadD-YFP fusion (colored line, left axis) and OD_{600} (black line, right axis) after switches from carbon sources to FA with ampicillin, n = 3, Error Bars

represent SEM. The dotted line indicates the FadD threshold as determined in Figure 4.3B, OD_{600} data normalized to the OD_{600} at the tolerance time determined by OD_{600}. **(B)** Correlation between tolerance time and time for FadD to accumulate to the FadD threshold (accumulation time) in the presence of ampicillin. Tolerance time data calculated from data in Figure 4.2B. Dashed line is a linear fit. **(C)** Correlation between FadD accumulation time in the presence and absence of ampicillin. Dashed line is linear fit to data.

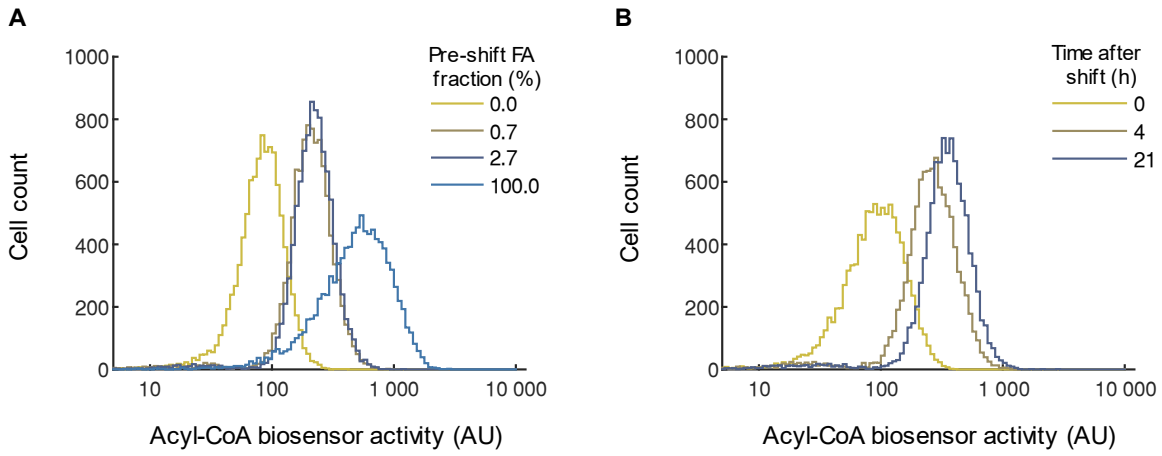

Figure C.2. Single-cell distribution of acyl-CoA biosensor activity during pyruvate to FA shifts. (A) Single-cell distribution of acyl-CoA biosensor activity during co-utilization of FA and pyruvate at different ratios. A single representative distribution is shown per condition, n = 10,000 per distribution. All distributions are unimodal, with the mean shifting higher for higher fractions of FA. **(B)** Time course single-cell distribution of acyl-CoA biosensor activity after shift from pyruvate to FA with ampicillin. A single representative distribution is shown per time point, n = 10,000. All distributions are monomodal, with mean biosensor activity increasing over time after shift to FA. The acyl-CoA biosensor kinetics after the shift are consistent with the FadD kinetics measured on plate reader (Figure C.1, pyruvate).

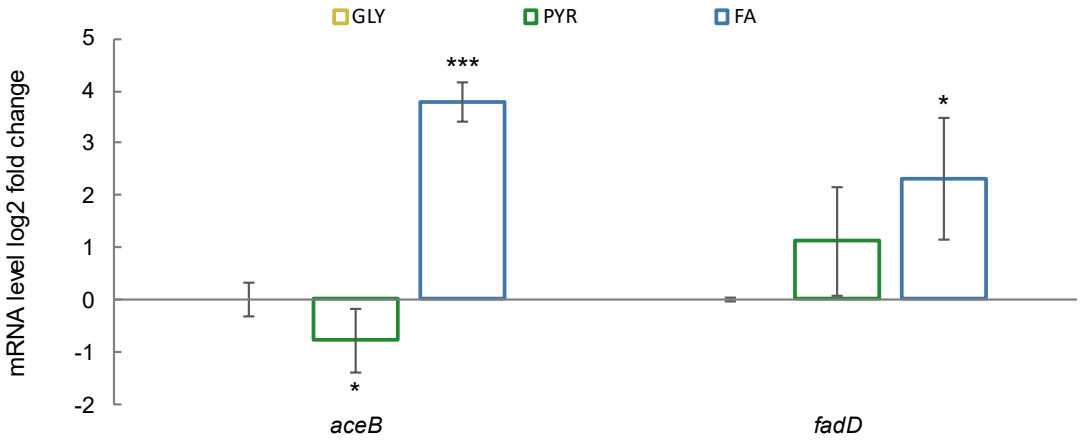

Figure C.3. Pre-shift relative transcription levels for *aceB* and *fadD* genes. mRNA levels of genes measured from steady state cultures growing in glycerol (left, yellow), pyruvate (middle, green), or FA, (right, blue). Transcription levels are relative to pre-shift growth in glycerol. n = 3 biological replicates, Error bars represent standard deviation. Stars indicate significant change in transcription compared to glycerol, two-tailed t-test (*, $p < 0.05$, *** $p < 0.001$)

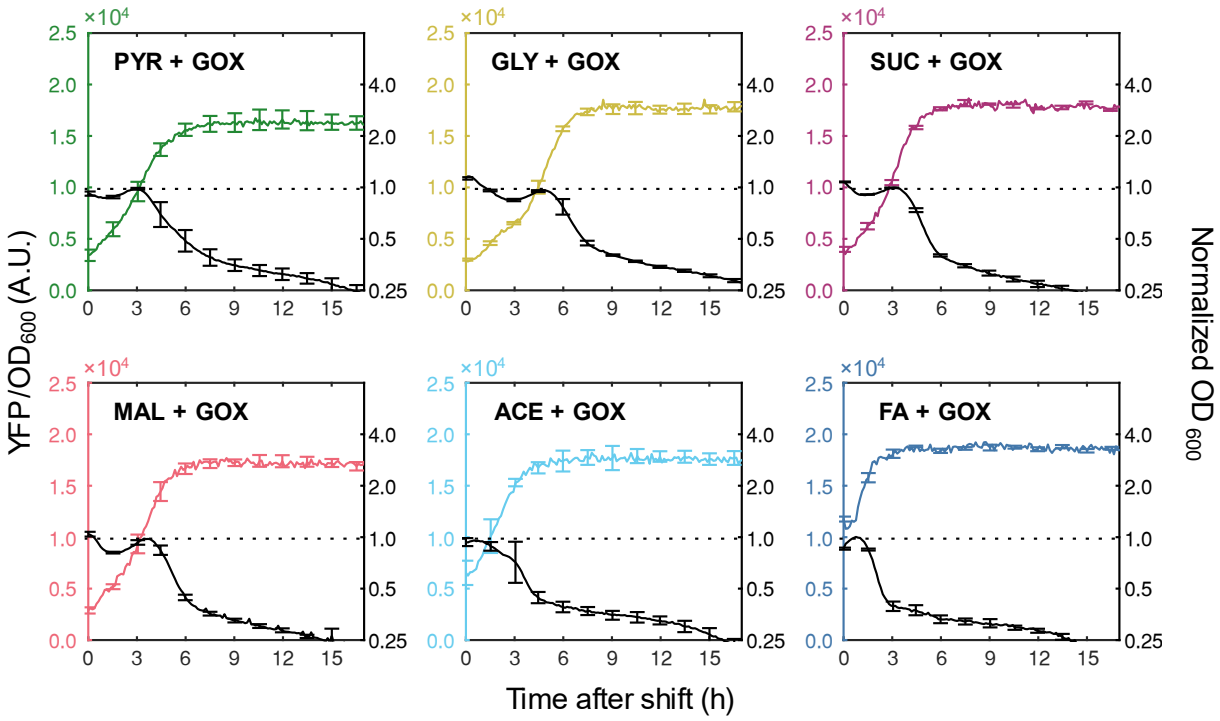

Figure C.4. FadD accumulation dynamics in the presence of ampicillin after nutrient shift with pre-shift glyoxylate. Time course of YFP/OD_{600} from FadD-YFP fusion (colored line, left axis) and OD_{600} (black line, right axis) after shifts from a glyoxylate supplemented gluconeogenic carbon source to FA with ampicillin (not supplemented with glyoxylate), n = 3, Error Bars represent SEM. The dotted line indicates the FadD threshold as determined in Figure 4.3B, OD_{600} data is normalized to the OD_{600} at the tolerance time determined by OD_{600} (Note: Normalized OD_{600} serves only as approximate measure of cell survival, since OD cannot accurately determine the fraction of live and dead cells).

C.2 Chapter 4 Supplemental Tables

Table C.1. Fitted parameters for two-population Gompertz model.

Model parameters are given along with their 95% confidence intervals, N.D.: Not Determined

Pre-Shift Medium	Tolerance Time (τ) (hours)	Transient Tolerant Killing Rate (μ_{TT}) ($hour^{-1}$)	Persister Killing Rate (μ_{TT}) ($hour^{-1}$)	Log_{10} Persister Fraction ($log_{10}(p)$)
4mM FA	0.9 ± 0.3	1.25 ± 0.22	0.076 ± 0.011	-4.1 ± 0.2
24 mM Acetate	3.3 ± 0.4	0.62 ± 0.09	0.122 ± 0.014	-2.9 ± 0.2
18 mM Malate	4.7 ± 0.6	0.43 ± 0.05	0.053 ± 0.023	-4.3 ± 0.4
18 mM Succinate	6.0 ± 0.8	0.59 ± 0.14	0.101 ± 0.020	-3.1 ± 0.3
24 mM Glycerol	7.8 ± 2.2	1.22 ± 11.91	0.167 ± 0.025	-1.9 ± 0.3
24 mM Pyruvate	44.0 ± 3.2	0.13 ± 0.04	0.015 ± 0.008	-3.2 ± 0.4
23.8 mM Glycerol, 0.03 mM FA	2.7 ± 0.4	0.68 ± 0.07	N.D.	N.D.
23.3 mM Glycerol, 0.11 mM FA	1.7 ± 0.4	1.06 ± 0.23	0.249 ± 0.156	-3.2 ± 0.9

Table C.2. Strains, plasmids, and primers used in this study.

Strain	**Genotype**	**Source or Reference**
NCM3722 (WT)	F^+	CGSC#:12355
Acyl-CoA-Biosensor Strain	NCM3722 pSARk-yemGFP	This work
FadD-YFP Strain	NCM3722 Φ(*fadD-YFP*)	This work
Plasmids	**Genotype**	**Source**
pSARk-yemGFP	SC101 ori, KAN^R, P_{AR}-*yemgfp*	This work
pTargetF-FadD-YFP	colE1 ori, $SPEC^R$,	This work
Cloning primers	**Sequence**	**Source**
yemGFP_F	TTCAAAAGATCTTTTAAGAA GGAGATATACATATGTCTAA AGGTGAAGAATTATTCAC	This work
yemGFP_R	GAGTTTGGATCCTTATTTGTA CAATTCATCCATACC	This work
pTargetF_FadDN20_F	GGCATTGGTCTCGGACTTAAC GCTCGTTTTAGAGCTAGAAAT AGCAAGTTAAAATAA	This work
pTargetF_FadDN20_R	TTCCACGGTCTCCCCAGATCT AAGCTTCTGCAGG	This work
pTargetF_FadD_ upstream_F	TTCCACGGTCTCCCTGGTTTTA ACGTCTATCCCAAC	This work
pTargetF_FadD_ upstream_16L_part1_R	CCGCCGCCGTTAGAGGGAGTG CTACCACCGGCTTTATTGTCCA CTTTGCC	This work
pTargetF_FadD_ upstream_16L_part2	ACAGCTGGTCTCCCTACCACCG CTGCCGCTGCCGTCGTCGCCGC CGCCGTTAGAGGG	This work
pTargetF_YFP_F	ACAGCTGGTCTCCGTAGCAAAG GTGAAGAACTGTTCAC	This work
pTargetF_YFP_R	TTCCACGGTCTCCCATTATTTAT ACAGTTCGTCCATACCC	This work
pTargetF_FadD_ downstream_F	TTCCACGGTCTCGAATGAGCGT TAAGTCAGTCG	This work
pTargetF_FadD_ downstream_R	TTCCACGGTCTCGAGAACCCCA GCTGCGGGTAA	This work
pTargetF_ Backbone_F	TTCCACGGTCTCGTTCTCGAGTT CATGTGCAGC	This work
pTargetF_ Backbone_R	GGCATTGGTCTCGAGTCAGTCG TCAACTAGTATTATACCTAGGACTGAGC	This work

qPCR primers	Sequence	Source or Reference
gyrA_F	GTCGTGGCGGGAAAGGTAAA	
gyrA_R	CGGCTGGAGAAGCACAGAA	
aceB_F	ACCTTGTGATGGTGAACGCA	
aceB_R	TCCACTGCCAGATCGAGGTA	
fadD_F	CCGATCAACCTGCGTTTGTG	
fadD_R	TTCTTCAGCCCCAACCCTTG	

Table C.3. DNA sequences of plasmids and strains constructed in this study.

DNA	Sequence	Feature Notes
pSARk-yemGFP	aaaatttatcaaaaagagtgttgactatctggtacgaccagatgatacttagattcat ctggtacgaccagataccgaattcaaaagatcttttaagaaggagatatacatatgtc taaaggtgaagaattattcactggtgttgtcccaattttggttgaattagatggtgat gttaatggtcacaaatttttctgtctccggtgaaggtgaaggtgatgctacttacggta aattgaccttaaaatttatttgtactactggtaaattgccagttccatggccaaccctt agtcactactttaacttatggtgttcaatgtttttctagatacccagatcatatgaaa caacatgacttttcaagtctgccatgccagaaggttatgttcaagaaagaactattt ttttcaaagatgacggtaactacaagaccagagctgaagtcaagtttgaaggtgatac cttagttaatagaatcgaattaaaaggtattgattttaaagaagatggtaacatttta ggtcacaaattggaatacaactataactctcacaatgtttacatcatggctgacaaac aaaagaatggtatcaaagttaacttcaaaattagacacaacattgaagatggttctgt tcaattagctgaccattatcaacaaaatactccaattggtgatggtccagtcttgtta ccagacaaccattacttatccactcaatctaaattatccaaagatccaaacgaaaaga gagaccacatggtcttgttagaatttgttactgctgctggtattacccatggtatgga tgaattgtacaaataaggatccaaactcgagtaaggatctccaggcatcaaataaaac gaaaggctcagtcgaaagactgggcctttcgttttatctgttgtttgtcggtgaacgc tctctactagagtcacactggctcaccttcgggtgggcctttctgcgtttatacctag ggtacgggttttgctgcccgcaaacgggctgttctggtgttgctagtttgttatcaga atcgcagatccggcttcagccggtttgccggctgaaagcgctatttcttccagaattg ccatgatttttttccccacgggaggcgtcactggctcccgtgttgtcggcagctttgat tcgataagcagcatcgcctgtttcaggctgtctatgtgtgactgttgagctgtaacaa gttgtctcaggtgttcaatttcatgttctagttgctttgttttactggtttcacctgt tctattaggtgttacatgctgttcatctgttacattgtcgatctgttcatggtgaaca gctttgaatgcaccaaaaactcgtaaaagctctgatgtatctatctttttacaccgt tttcatctgtgcatatggacagttttcccttgatatgtaacggtgaacagttgttct acttttgtttgttagtcttgatgcttcactgatagatacaagagccataagaacctca gatccttccgtatttagccagtatgttctctagtgtggttcgttgtttttgcgtgagc catgagaacgaaccattgagatcatacttactttgcatgtcactcaaaaattttgcct caaaactggtgagctgaatttttgcagttaaagcatcgtgtagtgtttttcttagtcc gttatgtaggtaggaatctgatgtaatggttgttggtattttgtcaccattcatttt atctggttgttctcaagttcggttacgagatccatttgtctatctagttcaacttgga aaatcaacgtatcagtcgggcggcctcgcttatcaaccaccaatttcatattgctgta agtgtttaaatctttacttattggtttcaaaacccattggttaagccttttaaactca tggtagttatttcaagcattaacatgaacttaaattcatcaaggctaatctctatat ttgccttgtgagttttcttttgtgttagttcttttaataaccactcataaatcctcat agagtatttgtttttcaaaagacttaacatgttccagattatattttatgaatttttt aactggaaaagataaggcaatatctcttcactaaaaactaattctaatttttcgcttg agaacttggcatagtttgtccactggaaaatctcaaagcctttaaccaaaggattcct gatttccacagttctcgtcatcagctctctggttgctttagctaatacaccataagca ttttccctactgatgttcatcatctgagcgtattggttataagtgaacgataccgtcc gttctttccttgtagggttttcaatcgtggggttgagtagtgccacacagcataaaat tagcttggtttcatgctccgttaagtcatagcgactaatcgctagttcatttgctttg aaaacaactaattcagacatacatctcaattggtctaggtgattttaatcactatacc aattgagatgggctagtcaatgataattactagtccttttcccgggtgatctgggtat ctgtaaattctgctagacctttgctggaaaacttgtaaattctgctagaccctctgta aattccgctagacctttgtgtgttttttttgtttatattcaagtggttataatttata	Blue: pAR promoter Green: yemGFP

	gaataaagaaagaataaaaaaagataaaaagaatagatcccagccctgtgtataactc actactttagtcagttccgcagtattacaaaaggatgtcgcaaacgctgtttgctcct ctacaaaacagaccttaaaaccctaaaggcttaagtagcaccctcgcaagctcgggca aatcgctgaatattccttttgtctccgaccatcaggcacctgagtcgctgtctttttc gtgacattcagttcgctgcgctcacggctctggcagtgaatgggggtaaatggcacta caggcgccttttatggattcatgcaaggaaactacccataatacaagaaaagcccgtc acgggcttctcagggcgttttatggcgggtctgctatgtggtgctatctgactttttg ctgttcagcagttcctgccctctgattttccagtctgaccacttcggattatcccgtg acaggtcattcagactggctaatgcacccagtaaggcagcggtatcatcaacaggctt acccgtcttactgtccctagtgcttggattctcaccaataaaaaacgcccggcggcaa ccgagcgttctgaacaaatccagatggagttctgaggtcattactggatctatcaaca ggagtccaagcgagctctcgaaccccagagtcccgctcagaagaactcgtcaagaagg cgatagaaggcgatgcgctgcgaatcgggagcggcgataccgtaaagcacgaggaagc ggtcagcccattcgccgccaagctcttcagcaatatcacgggtagccaacgctatgtc ctgatagcggtccgccacacccagccggccacagtcgatgaatccagaaaagcggcca ttttccaccatgatattcggcaagcaggcatcgccatgggtcacgacgagatcctcgc cgtcgggcatgcgcgccttgagcctggcgaacagttcggctggcgcgagcccctgatg ctcttcgtccagatcatcctgatcgacaagaccggcttccatccgagtacgtgctcgc tcgatgcgatgtttcgcttggtggtcgaatgggcaggtagccggatcaagcgtatgca gccgccgcattgcatcagccatgatggatactttctcggcaggagcaaggtgagatga caggagatcctgccccggcacttcgcccaatagcagccagtcccttcccgcttcagtg acaacgtcgagcacagctgcgcaaggaacgcccgtcgtggccagccacgatagccgcg ctgcctcgtcctgcagttcattcagggcaccggacaggtcggtcttgacaaaaagaac cgggcgcccctgcgctgacagccggaacacggcggcatcagagcagccgattgtctgt tgtgcccagtcatagccgaatagcctctccacccaagcggccggagaacctgcgtgca atccatcttgttcaatcatgcgaaacgatcctcatcctgtctcttgatcagatcatga tcccctgcgccatcagatccttggcggcaagaaagccatccagtttactttgcagggc ttcccaaccttaccagagggcgccccagctggcaattccgacgtc	
pTargetF-fadD-YFP	tgacgactgacttaacgctcgttttagagctagaaatagcaagttaaaataaggctag tccgttatcaacttgaaaaagtggcaccgagtcggtgctttttttgaattctctagag tcgacctgcagaagcttagatctggttttaacgtctatcccaacgagattgaagatgt cgtcatgcagcatcctggcgtacaggaagtcgcggctgttggcgtaccttccggctcc agtggtgaagcggtgaaaatcttcgtagtgaaaaaagatccatcgcttaccgaagaga gcttagtgacttttgccgccgtcagctcacgggatacaaagtaccgaagctggtgga gtttcgtgatgagttaccgaaatctaacgtcggaaaaatttttgcgacgagaattacgt gacgaagcgcgcggcaaagtggacaataaagccggtggtagcactccctctaacggcg gcggcgacgacggcagcggtggtagcaaaggtgaagaactgttcaccggcgttgtgcc aattctggttgagctggatggtgacgtgaatggccacaaattttccgtgtctggtgaa ggcgagggtgatgctacttatggcaaactgactctgaaactgatctgtaccaccggca aactgcctgttccgtggccaactctggtcactactctgggttacggcgtgcagtgttt tgcgcgttacccggatcacatgaaacagcatgacttcttcaaatctgccatgccggaa ggctatgtccaagaacgtacgatctttttcaaggacgacggcaactataaaacccgtg ccgaagttaaattcgagggtgacaccctggttaaccgcatcgaactgaaaggcattga cttcaaagaggacggcaacattctgggtcacaagctggaatacaactacaactcccac aacgtttacattactgctgacaagcagaaaaacggcatcaaagcaaacttcaagatcc gtcacaacattgaagatggtggcgtacagctggcagatcactaccagcagaacactcc aatcggtgatggcccagtactgctgccagataaccattacctgtcctaccagagcaaa ctgtctaaagacccgaacgaaaaacgtgaccacatggtactgctggaatttgttaccg cggcaggcattaccctgggtatggacgaactgtataaataatgagcgttaagtcagtc gtcagacgccggttaatccggcgtttttttgacgcccactaaagagaaaacaatttg aattaccaaatgattaccacggacgatgcgctggcttctttgtgtgaagccgtccgtg cctttccggcgatagccctggatactgaatttgttcgtacgcgcacttattacccgca gctggggttctcgagttcatgtgcagctccatcagcaaaaggggatgataagtttatc accaccgactatttgcaacagtgccgttgatcgtgctatgatcgactgatgtcatcag cggtggagtgcaatgtcatgagggaagcggtgatcgccgaagtatcgactcaactatc agaggtagttggcgtcatcgagcgccatctcgaaccgacgttgctggccgtacatttg tacggctccgcagtggatggcggcctgaagccacacagtgatattgatttgctggtta cggtgaccgtaaggcttgatgaaacaacgcggcgagctttgatcaacgacctttttgga aacttcggcttcccctggagagagcgagattctccgcgctgtagaagtcaccattgtt gtgcacgacgacatcattccgtggcgttatccagctaagcgcgaactgcaatttggag aatggcagcgcaatgacattcttgcaggtatcttcgagccagccacgatcgacattga tctggctatcttgctgacaaaagcaagagaacatagcgttgccttggtaggtccagcg gcggaggaactctttgatccggttcctgaacaggatctatttgaggcgctaaatgaaa ccttaacgctatggaactcgccgcccgactgggctggcgatgagcgaaatgtagtgct tacgttgtcccgcatttggtacagcgcagtaaccggcaaaatcgcgccgaaggatgtc gctgccgactgggcaatggagcgcctgccggcccagtatcagcccgtcatacttgaag ctagacaggcttatcttggacaagaagaagatcgcttggcctcgcgcgcagatcagtt ggaagaatttgtccactacgtgaaaggcgagatcaccaaggtagtcggcaaataagat gccgctcgccagtcgattggctgagctcatgaagttcctattccgaagttccgcgaac gcgtaaaggatctaggtgaagatccttttgataatctcatgaccaaaatcccttaac gtgagttttcgttccactgagcgtcagaccccgtagaaaagatcaaaggatcttcttg	Blue: *fadD* N20, Red: *fadD* homology arms, Purple: Glycine-Serine rich linker; Yellow: YFP

	agatccttttttttctgcgcgtaatctgctgcttgcaaacaaaaaaaccaccgctacca gcggtggtttgtttgccggatcaagagctaccaactctttttccgaaggtaactggct tcagcagagcgcagataccaaatactgtccttctagtgtagccgtagttaggccacca cttcaagaactctgtagcaccgcctacatacctcgctctgctaatcctgttaccagtg gctgctgccagtggcgataagtcgtgtcttaccgggttggactcaagacgatagttac cggataaggcgcagcggtcgggctgaacgggggggttcgtgcacacagcccagcttgga gcgaacgacctacaccgaactgagatacctacagcgtgagctatgagaaagcgccacg cttcccgaagggagaaaggcggacaggtatccggtaagcggcagggtcggaacaggag agcgcacgagggagcttccagggggaaacgcctggtatctttatagtcctgtcgggtt tcgccacctctgacttgagcgtcgatttttgtgatgctcgtcaggggggcggagccta tggaaaaacgccagcaacgcggccttttacggttcctggccttttgctggccttttg ctcacatgttctttcctgcgttatcccctgattctgtggataaccgtattaccgcctt tgagtgagctgataccgctcgccgcagccgaacgaccgagcgcagcgagtcagtgagc gaggaagcggaagagcgcctgatgcggtattttctccttacgcatctgtgcggtattt cacaccgcatatgctggatccttgacagctagctcagtcctaggtataatactagt	
NCM3722 Φ(fadD-YFP) *fadD* genome region	ttgcttgtttttaaagaaaaagaaacagcggctggtccgctgtttctgcattcttacg gtaaagataaaaataaatagtgacgcgcttcgcaacctttcgttgggtaattatcaa gctggtatgatgagttaatattatgttaacggcatgtatatcatttggggttgcgatg acgacgaacacgcattttagaggtgaagaattgaagaaggtttggcttaaccgttatc ccgcggacgttccgacggagatcaaccctgaccgttatcaatctctggtagatatgtt tgagcagtcggtcgcgcgctacgccgatcaacctgcgtttgtgaatatgggggaggta atgaccttccgcaagctggaagaacgcagtcgcgcgtttgccgcttatttgcaacaag ggttggggctgaagaaaggcgatcgcgttgcgttgatgatgcctaatttattgcaata tccggtggcgctgtttggcattttgcgtgccgggatgatcgtcgtaaacgttaacccg ttgtataccccgcgtgagcttgagcatcagcttaacgatagcggcgcatcggcgattg ttatcgtgtctaactttgctcacacactggaaaaagtggttgataaaaccgccgttca gcacgtaattctgacccgtatgggcgatcagctatctacggcaaaaggcacggtagtc aatttcgttgttaaatacatcaagcgtttggtgccgaaataccatctgccagatgcca tttcatttcgtagcgcactgcataacggctaccggatgcagtacgtcaaacccgaact ggtgccggaagatttagcttttctgcaatacaccggcggcaccactggtgtggcgaaa ggcgcgatgctgactcaccgcaatatgctggcgaacctggaacaggttaacgcgacct atggtccgctgttgcatccgggcaaagagctggtggtgacggcgctgccgctgtatca catttttgccctgaccattaactgcctgctgtttatcgaactgggtgggcagaacctg cttatcactaacccgcgcgatattccagggttggtaaaagagttagcgaaatatccgt ttaccgctatcacgggcgttaacaccttgttcaatgcgttgctgaacaataaagagtt ccagcagctggatttctccagtctgcatctttccgcaggcggtgggatgccagtgcag caagtggtggcagagcgttgggtgaaactgaccggacagtatctgctggaaggctatg gccttaccgagtgtgcgccgctggtcagcgttaacccatatgatattgattatcatag tggtagcatcggtttgccggtgccgtcgacggaagccaaactggtggatgatgatgat aatgaagtaccaccaggtcaaccgggtgagctttgtgtcaaaggaccgcaggtgatgc tgggttactggcagcgtcccgatgctaccgatgaaatcatcaaaaatggctggttaca caccggcgacatcgcggtaatggatgaagaaggattcctgcgcattgtcgatcgtaaa aaagacatgattctggtttccggttttaacgtctatcccaacgagattgaagatgtcg tcatgcagcatcctggcgtacaggaagtcgcggctgttggcgtaccttccggctccag tggtgaagcggtgaaaatcttcgtagtgaaaaaagatccatcgcttaccgaagagtca ctggtgacttttgccgccgtcagctcacgggatacaaagtaccgaagctggtggagt ttcgtgatgagttaccgaaatctaacgtcggaaaaatttgcgacgagaattacgtga cgaagcgcgcggcaaagtggacaataaagccggtggtagcactccctctaacggcggc ggcgacgacggcagcggtggtagcaaaggtgaagaactgttcaccggcgttgtgccaa ttctggttgagctggatggtgacgtgaatggccacaaatttttccgtgtctggtgaagg cgagggtgatgctacttatggcaaactgactctgaaactgatctgtaccaccggcaaa ctgcctgttccgtggccaactctggtcactactctgggttacggcgtgcagtgttttg cgcgttacccggatcacatgaaacagcatgacttcttcaaatctgccatgccggaagg ctatgtccaagaacgtacgatctttttcaaggacgacggcaactataaaacccgtgcc gaagttaaattcgagggtgacaccctggttaaccgcatcgaactgaaaggcattgact tcaaagaggacggcaacattctgggtcacaagctggaatacaactacaactcccacaa cgtttacattactgctgacaagcagaaaaacggcatcaaagcaaacttcaagatccgt cacaacattgaagatggtggcgtacagctggcagatcactaccagcagaacactccaa tcggtgatggcccagtactgctgccagataaccattacctgtcctaccagagcaaact gtctaaagacccgaacgaaaaacgtgaccacatggtactgctggaatttgttaccgcg gcaggcattaccctgggtatggacgaactgtataaataatgagcgttaagtcagtcgt cagacgccggttaatccggcgtttttttttgacgcccactaaagagaaaacaat	Red: *fadD* CDS Purple: Glycine-Serine rich linker; Yellow: YFP